

UCLA

UCLA Electronic Theses and Dissertations

Title

Design and Synthesis of Multifunctional Mesoporous Silica Nanoparticles for Drug Delivery and Bioimaging Applications

Permalink

<https://escholarship.org/uc/item/7mk42466>

Author

Chen, Wei

Publication Date

2019

Peer reviewed|Thesis/dissertation

UNIVERSITY OF CALIFORNIA
Los Angeles

Design and Synthesis of
Multifunctional Mesoporous Silica Nanoparticles
for Drug Delivery and Bioimaging Applications

A dissertation submitted in partial satisfaction of the
requirements for the degree Doctor of Philosophy
in Chemistry

by

Wei Chen

2019

© Copyright by

Wei Chen

2019

ABSTRACT OF THE DISSERTATION

Design and Synthesis of
Multifunctional Mesoporous Silica Nanoparticles
for Drug Delivery and Bioimaging Applications

by

Wei Chen

Doctor of Philosophy in Chemistry

University of California, Los Angeles, 2019

Professor Jeffrey I. Zink, Chair

Multifunctional mesoporous silica nanoparticles (MSNs) have aroused much attention during the past decades for drug delivery and bioimaging applications because of their intrinsic properties including extremely high surface area, large pore volume, tunable pore diameter, easy surface modification, and high biocompatibility. Even though MSNs have these preeminent properties, rendering this unique nanostructure a promising nanocarrier for biomedical applications, several hurdles still challenge the fields of drug delivery and bioimaging when using MSNs as the nanocarriers: (i) high loading and high release amounts of water-insoluble drugs delivered to the site of diseases; (ii) precise control of the dosage of drugs delivered to the site of diseases using non-invasive external stimuli; and (iii) construction of MSNs-based shortwave infrared optical

imaging contrast agents as an innovative tool for bioimaging and cancer diagnostics. Therefore, this dissertation primarily focuses on the development of innovative strategies that solve these unmet needs and that advance the research in the field of biomedical applications using MSNs as the nanocarriers.

In this dissertation, first of all, we review the research work, which mainly focuses on the design and synthesis of multifunctional MSNs and nanomachines for biomedical applications in *Accounts of Chemical Research*. A wide variety of nanomachines responsive to the different stimuli (pH, redox, enzyme, heat, light, and/or magnetic field) are discussed in this Account. Additionally, we develop a facile strategy for MSNs delivery and release of the water-insoluble drug clofazimine (CFZ), which is used to treat multidrug-resistant tuberculosis. The strategy employs a companion molecule as a chaperone to improve both the loading of CFZ into the pores of MSNs and its subsequent release, thus enabling both high loading and high release of this water-insoluble drug by MSNs. *In vitro* treatment of macrophages infected with *Mycobacterium tuberculosis* with the optimized CFZ-loaded MSNs killed the bacteria in the cells in a dose-dependent manner. These studies demonstrate a highly efficient method for loading nanoparticles with water-insoluble drug molecules and the efficacy of the nanoparticles in delivering drugs into eukaryotic cells in aqueous media. Additionally, we used a noninvasive alternating magnetic field (AMF) to stimulate and control the dosage of drug release from MSNs. Noninvasive stimuli-responsive drug delivery using AMF in conjunction with superparamagnetic nanoparticles also offers the potential for the spatial and temporal control of drug release. *In vitro* studies showed that the death of pancreatic cancer cells treated by drug-loaded nanoparticles was controlled by

different lengths of AMF exposure time due to different amounts of drug released from the carriers. Finally, to develop a new shortwave infrared (SWIR) optical imaging contrast agent which has a higher tissue penetration depth, we demonstrate that J-aggregates of near infrared (NIR) fluorophore IR-140 can be prepared inside hollow mesoporous silica nanoparticles (HMSNs) to result in nanomaterials that absorb and emit SWIR light. The use of J-aggregates stabilized in HMSNs as SWIR imaging agents has the potential to overcome the stability, toxicity, and brightness challenges of contrast agents for this compelling region of the electromagnetic spectrum. Collectively, in this dissertation, we explore and develop innovative strategies to load and deliver high amounts of water-insoluble drugs; control the dosage of anticancer drugs released from MSNs triggered by an AMF; and establish a new SWIR optical imaging contrast agent based on the superior carriers – MSNs.

The dissertation of Wei Chen is approved.

Ellen M. Sletten

Xiangfeng Duan

Marcus A. Horwitz

Jeffrey I. Zink, Committee Chair

University of California, Los Angeles

2019

TABLE OF CONTENTS

Abstract	ii
Committee Page	v
List of Figures	vii
List of Tables	xvi
List of Schemes	xvii
Acknowledgements	xviii
Vita	xxiv
CHAPTER 1 Introduction	1
References 1.1	5
References 1.2	34
CHAPTER 2 Facile Strategy Enabling Both High Loading and High Release Amounts of the Water-Insoluble Drug Clofazimine Using Mesoporous Silica Nanoparticles	40
References	77
CHAPTER 3 Spatial, Temporal, and Dose Control of Drug Delivery using Noninvasive Magnetic Stimulation	83
References	137
CHAPTER 4 Shortwave Infrared Imaging with J-aggregates Stabilized in Hollow Mesoporous Silica Nanoparticles	145
References	209
CHAPTER 5 Analyte-Responsive Gated Hollow Mesoporous Silica Nanoparticles Exhibiting Inverse Functionality and an AND Logic Response	215
References	235

LIST OF FIGURES

Figure 1.1	Table of content figure of nanomachines and other caps on mesoporous silica nanoparticles (MSNs) for drug delivery	9
Figure 1.2	Collage of MSNs described in this <i>Accounts of Chemical Research</i>	11
Figure 1.3	Bioluminescence imaging of mice and quantification of bioluminescence	17
Figure 1.4	Quantification of the weight loss of tumor, metastasis, and ascites of mice	18
Figure 1.5	Schematic illustration of the pH-responsive benzimidazole nanovalve	20
Figure 1.6	Schematic illustration of the redox-responsive disulfide nanovalve	21
Figure 1.7	MSNs are avidly ingested by human macrophages infected with <i>Mycobacterium tuberculosis</i> and <i>Francisella tularensis</i>	24
Figure 1.8	Antibiotic-loaded MSNs rapidly kill <i>Mycobacterium tuberculosis in vitro</i> and <i>Francisella tularensis in vivo</i>	26
Figure 1.9	Schematic illustration of the construction and operation of the thermo-responsive cucurbit[6]uril nanovalve	29
Figure 1.10	Schematic illustration of the synthesis and operation of the thermo-sensitive azo cap	30
Figure 1.11	Effects of alternating magnetic field (AMF) stimulated doxorubicin (DOX) release on PANC-1 cells	31
Figure 2.1	Chaperone-assisted delivery strategy for water-insoluble clofazimine drugs ...	45
Figure 2.2	Characterization of mesoporous silica nanoparticles (MSNs)	52
Figure 2.3	Clofazimine (CFZ) solubility enhancement in the presence of various hydrotropes	53
Figure 2.4	CFZ solubility enhancement in the presence of different concentrations of	

	acetophenone (AP) in H ₂ O	58
Figure 2.5	Conventional method and chaperone-assisted method for water-insoluble CFZ loading and release	60
Figure 2.6	UV-Vis spectra of CFZ in AP as a function of concentration, calibration curve of CFZ in AP at room temperature, and photograph of CFZ dissolved in AP ...	61
Figure 2.7	UV-Vis spectra of time-dependent CFZ release in buffer solution by using (a) dimethyl sulfoxide (DMSO) or (b) AP as loading solvents	64
Figure 2.8	UV-Vis spectra, calibration curve of CFZ in buffer solution at room temperature, and photograph of CFZ dissolved in buffer solution	65
Figure 2.9	Time-dependent release capacity of (a) CFZ and (c) AP and release efficiency of (b) CFZ and (d) AP in buffer solution	66
Figure 2.10	(a) Concentration dependent UV-Vis spectra and (b) calibration curve of AP in ethanol buffer solution	68
Figure 2.11	Time-dependent release efficiency of CFZ in buffer solution with or without the addition of AP to the buffer solution.....	71
Figure 2.12	(a) Schematic illustration of applying chaperone-assisted CFZ delivery strategy to selectively killing <i>M. tuberculosis</i> in macrophage. (b) AP/CFZ loaded MSNs kill <i>M. tuberculosis in vitro</i> in macrophage cultures. <i>M. tuberculosis</i> -infected THP-1 macrophages were untreated, treated with MSN loaded with AP (AP-MSN), treated with MSN loaded with CFZ and AP (AP/CFZ-MSN), or treated with CFZ dissolved in a mixture of DMSO and H ₂ O (CFZ/DMSO) for 4 days	73
Figure 3.1	(a) Schematic illustration of the synthesis of MnFe ₂ O ₄ @CoFe ₂ O ₄ nanoparticles by a seed-mediated thermal decomposition method. (b) Corresponding transmission electron microscope (TEM) images and (b) diameter distributions of MnFe ₂ O ₄ and MnFe ₂ O ₄ @CoFe ₂ O ₄ nanoparticles after each step	105

Figure 3.2	(a) TEM image and (b) size distribution of 11.4 nm MnFe ₂ O ₄ @CoFe ₂ O ₄ nanoparticles. (c) Field dependent magnetization curve of MnFe ₂ O ₄ @CoFe ₂ O ₄ nanoparticles at 300 K. (d) Time- and concentration-dependent temperature increase profiles of toluene solution containing MnFe ₂ O ₄ @CoFe ₂ O ₄ nanoparticles triggered by an alternating magnetic field (AMF)	106
Figure 3.3	High angle X-ray diffraction pattern of MnFe ₂ O ₄ @CoFe ₂ O ₄ nanoparticles ...	107
Figure 3.4	(a) Fourier-transform Infrared (FT-IR) spectrum and (b) thermogravimetric analysis (TGA) of MnFe ₂ O ₄ @CoFe ₂ O ₄ nanoparticles	108
Figure 3.5	(a) TEM image of core@shell nanoparticles (Mag@MSNs-APTS). (b) Nitrogen adsorption/desorption isotherms of Mag@MSNs-APTS at 77 K	111
Figure 3.6	Size distribution of 55.0 nm Mag@MSNs-APTS core@shell nanoparticles ...	112
Figure 3.7	Dynamic light scattering diameter distribution of Mag@MSNs-APTS in deionized H ₂ O at room temperature	112
Figure 3.8	(a) Zeta potential values, (b) FT-IR, and (c) TGA of Mag@MSNs, Mag@MSNs-APTS, Mag@MSNs-ACVA, and Mag@MSNs-AMA, respectively. (d) TEM image of Mag@MSNs-AMA. (e) N ₂ adsorption/desorption isotherms of Mag@MSNs-AMA at 77 K	113
Figure 3.9	(a) The cleavage of C-N bonds caused by bulk heating for 10 min. (b) Zeta potential values of Mag@MSNs-ACVA after 10 min of bulk heating in D.I. water. (c) The release of fluorescein from Mag@MSN- caused by bulk heating trigger in water bath at 37 °C, 60 °C, or 80 °C. The sample held at room temperature (23 °C) was also recorded as a control. (d) Release efficiency of fluorescein from Mag@MSNs- after bulk heating at 23 °C, 37 °C, 60 °C, or 80 °C trigger for 10 min	117
Figure 3.10	Time dependent release efficiency of fluorescein from Mag@MSN- caused by bulk heating trigger in water bath at 37 °C, 60 °C, and 80 °C. The sample held at room temperature (23 °C) was also recorded as a control	119
Figure 3.11	(a) Dose control of cargo release from Mag@MSNs- by adjusting the AMF	

	“ON” time. Time-dependent release profile of fluorescein from Mag@MSNs- through magnetic actuation under AMF for (b) 1, (c) 2, (d) 3, (e) 5, and (f) 10 min, respectively. (g) The release efficiency of fluorescein at plateau and the solution temperature after the various time periods of trigger under AMF	121
Figure 3.12	TEM images of fluorescein-loaded Mag@MSN-AMA-CD after 10 min exposure of the AMF trigger	123
Figure 3.13	(a) The cleavage of C-N bonds caused by 10 min of AMF trigger. (b) Zeta potential values of Mag@MSNs-ACVA before and after 10 min of AMF trigger in D.I. water	124
Figure 3.14	Time dependent release profile of fluorescein from Mag@MSNs- through magnetic actuation under AMF for 3 min for 3 cycles	125
Figure 3.15	(a) UV-Vis spectra of Mag@MSNs-AMA-CD and doxorubicin (DOX)-loaded Mag@MSNs-AMA-CD in PBS. Inset shows the photograph of tubes containing (1) Mag@MSNs-AMA-CD and (2) DOX-loaded Mag@MSNs-AMA-CD in PBS. Time-dependent release profile of DOX from Mag@MSNs- in PBS through magnetic actuation under AMF for (b) 2, (c) 5, and (d) 10 min, respectively	126
Figure 3.16	(a) Cytotoxicity of Mag@MSNs-AMA-CD. PANC-1 was incubated with Mag@MSNs-AMA-CD at various nanoparticle concentrations for 20 and 70 h, and the viability was determined by a CCK-8 assay. (b) Cytotoxicity of DOX-loaded Mag@MSNs-AMA-CD. PANC-1 was incubated with DOX-loaded Mag@MSNs-AMA-CD at various concentrations for 4 h. (c) After the 4 h treatment of DOX-loaded Mag@MSNs-AMA-CD, cells were allowed to grow in the regular culture medium for 12 h	129
Figure 3.17	(a) <i>In vitro</i> cellular killing effect of DOX-loaded Mag@MSNs-AMA-CD after AMF exposure. PANC-1 cells were treated with DOX-loaded Mag@MSNs-AMA-CD followed by various lengths of AMF exposure. (b) The viability of PANC-1 after treatment by Mag@MSNs-AMA-CD, or DOX-loaded Mag@MSNs-AMA-CD. (c) Fluorescence microscope images of PANC-1	

	cells (ii) after 4 h treatment by DOX-loaded Mag@MSNs-AMA-CD, and (iii) after 4 h incubation with DOX-loaded Mag@MSNs-AMA-CD followed by 10 min of AMF exposure. The control group (i) is cells without the treatment by nanoparticles	132
Figure 4.1	(A) Regions of the electromagnetic spectrum employed for optical imaging. (B) J-aggregation and characteristic photophysical properties. (C) IR-140. (D) Work reported herein: the stabilization of IR-140 J aggregates in hollow mesoporous silica nanoparticles (HMSNs) to result in biocompatible shortwave infrared (SWIR)-emissive contrast agents	148
Figure 4.2	TEM images of (A) Stöber silica spheres, (B) dSiO ₂ @MSNs, and (C) HMSNs	159
Figure 4.3	(A) Schematic of loading IR-140 into HMSNs. (B) Washing conditions facilitate J-aggregation. Ten mg/mL HMSNs were combined with 10 mM IR-140 in DMSO and washed with PBS with (green) and without (dark blue) sonication. Pre-wash spectrum, diluted 1:350 is shown in orange. Loading control for solid, non-porous Stöber spheres is shown in gray. (C/D) TEM images of HMSNs with (D) and without (C) IR-140 treatment	160
Figure 4.4	UV/Vis/NIR spectra of HMSNs or dSiO ₂ @MSNs containing IR-140. The loading concentrations of IR-140 were (A) 20 mM and (B) 5 mM	161
Figure 4.5	Control experiment with Stöber silica spheres. (A) The zeta potential of Stöber silica spheres (black), and Stöber silica spheres-APTS (red) in D.I. water at room temperature. (B/C/D) UV/Vis/NIR spectra of Stöber silica spheres (black) or Stöber silica spheres-APTS (red) containing IR-140. The loading concentrations of IR-140 were (B) 20 mM, (C) 10 mM, or (D) 5 mM	162
Figure 4.6	UV/Vis/NIR spectra of IR-140 loaded HMSNs, Stöber silica spheres, Stöber silica spheres-APTS, or dSiO ₂ @MSNs	163
Figure 4.7	The loading capacity, defined as (grams IR-140/grams HMSNs or HMSNs-APTS) x 100%, of IR-140 in HMSNs (black) or HMSNs-APTS (red) at different IR-140 loading concentrations	164
Figure 4.8	Nitrogen adsorption (black)/desorption (red) isotherms of (A) HMSNs, (C) HMSNs-APTS, and (E) dSiO ₂ @MSNs. Pore diameter distributions of (B)	

	HMSNs, (D) HMSNs-APTS, and (F) dSiO ₂ @MSNs	165
Figure 4.9	TEM images of HMSNs with (C) and without (A) IR-140 treatment. (B) As a control, HMSNs were washed with PBS but without the loading of IR-140. (D) Mixture of HMSNs with and without IR-140 treatment	166
Figure 4.10	UV/Vis/NIR spectra of HMSNs-APTS containing IR-140 for dye loading concentrations of 20 mM (black), 10 mM (red), or 5 mM (blue) in PBS, after washing the particles with PBS	169
Figure 4.11	The dynamic light scattering size distribution of HMSNs-APTS (black), HMSNs-APTS containing IR-140 (red), and HMSNs-PEG containing IR-140 in PBS (blue)	169
Figure 4.12	The zeta potential of HMSNs (black), HMSNs-APTS (red), HMSNs-APTS containing IR-140 (blue), and HMSNs-PEG containing IR-140 (pink) in D.I. water	170
Figure 4.13	(A) Normalized absorption and emission of IR-140 J-aggregate in HMSNs-PEG (blue), J-aggregate in solution (red), and monomer (yellow). (B) Emission (1000–1700 nm) of IR-140 monomer (left), J-aggregate in solution (middle) and J-aggregate in HMSNs-PEG (right) upon 980 nm excitation. (C) Normalized relative absorption of IR-140 J-aggregate in 35% DMSO/0.9% NaCl in water (red) and in HMSNs-PEG in PBS (blue) on day zero (solid) and day 1 or 14 (dotted). (D) Photostability under laser irradiation (97 mW/cm ²) at 980 nm for IR-140 J-aggregate in HMSNs-PEG (blue) and IR-140 J-aggregate in 35% DMSO/0.9% NaCl in water (red), and at 785 nm for monomer in DMSO (yellow)	172
Figure 4.14	UV/Vis/NIR characterization of IR-140 J-aggregate formation in solution at 0.01 mg/mL in (A) DMSO/water (B) DMSO/1xPBS and (C) DMSO/0.9% NaCl in water	173
Figure 4.15	Emission of monomer and J-aggregate states of IR-140 under 980 nm excitation. (A) Absorbance traces of samples used in vial images in B and in Figure 4.13B, baseline corrected to 521 nm. (B) Images of IR-140 monomer in DMSO (left), IR-140 J-aggregate in solution (center) and J-aggregate in	

	HMSNs-PEG (right) under 980 nm irradiation ($99 \pm 3 \text{ mWcm}^{-1}$)	174
Figure 4.16	Stability of J-aggregates over time, displayed as the normalized, relative absorbance remaining for IR-140 in HMSNs-PEG after 14 days, and IR-140 in solution after 1 day	175
Figure 4.17	Photostability of J-aggregates in the presence and absence of oxygen. (A) Raw data of IR-140 J-aggregate in 35 % DMSO/0.9% NaCl at 0.01 mg/mL under 980 nm irradiation with 79 mWcm^{-2} power density. (B) Raw data of HMSNs-PEG loaded with IR-140 at 1.0 mg/mL in 1x PBS under 980 nm irradiation with 101 mWcm^{-2} power density	176
Figure 4.18	Cytotoxicity study of IR-140 loaded HMSNs-PEG examined by a CCK-8 assay	177
Figure 4.19	Whole-mouse imaging at 16 fps (980 nm, 91 mW/cm^2 excitation; 1000–1700 nm collection) upon i.v. delivery of IR-140 HMSNs-PEG. Background subtracted stills were averaged over 5 frames at 3 s (A), 8 s (B), 25 s (C), and 120 s (D) post injection	178
Figure 4.20	Images from the front (A/C) and left side (B/D) of a nude mouse directly after vascular clearance (>2 m post injection) (A/B), and after 50 minutes (C/D), showing uptake of IR-140 loaded HMSNs-PEG in the liver and spleen	179
Figure S4.1	HMSN or HMSN-APTS used in this work	194
Figure S4.2	Absorption coefficient of IR-140 monomer in DMSO	198
Figure S4.3	Uncorrected absorption coefficient of IR-140 J-aggregate in 35% DMSO/0.9% NaCl in water	199
Figure S4.4	Corrected absorption coefficient of IR-140 J-aggregate in 35% DMSO/0.9% NaCl in water	200
Figure S4.5	Solvent corrected integrated fluorescence intensity versus absorbance plots for (A) IR-26 and (B) IR-140 J-aggregate, also corrected for reabsorption	202
Figure S4.6	Photobleaching data plotted as the $\ln[A]$ vs time and the corresponding linear fits	205

Figure 5.1	The stalks on the nanoparticles (left) protect the $1\bullet\text{PF}_6$ crystal in the hollow interior from perchlorate until pH 3 is reached. After acidification, perchlorate is able to access the nanoparticle, reach the crystal and produce brightly luminescent $1\bullet\text{ClO}_4\cdot\text{H}_2\text{O}$ (middle). Particles capped with α -cyclodextrin (αCD) (right) function similarly	223
Figure 5.2	$1\bullet\text{PF}_6$ converting to $1\bullet\text{ClO}_4\cdot\text{H}_2\text{O}$ after the addition of ClO_4^- anion	223
Figure 5.3	TEM images of the polystyrene beads	225
Figure 5.4	TEM images of template free HMSNs	225
Figure 5.5	(a) N_2 adsorption/desorption isotherms of HMSNs. (b) Pore size distribution of HMSNs	226
Figure 5.6	FT-IR spectra of HMSNs and HMSNs after phenylaminomethyltriethoxysilane (PhAMTES) modification	226
Figure 5.7	Powder X-ray diffraction of (a) crystalline $1\bullet\text{PF}_6$, (b) bare HMSNs showing a peak around 2.3° from the ordered mesopores, and (c) HMSNs containing the crystallized $1\bullet\text{PF}_6$	227
Figure 5.8	Experimental set up for sequential fluorescence spectra measurements	229
Figure 5.9	Luminescence spectra of the $1\bullet\text{PF}_6$ crystal-loaded HMSNs with aniline stalks as a function of time (a) without the addition, (b) after the addition of ClO_4^- , and (c) after the addition of HCl when αCD is not used as a cap	229
Figure 5.10	Luminescence spectra of nanoparticles gated by the PhAMTES stalk as a function of time after the addition of acid and perchlorate. A similar response occurs with particles capped with αCD	230
Figure 5.11	Luminescence spectra of the $1\bullet\text{PF}_6$ crystal-loaded HMSNs without aniline stalks as a function of time (a) without the addition, (b) after the addition of the HCl, (c) after the addition of ClO_4^- , and (d) after the addition of HCl and ClO_4^-	230
Figure 5.12	Luminescence spectra of nanoparticles gated by the PhAMTES stalk and αCD as a function of time after the addition of acid and perchlorate	232

Figure 5.13 (a) Emission intensity at 690 nm as a function of time. At ~45 minutes NaClO_4^- was added and after 2.5 hours the system was brought to a pH of 3. (b) Emission intensity at 690 nm as a function of time. At ~55 minutes the system was brought to a pH of 3 and no change in the intensity was observed ... 232

Figure 5.14 Truth table of the AND gate. Input 1 is acidification to pH 3, and input 2 is the perchlorate ion. The numbers 1 and 0 in the figure represent “True” and “False”, respectively. The output is the luminescence of $1 \cdot \text{ClO}_4 \cdot \text{H}_2\text{O}$ inside the hollow nanoparticles. Nanoparticles with only the stalk (left of dashed line) and those capped by αCD (right) function similarly 233

LIST OF TABLES

Table 2.1	Chemical structures of possible hydrotropes for clofazimine (CFZ) and their water solubilities	54
Table 2.2	Summary of the amount of loaded CFZ and acetophenone (AP) in mesoporous silica nanoparticles (MSNs) (nmole/mg) and the mole ratio of AP/CFZ loaded in MSNs	62
Table 4.1	Photophysical characterization of IR-140	171
Table 4.2	Photobleaching rates of IR-140 (1)	176
Table S4.1	Photobleaching rates and values used in calculations and corrections	207

LIST OF SCHEMES

Scheme 3.1	(a) Schematic illustration of the synthesis of azo snap-top core@shell mesoporous silica nanoparticles and triggered release under an alternating magnetic field. (b) Scheme of the conjugation and capping of 3-aminopropyltriethoxysilane (APTS), 4,4'-azobis(4-cyanovaleric acid) (ACVA), 1-adamantylamine (AMA), and β -cyclodextrin (β -CD) on the surface of core@shell nanoparticles	89
Scheme 4.1	Synthesis of hollow mesoporous silica nanoparticles (HMSNs)	159
Scheme 4.2	Synthesis of IR-140-loaded HMSN-PEG. (A) Overall synthesis starting from Stöber spheres. (B) Detailed schematic of conjugation of polyethylene glycol (PEG) to the surface of HMSN-APTS	168

ACKNOWLEDGEMENTS

Studying abroad has challenged me for the past 5 years, and thus has enabled me to learn how to tackle the difficulties arising during my Ph.D. student life. Firstly, I would like to deeply acknowledge my greatest advisor, Professor Jeffrey Zink, for letting me join his wonderful group. His clear academic advice and significant financial support has guided me to be a better scientist. In addition, his attitude toward scientific questions has stimulated me always to meticulously consider science from different angles – important and beneficial training throughout my Ph.D. studies. In his group, I also learned how to collaborate with excellent students, postdoctoral researchers, and visiting scholars from all over the world with various backgrounds. Most importantly, without his continuous guidance and support, I couldn't have finished my Ph.D. studies and dissertation at this moment. I would also like to acknowledge my committee members, Professor Ellen Sletten, Professor Xiangfeng Duan, Professor Marcus Horwitz, Professor Fuyuhiko Tamanoi, and Professor Yung-Ya Lin for their advice during my Ph.D. studies. Their advice has benefitted me enormously.

Additionally, I would also like to thank all past and present Zink group members. I would like to acknowledge Dr. Bastian Rühle, Dr. Wen-Yen Huang, Dr. Philippe Saint-Cricq, and Dr. Yen-Ting (Janie) Chen for their great help when I first joined this group. All your guidance and advice played important roles during my Ph.D. studies. Special acknowledgment goes to my wife, Chi-An (Annie) Cheng, who is also my partner in this group. Without her support and help throughout my Ph.D. studies, I couldn't have finished the dissertation at this moment. My Ph.D. studies could not have been done without the help of my labmates, including Professor Liping Ruan, Professor

Changli Zhang, Professor Sandra Sanchez-Salcedo, Professor Kun Nie, Professor Xiao-Jie Ju, Dr. Juyao Dong, Dr. Angela Hwang, Dr. Zilu Li, Dr. Jonas Croissant, Dr. Tania Guardado-Alvarez, Dr. Jonathan Brosmer, Dr. Yao Cai, Dr. Sheba Plamthottam, Dr. Navnita Kumar, Dr. Chia-Jung Yu, Dr. Zhao Li, Ruining Wang, Fang-Chu Lin, Tian Deng, Jaime Fidel Ruiz-Robles, and Danlei Xiang.

Special acknowledgment goes to our collaborators, Professor Ellen Sletten and her talented student, Emily (Maly) Cosco in our department. Because of your clear guidance and cleverness, we can finally publish our first collaborative work in *J. Am. Chem. Soc.* I actually acquired a broad knowledge of photophysics from you. I would also like to acknowledge Professor Oliver Bruns and his group members, Shyam Ramakrishnan, and Jakob Lingg for the shortwave infrared imaging and animal studies in Germany. Acknowledgment also goes to Professor Marcus Horwitz and his group members, Dr. Bai-Yu Lee, and Dr. Daniel Clemens for the bacteria and animal studies. Your guidance and advice allowed me to learn more about the knowledge of bacteria in the field of nanomedicine. I would like to thank Dr. Wen-Yen Huang who also first proposed the ideas of this work. Fortunately, we finally realized our ideas and published our work in *ACS Appl. Mater. Interfaces*. I would like to thank Professor Carlotta Glackin and Professor Marcus Horwitz for their writing on the wonderful paper published in *Acc. Chem. Res.* I would also like to acknowledge Professor Holden Wu and his postdoctoral researcher, Dr. Le Zhang, for their guidance and advice about the research on high-intensity focused ultrasound and magnetic resonance imaging experiments. Your expertise on these extremely expensive instruments and this technique helped me broaden my horizon and knowledge. I would like to acknowledge Dr. Tania

Guardado-Alvarez, Dr. Amie Norton, Dr. Melissa Russell, and Professor William Connick. Because of your organization and guidance, I was able to publish my first paper in the U.S. I would like to acknowledge Professor Yung-Ya Lin and his student, Dr. Sayoni Ray, and Dr. Zhao Li for collaborating on studies of magnetic heating triggered cargo release from liposome studies. I would also like to acknowledge Daniel Estabrook, and his undergraduate student, John Chapman in Professor Ellen Sletten's group, for our ongoing fluoruous-emulsions project. I would also like to acknowledge Professor Caius Radu's and his students, Dr. Soumya Poddar, and Roy Pan, for our ongoing drug delivery project.

In addition, my Ph.D. studies were also supported by many professors, friends, and seniors in Los Angeles. A special acknowledgment goes to Professor Hsian-Rong Tseng. Your guidance and advice on every aspect of my Ph.D. life definitely encouraged me, and I would always keep what you said in my mind. I would also like to acknowledge Dr. Po-Yuan Wang and his wife, Ya-Husan Chuang, for being my roommates and for their great support in my daily life. Special acknowledgment goes to Dr. Cheng-Wei Lin for frequently sharing in our daily life. His name is similar to mine and our names always confuse the staff in our department. I would also like to acknowledge Dr. Yao-Tsung Hsieh for being one of our baseball team members. By the way, we have forever had the dream of being able to join one of the professional teams of Major League Baseball someday. I would also like to acknowledge Dr. Chun-Han Lai for food-hunting during the weekend and introducing so many National Parks to me. I would also like to acknowledge my classmate, Dr. Yiliu Wang, for sharing our difficulties during our first year of studies. What I learned from him are not only a wide knowledge but also his perseverance in the face of difficulties.

I would also like to acknowledge Dr. Chi-Ping Liu, Dr. Edward Chang, Dr. Yi-Ting Chen, Dr. Yu-Jen (Alex) Jan, and Dr. Po-Hung Hsieh for sharing many good memories with me in Los Angeles.

I would also like to acknowledge two of my seniors, Professor Si-Han Wu, and Professor Yi-Ping Chen. Your stay in Los Angeles also made my life here more colorful. I would also like to thank Mr. Yang-Chan Chang and Ms. Zoe Hsu in Science and Technology Division, Taipei Economic and Cultural Office in Los Angeles for sharing many good social connection opportunities and many wonderful events.

Finally, the deepest appreciation goes to my father, mother, and younger sister. Your significant support and encouragement throughout my entire student life are definitely my motivation to achieve my goal. Actually, my father has worked on silica (the scale in meter) for 28 years for raising our family; I have also worked on silica (the scale in nanometer) for many years; hopefully, what I have worked on will be able to contribute to people someday.

Part of Chapter 1 (Chapter 1.2) is reprinted and adapted with permission from (Chen, W.; Glackin, C. A.; Horwitz, M. A.; Zink, J. I. “Nanomachines and Other Caps on Mesoporous Silica Nanoparticles for Drug Delivery” *Acc. Chem. Res.* **2019**, *52*, 1531-1542) Copyright 2019 American Chemical Society. Co-author contributions: Chen, W., Glackin, C. A., Horwitz, M. A., and Zink, J. I. wrote the paper, Jeffrey I. Zink was the P.I.

Chapter 2 is reprinted and adapted with permission from (Chen, W.; Cheng, C. A.; Lee, B. Y.; Clemens, D. L.; Huang, W. Y.; Horwitz, M. A.; Zink J. I. “Facile Strategy Enabling Both High Loading and High Release Amounts of the Water-Insoluble Drug Clofazimine Using Mesoporous Silica Nanoparticles” *ACS Applied Materials & Interfaces* **2018**, *10*, 31870-31881) Copyright

2018 American Chemical Society. Co-author contributions: Chen W., Cheng C. A., and Huang W. Y. performed the chemistry-related studies. Lee B. Y., and Clemens D. L. performed the cells and bacteria studies. Marcus A. Horwitz, and Jeffrey I. Zink were the P.Is.

Chapter 3 is reprinted and adapted with permission from (Chen, W.; Cheng, C. A.; Zink, J. I. “Spatial, Temporal, and Dose Control of Drug Delivery using Noninvasive Magnetic Stimulation” *ACS Nano* **2019**, *13*, 1292-1308) Copyright 2019 American Chemical Society. Co-author contributions: Chen W., and Cheng C. A. performed the experiments, Jeffrey I. Zink was the P.I.

Chapter 4 is reprinted and adapted with permission from (Chen, W.; Cheng, C. A.; Cosco, E. D.; Ramakrishnan, S.; Lingg, J. G. P.; Bruns, O. T.; Zink, J. I.; Sletten, E. M. “Shortwave Infrared Imaging with J-aggregates Stabilized in Hollow Mesoporous Silica Nanoparticles” *J. Am. Chem. Soc.* **2019**, *141*, 12475–12480) Copyright 2019 American Chemical Society. Co-author contributions: Chen W., Cheng C. A., and Cosco E. D. performed the materials synthesis, characterization, photophysics, and cells studies. Cosco E. D., Ramakrishnan S., and Lingg J. G. P. performed the shortwave infrared imaging and animal studies. Oliver T. Bruns, Jeffrey I. Zink, and Ellen M. Sletten were the P.Is. The texts of introduction, result and discussion were mainly organized and written by Professor Ellen M. Sletten when preparing the manuscript for publication.

Chapter 5 is reprinted and adapted with permission from (Guardado-Alvarez, T. M.; Chen, W.; Norton, A. E.; Russell, M. M.; Connick, W. B.; Zink, J. I. “Analyte-Responsive Gated Hollow Mesoporous Silica Nanoparticles Exhibiting Inverse Functionality and an AND Logic Response” *Nanoscale*, **2016**, *8*, 18296-18300) Copyright 2016 The Royal Society of Chemistry. Co-author contributions: Guardado-Alvarez T. M., Chen W., Norton A. E., and Russell, M. M. performed the

experiments. William B. Connick, and Jeffrey I. Zink were the P.Is.

VITA

- 2014 – 2019 Graduate Student with Professor Jeffrey I. Zink
Department of Chemistry and Biochemistry, University of California, Los Angeles
Los Angeles, California
- 2011 – 2014 Research Assistant with Professor Chung-Yuan Mou
Department of Chemistry, National Taiwan University
Taipei, Taiwan
- 2009 – 2011 Master Student with Professor Chung-Yuan Mou
Department of Chemistry, National Taiwan University
Taipei, Taiwan
- 2005 – 2009 Bachelor of Science (Undergraduate Research with Professor Chung-Yuan Mou)
Department of Chemistry, National Taiwan University
Taipei, Taiwan

Publications

16. **Chen, W.**; Cheng, C.A.; Cosco, E.D.; Ramakrishnan, S.; Lingg, J.G.P.; Bruns, O.T.; Zink, J.I.; Sletten, E.M., “Shortwave Infrared Imaging with J-aggregates Stabilized in Hollow Mesoporous Silica Nanoparticles.” *J. Am. Chem. Soc.* **2019**, 141, 12475–12480.
15. **Chen, W.**; Cheng, C.A.; Zink, J.I., “Spatial, Temporal, and Dose Control of Drug Delivery Using Noninvasive Magnetic Stimulation.” *ACS Nano* **2019**, 13, 1292–1308.
14. **Chen, W.**; Glackin, C.A.; Horwitz, M.A.; Zink, J.I., “Nanomachines and Other Caps on Mesoporous Silica Nanoparticles for Drug Delivery.” *Acc. Chem. Res.* **2019**, 52, 1531–1542.
13. Ray, S.; Cheng, C.A.; **Chen, W.**; Li, Z.; Zink, J.I.; Lin, Y.Y., “Magnetic Heating Stimulated Cargo Release with Dose Control using Multifunctional MR and Thermosensitive Liposome.” *Nanotheranostics* **2019**, 3, 166–178. (selected as Front Cover)
12. Tsai, P.H.; Wang, M.L.; Chang, J.H.; Yarmishyn, A.A.; Nguyen, P.N.N., **Chen, W.**; Chien, Y.; Huo, T.I.; Mou C.Y.; Chiou, S.H., “Dual Delivery of HNF4 α and Cisplatin by Mesoporous Silica Nanoparticles Inhibits Cancer Pluripotency and Tumorigenicity in Hepatoma-derived CD133-expressing Stem Cells.” *ACS Appl. Mater. Interfaces* **2019**, 11, 19808–19818.
11. **Chen, W.**; Cheng, C.A.; Lee, B.Y.; Clemens, D.L.; Huang, W.Y.; Horwitz, M.A.; Zink, J.I., “Facile Strategy Enabling Both High Loading and High Release Amounts of the Water-Insoluble Drug Clofazimine Using Mesoporous Silica Nanoparticles.” *ACS Appl. Mater. Interfaces* **2018**, 7, 31870–31881.

10. Kumar, N.; **Chen, W.**; Cheng, C.A.; Deng, T.; Wang, R.; Zink, J.I. “Stimuli-Responsive Nanomachines and Caps for Drug Delivery.” *The Enzymes* **2018**, *43*, 31–65.
9. Chou, C.C.; **Chen, W.**; Hung, Y.; Mou, C.Y., “Molecular Elucidation of Biological Response to Mesoporous Silica Nanoparticles *in Vitro* and *in Vivo*.” *ACS Appl. Mater. Interfaces* **2017**, *6*, 22235–22251.
8. Chang, J.H.; Tsai, P.H.; **Chen, W.**; Chiou, S.H.; Mou, C.Y., “Dual Delivery of siRNA and Plasmid DNA Using Mesoporous Silica Nanoparticles to Differentiate Induced Pluripotent Stem Cells into Dopaminergic Neurons.” *J. Mater. Chem. B* **2017**, *5*, 3012–3023.
7. Guardado-Alvarez, T.M.; **Chen, W.**; Norton, A.E.; Russell, M.M.; Connick, W.B.; Zink J.I., “Analyte-responsive Gated Hollow Mesoporous Silica Nanoparticles Exhibiting Inverse Functionality and an AND Logic Response.” *Nanoscale* **2016**, *8*, 18296–18300.
6. Chen, J.Y.; Ho, C.Y.; Lu, M.L.; Chu, L.J.; Chen, K.C.; Chu, S.W.; **Chen, W.**; Mou, C.Y.; Chen, Y.F., “Efficient Spin Light Emitting Diodes Arising from InGaN/GaN Quantum Disks at Room Temperature: A New Self-polarized Paradigm.” *Nano Lett.* **2014**, *14*, 3130–3137.
5. **Chen, W.**; Tsai, P.H.; Hung, Y.; Chiou, S.H.; Mou, C.Y., “Nonviral Cell Labeling and Differentiation Agent for Induced Pluripotent Stem Cells Based on Mesoporous Silica Nanoparticles.” *ACS Nano* **2013**, *7*, 8423–8440.
4. **Chen, W.**; Lu, F.; Chen, C.C.V.; Mo, K.C.; Hung, Y.; Guo, Z.X.; Lin, C.H.; Lin, M.H.; Lin, Y.H.; Chang, C.; Mou, C.Y., “Manganese-Enhanced Magnetic Resonance Imaging of Rat Brain Based on Slow Cerebral Delivery of Mn(II) with Silica-Encapsulated Mn_xFe_{1-x}O Nanoparticles.” *NMR Biomed.* **2013**, *26*, 1176–1185.
3. Li, L.H.; Yen, M.Y.; Ho, C.C.; Wu, P.; Wang, C.C.; Maurya, P.K.; Chen, P.S.; **Chen, W.**; Chen, H.W., “Non-Cytotoxic Nanomaterials Enhance Antimicrobial Activities of Cefmetazole against Multidrug-Resistant *Neisseria gonorrhoeae*.” *PLoS ONE* **2013**, *8*, e64794.
2. Wu, P.; Yuan, S.S.; Ho, C.C.; Hsieh, W.Y.; Hong, Q.S.; Yu, S.L.; **Chen, W.**; Chen, H.Y.; Wang, C.D.; Li, K.C.; Yang, P.C.; Chen, H.W., “Focal Amplification of HOXD-harboring Chromosome Region is Implicated in Multiple-Walled Carbon Nanotubes-Induced Carcinogenicity.” *Nano Lett.* **2013**, *13*, 4632–4641.
1. Wu, S.H.; Lin, C.Y.; Hung, Y.; **Chen, W.**; Chang, C.; Mou, C.Y., “PEGylated Silica Nanoparticles Encapsulating Multiple Magnetite Nanocrystals for High-Performance Microscopic Magnetic Resonance Angiography.” *J. Biomed. Mater. Res. B* **2011**, *99B*, 81–88.

Chapter 1

Introduction

This introduction consists of two parts. First, in section 1, I introduce and give an overview of the research work in each of the chapters of my dissertation. In section 2, I provide a background to the field taken from a review article we published in *Accounts of Chemical Research*.

1.1 Introduction of the research work of this dissertation

Mesoporous silica nanoparticles (MSNs) were first reported in the patent literature in 1971.¹ Yet MSNs did not get much attention until Mobil Oil Corporation synthesized mesoporous silica materials from aluminosilicate gels using a liquid crystal template mechanism in 1992; the materials are now known as Mobil Crystalline Materials (MCM-41).² Among the widespread applications, biology and medicine-related research using MSNs as the nanocarriers has aroused much attention because MSNs possess preeminent properties including extremely high surface area, large pore volume, tunable pore size, easy surface functionalization, and high biocompatibility.³⁻¹¹ The high surface area and large pore volume make MSNs serve as superior nanocarriers to carry large amounts of drugs or biomolecule cargos.¹²⁻¹⁶ The easy surface functionalization allows MSNs to be tailored and possess a variety of surface chemistries for their specific applications, *e.g.* cell targeting.^{10,11,17-19} Of particular importance, their low toxicity enables MSNs to be used as practical nanocarriers to achieve a variety of biomedical applications. Among the biomedical applications, of particular interest to us are (1) high loading and high release amounts of water-insoluble drugs delivered to the site of diseases; (2) precise control of the drug or cargo molecules released from the MSNs triggered by external stimuli; (3) construction of

MSNs-based shortwave infrared optical imaging contrast agents as an innovative tool for bioimaging and cancer diagnostics; and (4) the development of nanosensors to detect molecules of interest. The introduction to the following chapters, which mainly focus on the biomedical applications of MSNs, are presented in the following paragraphs.

In Chapter 2, we developed a facile “chaperone-assisted” delivery strategy which improves the loading of clofazimine (CFZ), an antibiotic used to treat tuberculosis, and delivers a large amount of CFZ with MSNs into an aqueous environment.⁶ We found that acetophenone (AP) is the most promising chaperone among nine candidate molecules tested. Then, we compared the efficacy of AP and DMSO as nonaqueous solvents for CFZ loading and release. Next, we measured the effect of the CFZ loading concentration on CFZ release and AP release and determined the optimized CFZ loading concentration. The effect of the location of AP relative to MSNs on CFZ was also explored. Finally, using the optimized AP/CFZ-loaded MSNs, we investigated the antibacterial effect of this hydrotrophy-based delivery strategy on intracellular *M. tuberculosis* to further validate their potential use in medicine and biomedical research. To the best of our knowledge, this is the first work to demonstrate an appropriate chaperone for CFZ and to apply the strategy to the construction of nanoparticles with enhanced CFZ loading and release efficiency.

In Chapter 3, monodispersed manganese- and cobalt-doped iron oxide ($\text{MnFe}_2\text{O}_4@ \text{CoFe}_2\text{O}_4$) nanoparticles with a high magnetization (105 emu/g) and high specific loss power (1510.8 W/g) were synthesized.²⁰ The high magnetization of these superparamagnetic nanoparticles provides efficient magnetic heating under an alternating magnetic field (AMF), thus holding great promise

for magnetic heating-triggered drug delivery. To increase the amount of drug over that available using the nanoparticles themselves, we synthesized mesoporous silica shell “containers” around the magnetic core, forming a spherical core@shell structure 55 nm in diameter. The spatial, temporal, and dose control of drug release was achieved using a thermo-responsive gatekeeper containing a thermo-labile molecule 4,4'-azobis(4-cyanovaleric acid) and a host guest complexation formed by adamantylamine and β -cyclodextrin. Most importantly, in this study we demonstrated externally controlled dosage of fluorescein or doxorubicin (DOX) by controlling the AMF exposure time. Multiple sequential exposures of AMF allow cargo release in a step-wise manner. *In vitro* studies show that the drug-delivery system is biocompatible. DOX-loaded nanoparticles did not cause a decrease in cell viability in the absence of AMF stimulation, but the viabilities of the pancreatic cancer cells decreased by 28%, 37%, and 53% as the AMF exposure time increased from 2, to 5, to 10 min. Taken together, the thermo-responsive drug delivery actuated by AMF offers the potential of becoming an emerging chemotherapy that noninvasively and precisely controls the dosage of drugs, avoiding the risk generated when overheating the surroundings.

In Chapter 4, we have presented J-aggregation as an approach to prepare biocompatible, shortwave infrared (SWIR) imaging contrast agents and demonstrated this concept by stabilizing J-aggregates of the near infrared (NIR) fluorophore IR-140 inside hollow mesoporous silica nanoparticles (HMSNs).²¹ The J-aggregates inside polyethylene glycol conjugated HMSNs (HMSNs-PEG) are stable for multiple weeks in phosphate-buffered saline and enable high resolution imaging *in vivo* with 980 nm excitation. The bathochromically-shifted absorption and

emission and small Stokes shifts of the IR-140 J-aggregate allow imaging with 980 nm excitation and 1000–1700 nm acquisition, providing high resolution *in vivo* images. Collectively, the use of J-aggregates stabilized in HMSNs-PEG as SWIR imaging agents has the potential to overcome the stability, toxicity, and brightness challenges of contrast agents for this compelling region of the electromagnetic spectrum.

In Chapter 5, we developed multifunctional nanoparticles with designed selectivity using hollow mesoporous silica nanoparticles, ship-in-a-bottle synthesis of a crystalline solid-state detector, and protection of the crystal by acid-responsive nanogates.²² The system demonstrated the inverse application of the usual trapping of contents by the gate followed by their release. Instead, the gate protected the contents followed by selective exposure. Crystallization of [Pt(tpy)Cl](PF₆) (tpy = 2,2':6',2''-terpyridine) inside the cavity of hollow mesoporous silica created the unique core@shell nanoparticle. The crystalline core becomes fluorescent in the presence of perchlorate ion. By condensing an acid-sensitive gate onto the particle, access to the pores is blocked and the crystal is protected. The new nanomaterial obeys Boolean AND logic; only the presence of both the analyte (ClO₄⁻) and acid results in the optical response.

1.1.1 References

- (1) Chiola, V.; Ritsko, J. E.; Vanderpool, C. D. Process for Producing Low-Bulk Density Silica. U.S. Patent 3, **1971**, 556–725.
- (2) Beck, J. S.; Vartuli, J. C.; Roth, W. J.; Leonowicz, M. E.; Kresge, C. T.; Schmitt, K. D.; Chu, C. T. W.; Olson, D. H.; Sheppard, E. W.; McCullen, S. B.; Higgins, J. B.; Schlenker, J. L. A New Family of Mesoporous Molecular Sieves Prepared with Liquid Crystal Templates. *J. Am. Chem. Soc.* **1992**, *114*, 10834–10843.
- (3) Chen, W.; Glackin, C. A.; Horwitz, M. A.; Zink, J. I. Nanomachines and Other Caps on Mesoporous Silica Nanoparticles for Drug Delivery. *Acc. Chem. Res.* **2019**, *52*, 1531–1542.
- (4) Chen, W.; Tsai, P. H.; Hung, Y.; Chiou, S. H.; Mou, C. Y. Nonviral Cell Labeling and Differentiation Agent for Induced Pluripotent Stem Cells Based on Mesoporous Silica Nanoparticles. *ACS Nano* **2013**, *7*, 8423–8440.
- (5) Chou, C. C.; Chen, W.; Hung, Y.; Mou, C. Y. Molecular Elucidation of Biological Response to Mesoporous Silica Nanoparticles in Vitro and in Vivo. *ACS Appl. Mater. Interfaces* **2017**, *9*, 22235–22251.
- (6) Chen, W.; Cheng, C. A.; Lee, B. Y.; Clemens, D. L.; Huang, W. Y.; Horwitz, M. A.; Zink, J. I. Facile Strategy Enabling Both High Loading and High Release Amounts of the Water-Insoluble Drug Clofazimine Using Mesoporous Silica Nanoparticles. *ACS Appl. Mater. Interfaces* **2018**, *10*, 31870–31881.
- (7) Li, Z.; Barnes, J. C.; Bosoy, A.; Stoddart, J. F.; Zink, J. I. Mesoporous Silica Nanoparticles in Biomedical Applications. *Chem. Soc. Rev.* **2012**, *41*, 2590–2605.
- (8) Tarn, D.; Ashley, C. E.; Xue, M.; Carnes, E. C.; Zink, J. I.; Brinker, C. J. Mesoporous Silica Nanoparticle Nanocarriers: Biofunctionality and Biocompatibility. *Acc. Chem. Res.* **2013**, *46*, 792–801.
- (9) Ambrogio, M. W.; Thomas, C. R.; Zhao, Y. L.; Zink, J. I.; Stoddart, J. F. Mechanized Silica Nanoparticles: A New Frontier in Theranostic Nanomedicine. *Acc. Chem. Res.* **2011**, *44*, 903–913.
- (10) Wu, S. H.; Mou, C. Y.; Lin, H. P. Synthesis of Mesoporous Silica Nanoparticles. *Chem. Soc. Rev.* **2013**, *42*, 3862–3875.
- (11) Ruehle, B.; Saint-Cricq, P.; Zink, J. I. Externally Controlled Nanomachines on Mesoporous Silica Nanoparticles for Biomedical Applications. *Chemphyschem* **2016**, *17*, 1769–1779.
- (12) Chang, J. H.; Tsai, P. H.; Chen, W.; Chiou, S. H.; Mou, C. Y. Dual Delivery of siRNA and Plasmid DNA Using Mesoporous Silica Nanoparticles to Differentiate Induced Pluripotent Stem Cells into

- Dopaminergic Neurons. *J. Mater. Chem. B* **2017**, *5*, 3012–3023.
- (13) Tsai, P. H.; Wang, M. L.; Chang, J. H.; Yarmishyn, A. A.; Nhi Nguyen, P. N.; Chen, W.; Chien, Y.; Huo, T. I.; Mou, C. Y.; Chiou, S. H. Dual Delivery of HNF4 α and Cisplatin by Mesoporous Silica Nanoparticles Inhibits Cancer Pluripotency and Tumorigenicity in Hepatoma-Derived CD133-Expressing Stem Cells. *ACS Appl. Mater. Interfaces* **2019**, *11*, 19808–19818.
- (14) Liong, M.; Lu, J.; Kovoichich, M.; Xia, T.; Ruehm, S. G.; Nel, A. E.; Tamanoi, F.; Zink, J. I. Multifunctional Inorganic Nanoparticles for Imaging, Targeting, and Drug Delivery. *ACS Nano* **2008**, *2*, 889–896.
- (15) Lu, J.; Liong, M.; Zink, J. I.; Tamanoi, F. Mesoporous Silica Nanoparticles as a Delivery System for Hydrophobic Anticancer Drugs. *Small* **2007**, *3*, 1341–1346.
- (16) Hom, C.; Lu, J.; Liong, M.; Luo, H.; Li, Z.; Zink, J. I.; Tamanoi, F. Mesoporous Silica Nanoparticles Facilitate Delivery of siRNA to Shutdown Signaling Pathways in Mammalian Cells. *Small* **2010**, *6*, 1185–1190.
- (17) Lin, Y. S.; Abadeer, N.; Hurley, K. R.; Haynes, C. L. Ultrastable, Redispersible, Small, and Highly Organomodified Mesoporous Silica Nanotherapeutics. *J. Am. Chem. Soc.* **2011**, *133*, 20444–20457.
- (18) Tang, F.; Li, L.; Chen, D. Mesoporous Silica Nanoparticles: Synthesis, Biocompatibility and Drug Delivery. *Adv. Mater.* **2012**, *24*, 1504–1534.
- (19) Kumar, N.; Chen, W.; Cheng, C. A.; Deng, T.; Wang, R.; Zink, J. I. Stimuli-Responsive Nanomachines and Caps for Drug Delivery. *The Enzymes* **2018**, *43*, 31–65.
- (20) Chen, W.; Cheng, C. A.; Zink, J. I. Spatial, Temporal, and Dose Control of Drug Delivery Using Noninvasive Magnetic Stimulation. *ACS Nano* **2019**, *13*, 1292–1308.
- (21) Chen, W.; Cheng, C.; Cosco, E.; Ramakrishnan, S.; Lingg, J.; Bruns, O.; Zink, J. I.; Sletten, E. M. Shortwave Infrared Imaging with J-Aggregates Stabilized in Hollow Mesoporous Silica Nanoparticles. *J. Am. Chem. Soc.* **2019**, *141*, 12475–12480.
- (22) Guardado-Alvarez, T. M.; Chen, W.; Norton, A. E.; Russell, M. M.; Connick, W. B.; Zink, J. I. Analyte-responsive Gated Hollow Mesoporous Silica Nanoparticles Exhibiting Inverse Functionality and an AND Logic Response. *Nanoscale* **2016**, *8*, 18296–18300.

1.2 Introduction to nanomachines and other caps on mesoporous silica nanoparticles for drug delivery

We reviewed the research work in Professor Jeffrey I. Zink's group in *Accounts of Chemical Research*. This review article provides a good introduction to the subjects of my dissertation. The following sections are adapted from Wei Chen, Carlotta A. Glackin, Marcus A. Horwitz, Jeffrey I. Zink *Accounts of Chemical Research* **2019**, *52*, 1531–1542. Copyright 2019 American Chemical Society.

Mesoporous silica nanoparticles (MSNs) are delivery vehicles that can carry cargo molecules and release them on command. The particles used in the applications reported in this Account are around 100 nm in diameter (about the size of a virus) and contain 2.5 nm tubular pores with a total volume of about 1 cm³/g. For the biomedical applications discussed here, the cargo is trapped in the pores until the particles are stimulated to release it. The challenges are to get the particles to the site of a disease and then to deliver the cargo on command. We describe methods to do both, and we illustrate the applicability of the particles to cure cancer and intracellular infectious disease. Our first steps were to design multifunctional nanoparticles with properties that allow them to carry and deliver hydrophobic drugs. Many important pharmaceuticals are hydrophobic and cannot reach the diseased sites by themselves. We describe how we modified MSNs to make them dispersible, imageable, and targetable and discuss *in vitro* studies. We then present examples of surface modifications that allow them to deliver large molecules such as siRNA. *In vivo* studies of siRNA delivery to treat triple-negative breast and ovarian cancers are presented. The next steps are to attach nanomachines and other types of caps that trap drug molecules but release them when stimulated. We describe nanomachines that respond autonomously (without human intervention)

to stimuli specific to disease sites. A versatile type of machine is a nanovalve that is closed at neutral (blood) pH but opens upon acidification that occurs in endolysosomes of cancer cells. Another type of machine, a snap-top cap, is stimulated by reducing agents such as glutathione in the cytosol of cells. Both of these platforms were studied *in vitro* to deliver antibiotics to infected macrophages and *in vivo* to cure mice infected with intracellular bacteria *Mycobacterium tuberculosis* and *Francisella tularensis*. The latter is a tier 1 select agent of bioterrorism. Finally, we describe nanomachines for drug delivery that are controlled by externally administered light and magnetic fields. A futuristic dream for nanotherapy is the ability to control a nano-object everywhere in the body. Magnetic fields penetrate completely and have spatial selectivity governed by the size of the field-producing coil. We describe how to control nanovalves with alternating magnetic fields (AMFs) and superparamagnetic cores inside the MSNs. The AMF heats the cores, and temperature-sensitive caps release the cargo. *In vitro* studies demonstrate dose control of the therapeutic to cause apoptosis without overheating the cells. Nanocarriers have great promise for therapeutic applications, and MSNs that can carry drugs to the site of a disease to produce a high local concentration without premature release and off-target damage may have the capability of realizing this goal.

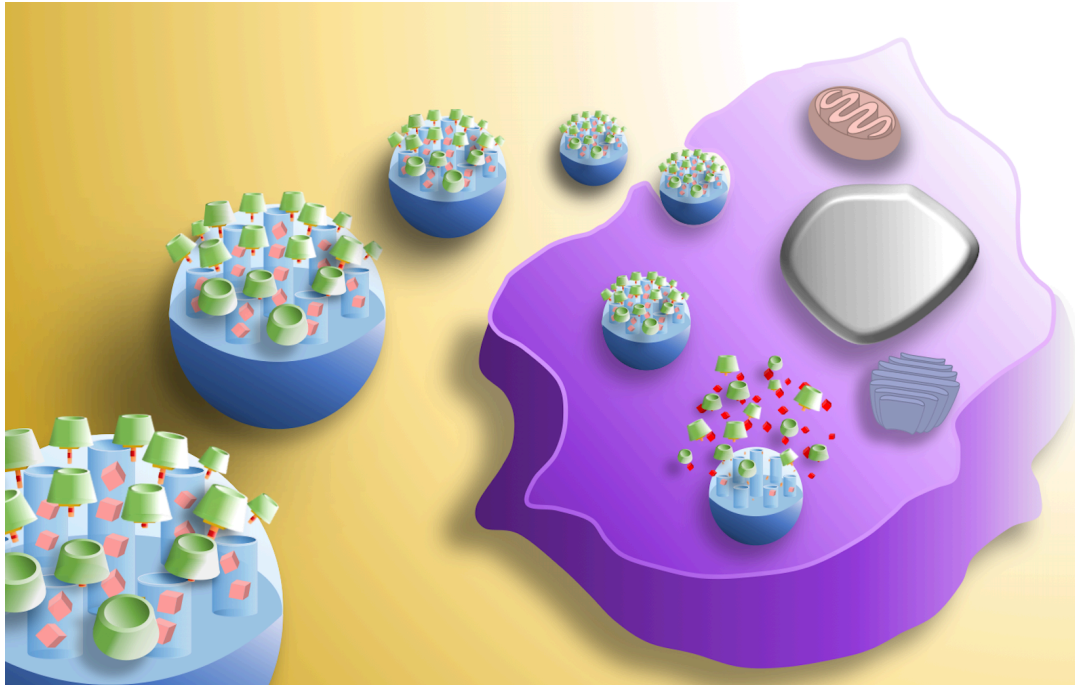


Figure 1.1. Table of content figure of nanomachines and other caps on mesoporous silica nanoparticles for drug delivery.

1.2.1 Introduction and background

The development of mesoporous silica nanoparticles in our research group for biomedical applications began with a completely unrelated line of research: investigation of transparent matrices for room temperature matrix isolation spectroscopy. The popularity of sol-gel synthesis of inorganic metal oxides was on the rise, and silica seemed to be a promising matrix candidate. The precursors, tetraalkoxy silanes, alcohol and water were readily available, and the formation of monolithic silica glass by hydrolysis and condensation occurred at room temperature in the air.¹

Molecules of spectroscopic interest to us dissolved in the initial sol and the glass formed around them and trapped them. Under acidic conditions and slow drying (to prevent cracking) in a cuvette, beautiful transparent rectangular prismatic pieces of glass were formed. Because of the mild synthesis conditions, even delicate biomolecules such as enzymes and other proteins could be trapped and retain their functions.²⁻⁵

The next important step was stimulated by reports that surfactant molecules coupled with the sol-gel synthesis could template well-ordered pores.⁶ Liquid crystalline phases such as rods or sheets could template tubular and lamellar structures. When the surfactant was removed by extraction or heating the former phase produced 2-dimensional hexagonal pores. (These structures were actually reported in the patent literature 20 years earlier but not appreciated at that time.)⁷ The original morphologies were macro-sized translucent pieces, but we wanted uniform transparent pieces so we explored and develop methods of synthesizing thin films.⁸⁻¹¹ We prepared and studied photophysical properties of molecules trapped in films on the order of 100 nm thick.

The final step was the discovery that under basic conditions, nanoparticles of the templated

silica could be prepared.¹² Formation of monodisperse particles was very sensitive to not only the concentrations of reactants but also to temperature and stirring speed in a flask. A cascade of synthetic papers followed and now it is standard to produce particles under 100 nm in diameter with highly ordered porosity.^{13–18} These particles are generally called “mesoporous silica nanoparticles” or MSNs (Figure 1.2AB). The MSNs that will be described in this account typically have a diameter of about 100 nm with 2.5 nm tubular pores, a surface area of about 1000 m²/g and a volume of about 1 cm³/g.^{19,20}

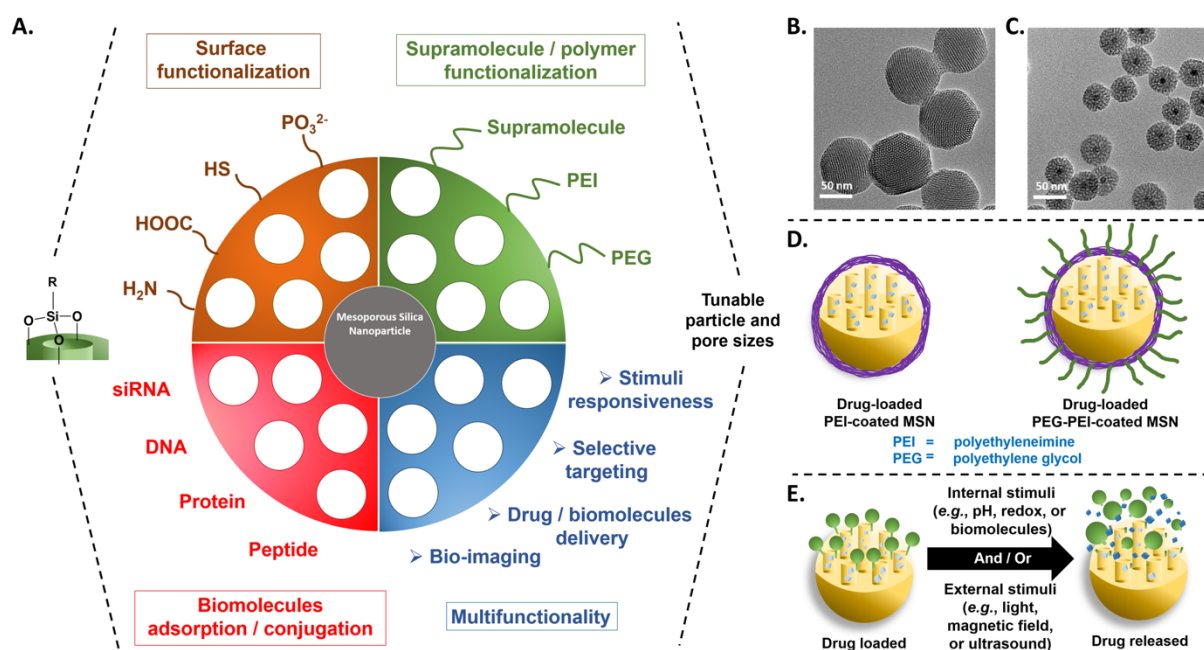


Figure 1.2. Collage of MSNs described in this Account. (A) Overview of functionalities of MSNs. Portrait of (B) MSNs and (C) magnetic core@shell nanoparticles. (D) Polymer coating. (E) Stimuli-responsive drug release particles.

As the synthetic challenges were being overcome, the question became what to do with the particles? In our work, we adapted multiple techniques that we had developed for attaching molecules to films to derivatizing the particles' surfaces (both the outer particle surface and the huge internal pore surfaces).¹⁹ Attachment of fluorescent dye molecules enabled the particles to be tracked by optical spectroscopy (even though the particles themselves were only imageable by transmission electron microscopy). After derivatization and surfactant extraction, the empty pores invited being filled with other molecules, and drug molecules brought the MSNs into the biomedical world.

1.2.2 *In Vitro* hydrophobic drug delivery

Our first foray into *in vitro* applications of our particles involved hydrophobic anticancer drugs as the cargo molecules in the pores.²¹ A challenge in cancer therapy is to deliver hydrophobic drugs to the sites of the disease. Many important anticancer drugs are poorly soluble and some sort of delivery system is needed. (The most important such systems currently in use are liposomes and albumins.) We wanted to see if MSNs could be suitable. A problem immediately arose: MSNs as synthesized aggregated extensively in water and biorelevant fluids. To achieve dispersity, we attached and tested many different types of molecules and settled on phosphonate for our initial studies and fluorescein as our fluorescent label. Anionic phosphonate groups were attached by using trihydroxysilylpropylphosphonate (THMP). This choice was unconventional because the current lore stated that positively charged particles would be better taken up by cells. It turned out to be a great choice because the particles had good circulation times in mice, were endocytosed readily by cancer cells, and accumulated in xenograft tumors as will be discussed later.

Our first demonstration of hydrophobic drug delivery used camptothecin (CPT), a representative anticancer drug that is also fluorescent. Derivatives of CPT are promising and effective drugs against a wide variety of carcinomas, but have much lower cytotoxicity than CPT. (FDA approved Irinotecan has a potency of 10% of that of CPT.) CPT was loaded into the pores by soaking MSNs in a DMSO solution of the drug overnight. The loaded nanoparticles were sonicated and washed with PBS solution to remove any weakly adsorbed drugs from the surfaces. A dispersion of the CPT-loaded MSNs was added to PANC-1 cells to determine if the nanoparticles transported the CPT into the cells and fluorescence microscopy was used to monitor the uptake. The delivery inhibited growth and caused apoptotic cell death.

We have also utilized mesoporous organosilica nanoparticles (MONs) and a chaperone-assisted strategy to facilitate both the loading and the release of hydrophobic drugs from nanoparticles. MONs have bridged organoalkoxysilanes in their frameworks that enable a very high loading of hydrophobic drugs in their pores. We used biodegradable oxamide-phenylene based MONs to achieve 84 wt% of hydrophobic CPT and CPT delivery in lung cancer cells.²² For pure MSNs, we recently developed a chaperone-assisted strategy to achieve both substantial loading and release amounts of the water-insoluble drug clofazimine (CFZ).²³ The interaction between the chaperone acetophenone (AP) molecules and CFZ provides the driving force for AP to carry large concentrations of CFZ into the pores, and thus significantly enhances the release of CFZ in buffer solution. *In vitro* studies show that the optimized CFZ-loaded MSNs effectively kill *Mycobacterium tuberculosis* in macrophages. This chaperone-assisted delivery strategy can be applied to the loading and delivery of other hydrophobic drugs with their suitable chaperone

molecules.

1.2.3 Multifunctional MSNs

The MSNs used in the hydrophobic CPT delivery study had two different molecules attached to their surfaces: phosphonate for dispersibility and fluorescein for optical imaging. We wanted to push the limits and to demonstrate that more functionality and versatility could be achieved (Figure 1.2A). To that end, we synthesized a different type of MSN containing a superparamagnetic iron oxide core for magnetic manipulation and MRI imaging (Figure 1.2C).¹⁹ The pores were available for filling with cargo. On the outer surface we attached a biomolecule, folate, that we wanted to test for active targeting of cancer cells. The resulting paper had a large impact because it brought attention to the versatility of MSNs as a platform for multiple actions including imaging and drug delivery.

An important aspect of our explorations of multifunctional MSNs was our investigation of active targeting agents. In order to be effective therapeutic agents, MSNs need to be carried “passively” by the blood to the site of the tumor. In addition, “active” targeting of specific receptors on tumor cells could be achieved by attaching appropriate molecules to the MSNs. Our initial studies involved folate and we found that uptake of the particles by cells having folate receptors was almost always enhanced *in vitro* but that *in vivo* tumor shrinkage was often but not always enhanced. Similar results were obtained with MSNs containing attached ferritin and an RGD peptide.²⁴ Excellent results with hyaluronic acid are discussed in the following section. It is clear that active targeting can occur but each type of targeting agent must be evaluated on a case by case basis.

We further extended the functionality of MSNs by coating the outside surface with polymers. The two most important polymers (evidenced by the *in vitro* and *in vivo* studies described in detail below) were PEG and low molecular weight PEI (Figure 1.2D). In some cases, we chemically bonded the PEI to the particles and in others we used electrostatic attraction of the cationic PEI to the anionic phosphonate-coated surface. We showed that low molecular weight PEI (1.2 kD) has negligible toxicity compared to that of the high molecular weight polymer.²⁵ Its importance lies in its abilities to carry, protect and deliver siRNA (next section) as well as to facilitate endosomal escape through the proton sponge effect for the nucleotide delivery. The PEG coatings were used to improve dispersibility and also for their ability to increase circulation time in mice (stealth particles).²⁶

1.2.4 Nanoparticle delivery of small interfering RNAs – from basic science to clinical applications

Recently efforts have begun to use siRNA as a therapeutic agent.²⁷ Preclinical and clinical trials have demonstrated that siRNA can be delivered to cells *in vivo* and retain its function, knocking down target genes in both prostate cancer and melanoma.²⁷ A drawback to RNAi-based therapy is that RNA tends to be susceptible to nuclease degradation, and is thus unstable in the body. Our polymer-coated MSNs proved to be very effective in protecting siRNA and carrying it to tumors in mice.

RNA interference (RNAi) using double-stranded RNA was first demonstrated in *C. elegans*.^{27,28} In mammals, 21-nucleotide long RNA fragments called small interfering RNAs (siRNAs) are the effectors of RNAi.²⁹ These fragments bind to a target mRNA, and then form the

RNA induced silencing complex (RISC).³⁰ RISC also contains Argonaute proteins, specifically Ago2, that cleave the mRNA, thus preventing protein translation.³¹

Our earliest successful demonstration of RNA delivery using MSNs involved delivery of siRNA to drug-resistant KB-V1 cells to silence the expression of efflux transporter P-glycoprotein (PPgp). We used low molecular weight cationic PEI coating (described in section 1.2.3) in which the anionic siRNA was entrained and protected. Dox was loaded in the pores.³² The dual delivery demonstrated that MSN delivery effectively knocked down gene expression of a drug exporter and increased intracellular DOX levels to improve cytotoxic killing.³²

We have recently shown *in vivo* efficacy of MSN-delivered siRNA in a mouse model of melanoma. Mice treated with siRNA against *TWIST* had smaller, less vascularized tumors, likely the result of inhibition of CCL2-driven angiogenesis within the growing tumors.³³ We obtained similar data in ovarian cancer, where mice treated with siTWIST-MSN plus chemotherapy had 75% less tumor burden than control mice treated with chemotherapy only.³⁴

In a second series of studies, we combined active targeting of Cancer Stem Cells (CSC) with siRNA delivery (Figure 1.3).³⁵ Cluster of differentiation 44 (CD44) is a ubiquitously present glycoprotein on the surface of mammalian cells. Since the discovery that the receptor is over-expressed in a variety of solid tumors, such as pancreatic, breast and lung cancer, many studies have focused on methods for targeting CD44 in an attempt to improve drug delivery and discrimination between healthy and malignant tissue, while reducing residual toxicity and off-target accumulation. Hyaluronic acid (HA), the primary CD44 binding molecule, has proved a

significant ally in developing nanocarriers that demonstrate preferential tumor accumulation and increased cell uptake.

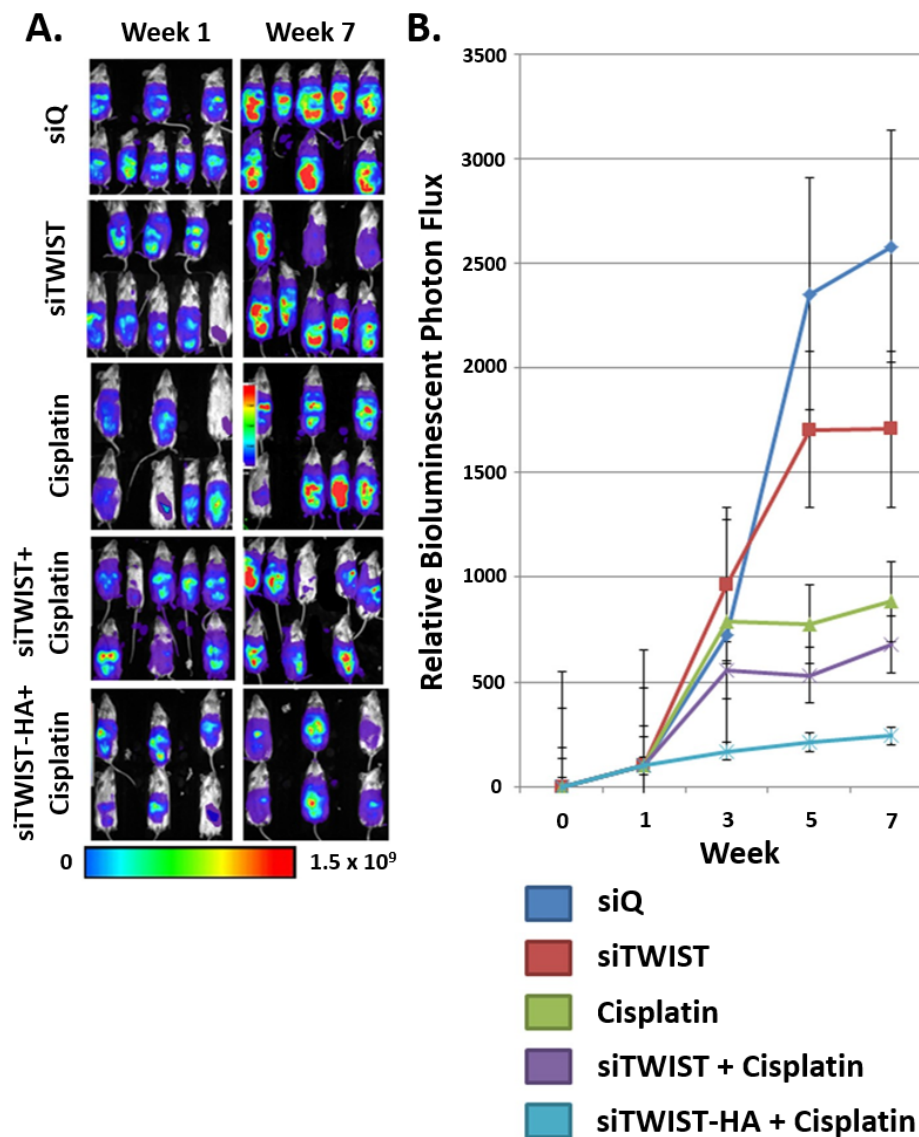


Figure 1.3. (A) Bioluminescence imaging of Ovar8-IP tumors. Tumors treated with cisplatin emit noticeably weaker signal than siTWIST or siQ only control mice, while those treated with siTWIST-MSNs plus cisplatin exhibit a further loss of signal. siTWIST-MSN-HAs plus cisplatin exhibit a greatest loss of signal. (B) Quantification of bioluminescence depicted in A. Units for luminescence are photons/sec/cm²/steradian. Adapted with permission from ref. 35. Copyright 2018 Elsevier.

We studied HA-coated MSNs as a therapeutic approach to deliver oligonucleotides to tumors that overexpress CD44+ (Figure 1.4).³⁵ We delivered TWIST siRNA to breast and ovarian cancer xenografts and reduced tumor burden.³³⁻³⁵ Our particles inhibited EMT signaling, reduced tumor burden and exhibited synergistic efficacy in combination with cisplatin.³⁵ These results demonstrated a useful therapeutic strategy for chemoresistant ovarian cancer. Successful application of these types of approaches could pave the way for future RNA-based therapies against other targets of interest currently thought to be “undruggable”.

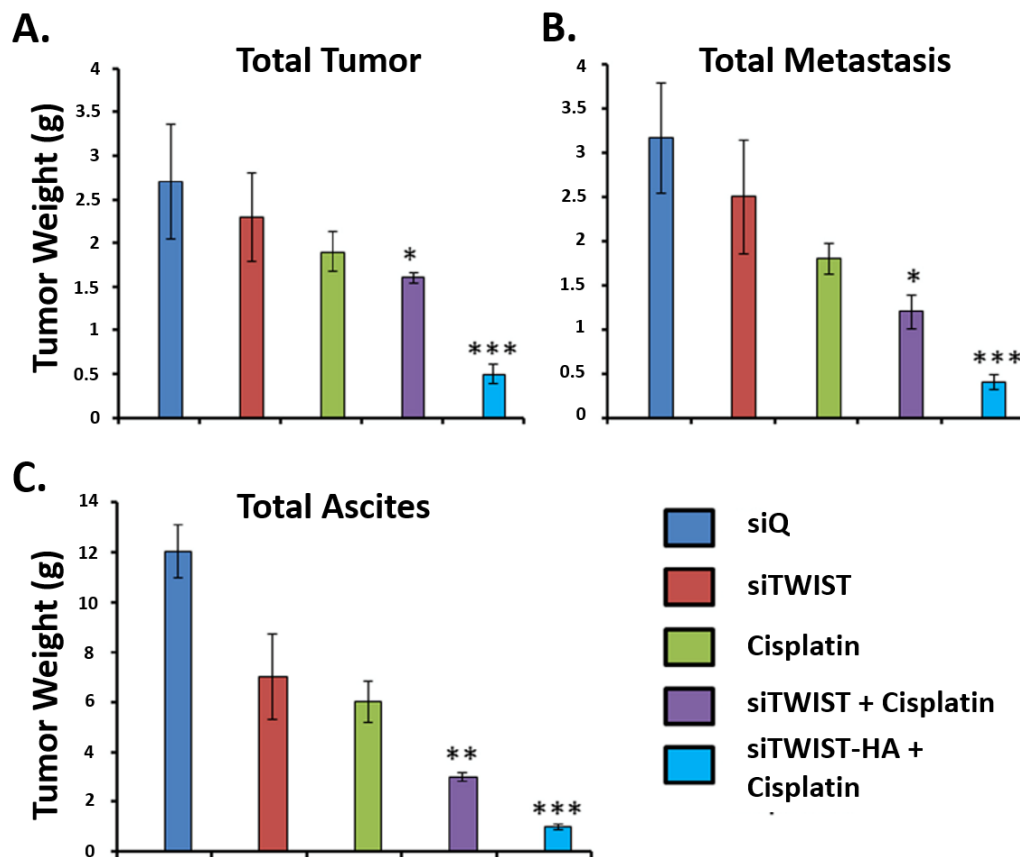


Figure 1.4. Quantification of the weight loss of (A) tumor, (B) metastasis, and (C) ascites of mice treated as described in Figure 2. The combination of HA targeted MSNs carrying siRNA and cisplatin was the most efficacious. Adapted with permission from ref. 35. Copyright 2018 Elsevier.

1.2.5 Nanomachines

Our next major goal was to design a system that could carry a therapeutic through the blood stream to the site of a disease with no leakage, release a high local concentration of the drug, release it only on an autonomous or external command, and kill the cancer cells or an infectious agents. The release itself required a pore cap that could be closed to trap cargo molecules and open in response to a desired stimulus and release the cargo.^{13,15,20,36} We named our original system a “nanovalve” which consisted of a stalk and a large cyclic molecule that blocked the pore in the closed position and slid along the stalk away from the pore opening to release the pore’s contents. The large amplitude motion of this nanomachine, like that of any machine, needs a power supply. What kinds of motions and what kinds of stimuli could we use that would be compatible with a machine deep in the body of an animal? Answering these questions and making suitable machines required both imagination and hard work.

We categorize nanomachines according to the source of the stimulus required to operate them (Figure 1.2E).¹⁴ When the stimulus is a direct result of human intervention, we call it “external”. The most important external sources are light, magnetism and ultrasound. Each of these sources can produce large amplitude motion in molecules by multiple mechanisms. For example, light energy can cause photochemical reactions, produce heat that causes a chemical reaction, or be absorbed by “transducer” molecules that change the pH (photoacids) or cause electron transfer (photooxidants or reductants). Heat production is the primary usable effect of alternating magnetic fields and ultrasound.

The second category of operation we call “internal” or “autonomous”. The stimulus for

operation originates from the change in the particles' surroundings. For example, when the machine goes from the blood stream to a cell's endolysosome as a result of endocytosis, the pH changes from 7.4 to less than 6 and a pH sensitive valve opens. When it enters the cytosol, the presence of antioxidants such as glutathione cause a redox active valve to open. No external intervention is required. Autonomous nanomachines such as these are the most widely studied *in vitro* and *in vivo*.

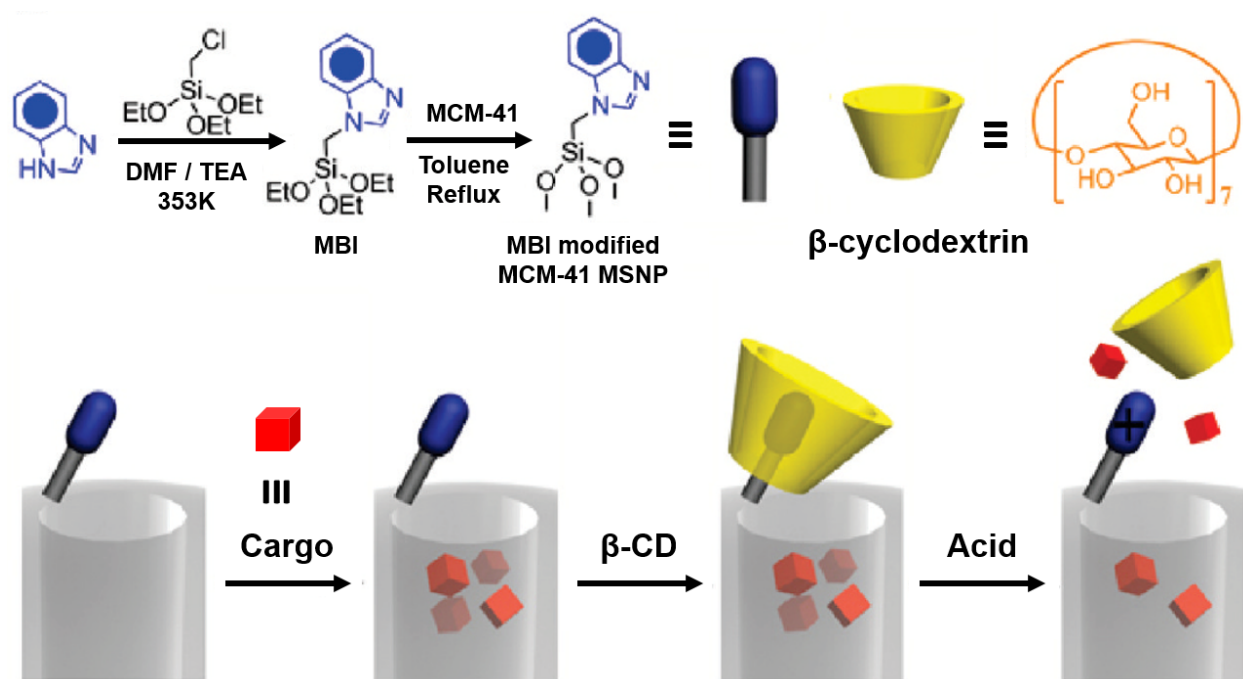


Figure 1.5. Schematic illustration of the pH-responsive benzimidazole nanovalve. Adapted with permission from ref. 37. Copyright 2010 American Chemical Society.

The most actively studied pH valve is based on the design principle of a cyclic cap that has a large binding constant to a stalk that is hydrophobic at the pH of blood but becomes protonated and hydrophilic in the acidic environment of an endolysosome. A widely used example is shown

in Figure 1.5.³⁷ The cyclic molecule is β -cyclodextrin (β CD), a cyclic sugar with a hydrophobic interior. The stalk is a specific benzimidazole with a pKa of about 7. Above pH 7, the hydrophobic-hydrophobic non-covalent interaction holds the pseudorotaxane together but at lower pH it dissociates. When the stalk is attached at a pore opening on MSNs, the β CD traps cargo molecules in the pore but releases them upon acidification. *In vivo* applications of this autonomous pH nanovalve are discussed in the following section.

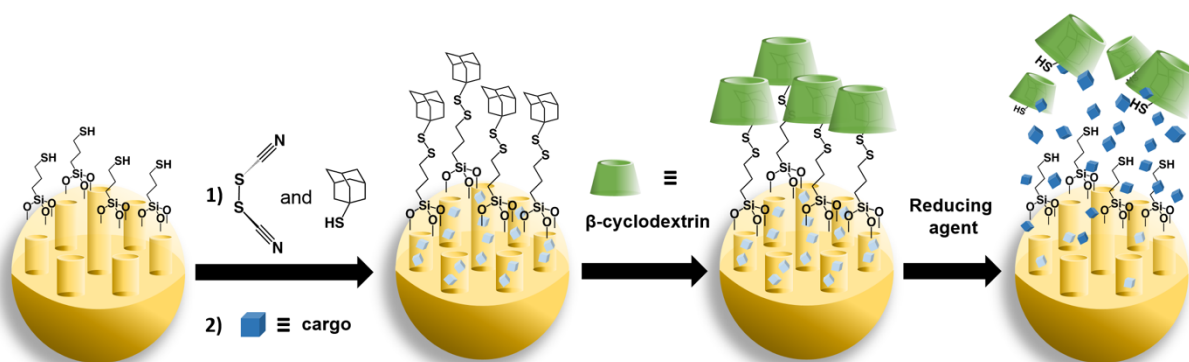


Figure 1.6. Schematic illustration of the redox-responsive disulfide nanovalve.

The most-used redox activated system that we named a “snap-top” is based on the design principle that a redox-sensitive chemical bond can be broken in the presence of reducing agents in the cytosol of a cell.³⁸ This simple design utilizes a disulfide stalk containing a bulky cap on its end (Figure 1.6). When attached at an MSNs pore surface the cap traps the cargo, but when the particle escapes the lysosome the reducing agents such as glutathione cause the disulfide to dissociate into two thiols, releasing the bulky group and the trapped drug molecules. *In vivo* studies using this redox snap-top are described in the following section.

Many other autonomous nanomachines and capping agents have been studied and several thorough reviews have been published recently.^{13,15,20} One additional example from our group is the original enzyme-activated snap-top in which a β CD slides on a stalk but is blocked from leaving by a bulky stopper held in place by a functional group (an ester) that is a substrate for an enzyme (porcine liver esterase).³⁹ When the particle encounters the enzyme the bulky group is “snapped off” and the cargo is released. This type of snap-top is a prototype for a nanocarrier that could respond only to a specific enzyme overexpressed by a particular cancer cell.

1.2.6 Nanoparticles against infectious diseases caused by intracellular pathogens

We used both of the nanomachines in Figures 1.5 and 1.6 to kill pathogenic bacteria in phagocytes *in vitro* and *in vivo*. Mononuclear phagocytes, primarily monocytes and tissue macrophages, are known as professional phagocytes because of their reputation for avidly ingesting particles of many kinds. Such particles include numerous pathogens that are readily killed by macrophage antimicrobial armaments. However, one class of pathogens, known as intracellular parasites, intentionally induce their uptake by macrophages with the aim of hijacking host cell machinery towards their own end – survival and intracellular replication. Intracellular pathogens include the agents of tuberculosis and what are referred to by the US government as Tier 1 Select Agents because of especially high concern that they may be intentionally employed in a bioterrorist attack. Such pathogens include *Francisella tularensis*, the agent of tularemia.

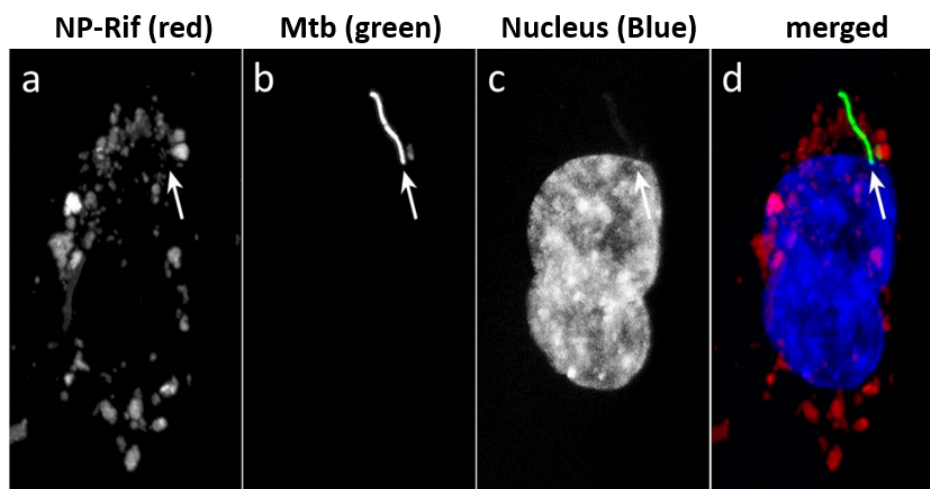
For treatment of many diseases, mononuclear phagocytes – especially those in the liver, spleen and lung – pose an obstacle to MSN delivery of nanotherapeutics, since they readily ingest intravenously administered nanoparticles intended for delivery elsewhere, *e.g.* to cancer cells.

MSNs designed for cancer therapy need to be specially designed to evade macrophages, but for treatment of diseases caused by intracellular pathogens, the avidity with which macrophages ingest MSNs provides a tremendous advantage – no specific targeting ligands are necessary to deliver copious amounts of antibiotic-loaded particles to macrophages harboring intracellular pathogens. Nanotherapeutic delivery of antibiotics maximizes antibiotic delivery to infected host macrophages while minimizing systemic toxicity.

Our nanotherapeutics have been designed primarily to treat two diseases caused by intracellular pathogens – tuberculosis, caused by *Mycobacterium tuberculosis* (Mtb),^{23,40,41} and tularemia, caused by *Francisella tularensis* (Ft).^{42,43} Both diseases pose major challenges to treatment with conventionally delivered antibiotics. TB caused by drug-sensitive organisms requires 6-9 months treatment and drug-resistant Mtb, which is even more difficult to treat requires multidrug therapy for up to 2 years. Hence, more efficient delivery of antibiotics to host macrophages via nanotherapeutics has the potential to shorten the treatment course, improve adherence, impede the emergence of drug resistance, and reduce systemic drug toxicity.

Tularemia, a bacterial zoonosis, can manifest as one of several syndromes depending upon the mode of Ft transmission. Pneumonic tularemia, the most dangerous form and the one of greatest concern from a bioterrorism perspective, is contracted via inhalation. With current therapy, tularemia can still be fatal, resolve slowly, or relapse. Hence functionalized nanotherapeutics targeting infected macrophages have the potential for more rapid cure, reduced time in intensive care, and less frequent relapse.

A. *M. tuberculosis*



B. *F. tularensis*

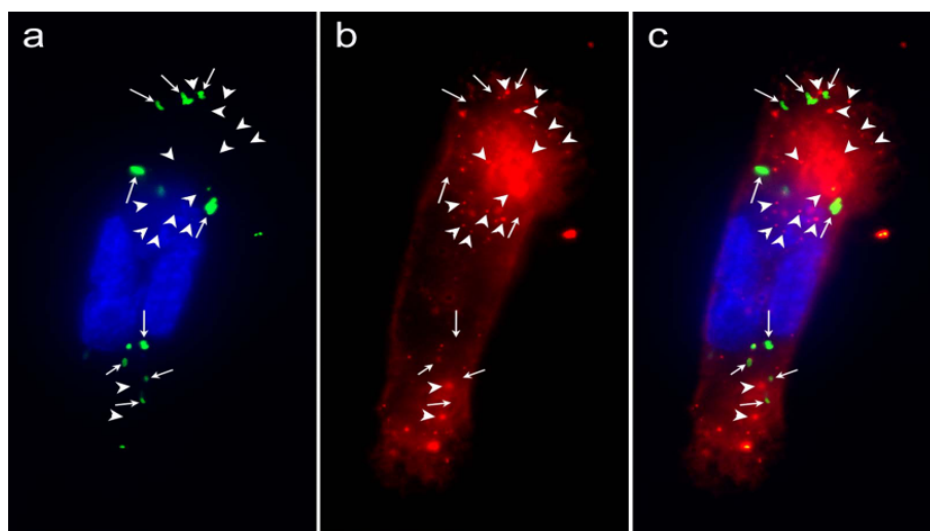


Figure 1.7. MSNs are avidly ingested by human macrophages infected with *Mycobacterium tuberculosis* (A) and *Francisella tularensis* (B). (A) Human THP-1 macrophages were infected with GFP-expressing Mtb, incubated with red fluorescent MSNs loaded with rifampin (NP-RIF), fixed, stained with nuclear stain DAPI, and imaged by confocal microscopy. Large numbers of NP-RIF (a) and an Mtb bacillus (b, arrow) are observed in the macrophage, whose nucleus is stained blue (c); the merged image is shown in panel d. Adapted with permission from ref. 41. Copyright 2012 American Society for Microbiology. (B) Human THP-1 macrophages were infected with GFP-expressing Ft, incubated with RITC-labelled MSN-MBI, fixed, stained with DAPI, and imaged by confocal microscopy. Green Ft (a, c, arrows), red MSNs (b, c, arrowheads) and DAPI-stained nucleus (a, c, blue) are seen in individual images (a, b) and merged image (c). Adapted with permission from ref. 42. Copyright 2015 American Chemical Society.

We designed and evaluated PEI-coated MSNs (~100 nm) loaded with the antibiotic drug Rifampin for treatment of TB.⁴¹ These MSNs were all avidly ingested by Mtb-infected human macrophages (Figure 1.7A). By fluorescence microscopy, the MSNs co-localized with CD63, indicating uptake into endolysosomes.⁴¹ In *In vitro* studies in which these MSNs were added to human macrophages infected with the highly virulent Mtb Erdman strain, the MSNs readily killed Mtb, and they did so significantly more efficiently than an equivalent amount of free drug (Figure 1.8A).

We developed MSNs with pH- and redox potential- sensitive nanovalves for delivery of the antibiotic moxifloxacin (MXF).^{42,43} Both types of MSNs were avidly ingested by Ft-infected macrophages (Figure 1.7B) and rapidly killed intramacrophage Ft in a dose-dependent fashion. These MSNs were evaluated for efficacy in a murine model of lethal pneumonic tularemia in which mice were infected intranasally with a lethal dose of Ft LVS (6xLD₅₀). The mice were treated with free MXF or MXF-loaded MSNs intravenously every other day for three doses; euthanized one day later; and Ft CFU assayed in lung, liver, and spleen. In untreated mice, bacteria multiplied to high levels (~7.5 logs in the lung) and the mice lost 12-24% of their total body weight. In contrast, mice treated with MXF-loaded MSNs maintained their body weight and CFU in the lungs decreased by 1-2 logs (Figure 1.8B).⁴³ The MXF-loaded MSNs were significantly more effective than an equivalent amount of free drug in reducing CFU in all organs; in the lung, they were more effective than ~3 fold greater dose of free MXF.

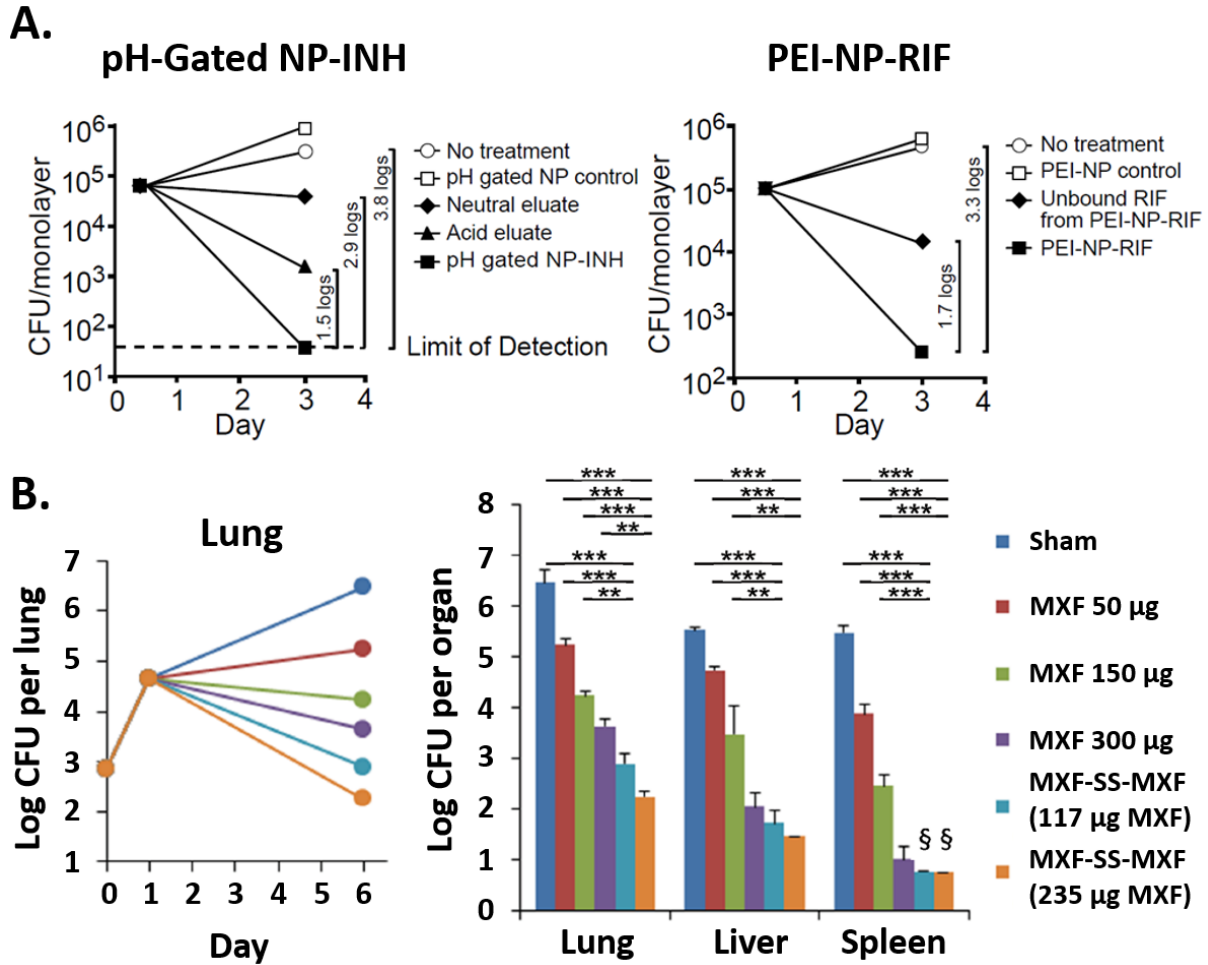


Figure 1.8. Antibiotic-loaded MSNs rapidly kill *M. tuberculosis* *in vitro* (A) and *F. tularensis* *in vivo* (B). (A) MSNs loaded with Isoniazid (INH) or Rifampin (RIF) kill Mtb to a greater extent than an equivalent amount of free drug. Compared with no treatment, the INH- and RIF-loaded MSNs reduced the colony-forming units (CFU) by 3.8 and 3.3 log CFU, respectively, and compared with an equivalent amount of free drug, they reduced CFU by an additional 1.5 and 1.7 log CFU, respectively. Adapted with permission from ref. 41. Copyright 2012 American Society for Microbiology. (B) MXF-loaded MSNs rapidly kill Ft *in vivo* in a mouse model of lethal pneumonic tularemia and are much more efficacious in reducing the lung burden of Ft than equivalent amounts of free MXF (Efficacy ratios 3-5:1).⁴³ The CFUs in lung, liver and spleen were determined on day 6. Adapted with permission from ref. 43. Copyright 2016 Wiley-VCH.

1.2.7 Externally operated nanomachines and caps

A futuristic dream for nanotherapy is the ability to control a nano-object everywhere in the body. Although total control including mobility is far from reality, it is possible to stimulate nanocarriers anywhere and to release therapeutic molecules with spatial and temporal accuracy. The major methods of external control are light, ultrasound and magnetism. For diseases on or near the skin, photothermal therapy is useful, but for tumors deep in the body, magnetism penetrates the best. Externally operated drug release is a step beyond autonomous release because it can be turned on and off at will and does not have to rely on specific chemical changes or the presence of specific molecules in order to operate. It is also more complex than autonomously stimulated release because the external control also requires external instrumentation and an operator. These issues contribute to the sparsity of *in vivo* studies reported to date.

Progress in synthesizing and making functioning nanomachines and caps that can be remotely activated has been rapid.^{13,14,20,36} The most prevalent and highly developed systems are light activated. We were interested in using light to power nanomachines, including by direct photochemical bond breaking or photoisomerization and by indirect phototransducers to activate pH and redox valves. Direct photocleavage is a convenient way to remove caps from pores. Molecules in their excited state can transfer protons (photoacids)⁴⁴ or electrons (photo-redox)⁴⁵ and can be used to activate machines originally designed to be activated by chemical acidification or redox. Excited state energy transfer from molecules with high two photon cross sections can trigger the above reactions using two near infrared photons.

We used our impeller for our first *in vitro* studies.⁴⁶ Photo-induced trans-cis isomerization of

azobenzene derivatives bonded to the insides of MSN pore walls trap cargo molecules in the dark but allow them to escape when they wag back and forth.^{47,48} We delivered an anticancer drug into pancreatic cancer cells and observed no killing in the dark but efficient apoptosis when the impellers were excited.⁴⁶

Other photo-responsive gatekeepers include azobenzene and cyclodextrin supramolecular complex,^{49,50} photolabile coumarin-based nanovalves,⁵¹ cucurbit[6]uril (CB[6]) and stalk supramolecular complexes,⁵² photoacid molecules and pH-sensitive nanovalves,⁴⁴ and photo-transduced molecules and redox environment-sensitive nanovalves.⁵³ We later demonstrated two photon near IR excitation of a transducer molecule that transferred energy to the azobenzene molecules and released cargo.⁵⁴ Interesting progress continues to be made in the two-photon field for potential biomedical applications.

In our current research for biological applications, we are focusing on magnetism as the stimulus, specifically alternating magnetic fields (AMF). Nanoparticles containing superparamagnetic components are heated by the AMF and thermo-stimulated machines or caps can be activated by the heat to release cargo. Magnetic heating is currently being used to kill cells or destroy tumors by hypothermia,⁵⁵⁻⁵⁷ but it can also create tumor metastasis. We are focusing on drug delivery by taking advantage of the localized particle heating without bulk heating.

To understand what degree of local heating can be attained, we designed nanothermometers in the MSNs containing the superparamagnetic heaters and measured internal temperature changes of over 20 °C above that of the surrounding aqueous medium, more than enough to activate thermosensitive caps without causing hyperthermia.⁵⁸⁻⁶⁰

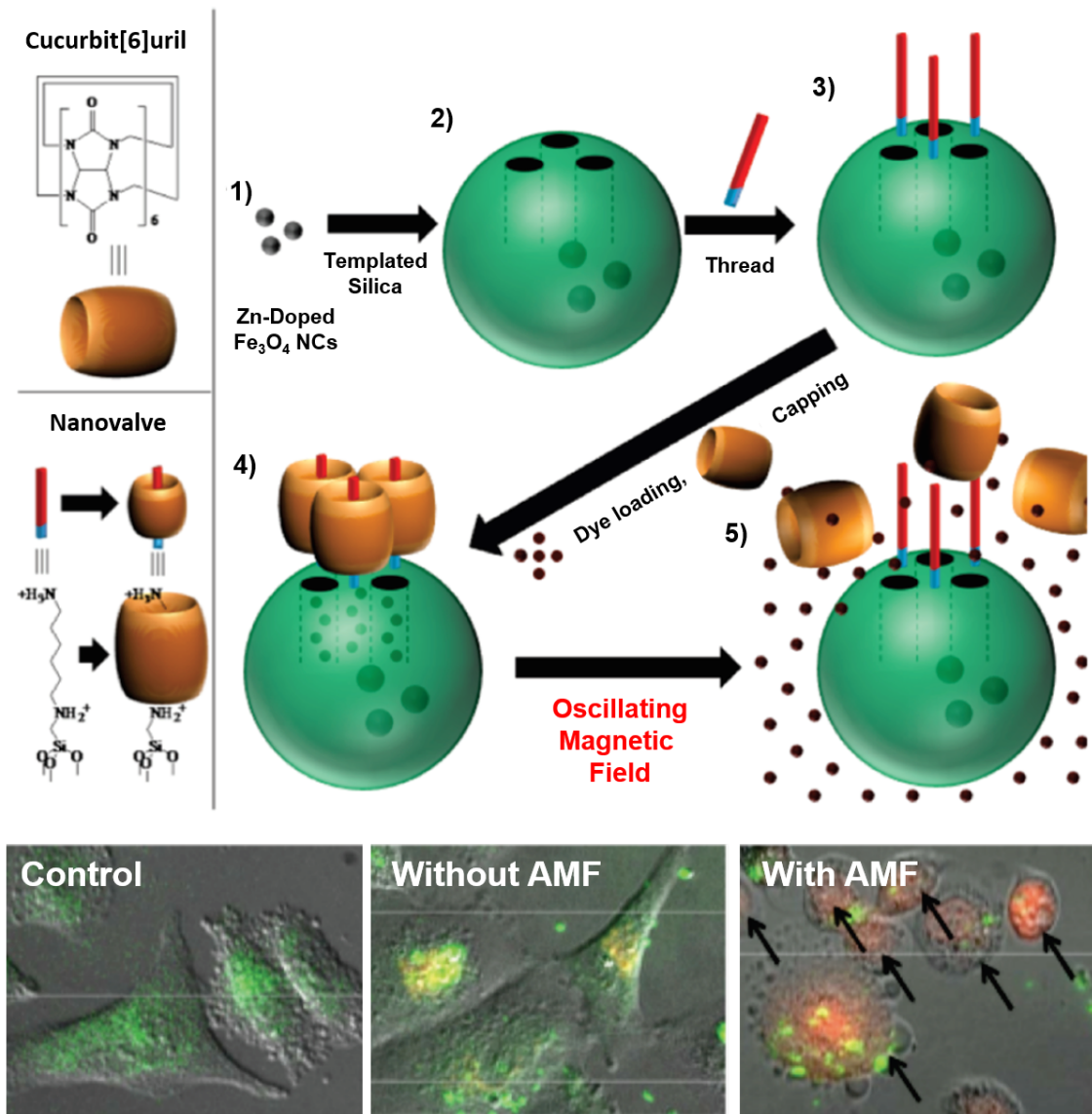


Figure 1.9. Schematic illustration of the construction and operation of the thermo-responsive cucurbit[6]uril nanovalve. Fluorescence microscope images show breast cancer cells were killed by the released DOX after the exposure to an AMF. Adapted with permission from ref. 61. Copyright 2010 American Chemical Society.

Our first *in vitro* study used core@shell nanoparticles to carry and deliver drugs actuated by AMF and used a supramolecular valve comprised of a bulky cucurbit[6]tril (CB[6]) ring and an alkylammonium thread attached on the surface of MSNs that acts as a thermo-sensitive gatekeeper

(Figure 1.9).⁶¹ When the temperature increases, the binding constant between the CB[6] ring and the alkylammonium thread decreases leading to the detachment of CB[6] from the thread followed by drug release. The release of drugs was not triggered by bulk heating from the solutions but by localized heating generated from the interior magnetic cores. We showed that doxorubicin released intracellularly by AMF stimulation effectively kills MDA-MB-231 breast cancer cells.

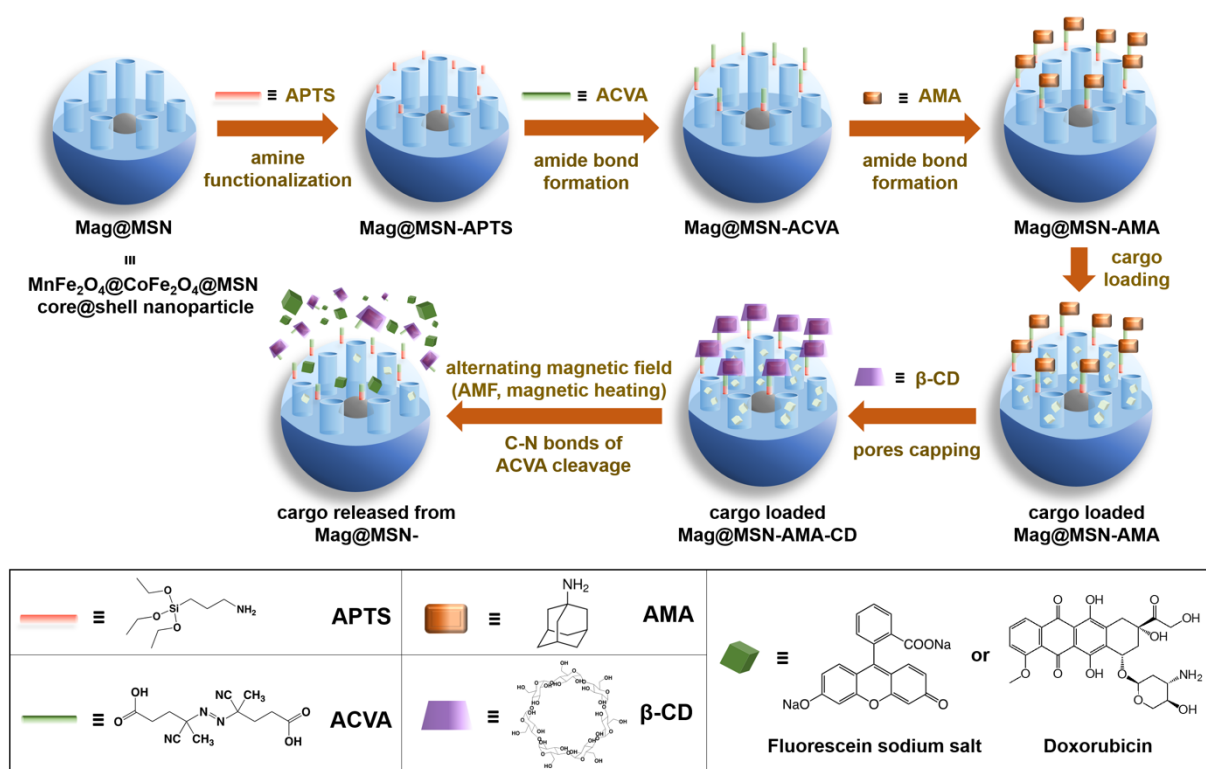


Figure 1.10. Schematic illustration of the synthesis and operation of the thermo-sensitive azo cap. Adapted with permission from ref. 62. Copyright 2019 American Chemical Society.

Very recently, we demonstrated spatial, temporal, and dose control of drug delivery using superparamagnetic $\text{MnFe}_2\text{O}_4@\text{CoFe}_2\text{O}_4$ nanoparticles with high specific loss power (1510.8 W/g) and high saturation magnetization (105 emu/g) (Figure 1.10).⁶² Thermo-sensitive gatekeepers that

contain an aliphatic azo moiety release a bulky cap and regulate the release of drugs. The dose of the drug release was controlled by the AMF exposure time and triggered by the localized high temperature from the interior magnetic core and not by bulk heating. Multiple sequential exposure of AMF causes drug release in a step-wise manner. *In vitro* studies show that the drug delivery platform is biocompatible, that drug-loaded nanocarriers do not kill the cells without the AMF stimulation, and that cell death was correlated with the AMF exposure time (Figure 1.11). Thermo-responsive drug delivery stimulated by an AMF offers the potential of becoming an innovative chemotherapy that noninvasively, remotely, and precisely controls the dosage of drugs, avoiding the risk generated when overheating the bulk solution.

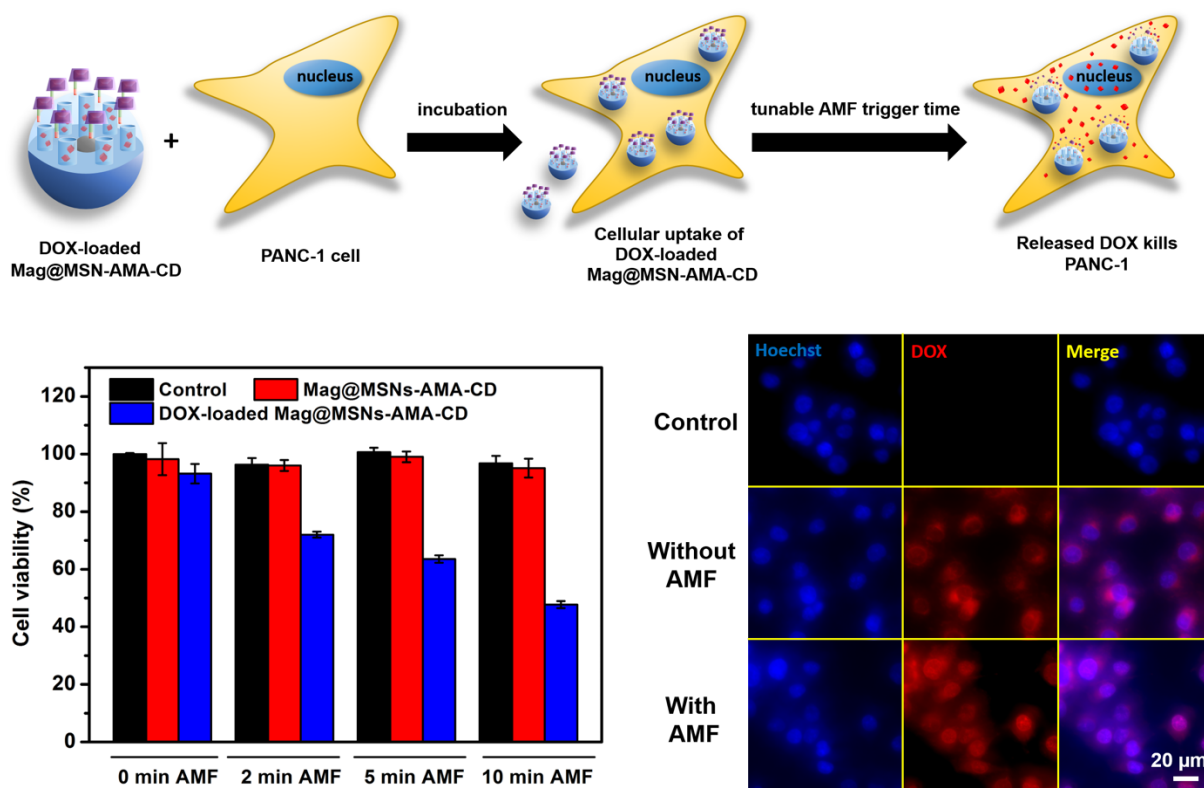


Figure 1.11. Effects of AMF stimulated DOX release on PANC-1 cells. *In vitro* cellular killing and fluorescence microscope images of DOX-loaded nanoparticles after AMF exposure are shown left and right, respectively. Adapted with permission from ref. 62. Copyright 2019 American Chemical Society.

1.2.8 Future perspectives

Mesoporous silica is a versatile platform for drug delivery applications. The nanoparticles are nontoxic, carry large payloads of therapeutic drugs, and can be capped to prevent premature drug release until the nanoparticles reach their target where they can then be stimulated to release a high local concentration of the therapeutic. The particles can carry other important therapeutic molecules such as siRNA, protect them from enzymes and degradation, and release them intracellularly. Their potential for curing cancer occupies most current research attention, but they can be used to treat other diseases including infectious diseases.

The route of administration is important. We emphasized intravenous administration, but for treatment of intracellular pathogens, we found that intramuscular injection was extremely beneficial because of superior pharmacokinetics.⁶³ Preliminary studies show inhalation administration to be extremely promising for treatment of lung infections.

The multifunctionality of nanotherapeutics including MSNs promises to revolutionize drug delivery. It allows for active targeting of drug-loaded particles (– our best *in vivo* example of a successful agent is hyaluronic acid – other targeting agents (*e.g.* folic acid, and RGD peptide) toward their specific cancer cells were also demonstrated). The drug-loaded particles can additionally contain molecules for image guided therapy, such as paramagnetic metals or superparamagnetic cores for imaging by MRI, fluorescent dyes (especially in near-IR for optical imaging), and atoms for PET imaging. The multifunctionality of nanotherapeutics also allows for theranostics – the combining of therapeutic and diagnostic agents into a single nanoparticle. Finally, the multifunctionality of nanotherapeutics allows for the delivery of combination drug therapy at

optimal drug dose ratios, thereby enhancing drug synergy and safety.

It would be extremely beneficial if MSNs could move forward toward clinics. Before then, many prerequisites need to be fulfilled, such as industrial-scale production of MSNs under Good Manufacturing Practice (GMP) to guarantee that the properties of the MSNs are reproducible from batch to batch, detailed investigations of the potential toxicity, bio-distribution, and clearance from the animal body, and whether drug-loaded MSNs have higher treatment efficacy and fewer side effects than those of the free drugs alone. It is a long and complicated road to clinical trials and eventual use in the clinic, but the attractive properties make MSNs worthy of the attention that they are being given.

1.2.9 Acknowledgment

We gratefully acknowledge financial support through the years by the National Science Foundation, the National Institutes of Health, and the Defense Threat Reduction Agency. Manuscript writing was supported in part by the Zink Research and Student Support Fund.

1.2.10 References

- (1) Brinker, C. J.; Scherer, G. W. *Sol-Gel Science: The Physics and Chemistry of Sol-Gel Processing*; Academic Press: Cambridge, **1990**.
- (2) Ellerby, L. M.; Nishida, C. R.; Nishida, F.; Yamanaka, S. A.; Dunn, B.; Valentine, J. S.; Zink, J. I. Encapsulation of Proteins in Transparent Porous Silicate Glasses Prepared by the Sol-Gel Method. *Science*, **1992**, *255*, 1113–1115.
- (3) Chung, K. E.; Valentine, J. S.; Zink, J. I.; Lan, E. H.; Davidson, M. S.; Dunn, B. S. Measurement of Dissolved Oxygen in Water Using Glass-Encapsulated Myoglobin. *Anal. Chem.* **1995**, *67*, 1505–1509.
- (4) Dunn, B.; Miller, J. M.; Dave, B. C.; Valentine, J. S.; Zink, J. I. Strategies for Encapsulating Biomolecules in Sol-Gel Matrices. *Acta Mater.* **1998**, *46*, 737–741.
- (5) Miller, J. M.; Dunn, B.; Valentine, J. S.; Zink, J. I. Synthesis Conditions for Encapsulating Cytochrome c and Catalase in SiO₂ Sol-Gel Materials. *J. Non. Cryst. Solids* **1996**, *202*, 279–289.
- (6) Kresge, C. T.; Leonowicz, M. E.; Roth, W. J.; Vartuli, J. C.; Beck, J. S. Ordered Mesoporous Molecular Sieves Synthesized by a Liquid-Crystal Template Mechanism. *Nature* **1992**, *359*, 710–712.
- (7) Chiola, V.; Ritsko, J. E.; Vanderpool, C. D. Process for Producing Low-Bulk Density Silica, **1971** US Patent App 3556725A.
- (8) Nishida, F.; McKiernan, J. M.; Dunn, B.; Zink, J. I.; Brinker, C. J.; Hurd, A. J. In Situ Fluorescence Probing of the Chemical Changes during Sol–Gel Thin Film Formation. *J. Am. Ceram. Soc.* **1995**, *78*, 1640–1648.
- (9) Dave, B. C.; Soyez, H.; Miller, J. M.; Dunn, B.; Valentine, J. S.; Zink, J. I. Synthesis of Protein-Doped Sol-Gel SiO₂ Thin Films: Evidence for Rotational Mobility of Encapsulated Cytochrome C. *Chem. Mater.* **1995**, *7*, 1431–1434.
- (10) Huang, M. H.; Dunn, B. S.; Soyez, H.; Zink, J. I. In Situ Probing by Fluorescence Spectroscopy of the Formation of Continuous Highly-Ordered Lamellar-Phase Mesostructured Thin Films. *Langmuir* **1998**, *14*, 7331–7333.
- (11) Huang, M. H.; Dunn, B. S.; Zink, J. I. In Situ Luminescence Probing of the Chemical and Structural Changes during Formation of Dip-Coated Lamellar Phase Sodium Dodecyl Sulfate Sol-Gel Thin Films. *J. Am. Chem. Soc.* **2000**, *122*, 3739–3745.
- (12) Grün, M.; Lauer, I.; Unger, K. K. The Synthesis of Micrometer- and Submicrometer-Size Spheres of Ordered Mesoporous Oxide MCM-41. *Adv. Mater.* **1997**, *9*, 254–257.

- (13) Li, Z.; Barnes, J. C.; Bosoy, A.; Stoddart, J. F.; Zink, J. I. Mesoporous Silica Nanoparticles in Biomedical Applications. *Chem. Soc. Rev.* **2012**, *41*, 2590–2605.
- (14) Ambrogio, M. W.; Thomas, C. R.; Zhao, Y. L.; Zink, J. I.; Stoddart, J. F. Mechanized Silica Nanoparticles: A New Frontier in Theranostic Nanomedicine. *Acc. Chem. Res.* **2011**, *44*, 903–913.
- (15) Cotí, K. K.; Belowich, M. E.; Liong, M.; Ambrogio, M. W.; Lau, Y. A.; Khatib, H. A.; Zink, J. I.; Khashab, N. M.; Stoddart, J. F. Mechanised Nanoparticles for Drug Delivery. *Nanoscale* **2009**, *1*, 16–39.
- (16) Tarn, D.; Ashley, C. E.; Xue, M.; Carnes, E. C.; Zink, J. I.; Brinker, C. J. Mesoporous Silica Nanoparticle Nanocarriers: Biofunctionality and Biocompatibility. *Acc. Chem. Res.* **2013**, *46*, 792–801.
- (17) Chen, W.; Tsai, P. H.; Hung, Y.; Chiou, S. H.; Mou, C. Y. Nonviral Cell Labeling and Differentiation Agent for Induced Pluripotent Stem Cells Based on Mesoporous Silica Nanoparticles. *ACS Nano* **2013**, *7*, 8423–8440.
- (18) Klichko, Y.; Liong, M.; Choi, E.; Angelos, S.; Nel, A. E.; Stoddart, J. F.; Tamanoi, F.; Zink, J. I. Mesoporous Silica for Optical Functionality, Nanomachines, and Drug Delivery. *J. Am. Ceram. Soc.* **2009**, *92*, S2-S10.
- (19) Liong, M.; Lu, J.; Kovoichich, M.; Xia, T.; Ruehm, S. G.; Nel, A. E.; Tamanoi, F.; Zink, J. I. Multifunctional Inorganic Nanoparticles for Imaging, Targeting, and Drug Delivery. *ACS Nano* **2008**, *2*, 889–896.
- (20) Kumar, N.; Chen, W.; Cheng, C. A.; Deng, T.; Wang, R.; Zink, J. I. Stimuli-Responsive Nanomachines and Caps for Drug Delivery. *The Enzymes* **2018**, *43*, 31–65.
- (21) Lu, J.; Liong, M.; Zink, J. I.; Tamanoi, F. Mesoporous Silica Nanoparticles as a Delivery System for Hydrophobic Anticancer Drugs. *Small* **2007**, *3*, 1341–1346.
- (22) Croissant, J. G.; Fatieiev, Y.; Julfakyan, K.; Lu, J.; Emwas, A. H.; Anjum, D. H.; Omar, H.; Tamanoi, F.; Zink, J. I.; Khashab, N. M. Biodegradable Oxamide-Phenylene-Based Mesoporous Organosilica Nanoparticles with Unprecedented Drug Payloads for Delivery in Cells. *Chem. Eur. J.* **2016**, *22*, 14806-14811.
- (23) Chen, W.; Cheng, C. A.; Lee, B. Y.; Clemens, D. L.; Huang, W. Y.; Horwitz, M. A.; Zink, J. I. Facile Strategy Enabling Both High Loading and High Release Amounts of the Water-Insoluble Drug Clofazimine Using Mesoporous Silica Nanoparticles. *ACS Appl. Mater. Interfaces* **2018**, *10*, 31870–31881.
- (24) Ferris, D. P.; Lu, J.; Gothard, C.; Yanes, R.; Thomas, C. R.; Olsen, J. C.; Stoddart, J. F.; Tamanoi, F.;

- Zink, J. I. Synthesis of Biomolecule-Modified Mesoporous Silica Nanoparticles for Targeted Hydrophobic Drug Delivery to Cancer Cells. *Small* **2011**, *7*, 1816–1826.
- (25) Xia, T.; Kovoichich, M.; Liong, M.; Meng, H.; Kabehie, S.; George, S.; Zink, J. I.; Nel, A. E. Polyethyleneimine Coating Enhances the Cellular Uptake of Mesoporous Silica Nanoparticles and Allows Safe Delivery of siRNA and DNA Constructs. *ACS Nano* **2009**, *3*, 3273–3286.
- (26) Meng, H.; Xue, M.; Xia, T.; Ji, Z.; Tarn, D. Y.; Zink, J. I.; Nel, A. E. Use of Size and a Copolymer Design Feature to Improve the Biodistribution and the Enhanced Permeability and Retention Effect of Doxorubicin-Loaded Mesoporous Silica Nanoparticles in a Murine Xenograft Tumor Model. *ACS Nano* **2011**, *5*, 4131–4144.
- (27) Sontheimer, E. J. Assembly and Function of RNA Silencing Complexes. *Nat. Rev. Mol. Cell Biol.* **2005**, *6*, 127–138.
- (28) Fire, A.; Xu, S.; Montgomery, M. K.; Kostas, S. A.; Driver, S. E.; Mello, C. C. Potent and Specific Genetic Interference by Double-Stranded RNA in *Caenorhabditis Elegans*. *Nature* **1998**, *391*, 806–811.
- (29) Elbashir, S. M.; Harborth, J.; Lendeckel, W.; Yalcin, A.; Weber, K.; Tuschl, T. Duplexes of 21-Nucleotide RNAs Mediate RNA Interference in Cultured Mammalian Cells. *Nature* **2001**, *411*, 494–498.
- (30) Tijsterman, M.; Plasterk, R. H. A. Dicers at RISC: The Mechanism of RNAi. *Cell* **2004**, *117*, 1–3.
- (31) Liu, J.; Carmell, M. A.; Rivas, F. V.; Marsden, C. G.; Thomson, J. M.; Song, J. J.; Hammond, S. M.; Joshua-Tor, L.; Hannon, G. J. Argonaute2 Is the Catalytic Engine of Mammalian RNAi. *Science* **2004**, *305*, 1437–1441.
- (32) Meng, H.; Mai, W. X.; Zhang, H.; Xue, M.; Xia, T.; Lin, S.; Wang, X.; Zhao, Y.; Ji, Z.; Zink, J. I.; Nel, A. E. Codelivery of an Optimal Drug/siRNA Combination Using Mesoporous Silica Nanoparticles to Overcome Drug Resistance in Breast Cancer *in Vitro* and *in Vivo*. *ACS Nano* **2013**, *7*, 994–1005.
- (33) Finlay, J.; Roberts, C. M.; Dong, J.; Zink, J. I.; Tamanoi, F.; Glackin, C. A. Mesoporous Silica Nanoparticle Delivery of Chemically Modified siRNA against TWIST1 Leads to Reduced Tumor Burden. *Nanomedicine* **2015**, *11*, 1657–1666.
- (34) Roberts, C. M.; Shahin, S. A.; Wen, W.; Finlay, J. B.; Dong, J.; Wang, R.; Dellinger, T. H.; Zink, J. I.; Tamanoi, F.; Glackin, C. A. Nanoparticle Delivery of siRNA against TWIST to Reduce Drug Resistance and Tumor Growth in Ovarian Cancer Models. *Nanomedicine* **2017**, *13*, 965–976.
- (35) Shahin, S. A.; Wang, R.; Simargi, S. I.; Contreras, A.; Parra Echavarria, L.; Qu, L.; Wen, W.;

- Dellinger, T.; Unternaehrer, J.; Tamanoi, F.; Zink, J. I.; Glackin, C. A. Hyaluronic Acid Conjugated Nanoparticle Delivery of siRNA against TWIST Reduces Tumor Burden and Enhances Sensitivity to Cisplatin in Ovarian Cancer. *Nanomedicine* **2018**, *14*, 1381–1394.
- (36) Ruehle, B.; Saint-Cricq, P.; Zink, J. I. Externally Controlled Nanomachines on Mesoporous Silica Nanoparticles for Biomedical Applications. *Chemphyschem* **2016**, *17*, 1769–1779.
- (37) Meng, H.; Xue, M.; Xia, T.; Zhao, Y. L.; Tamanoi, F.; Stoddart, J. F.; Zink, J. I.; Nel, A. E. Autonomous *in Vitro* Anticancer Drug Release from Mesoporous Silica Nanoparticles by pH-Sensitive Nanovalves. *J. Am. Chem. Soc.* **2010**, *132*, 12690–12697.
- (38) Ambrogio, M. W.; Pecorelli, T. A.; Patel, K.; Khashab, N. M.; Trabolsi, A.; Khatib, H. A.; Botros, Y. Y.; Zink, J. I.; Stoddart, J. F. Snap-Top Nanocarriers. *Org. Lett.* **2010**, *12*, 3304–3307.
- (39) Patel, K.; Angelos, S.; Dichtel, W. R.; Coskun, A.; Yang, Y. W.; Zink, J. I.; Stoddart, J. F. Enzyme-Responsive Snap-Top Covered Silica Nanocontainers. *J. Am. Chem. Soc.* **2008**, *130*, 2382–2383.
- (40) Hwang, A. A.; Lee, B. Y.; Clemens, D. L.; Dillon, B. J.; Zink, J. I.; Horwitz, M. A. pH-Responsive Isoniazid-Loaded Nanoparticles Markedly Improve Tuberculosis Treatment in Mice. *Small* **2015**, *11*, 5066–5078.
- (41) Clemens, D. L.; Lee, B. Y.; Xue, M.; Thomas, C. R.; Meng, H.; Ferris, D.; Nel, A. E.; Zink, J. I.; Horwitz, M. A. Targeted Intracellular Delivery of Antituberculosis Drugs to Mycobacterium Tuberculosis-Infected Macrophages via Functionalized Mesoporous Silica Nanoparticles. *Antimicrob. Agents Chemother.* **2012**, *56*, 2535–2545.
- (42) Li, Z.; Clemens, D. L.; Lee, B. Y.; Dillon, B. J.; Horwitz, M. A.; Zink, J. I. Mesoporous Silica Nanoparticles with pH-Sensitive Nanovalves for Delivery of Moxifloxacin Provide Improved Treatment of Lethal Pneumonic Tularemia. *ACS Nano* **2015**, *9*, 10778–10789.
- (43) Lee, B. Y.; Li, Z.; Clemens, D. L.; Dillon, B. J.; Hwang, A. A.; Zink, J. I.; Horwitz, M. A. Redox-Triggered Release of Moxifloxacin from Mesoporous Silica Nanoparticles Functionalized with Disulfide Snap-Tops Enhances Efficacy Against Pneumonic Tularemia in Mice. *Small* **2016**, *27*, 3690–3702.
- (44) Guardado-Alvarez, T. M.; Russell, M. M.; Zink, J. I. Nanovalve Activation by Surface-Attached Photoacids. *Chem. Commun.* **2014**, *50*, 8388–8390.
- (45) Saha, S.; Johansson, E.; Flood, A. H.; Tseng, H. R.; Zink, J. I.; Stoddart, J. F. A Photoactive Molecular Triad as a Nanoscale Power Supply for a Supramolecular Machine. *Chem. Eur. J.* **2005**, *11*, 6846–6858.
- (46) Lu, J.; Choi, E.; Tamanoi, F.; Zink, J. I. Light-Activated Nanoimpeller-Controlled Drug Release in

- Cancer Cells. *Small* **2008**, *4*, 421–426.
- (47) Angelos, S.; Choi, E.; Vögtle, F.; De Cola, L.; Zink, J. I. Photo-Driven Expulsion of Molecules from Mesoporous Silica Nanoparticles. *J. Phys. Chem. C* **2007**, *111*, 6589–6592.
- (48) Lau, Y. A.; Henderson, B. L.; Lu, J.; Ferris, D. P.; Tamanoi, F.; Zink, J. I. Continuous Spectroscopic Measurements of Photo-Stimulated Release of Molecules by Nanomachines in a Single Living Cell. *Nanoscale* **2012**, *4*, 3482–3489.
- (49) Ferris, D. P.; Zhao, Y. L.; Khashab, N. M.; Khatib, H. A.; Stoddart, J. F.; Zink, J. I. Light-Operated Mechanized Nanoparticles. *J. Am. Chem. Soc.* **2009**, *131*, 1686–1688.
- (50) Tarn, D.; Ferris, D. P.; Barnes, J. C.; Ambrogio, M. W.; Stoddart, J. F.; Zink, J. I. A Reversible Light-Operated Nanovalve on Mesoporous Silica Nanoparticles. *Nanoscale* **2014**, *6*, 3335–3343.
- (51) Guardado-Alvarez, T. M.; Sudha Devi, L.; Russell, M. M.; Schwartz, B. J.; Zink, J. I. Activation of Snap-Top Capped Mesoporous Silica Nanocontainers Using Two near-Infrared Photons. *J. Am. Chem. Soc.* **2013**, *135*, 14000–14003.
- (52) Croissant, J.; Zink, J. I. Nanovalve-Controlled Cargo Release Activated by Plasmonic Heating. *J. Am. Chem. Soc.* **2012**, *134*, 7628–7631.
- (53) Guardado-Alvarez, T. M.; Devi, L. S.; Vabre, J. M.; Pecorelli, T. A.; Schwartz, B. J.; Durand, J. O.; Mongin, O.; Blanchard-Desce, M.; Zink, J. I. Photo-Redox Activated Drug Delivery Systems Operating under Two Photon Excitation in the near-IR. *Nanoscale* **2014**, *6*, 4652–4658.
- (54) Croissant, J.; Chaix, A.; Mongin, O.; Wang, M.; Clément, S.; Raehm, L.; Durand, J. O.; Hugues, V.; Blanchard-Desce, M.; Maynadier, M.; Gallud, A.; Gary-Bobo, M.; Garcia, M.; Lu, J.; Tamanoi, F.; Ferris, D. P.; Tarn, D.; Zink, J. I. Two-Photon-Triggered Drug Delivery via Fluorescent Nanovalves. *Small* **2014**, *10*, 1752–1755.
- (55) Jang, J. T.; Nah, H.; Lee, J. H.; Moon, S. H.; Kim, M. G.; Cheon, J. Critical Enhancements of MRI Contrast and Hyperthermic Effects by Dopant-Controlled Magnetic Nanoparticles. *Angew. Chem. Int. Ed.* **2009**, *48*, 1234–1238.
- (56) Lee, J. H.; Jang, J. T.; Choi, J. S.; Moon, S. H.; Noh, S. H.; Kim, J. W.; Kim, J. G.; Kim, I. S.; Park, K. I.; Cheon, J. Exchange-Coupled Magnetic Nanoparticles for Efficient Heat Induction. *Nat. Nanotechnol.* **2011**, *6*, 418–422.
- (57) Noh, S. hyun; Moon, S. H.; Shin, T. H.; Lim, Y.; Cheon, J. Recent Advances of Magneto-Thermal Capabilities of Nanoparticles: From Design Principles to Biomedical Applications. *Nano Today* **2017**, *13*, 61–76.
- (58) Dong, J.; Zink, J. I. Taking the Temperature of the Interiors of Magnetically Heated Nanoparticles.

ACS Nano **2014**, *8*, 5199–5207.

- (59) Rühle, B.; Datz, S.; Argyo, C.; Bein, T.; Zink, J. I. A Molecular Nanocap Activated by Superparamagnetic Heating for Externally Stimulated Cargo Release. *Chem. Commun.* **2016**, *52*, 1843–1846.
- (60) Saint-Cricq, P.; Deshayes, S.; Zink, J. I.; Kasko, A. M. Magnetic Field Activated Drug Delivery Using Thermodegradable Azo-Functionalised PEG-Coated Core–Shell Mesoporous Silica Nanoparticles. *Nanoscale* **2015**, *7*, 13168–13172.
- (61) Thomas, C. R.; Ferris, D. P.; Lee, J. H.; Choi, E.; Cho, M. H.; Kim, E. S.; Stoddart, J. F.; Shin, J. S.; Cheon, J.; Zink, J. I. Noninvasive Remote-Controlled Release of Drug Molecules in Vitro Using Magnetic Actuation of Mechanized Nanoparticles. *J. Am. Chem. Soc.* **2010**, *132*, 10623–10625.
- (62) Chen, W.; Cheng, C. A.; Zink, J. I. Spatial, Temporal, and Dose Control of Drug Delivery Using Noninvasive Magnetic Stimulation. *ACS Nano* **2019**, *13*, 1292–1308.
- (63) Clemens, D. L.; Lee, B. Y.; Plamthottam, S.; Tullius, M. V.; Wang, R.; Yu, C J; Li, Z.; Dillon, B. J.; Zink, J. I.; Horwitz, M. A. Nanoparticle Formulation of Moxifloxacin and Intramuscular Route of Delivery Improve Antibiotic Pharmacokinetics and Treatment of Pneumonic Tularemia in a Mouse Model. *ACS Infect. Dis.* **2019**, *5*, 281–291.

Chapter 2

Facile Strategy Enabling Both High Loading and High Release Amounts of the Water-Insoluble Drug Clofazimine Using Mesoporous Silica Nanoparticles

This chapter of the dissertation was adapted and reprinted with permission from Wei Chen, Chi-An Cheng, Bai-Yu Lee, Daniel L. Clemens, Wen-Yen Huang, Marcus A. Horwitz, Jeffrey I. Zink *ACS Applied Materials & Interfaces* **2018**, *10*, 31870–31881. Copyright 2018 American Chemical Society. Co-author contributions: Chen W., Cheng C. A., and Huang W. Y. performed the chemistry-related studies. Lee B. Y., and Clemens D. L. performed the cells and bacteria studies. Marcus A. Horwitz, and Jeffrey I. Zink were the P.Is.

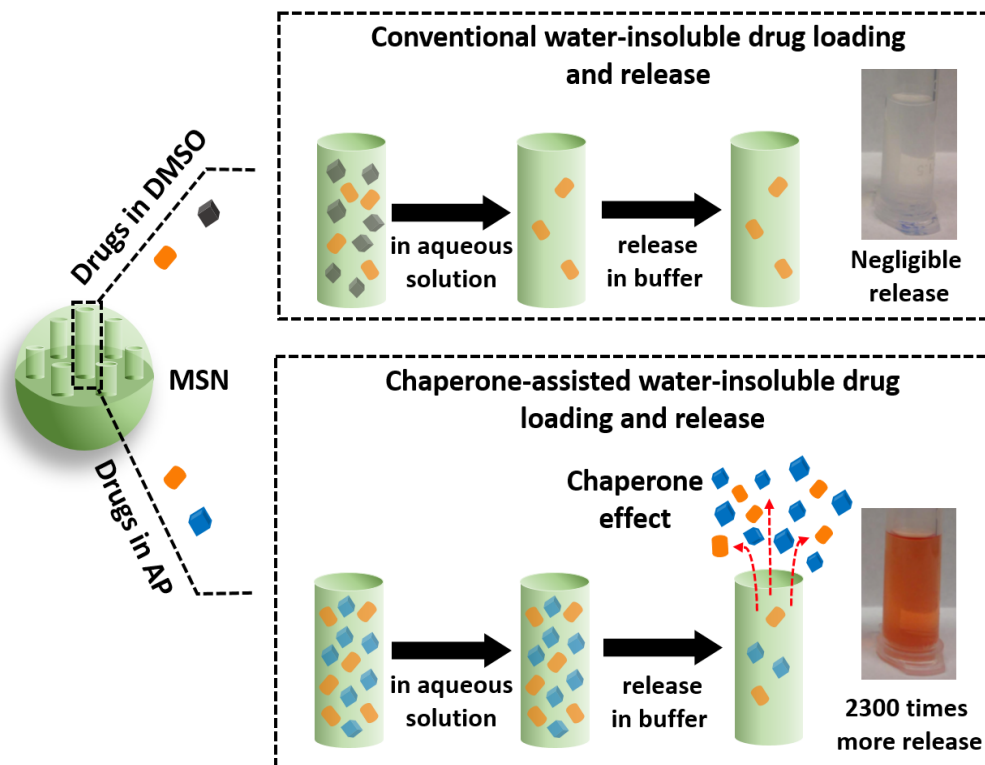
Keywords of this chapter: mesoporous silica nanoparticles, drug delivery, water-insoluble drugs, clofazimine, tuberculosis, chaperone

Abstract

The use of nanocarriers to deliver poorly soluble drugs to the sites of diseases is an attractive and general method, and mesoporous silica nanoparticles (MSNs) are increasingly being used as carriers. However, both loading a large amount of drugs into the pores and still being able to release the drug is a challenge. In this work, we demonstrate a general strategy based on a companion molecule that chaperones the drug into the pores and also aids it in escaping. A common related strategy is to use a miscible co-solvent dimethyl sulfoxide (DMSO), but although loading may be efficient in DMSO, this co-solvent frequently diffuses into an aqueous environment, leaving the drug behind. We demonstrate the method by using acetophenone (AP), an FDA-approved food

additive as the chaperone for clofazimine (CFZ), a water-insoluble antibiotic used to treat leprosy and multidrug-resistant tuberculosis. AP enables a high amount of CFZ cargo into the MSNs and also carries CFZ cargo out from the MSNs effectively when they are in an aqueous biorelevant environment. The amount of loading and the CFZ release efficiency from MSNs were optimized; 4.5 times more CFZ was loaded in MSNs with AP than that with DMSO and 2300 times more CFZ was released than that without the assistance of the AP. *In vitro* treatment of macrophages infected by *Mycobacterium tuberculosis* with the optimized CFZ-loaded MSNs killed the bacteria in the cells in a dose-dependent manner. These studies demonstrate a highly efficient method for loading nanoparticles with water-insoluble drug molecules and the efficacy of the nanoparticles in delivering drugs into eukaryotic cells in aqueous media.

Table of Content Figure



2.1 Introduction

Poor water solubility of drug molecules is a significant problem because almost 40% of the newly discovered drug molecules are hydrophobic which reduces their bioavailability and thus suppresses their efficacy.¹ Great effort has been devoted to solving the problem of getting them to the site of the disease. One important strategy is to use nanomaterials as carriers to deliver insoluble drugs.² Mesoporous silica nanoparticles (MSNs) have aroused much attention in this regard because their properties include high surface area (about 1000 m²/g), large pore volume (1 cc/g), tunable pore sizes (2-20 nm), easy surface functionalization, and high biocompatibility.³⁻¹² These excellent intrinsic properties enable MSNs to carry a wide variety of cargos, including drugs,¹³⁻¹⁷ genes,¹⁸⁻²¹ proteins,^{22,23} and other biomolecules for *in vitro* or *in vivo* biomedical applications.^{24,25} Additionally, MSNs can incorporate fluorescence and magnetic properties, and simultaneously serve as image contrast agents by integrating the relevant functional materials for diagnostics and therapeutics.²⁶⁻²⁸ Accordingly, these preeminent “theranostic” (therapeutic plus diagnostic) nanoparticles, serving as the excellent nanocarriers, are being broadly explored in biomedical applications.²⁹⁻³⁵

The major challenges are to get the insoluble drug into the pores and then allow the drugs to escape. One of the most widely-used methods to load the poorly water-soluble drugs in MSNs is to dissolve the drugs in dimethyl sulfoxide (DMSO).¹⁴ The loading step is done by soaking MSNs in the DMSO solution which allows the drug molecules to diffuse into the channels of MSNs efficiently. After the loading step, the drug-loaded MSNs are washed with water or buffer solutions thoroughly to remove DMSO from the pores. However, during this washing step, some of drugs

may be removed as well considering weak interactions between the hydrophobic drug molecules and the hydrophilic porous surface, thus decreasing the loading weight percent of drugs (defined as (weight of drugs / weight of MSNs) x 100%).^{2,14} To attempt to solve this problem of low drug loading, the channels of MSNs were functionalized with hydrophobic groups to increase the hydrophobic interactions between the drugs and the channels.^{36,37} However, those further surface modifications complicate the delivery systems and lead to colloidal instability in aqueous environment. Another critical challenge that remains is that the amount of the hydrophobic drug released from the carriers into an aqueous environment is poor, even though MSNs are able to carry the drugs to the location of a disease.³⁶⁻³⁸ Consequently, the bioavailability of the drugs may be reduced to a level insufficient for effective treatment, or an extremely high dosage of the particles may be required to achieve a sufficient local concentration of free drug for it to be effective. Hence, to enhance the bioavailability of the drug, it is essential to improve its release efficiency from the nanocarriers.

Hydrotropy is a technique that increases the water solubility of water insoluble molecules by adding a second solute (*i.e.* hydrotrope).^{39,40} Hydrotropes are short chain amphiphilic molecules, usually containing both the hydrophobic and hydrophilic moieties in their chemical structures, in which the hydrophobic part interacts with water-insoluble drugs through hydrophobic interactions, and the hydrophilic part helps solubilize the drug-hydrotropes complexation structure in water. The hydrotrope-assisted solubilization of water-insoluble drugs in water possesses a signature feature of a sigmoidal solubility curve.^{41,42} At low concentration of hydrotropes, the solubility of water-insoluble drugs hardly increases. The solubility of water-insoluble drugs significantly

increases above a certain hydrotrope concentration, usually called a minimum hydrotrope concentration (MHC), when self-aggregation of the hydrotropes happens.^{42,43} Other mechanisms may also involve in the hydrotrope-assisted solubilization of water-insoluble drugs.⁴⁴⁻⁴⁷ Two advantages of using hydrotrope are that it obviates the need for chemical modification of the drugs, which may interfere with pharmaceutical activity; and it does not require a specific formulation for emulsification. The water solubility of water-insoluble drugs could be enhanced from several folds to several orders of magnitude by the hydrotrope-assisted solubilization especially if the hydrotropes associate well with the drugs.^{40,41,48}

In this study, we choose clofazimine (CFZ) as an example of a water-insoluble drug (defined as having water solubility of less than 100 $\mu\text{g/mL}$) to demonstrate our strategy for hydrophobic drug delivery. CFZ has an extremely low (0.2 $\mu\text{g/mL}$) water solubility. The motivation for improving the delivery of CFZ lies in the fact that it has good efficacy against multidrug-resistant Tuberculosis (TB).⁴⁹⁻⁵² TB is a serious contagious disease caused by the bacterium *Mycobacterium tuberculosis* (*M. tuberculosis*) and has becoming a global health problem; in 2016, there were approximately 10.4 million new TB cases and 1.3 million TB deaths worldwide.⁵³ However, the extremely low water solubility of CFZ complicates its delivery by nanoparticles or other novel approaches *e.g. via* inhalation.

Herein, we developed a facile “chaperone-assisted” delivery strategy which improves the loading of CFZ and delivers a large amount of CFZ with MSNs into an aqueous environment (Figure 2.1). First, we found acetophenone (AP) is the most promising chaperone among 9 candidate molecules tested. Then, we compared the efficacy of AP and DMSO as non-aqueous

solvents for CFZ loading and release. Next, we measured the effect of CFZ loading concentration on CFZ release and AP release and determined the optimized CFZ loading concentration. The effect of the location of AP relative to MSNs on CFZ was also explored. Finally, using the optimized AP/CFZ loaded MSNs, we investigated the antibacterial effect of this hydrotropy-based delivery strategy on intracellular *M. tuberculosis* to further validate their potential use in medicine and biomedical research. To the best of our knowledge, this is the first work to demonstrate appropriate chaperone for CFZ and to apply the strategy to the construction of nanoparticles with enhanced CFZ loading and release efficiency.

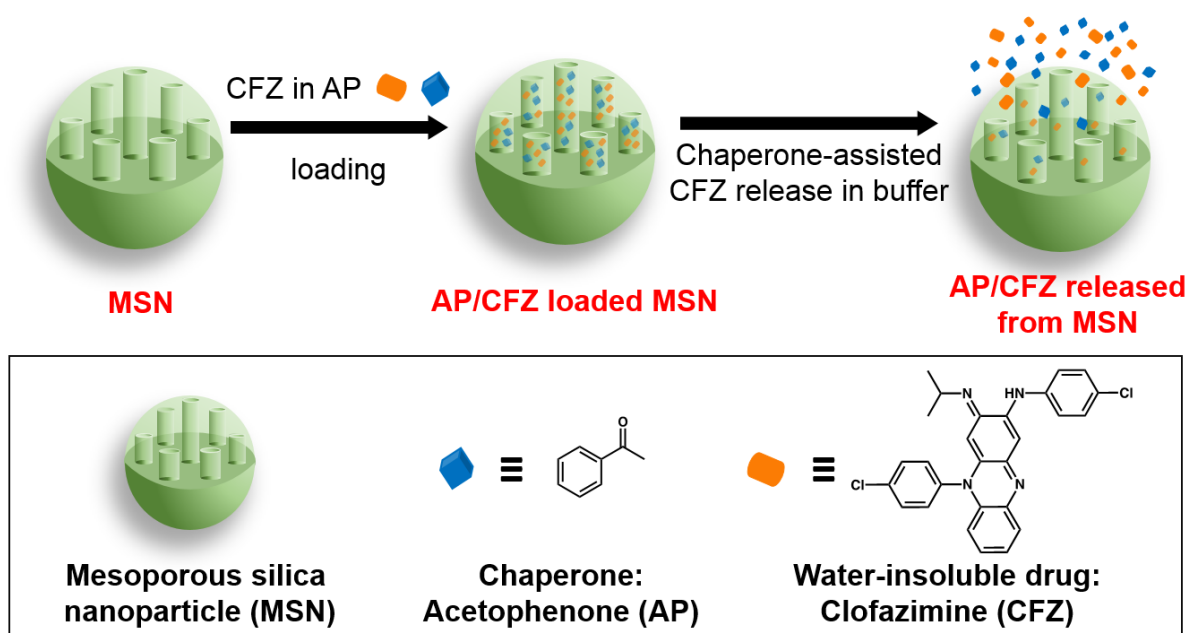


Figure 2.1. Chaperone-assisted delivery strategy for water-insoluble drugs. Clofazimine (CFZ) was chosen as an example of a water-insoluble antibiotic. Acetophenone (AP) acts like a chaperone bringing CFZ cargo into the vehicle — mesoporous silica nanoparticles (MSNs) and then carrying CFZ cargo out from the MSNs effectively.

2.2 Experimental Section

2.2.1 Materials

Hexadecyltrimethylammonium bromide (CTAB, 99+%), tetraethyl orthosilicate (TEOS, 98%), clofazimine (CFZ, 98+%), acetophenone (AP, 99%), 2-heptanone (98%), 2-hydroxyacetophenone (98%), sodium benzoate (99%), pyradinamide (97.5+%), nicotinamide (99.5+%), isoniazid (99+%), hexanoic acid (99+%), benzoic acid (99.5+%), sodium hydroxide (NaOH) (97+%), 4-(2-hydroxyethyl)-1-piperazineethanesulfonic acid (HEPES, 99.5+%), and ammonium nitrate (NH₄NO₃, 98+%) were purchased from Sigma-Aldrich. Dimethyl sulfoxide (DMSO, 99.9+%) was purchased from Fisher Chemical. Absolute ethanol (200 proof) was purchased from Decon Labs, Inc. All chemicals were used without further purification.

2.2.2 Characterization

The size and morphology of mesoporous silica nanoparticles (MSNs) were investigated by transmission electron microscopy (TEM, Tecnai T12). MSNs were dispersed in ethanol at a very low concentration (0.2 mg/mL). Ten microliters of the suspension were dropped onto the carbon-coated copper grid and dried at room temperature. The N₂ adsorption-desorption isotherms of MSNs were obtained at liquid N₂ temperature (77K) on a Autosorb-iQ (Quantachrome Instruments) apparatus. MSNs were degassed at 110 °C for 12 h before the measurement. The surface area and pore size distribution of MSNs were determined by Brunauer-Emmett-Teller (BET) and Barrett-Joyner-Halenda (BJH) methods. The dynamic light scattering (DLS) size and zeta potential value of MSNs were examined by a laser particle analyzer LPA-3100 at room temperature. The loading capacity, release capacity, and release efficiency of CFZ or AP were determined by UV-Vis

Spectroscopy (Cary 5000). The absorbance of the peaks was used for quantification by Beer-Lambert Law.

2.2.3 Synthesis of mesoporous silica nanoparticles (MSNs)

CTAB (250 mg) was dissolved in a mixture of deionized water (120 mL) and 2 M NaOH (875 μ L) under vigorous stirring. The solution was heated to 80 °C and tetraethyl orthosilicate (TEOS) (1.25 mL) was then added dropwise to the solution for about 20 seconds. The reaction was kept at 80 °C for 2 h. Subsequently, the solution was cooled to room temperature and MSNs were centrifuged and washed 3 times with ethanol. MSNs were then dispersed in 100 mL of ethanol containing 2 g of NH_4NO_3 and the reaction was refluxed for 1 h to remove the surfactant. The surfactant removal procedures were repeated twice and MSNs were washed thoroughly with ethanol and D.I. water to obtain the surfactant-free MSNs.

2.2.4 Screening of possible hydrotropes for CFZ

Nine different small molecules – nicotinamide, sodium benzoate, pyradinamide, isoniazid, 2-hydroxyacetophenone, benzoic acid, hexanoic acid, 2-heptanone, and acetophenone – were screened to investigate their hydrotropic ability for CFZ in H_2O . For the control lacking a hydrotrope, 1 μ mol of CFZ and 1 mL of H_2O were added into a 20 mL of glass vial and sonicated for 10 min to suspend CFZ in H_2O . The undissolved CFZ was removed by centrifugation at 14000 rpm for 15 min. Then, the supernatant was collected and measured by UV-Vis spectroscopy. For experimental samples with hydrotropes, 1 μ mol of CFZ, 1 mL of H_2O , and the respective hydrotrope [sodium benzoate (50 μ mol, 500 μ mol, or 1 mmol), pyrazinamide (50 μ mol, 500 μ mol, or 906 μ mol), nicotinamide (50 μ mol, 500 μ mol, or 1 mmol), isoniazid (50 μ mol, 500 μ mol, 1

mmol), 2-hydroxyacetophenone (50 μmol), hexanoic acid (50 μmol), benzoic acid (28 μmol), 2-heptanone (38 μmol), or acetophenone (50 μmol)] were added into 20 mL glass vials and sonicated for 10 min. The undissolved CFZ was removed by centrifugation as described above. Finally, the supernatant was collected and measured by UV-Vis spectroscopy. The solubility enhancement was determined by the change in absorbance at 490 nm.

2.2.5 Concentration dependent hydrotrophy effect of AP

To investigate the hydrotropic effect of AP in more detail, we prepared concentrations ranging from 0 to 60 mM of AP in H_2O to dissolve CFZ. Similarly, 1 μmol of CFZ, 1 mL of H_2O , and the respective concentration of AP were added into 20 mL glass vials and sonicated for 10 min. The undissolved CFZ was removed by centrifugation as described above. The solubility enhancement was determined by the change in absorbance at 490 nm.

2.2.6 Creation of calibration curve of CFZ in AP, CFZ in ethanol-water mixture, and AP in ethanol-water mixture

To determine the loading capacity, release efficiency, and release capacity of CFZ, the calibration curves were created by dissolving CFZ in AP. The concentration of CFZ in AP ranged from 0 to 50 μM . The absorption spectra of the solutions were measured by UV-Vis spectroscopy, and the absorbance maximum (490 nm for CFZ and 244 nm for AP) was used to plot the calibration curve. The calibration curves ranging from 0 to 25 μM of CFZ dissolved in a mixture of ethanol and HEPES buffer solution (10 mM, pH = 7.4) (v/v = 1/1) were also generated. To determine the release capacity and release efficiency of AP, the calibration curve of AP was generated by

dissolving AP in a mixture of ethanol and HEPES buffer solution (10 mM, pH = 7.4) (v/v = 1/1). The concentration of AP ranged from 0.25 to 66 μ M.

2.2.7 Loading capacity analysis of clofazimine (CFZ)

The loading of CFZ was studied using DMSO or AP as loading solvents. In general, 10 mg of MSNs were dispersed in AP or DMSO with 0.1, 1, 10, or 50 mM CFZ, respectively. After 24 h stirring, the CFZ loaded MSNs were centrifuged at 14000 rpm for 10 min and the pellets were washed three times with H₂O under sonication to remove the excess CFZ. Then, the CFZ loaded MSNs with AP or DMSO were washed with AP or DMSO, respectively, and pelleted by centrifugation. The washing steps were repeated several times until the supernatant was clear. The supernatants were collected and measured by UV-Vis spectroscopy. The loading capacity of CFZ was calculated using the maximum absorbance at 490 nm based on Beer's law, its calibration curve, and the following definition of loading capacity: (mass of loaded CFZ / mass of MSNs) x 100%.

2.2.8 Release of CFZ and AP in HEPES buffer

The release of CFZ and AP from MSNs was carried out in HEPES buffer solution (pH = 7.4, 10 mM). In general, 10 mg of MSNs loaded with 0.1, 1, 10, or 50 mM CFZ in AP were dispersed in 1 mL of HEPES buffer solution and stirred for 1, 2, 3, or 5 days, respectively. Afterwards, the CFZ loaded MSNs were spun down at 14000 rpm for 10 min. The supernatant was collected and mixed homogeneously with ethanol, which was then diluted and measured by UV-Vis spectroscopy. The release efficiency of CFZ and AP were calculated using their maximum absorbance at 490 nm and 244 nm, respectively, based on Beer's law, their calibration curves, and the definition of release efficiency: (mass of released CFZ / mass of loaded CFZ) x 100%.

2.2.9 Release of CFZ in HEPES buffer with addition of AP

To gain insight into whether the AP residing outside of the pores of MSNs would affect CFZ release, we added AP into the release buffer. After MSNs were loaded with 1 mM CFZ in DMSO, 10 mg of MSNs were dispersed in 1 mL of HEPES buffer (10 mM, pH = 7.4) with the addition of 10 μ L of AP. The solution was stirred for 24 h and then centrifuged at 14000 rpm for 10 min. The supernatant was collected and measured by UV-Vis spectroscopy; the pellet of CFZ loaded MSNs was resuspended by sonication in 1 mL of HEPES buffer with the addition of 10 μ L of AP and stirred for another 24 h. Again, the supernatant was collected as described above and measured by UV-Vis spectroscopy. The same procedures were repeated and the supernatant was collected and analyzed at 72 h and 120 h as described above.

2.2.10 Assay for killing of *M. tuberculosis* in macrophages

Human monocytic THP-1 cells (ATCC TIB202) were maintained in RPMI-1640 supplemented with 10% fetal bovine serum, GlutaMAX, and Penicillin-Streptomycin (100 IU-100 μ g/mL). Prior to infection, the cells were treated with phorbol 12-myristate 13-acetate (PMA) for 3 days to differentiate them into macrophage-like cells. *M. tuberculosis* virulent strain Erdman (ATCC 35801) was cultured on Middlebrook 7H11 plates for 10 days. Lawns of bacteria were scraped from the plates, suspended in RPMI with 20 mM HEPES, and a single bacterial suspension was prepared by sonication and repeated centrifugation to remove bacterial clumps. After opsonization with human serum type AB containing active complement, the bacteria were used to infect PMA-differentiated THP-1 macrophages at a multiplicity of infection of 1:1 (bacterium:macrophage). The bacteria were incubated with macrophages for 1 hour at 37 °C, after

which MSNs loaded with AP (AP-MSN), MSNs loaded with 10 mM CFZ in AP hydrotrope (AP/CFZ-MSN), or free CFZ were added to the culture of the *M. tuberculosis* infected macrophages. The concentrations of AP-MSN were 11 and 22 $\mu\text{g/mL}$. The concentrations of AP/CFZ-MSN were 5.5, 11, and 22 $\mu\text{g/mL}$, corresponding to 0.5, 1, and 2 $\mu\text{g/mL}$ of CFZ, respectively. Free CFZ was dissolved in DMSO first, and then added to *M. tuberculosis* infected macrophages at concentrations of 0.5, 1, and 2 $\mu\text{g/mL}$, those concentrations of free CFZ had 0.005%, 0.01%, and 0.02% DMSO, respectively. The cells were incubated for 4 days at 37 °C, 5% CO₂-95% air, lysed with 0.1% SDS, serially diluted in Middlebrook 7H9 broth supplemented with ADC enrichment and 0.05% Tween 80, and plated on Middlebrook 7H11 agar plates. The number of bacterial colonies on the plates was enumerated after incubation for 2.5 weeks at 37 °C, 5% CO₂-95% air.^{32,54}

2.3. Results and Discussion

2.3.1 Synthesis and characterization of mesoporous silica nanoparticles (MSNs)

MSNs were synthesized by a sol-gel synthetic strategy in the presence of cationic surfactant template.^{15,55} By transmission electron microscopy (TEM) (Figure 2.2a), MSNs have a well-ordered hexagonal mesoporous structure and the average size is 100 nm in diameter. The diameter of MSNs measured by dynamic light scattering (DLS) is 165.7 nm (Figure 2.2b), which implies that MSNs are well-suspended in deionized (D.I.) H₂O. The zeta potential value of MSNs is -21.2 mV in D.I. H₂O. Nitrogen adsorption/desorption isotherms of MSNs were measured at 77 K. The surface area, pore volume, and pore size are 1060 m²/g, 1.12 cm³/g, and 2.8 nm, respectively (Figure 2.2c and 2.2d). The high surface area, characteristic of MSNs,^{8,18} provides an advantage

for loading cargos such as clofazimine (CFZ) and acetophenone (AP).

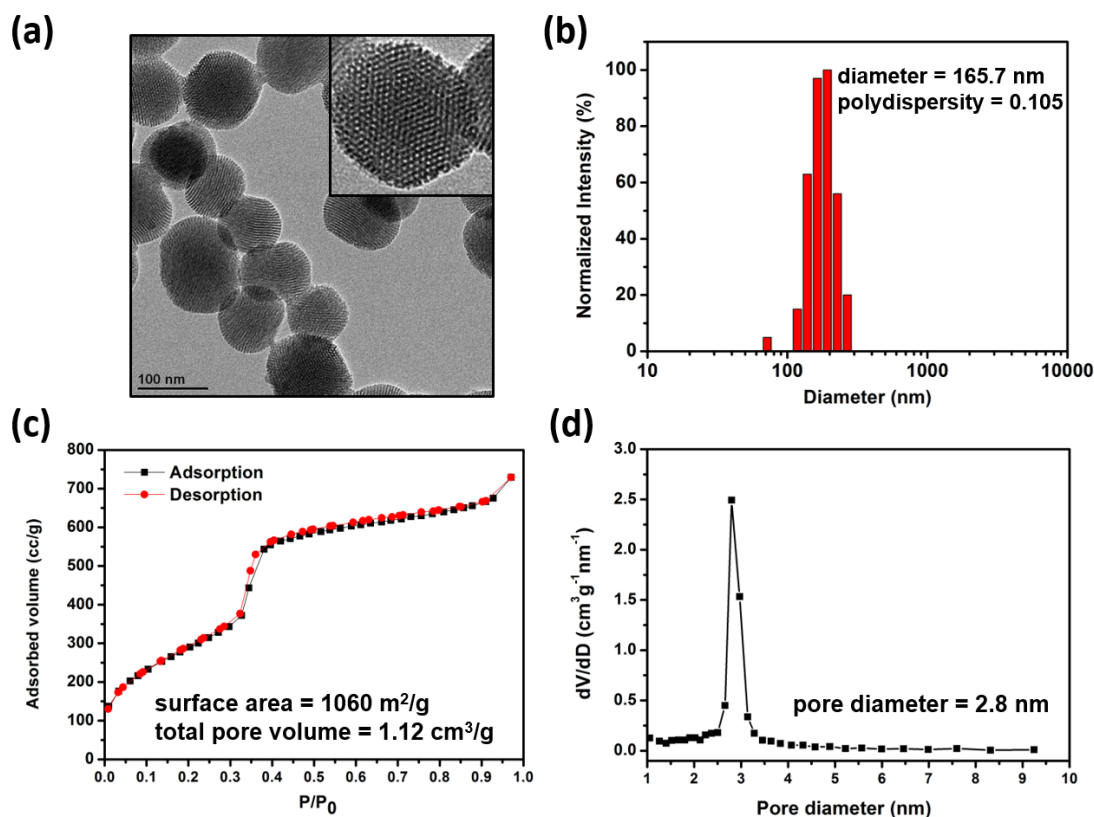


Figure 2.2. (a) TEM image of mesoporous silica nanoparticles (MSNs). Inset shows the enlarged image. (b) Dynamic light scattering diameter distribution of MSNs in D.I. H₂O. The diameter of the MSNs is 165.7 nm. (c) Nitrogen adsorption-desorption isotherms of MSNs at 77 K. BET surface area and pore volume are 1060 m²/g and 1.12 cm³/g, respectively. (d) Pore diameter distribution of MSNs. Average pore diameter of MSNs is 2.8 nm.

2.3.2 Clofazimine solubility enhancement

To enhance the water solubility of CFZ, we applied the concept of “hydrotropy” to the MSNs platform. During the past decades, the successful application of hydrotropy to the delivery of hydrophobic drugs by nanocarriers has been demonstrated by several research groups. For instance, Koo *et al.* used hydrotropic oligomer-conjugated glycol chitosan nanoparticles for

paclitaxel (PTX) delivery.⁵⁶ Wang, *et al.* used 70 nm hydrotropic polymer-based nanocarriers to load and deliver PTX in *in vitro* studies.⁵⁷ Most of their work involved anticancer drugs, especially PTX, whose water solubility is 5.6 $\mu\text{g/mL}$.^{40,58,59} To the best of our knowledge, no application of hydrotropy to the delivery of water-insoluble antibiotics from nanocarriers has been demonstrated.

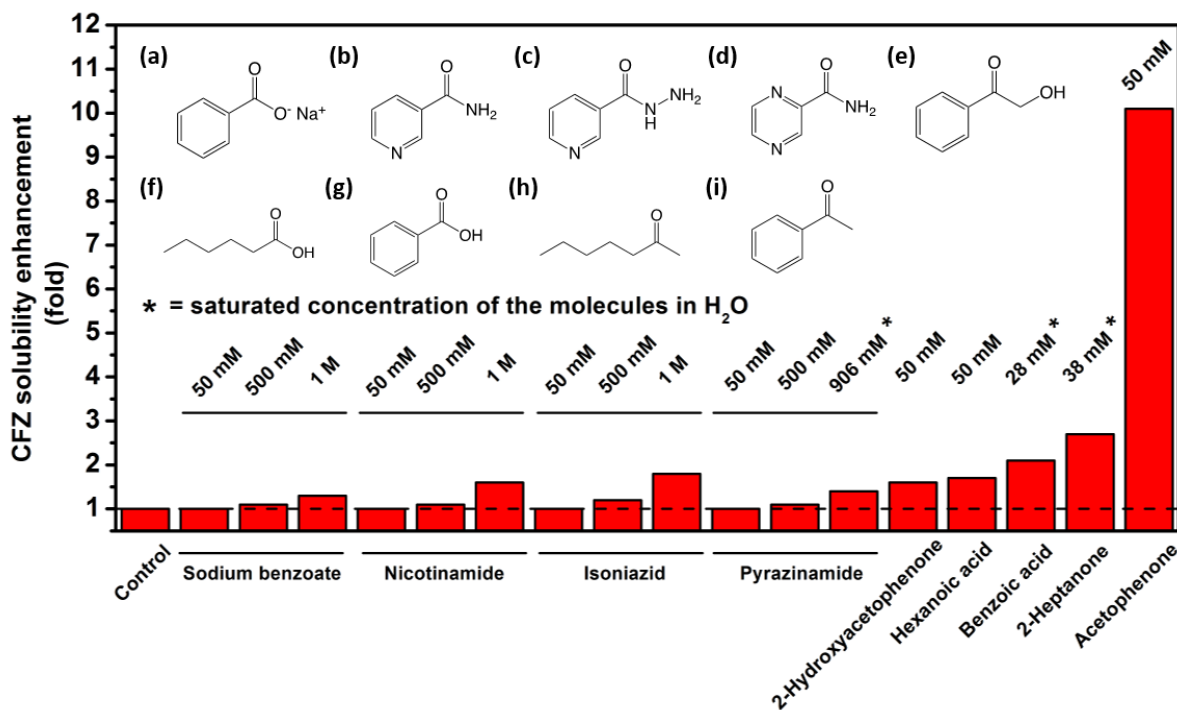


Figure 2.3. CFZ solubility enhancement in the presence of (a) sodium benzoate, (b) nicotinamide, (c) isoniazid, (d) pyrazinamide, (e) 2-hydroxyacetophenone, (f) hexanoic acid, (g) benzoic acid, (h) 2-heptanone, and (i) acetophenone. The solubility of CFZ in deionized water without the addition of any molecule served as a control.

It is known that highly effective hydrotrops frequently have either a phenyl ring or pyridine in their structures.^{59,60} For example, sodium benzoate and nicotinamide, with either a phenyl ring or pyridine in their structures, are effective hydrotrops for PTX.⁶⁰ Therefore, sodium benzoate, nicotinamide, and other molecules with similar structures, including isoniazid,

pyrazinamide, 2-hydroxyacetophenone, benzoic acid, and AP were considered candidates for hydrotropes to enhance the water solubility of CFZ. Figure 2.3 shows the solubility enhancement of CFZ in H₂O in the presence of the various hydrotropes mentioned above. The solubility of CFZ was determined from UV-Vis spectra where the maximum absorbance is at 490 nm. It is surprising that neither sodium benzoate nor nicotinamide is a good hydrotrope; compared with the control, the CFZ solubility enhancement is only 1.3- and 1.5-fold in 1 M of sodium benzoate and nicotinamide solution, respectively. The results indicate that isoniazid and pyrazinamide are also not effective hydrotropes for CFZ (1.7-fold in 1 M isoniazid and 1.4-fold in 1 M pyrazinamide solution). The poor hydrotropic performance of these four molecules may be due to their relatively high water solubility (629 mg/mL for sodium benzoate, 500 mg/mL for nicotinamide, 140 mg/mL for isoniazid, and 50 mg/mL for pyrazinamide) as shown in Table 2.1. It is very difficult to provide

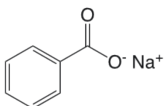
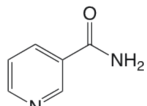
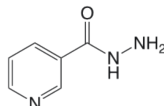
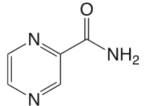
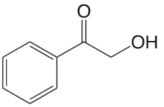
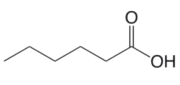
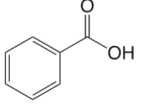
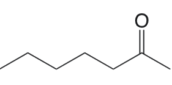
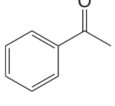
Chemical structure						
Chemical name	Sodium benzoate	Nicotinamide	Isoniazid	Pyrazinamide	2-Hydroxyacetophenone	
H₂O solubility (mg/mL)	629	500	140	50	20	
Chemical structure						
Chemical name	Hexanoic acid	Benzoic acid	2-Heptanone	Acetophenone		
H₂O solubility (mg/mL)	10.8	3.4	4.3	6.1		

Table 2.1. Chemical structures of possible hydrotropes for clofazimine (CFZ) and their water solubilities.

the hydrophobic interaction between the possible hydrotropes and CFZ. In this case, the strong intermolecular force of CFZ (mainly from the hydrophobic interaction of the phenyl rings of CFZ) is much stronger than the interaction between possible hydrotropes and CFZ. Such hydrophilicity of these molecules makes them unable to associate well with the hydrophobic CFZ molecules, and thus the water solubility of CFZ was only slightly enhanced effectively.

On the other hand, the water solubility enhancement of CFZ is 1.6-fold, 1.7-fold, 2.0-fold, and 2.6-fold for 2-hydroxyacetophenone, hexanoic acid, benzoic acid, and 2-heptanone hydrotropes, respectively. Benzoic acid and 2-heptanone have better water solubility enhancement than 2-hydroxyacetophenone or hexanoic acid. This is due to the fact that the water solubility of benzoic acid and 2-heptanone – only 3.4 mg/mL and 4.3 mg/mL, respectively – is lower than that of 2-hydroxyacetophenone and hexanoic acid – 20.0 mg/mL and 10.8 mg/mL, respectively. Thus, these hydrotropes may associate better with the hydrophobic CFZ molecules and enhance the water solubility of CFZ. In addition, the presence of the phenyl rings in the structure of hydrotropes could also contribute to improvement in the water solubility of CFZ because of the hydrophobic interactions exists between the phenyl rings of the hydrotropes and hydrophobic moiety (phenyl rings) of CFZ. For example, the solubility enhancement of CFZ in the presence of benzoic acid or hexanoic acid is 2.0 or 1.7-fold, respectively. By using benzoic acid, the solubility enhancement is higher than that of hexanoic acid due to the presence of the phenyl ring in benzoic acid. Additionally, the solubility enhancement of CFZ in the presence of 2-heptanone or AP is 2.6 or 10.1-fold. By using AP as the hydrotrope, the solubility enhancement is about four times greater than that with 2-heptanone. Therefore, the phenyl ring could effectively enhance the water

solubility of CFZ because either AP or benzoic acid could provide the hydrophobic interaction between their phenyl ring and the phenyl ring of CFZ.

The hydrogen bonding between water molecules and CFZ is not strong enough to solvate CFZ since the intermolecular hydrophobic interaction between the phenyl rings of CFZ is strong. Therefore, the water solubility of CFZ is low (only 0.2 $\mu\text{g/mL}$), or water-insoluble by definition. However, for AP or 2-heptanone, there exists both a hydrophobic phenyl ring or alkyl chain and a polar carbonyl group in their chemical structures. These molecules could provide both the hydrophobic interaction between the hydrophobic phenyl ring or alkyl chain of AP or 2-heptanone and the hydrophobic moiety of CFZ, and hydrogen bonding between the carbonyl group of AP or 2-heptanone and amine hydrogen in CFZ. Therefore, the presence of carbonyl group in AP or 2-heptanone could provide stronger interaction between the possible hydrotropes and CFZ, *e.g.* the CFZ solubility enhancement is 10.1 or 2.6-fold by using AP or 2-heptanone as the hydrotrope, higher than those of benzoic acid (2.0-fold) or hexanoic acid (1.7-fold). In terms of polarity of the possible hydrotropes, a carboxylic acid group has larger polarity than a ketone. Therefore, if we compare 2-heptanone with hexanoic acid, the solubility enhancement of CFZ is 2.6 or 1.7-fold in the presence of 2-heptanone or hexanoic acid, respectively. The higher polarity of hexanoic acid has less hydrotropic effect to increase the water solubility of CFZ. This could also be proved that the solubility enhancement of CFZ is 10.1 or 2.0-fold in the presence of AP or benzoic acid, respectively, since benzoic acid has higher polarity. Based on the above observations, AP, with good association with CFZ and both a phenyl ring and a ketone in its structure, was chosen as a promising hydrotrope for CFZ in this study. The hydrotropic efficacy of AP was examined in more

detail in section 3.3.

2.3.3 Hydrotropic efficacy of AP on CFZ solubility

The hydrotropic efficacy of AP was examined in more detail using UV-Vis spectra to determine the CFZ solubility enhancement as a function of AP concentration in H₂O (Figure 2.4a). When the AP concentration was below 2.2 mM, the absorbance at 490 nm was almost equal to that of the control (0 mM), whereas the absorbance rapidly increased as the AP concentration rose to more than 2.2 mM. The result shows that the water solubility of CFZ dramatically increases when the concentration of AP reaches around 2.2 mM. Figure 2.4b displays the fold enhancement of CFZ solubility by AP compared with the control. The maximum solubility enhancement of CFZ reached 12.2-fold at an AP concentration of 60 mM, which is the saturated concentration of AP in H₂O. Accordingly, the result indicates that the water solubility of CFZ can be enhanced from 0.2 mg/L to about 2.4 mg/L in the presence of AP in H₂O. From Figure 2.4a and 2.4b, no hydrotropic efficacy was observed at concentrations of AP below 2.2 mM. Below this threshold, the solubility enhancement of CFZ is independent of the AP concentration. In contrast, when the concentration of AP is more than 2.2 mM, the solubility enhancement of CFZ increases significantly with AP concentration. The critical AP concentration may imply that the minimum hydrotropic concentration (MHC) is about 2.2 mM. Above the concentration, the self-aggregation of AP occurred,^{41,42} which is similar to that the surfactant molecules form the ordered micelle structure above the critical micelle concentration but not identical.⁴² Such self-aggregation of hydrotropes interact the water-insoluble drugs through hydrophobic interaction between the hydrophobic benzene ring of AP and water-insoluble CFZ and simultaneously help the solubilization of CFZ.

Therefore, once the concentration of AP is higher than this threshold concentration, the self-aggregation of AP and its' hydrotropic effect could help the solubilization of CFZ in water. This behavior follows the mechanism of hydrotropy-assisted solubility enhancement of hydrophobic drugs which may be attributed to the preferential interaction between AP and CFZ.⁴³ A photograph of serial CFZ solutions with different AP concentrations is shown in Figure 2.4c. The color of the solutions became darker as the AP concentration increased, indicating that AP helps dissolve CFZ in H₂O. These results show that the water solubility of CFZ is significantly enhanced by the addition of the AP.

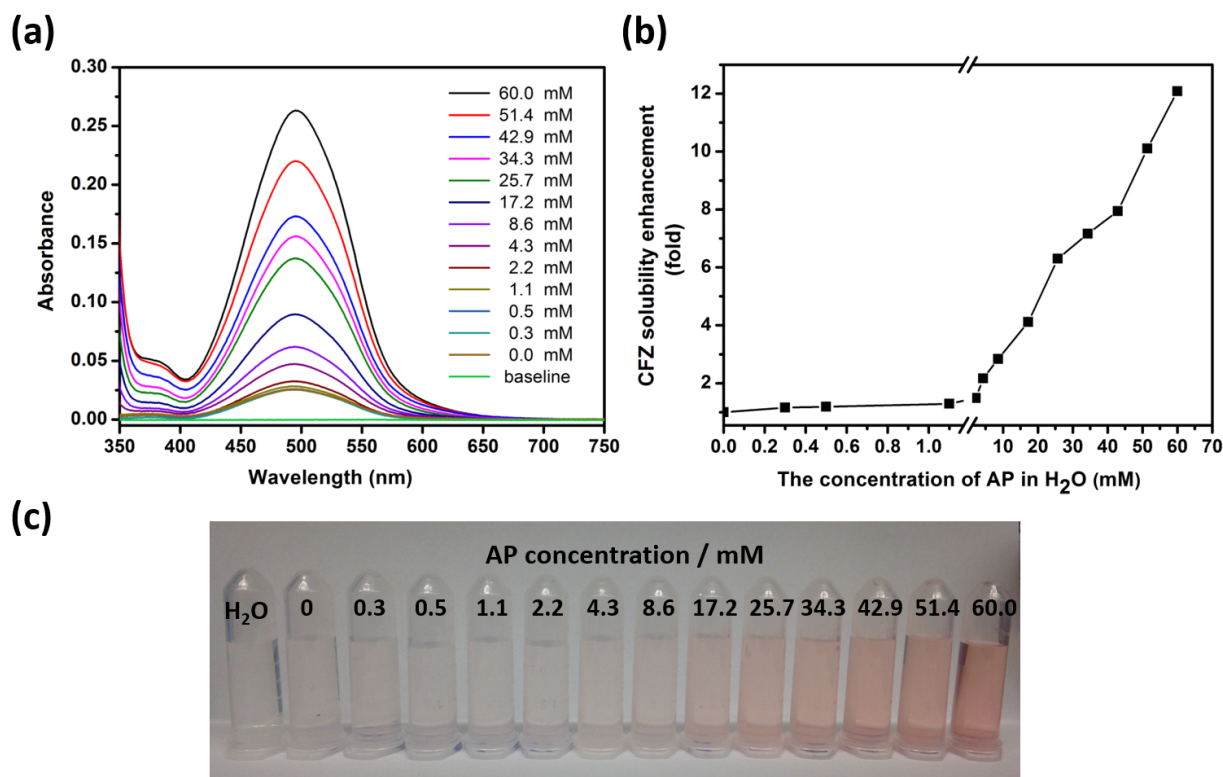


Figure 2.4. (a) UV-Vis spectra of CFZ dissolved in H₂O in the presence of different concentrations of AP. (b) CFZ solubility enhancement (fold increase compared with no AP) in the presence of different concentrations of AP in H₂O. (c) Photograph of CFZ dissolved in H₂O in the presence of different concentrations of AP.

2.3.4 Clofazimine loading by using different non-aqueous solvents: AP and DMSO

To realize whether AP could also facilitate the loading of CFZ in MSNs, we compared the loading amount of CFZ by using AP to that of conventional method using DMSO, a widely-used loading solvent for dissolving poorly water-soluble drugs.^{2,14} We called the method of using AP the “chaperone-assisted” method due to the preferential interaction between AP and CFZ, making AP act like a chaperone carrying the CFZ with it (Figure 2.5a). CFZ loading into MSNs was achieved by soaking MSNs in CFZ solutions with various concentrations dissolved in AP or DMSO. After 24 h loading of CFZ, the CFZ-loaded MSNs were introduced back to aqueous solution. To calculate the loading capacity, which is defined as (the mass of loaded CFZ / the mass of MSNs) x 100%, the CFZ loaded MSNs with AP or DMSO were respectively washed with AP or DMSO several times until the supernatant after centrifugation was clear. Those supernatants were collected and measured by UV-Vis spectroscopy. The total amount of CFZ loaded in MSNs was calculated based on Beer’s law and its calibration curve (Figure 2.6). From Figure 2.5b, the loading capacity of 0.1, 1, and 10 mM CFZ by using DMSO as the loading solvent were found to be 0.2, 0.9, and 5.9 %, respectively. However, with AP as the loading solvent, the higher loading capacity were achieved under all loading concentrations of CFZ, which were 0.3, 1.3, 9.6, and 26.8 % for 0.1, 1, 10, and 50 mM CFZ, respectively. The loading capacity of CFZ increased with the loading concentration of CFZ. The higher loading capacity of CFZ by using AP as the loading solvent can be explained by two reasons: (1) the CFZ solubility in AP (>71 mg/mL) is higher than in DMSO (5 mg/mL), so that the saturated concentration of CFZ in AP (more than 150 mM) is much higher than in DMSO (only 10.5 mM); (2) DMSO is miscible with water, so most of the

DMSO molecules were removed by water during the washing steps, leading to the release of some CFZ molecules from MSNs together with DMSO. However, the water solubility of AP is only 6.1 mg/mL, so a large amount of AP was still loaded in the pores of MSNs after they were re-dispersed in aqueous solution (Figure 2.5a). As will be shown in the next section, the AP in the pores is essential for good CFZ release.

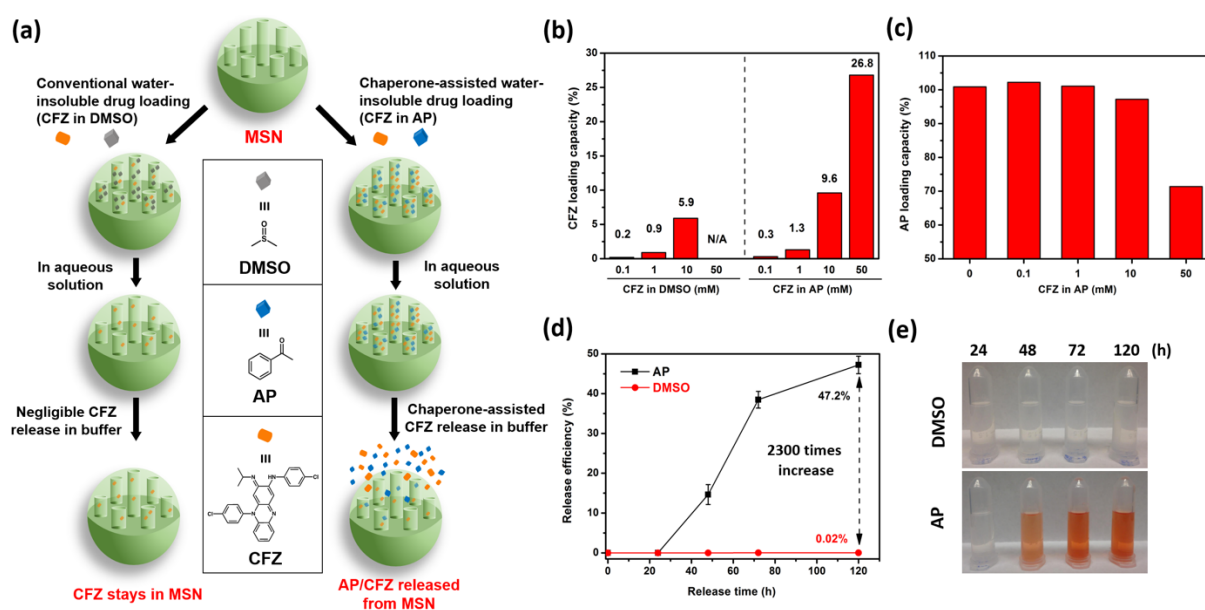


Figure 2.5. (a) Schematic illustration of conventional method (CFZ in DMSO) or chaperone-assisted method (CFZ in AP) for water-insoluble CFZ loading in MSN. By using AP as the chaperone, CFZ release from MSNs could be enhanced significantly. Loading capacity of (b) CFZ and (c) AP using 0.1, 1, or 10 mM CFZ in DMSO or 0, 0.1, 1, 10, or 50 mM CFZ in AP as the loading solution. The concentration of MSNs was 10 mg/mL. (d) Time-dependent release efficiency of CFZ in HEPES buffer solution (10 mM, pH = 7.4) with 1 mM CFZ in DMSO or 1 mM CFZ in AP as loading solutions. (e) Photographs of supernatant after CFZ release collected at selected time points. MSNs were loaded with 1 mM CFZ in DMSO or 1 mM CFZ in AP.

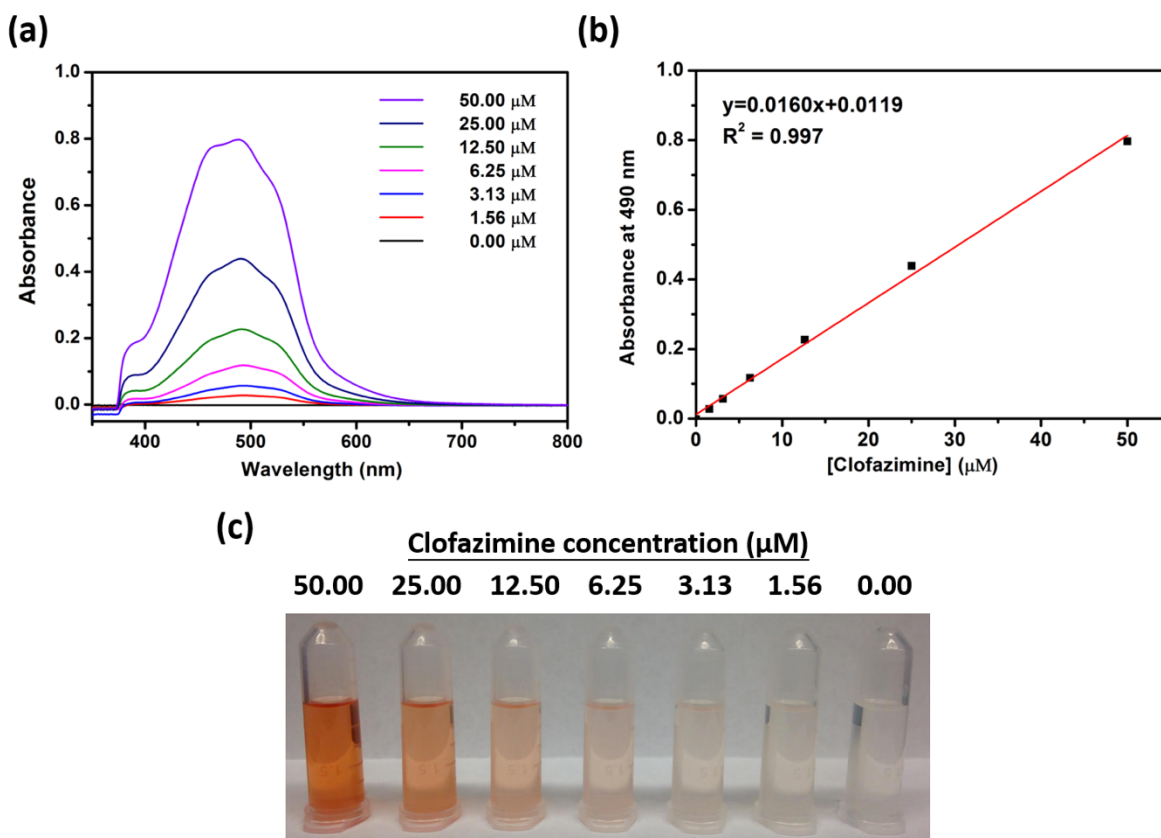


Figure 2.6. (a) UV-Vis spectra of CFZ in AP as a function of concentration and (b) calibration curve of CFZ in AP at room temperature. (c) Photograph of CFZ dissolved in AP.

Based on the significant enhancement of CFZ loading by AP, it was of interest to investigate the detailed relationship between the loading of AP chaperone and its cargo CFZ. MSNs were loaded with AP itself (no CFZ), or AP with 0.1, 1, 10, and 50 mM solubilized CFZ. The pore volume of MSNs is 1.12 cm³/g; hence the maximum volume for cargo loading is 1.12 μL/mg. The density of AP is 1.03 g/cm³, and thus the maximum loading capacity would be 115.4%. When AP itself (0 mM CFZ), or AP with 0.1, 1, 10, and 50 mM solubilized CFZ were used as the loading solvents, the loading capacity of AP was found to be 100.9 %, 102.4 %, 101.1%, 97.2 %, and 71.4

%, respectively (Figure 2.5c). The amount of loaded AP in MSNs corresponds to 8397.8, 8522.7, 8414.5, 8089.9, and 5942.6 nmole/mg, and the amount of loaded CFZ in MSNs was 6.3, 27.5, 202.8, and 566.1 nmole/mg at those respective CFZ loading concentrations (Table 2.2). This implies that when the CFZ loading capacity is low (no higher than 1.3 %, Figure 2.5b), regardless of the presence of CFZ, about 88% of the pore volume of MSNs is filled with AP after loading, which is reasonable since the low water solubility of AP (only 6.1 mg/mL) makes a large amount of AP remain in the pores of MSNs after they are re-dispersed in aqueous solution. The loading capacity of AP is lower at higher CFZ concentrations (10 and 50 mM), at which the loading capacity of CFZ was enhanced (9.6 % and 26.8 %, Figure 2.5b). This is because part of the pore volume of MSNs is occupied by CFZ, thus reducing the volume available for AP loading. The mole ratios of AP to CFZ loaded in MSNs with those CFZ loading concentrations was calculated to be 1352.8, 306.0, 39.9, and 10.5, respectively (Table 2.2). As CFZ loading concentrations in AP increase, both the amount of loaded CFZ and the mole ratio of CFZ to AP increase.

CFZ in AP (mM)	0	0.1	1	10	50
loaded CFZ/MSNs (nmole/mg)	0	6.3	27.5	202.8	566.1
loaded AP/MSNs (nmole/mg)	8397.8	8522.7	8414.5	8089.9	5942.6
mole ratio of AP/CFZ	n/a	1352.8	306.0	39.9	10.5

Table 2.2. Summary of the amount of loaded CFZ and AP in MSNs (nmole/mg) and the mole ratio of AP/CFZ loaded in MSNs.

2.3.5 Clofazimine release to aqueous solution by using different non-aqueous solvents: AP and DMSO

Before applying the methods with AP and DMSO to deliver CFZ to biological systems, we examined their capability for facilitating the release of CFZ into aqueous solution. MSNs loaded with CFZ (1 mM) either by DMSO or AP were dispersed in HEPES buffer solution (pH = 7.4) for 1, 2, 3, or 5 days, respectively (Figure 2.5a). Figure 2.7a shows the UV-Vis spectra of the supernatant after CFZ released from MSNs in buffer solution with DMSO as the loading solvent. The absorption peak of CFZ at 490 nm is not evident, indicating that the release of CFZ is negligible even after 5 days. This phenomenon could be explained as a result of the water-insoluble property of CFZ, making the drug molecules themselves prefer to stay in the pores of MSNs. On the contrary, with AP as the loading solvent, the release of CFZ could be easily found in the UV-Vis spectra with the apparent peaks at 490 nm (Figure 2.7b). The absorbance peaks at 490 nm increased with time between 5 days, and the absorbance is significantly different from those with DMSO. To quantify the release amount of CFZ, the time dependent release efficiency of CFZ using either DMSO or AP was calculated (Figure 2.5d) based on Beer's law and its calibration curve (Figure 2.8). The release efficiency is defined as (the mass of released CFZ / the mass of loaded CFZ) x 100%. By using the "chaperone-assisted" strategy with AP, the release efficiency of CFZ achieved 47.2%, which is 2300 times higher than that by the conventional method with DMSO (0.02%) (Figure 2.5d). This significant enhancement in the release efficiency of CFZ by AP could also be clearly observed in the photograph of the supernatant (Figure 2.5e).

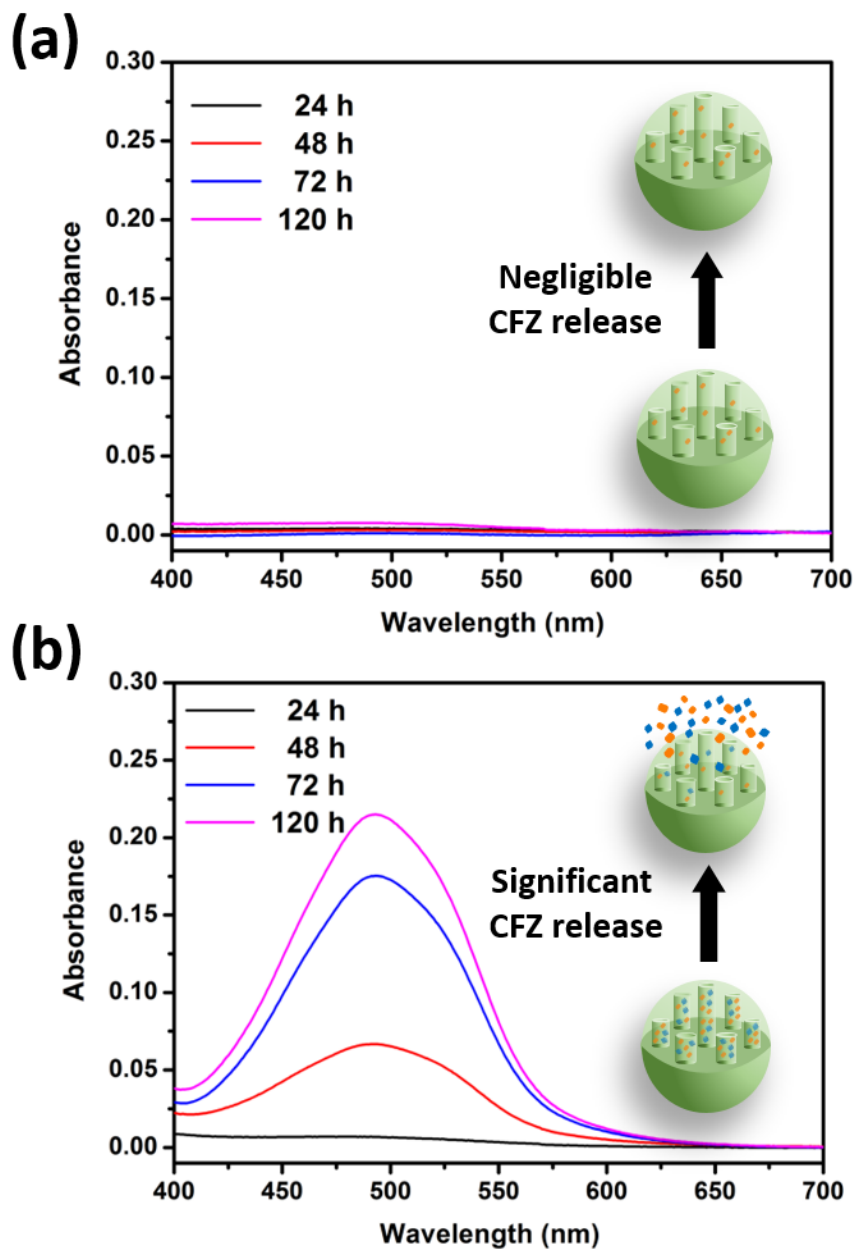


Figure 2.7 UV-Vis spectra of time-dependent CFZ release in HEPES buffer solution (10 mM, pH = 7.4) by using (a) DMSO or (b) AP as loading solvents. MSNs were loaded with 1 mM CFZ in DMSO or 1 mM CFZ in AP. The concentration of MSNs in both loading solution and release buffer solution were 10 mg/mL.

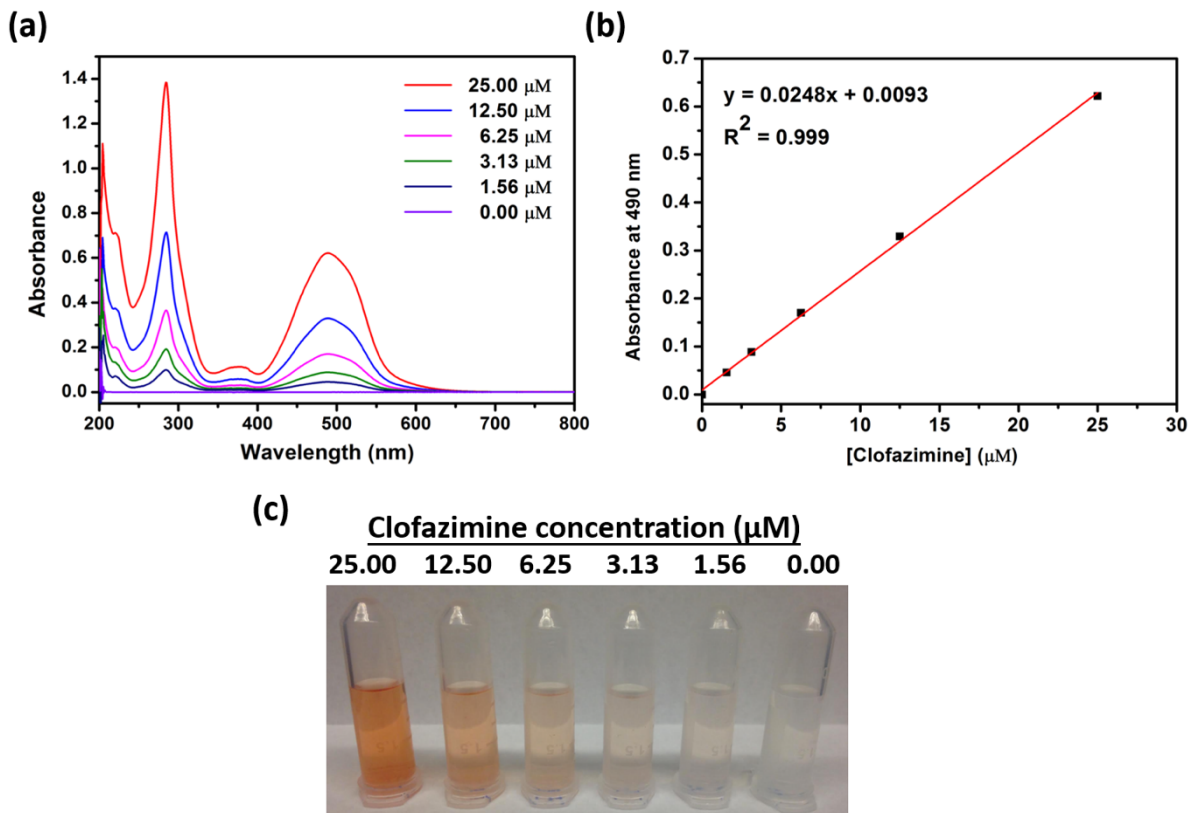


Figure 2.8. (a) Concentration dependent UV-Vis spectra and (b) calibration curve of CFZ in EtOH/HEPES buffer (10 mM, pH = 7.4) (v/v=1/1) solution at room temperature. (c) Photograph of CFZ dissolved in EtOH/HEPES buffer solution (10 mM, pH=7.4) (v/v=1/1).

2.3.6 Effect of clofazimine loading concentration on clofazimine release

To optimize the release of CFZ in aqueous environment using the “chaperone-assisted” delivery strategy, we explored the effect of CFZ loading concentration on the long-term release behavior of CFZ. The release of CFZ was confirmed by the absorbance peaks at 490 nm in the UV-Vis spectra measured from the supernatants collected after spinning down MSNs after 1, 2, 3, and 5 days (Figure 2.7b). The time-dependent release capacity of CFZ was calculated based on Beer’s law and its calibration curve (Figure 2.8). Release capacity is defined as: (the mass of

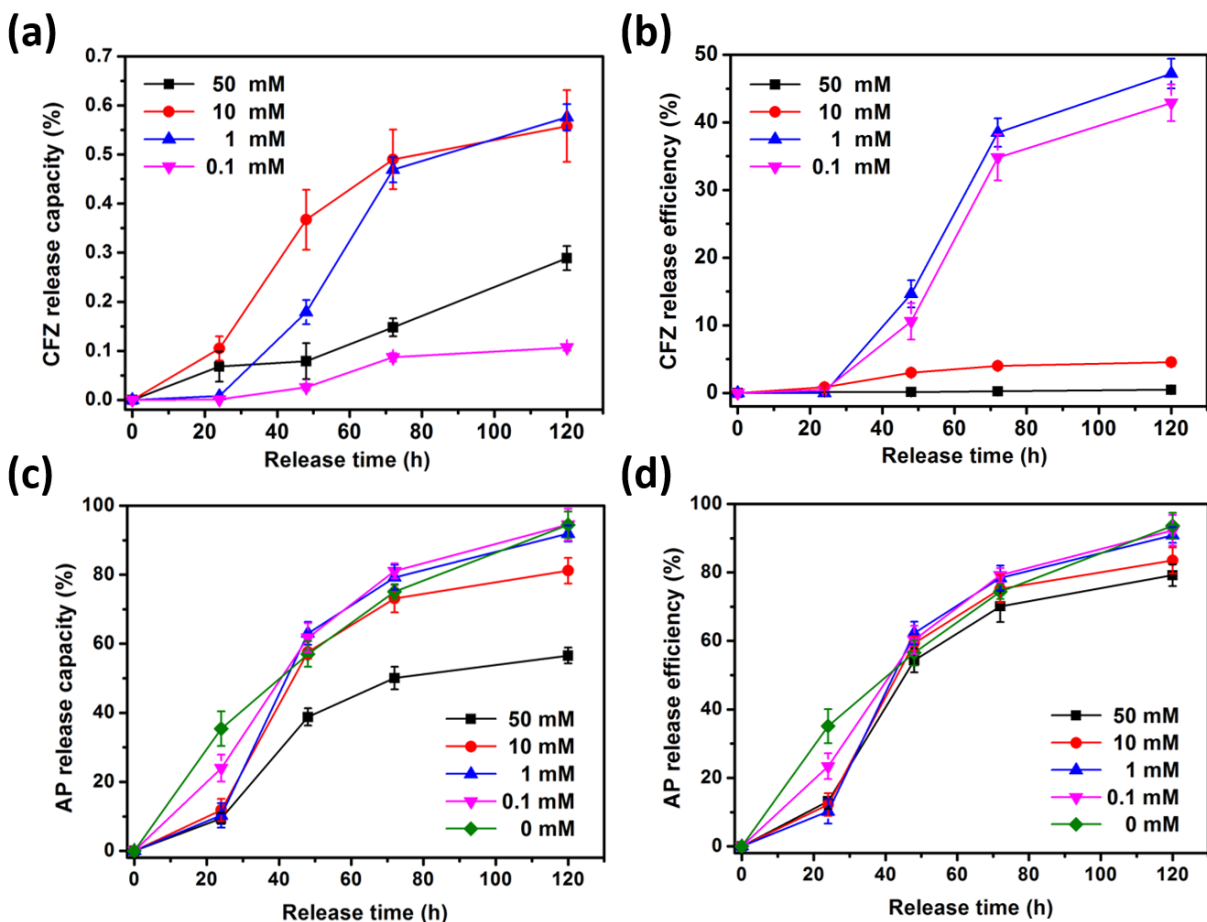


Figure 2.9. Time-dependent release capacity of (a) CFZ and (c) AP and release efficiency of (b) CFZ and (d) AP in HEPES buffer solution (10 mM, pH = 7.4) with 0, 0.1, 1, 10, and 50 mM CFZ in AP as loading solutions. The concentration of MSNs in both loading solution and release buffer solution was 10 mg/mL (n=3).

released CFZ / the mass of MSNs) x 100%. Figure 2.9a shows the time-dependent release capacity of CFZ in HEPES buffer solution (pH = 7.4) with four different CFZ loading concentrations (0.1, 1, 10, and 50 mM) in AP. The absorbance peaks increase with time up to 5 days. Regardless of the CFZ loading concentration, the amount of CFZ released gradually increases with time, until it levels off at about five days. The amount of CFZ released from MSNs loaded with 0.1 mM CFZ

in AP is only 0.10 % on day 5, which is mainly due to the tiny amount of CFZ (0.3 % loading capacity) loaded in MSNs. For the MSNs loaded with 1 and 10 mM CFZ in AP, the CFZ release capacity on day 5 was 0.56 % and 0.54 %, respectively. Even though the amount of CFZ loaded with those two samples (1.3 % and 9.6 % CFZ loading capacity, respectively) differed by 7-fold, the amount of CFZ released was nearly the same. However, the CFZ release capacity of the MSNs loaded with 50 mM CFZ in AP on day 5 is only 0.27 %, lower than those loaded with 1 and 10 mM CFZ in AP. This low CFZ release capacity at this high CFZ loading concentration may be due to a small amount of AP in the pores of MSNs that contain a large amount of CFZ (26.8 % CFZ loading capacity) as referred to Table 2.2, which shows the mole ratio of AP/CFZ to be only 10.5. This less amount of AP renders the environment inside the pores much more hydrophobic and thus reducing the “chaperone-assisted” effect or the hydrotropic effect. The time-dependent release efficiency of CFZ with four different CFZ loading concentrations (0.1, 1, 10, and 50 mM) was also calculated (Figure 2.9b). Release efficiency is defined as: (the mass of released CFZ / the mass of loaded CFZ in MSNs) x 100%. The time-dependent release efficiency on day 5 for MSNs loaded with 0.1, 1, 10, and 50 mM CFZ in AP is 42.3 %, 47.2 %, 4.6 %, and 0.1%, respectively. The lowest release efficiency, observed when MSNs were loaded with 50 mM CFZ in AP, indicates that most of the loaded CFZ remains in the pores of MSNs, which again may be due to the small amount of loaded AP and the enhanced hydrophobicity in the pores of MSNs as described above.

2.3.7 Effect of clofazimine loading concentration on acetophenone release

After the “chaperone-assisted” strategy was successfully demonstrated, we studied the effect of CFZ cargo loading concentration on the release of AP chaperone (Figure 2.9c and 2.9d). The

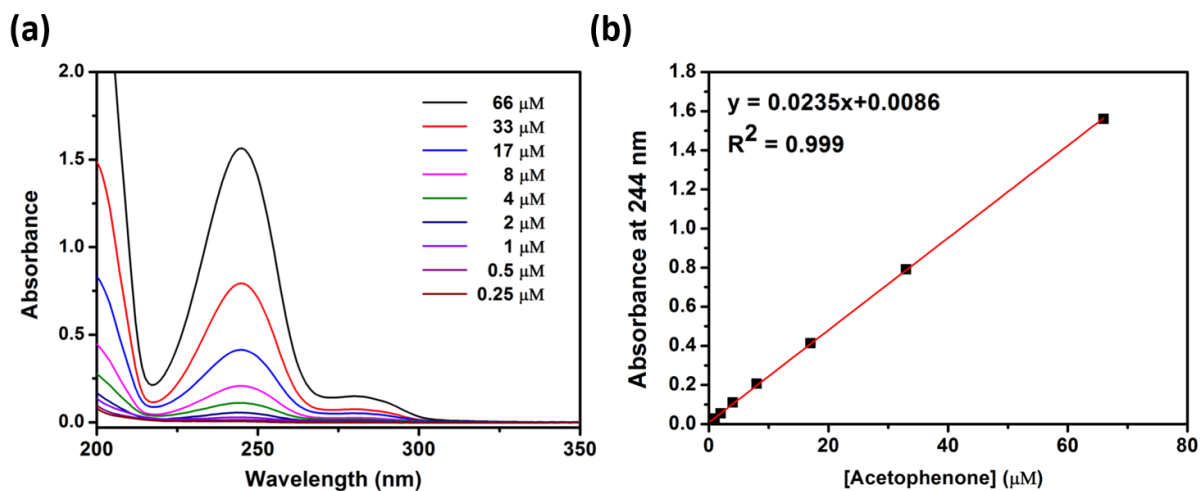


Figure 2.10 (a) Concentration dependent UV-Vis spectra and (b) calibration curve of AP in EtOH/ HEPES buffer solution (10 mM, pH = 7.4) (v/v=1/1).

release efficiency of AP was calculated based on Beer's law and its calibration curve (Figure 2.10). The time-dependent release capacity of AP from MSNs loaded with 0.1, 1, 10, and 50 mM CFZ in AP is lower than from MSNs not loaded with CFZ on day 1 (Figure 2.9c). Nevertheless, the release capacity of AP from MSNs loaded with CFZ substantially increases on day 2. Finally, the release capacity of AP on day 5 reaches 94.2, 90.0, 77.8, and 53.6 % from MSNs loaded with 0.1, 1, 10, and 50 mM CFZ in AP, respectively. For the release efficiency of AP from MSNs loaded with 0.1, 1, 10, and 50 mM CFZ, only 22, 11, 12, and 13 % were found on day 1, much lower than without loaded CFZ (33%) (Figure 2.9d). However, on day 2, the release efficiency of AP from MSNs loaded with 0.1, 1, 10, and 50 mM CFZ in AP achieves 60, 61, 59, and 57 %, respectively, which is close to that without loaded CFZ (58%). Finally, on day 5, the release efficiency of AP reaches about 92, 89, 80, and 75 % for MSNs loaded with 0.1, 1, 10, and 50 mM CFZ in AP, respectively,

and reaches about 95% for the MSNs loaded with AP itself (0 mM CFZ). Interestingly, the result on day 5 shows that the release efficiency of AP decreases as the loading concentration of CFZ increases. This finding together with the lower loading capacity of AP at 10 and 50 mM CFZ loading concentration (Figure 2.5c) adequately explain the much lower release capacity of AP when MSNs are loaded with 10 mM or 50 mM CFZ than when MSNs are loaded with AP without any CFZ (95.9%) (Figure 2.9c).

The sigmoidal release profiles of both CFZ and AP loaded in MSNs are characterized by slow release during the first day followed by increased release at later time points, and a final leveling off (Figure 2.9b and 2.9d). In the presence of both CFZ and AP in MSNs, almost all of the CFZ (Figure 2.9b) as well as the greater part of AP (Figure 2.9d) remain inside the pores on day 1, especially for the MSNs loaded with 1, 10, and 50 mM CFZ in AP. This supports that there may exist an interaction between CFZ and AP in the pores of MSNs, and that this association favors most of the AP molecules residing in the pores of MSNs, reducing the AP release on day 1. The loaded CFZ molecules may sterically block the release of AP from MSNs as well. The better AP release compared to that of CFZ on day 1 could be explained by the higher water solubility of AP than CFZ, so that the release of AP in aqueous environment can occur in a short period of time. For MSNs loaded with 0.1 and 1 mM CFZ in AP, the release efficiency of AP increases significantly after day 1 (Figure 2.9d), which corresponds to the substantial increase in CFZ release efficiency on day 2 (Figure 2.9b). This feature is due to the high mole ratio of AP/CFZ in the pores of MSNs with 0.1 and 1 mM CFZ (Table 2.2). The abundant AP chaperone in the pores carry CFZ out of MSNs and thus facilitates CFZ release into an aqueous environment. Interestingly, for

particles loaded with 10 and 50 mM CFZ, the CFZ release efficiency shows no significant increase during those five days compared with the dramatic increase in AP release efficiency after day 1. This is because the mole ratio of AP/CFZ is low at those CFZ loading concentrations (Table 2.2), and thus the interaction between AP and CFZ is not strong enough to carry CFZ out of MSNs and into the aqueous environment. In other words, when the mole ratio of AP/CFZ is low, even though the interaction between CFZ and AP in the pores retards the release of AP, the high water solubility of AP dominates such that more AP is released into an aqueous environment as the release time increases.

The “chaperone-assisted” delivery strategy makes use of the interaction between CFZ cargo and AP chaperone which provides the mechanism for the release of CFZ from MSNs, and thus significantly enhances the water solubility of CFZ. By carefully tuning the mole ratio of AP/CFZ, we can control the dosage and the release profile of CFZ over time. This would be favorable in terms of improving the bioavailability and the efficacy of CFZ, as well as reducing the side-effect causing by the overdose of CFZ.

2.3.8 Effect of external acetophenone on clofazimine release

As the chaperone, AP is supposed to be stayed together with its CFZ cargo in the pores of MSNs to bring its assistance into full play. To further confirm the idea of “chaperone-assisted” delivery, we studied the release of CFZ in a buffer solution with or without the addition of dissolved AP. Instead of using AP as the loading solvent, DMSO was used for loading CFZ to prevent AP from being present in the pores of MSNs. Release buffer with or without the addition of AP was used for CFZ release. With DMSO as the loading solution, the release efficiency of

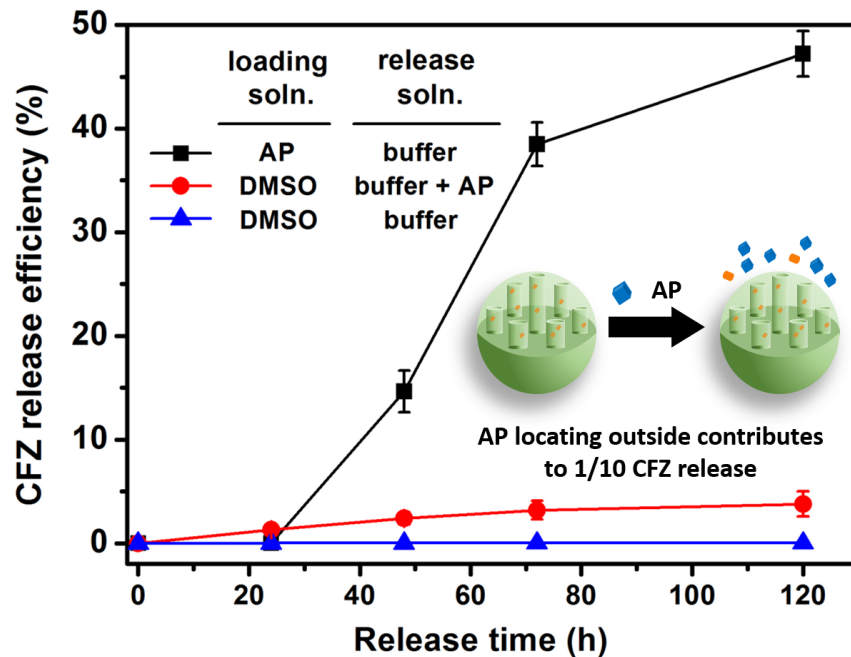


Figure 2.11. Time-dependent release efficiency of CFZ in HEPES buffer solution (10 mM, pH = 7.4) with or without the addition of AP to the buffer solution. After loading with 1 mM CFZ in DMSO, 10 μ L of AP was added to the buffer solution (10 mg MSNs/mL, 1 mL) (n=3).

CFZ released in HEPES buffer solution (10 mM, pH = 7.4) without the addition of AP is only 0.02% after 120 h, which indicates that almost all of the CFZ stays in the pores of MSNs (Figure 2.11). The release efficiency of CFZ released in HEPES buffer solution with the addition of AP, on the other hand, is only 4.3% after 120 h. Both of these CFZ release efficiencies are significantly lower than that with AP as the loading solvent and HEPES buffer solution as the release buffer (47.2%). This result suggests that the CFZ release efficiency is significantly enhanced by the AP loaded inside the pores of MSNs together with CFZ, of which the interaction between CFZ cargo and AP chaperone inside the pores contributes substantially to the significant improvement of CFZ release. On the other hand, AP outside of the MSNs that doesn't have good interaction with CFZ

only contributes to about 1/10th of the CFZ release. This slightly greater CFZ release could be explained by the increased hydrophobicity of the environment causing by the AP located in solution outside of MSNs. This study further strengthens the idea of “chaperone-assisted” delivery, where MSNs act like a primary vehicle carrying both a secondary vehicle – the AP chaperone – and the CFZ cargo inside. As the chaperone, AP carries the CFZ and brings it out and away from MSNs effectively.

2.3.9 Antibacterial effect of acetophenone-assisted clofazimine delivery by MSNs

To explore the antibacterial effect of the developed “chaperone-assisted” delivery strategy shown in Figure 2.12a, we examined the treatment efficacy of the CFZ loaded MSNs using a macrophage model of *Mycobacterium tuberculosis* (*M. tuberculosis*) infection. The mole ratio of AP/CFZ was tuned and the optimized CFZ loading concentration was found to be 10 mM considering both the loading capacity and release capacity of CFZ (Figure 2.5b and 2.9a). The *M. tuberculosis*-infected macrophages were treated with MSNs loaded with 10 mM CFZ in AP (AP/CFZ-MSN) for 4 days (Figure 2.12a). As controls, the macrophages were untreated or treated with MSNs loaded with AP only (AP-MSN), or with free CFZ dissolved in a mixture of DMSO and H₂O (CFZ/DMSO). All of the infected macrophages were lysed at day 4 post-infection and the lysates were plated for viable *M. tuberculosis*. The number of *M. tuberculosis* colony forming units (CFUs) recovered from the macrophages was enumerated to determine bacterial viability under each treatment. As shown in Figure 2.12b, treatment with AP-MSN (11 and 22 µg/mL) for 4 days without CFZ had little effect on *M. tuberculosis* because the number of bacteria in macrophage monolayers (6.29, and 6.25 log CFU, respectively) was similar to and not statistically

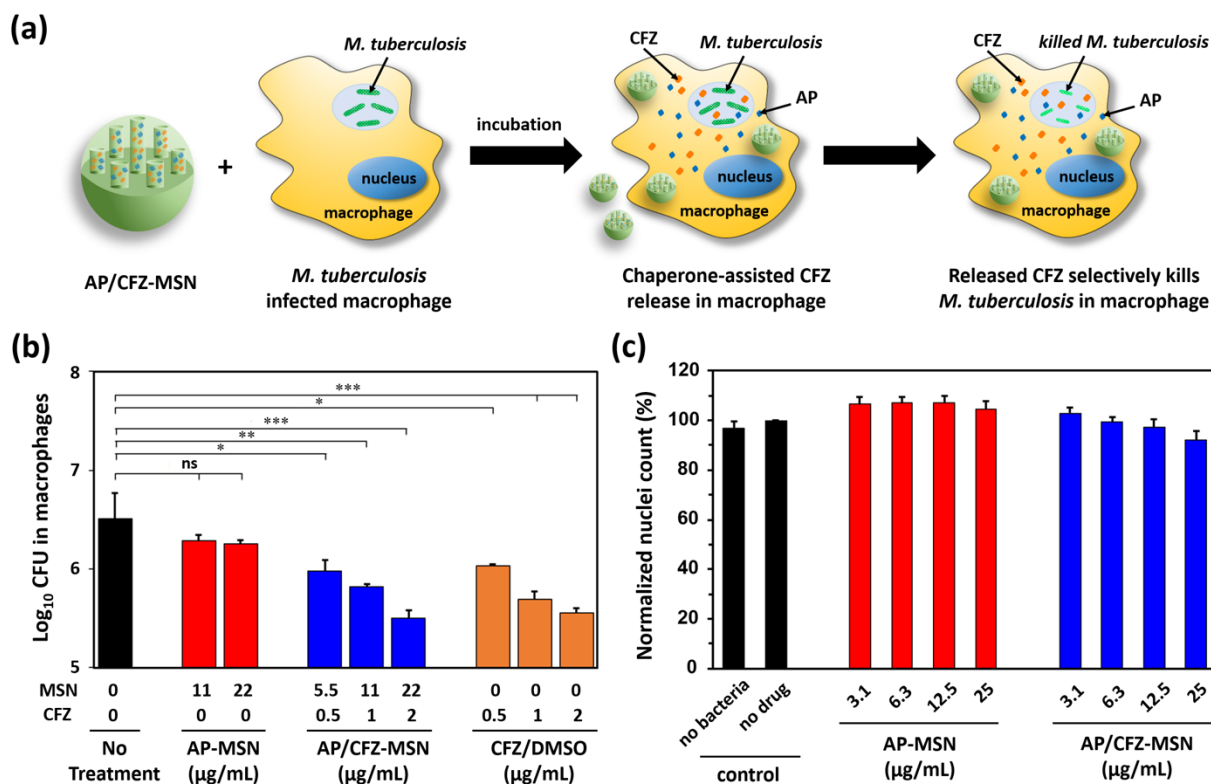


Figure 2.12. (a) Schematic illustration of applying chaperone-assisted CFZ delivery strategy to selectively killing *M. tuberculosis* in macrophage. (b) AP/CFZ loaded MSNs kill *M. tuberculosis* *in vitro* in macrophage cultures. *M. tuberculosis*-infected THP-1 macrophages were untreated, treated with MSN loaded with AP (AP-MSN), treated with MSN loaded with CFZ and AP (AP/CFZ-MSN), or treated with CFZ dissolved in a mixture of DMSO and H₂O (CFZ/DMSO) for 4 days. Bacterial colony forming units (CFUs) were determined by spreading serially diluted lysates of the infected macrophages on agar plates. CFU data are shown as the mean \pm standard deviation. Statistical analysis was performed using one-way ANOVA with Tukey's correction for multiple comparisons. ns, not significant; * $p < 0.05$; ** $p < 0.01$; *** $p < 0.001$ (c) Count of macrophage nuclei per 10x microscopic field normalized to that of the macrophage control wells without addition of drug. Count of macrophage nuclei per microscopic field is used as a surrogate of macrophage viability, as dead macrophages detach and are lost from the monolayer over the long incubation period. Human THP-1 macrophages were either not infected (no bacteria) or infected with *Mycobacterium tuberculosis* in the absence of nanoparticles (no drug) or in the presence of AP-MSN and AP/CFZ-MSN with serial two-fold increasing concentration ranging from 3.1 to 25 $\mu\text{g/mL}$, as indicated. At the end of a 4-day incubation, macrophages were fixed with paraformaldehyde and the nuclei were stained with DAPI and imaged with an ImageXpress High Content Screening system using a 10x objective

lens. The acquired images were analyzed using the Count Nuclei module of MetaXpress software to quantitate numbers of nuclei per 10x field. Data shown are mean \pm sem of three biological replicates.

different from the number in untreated macrophages (6.51 log CFU). In contrast, AP/CFZ-MSN killed the intracellular bacteria in a dose-dependent manner. AP/CFZ-MSN at concentrations of 5.5, 11, and 22 $\mu\text{g}/\text{mL}$ correspond to 0.5, 1, and 2 $\mu\text{g}/\text{mL}$ of free CFZ dissolved in DMSO. The number of viable bacteria after treatment with those concentrations of AP/CFZ-MSN was 5.97, 5.82, and 5.50 log CFU, respectively, suggesting that 90% of bacteria was killed (the number of bacteria decreased by 1 log CFU) in macrophages treated with 22 $\mu\text{g}/\text{mL}$ of AP/CFZ-MSN. We also compared the effect of free CFZ with that of the MSN-encapsulated CFZ. The treatment efficacy of AP/CFZ-MSN dispersed in culture medium was similar to that of an equivalent amount of CFZ dissolved in the mixture of DMSO and culture medium without MSNs. This comparison shows that with the help of the AP chaperone, most of the CFZ loaded inside MSNs is efficiently released in the macrophages and kill the bacteria effectively and selectively (Figure 2.12a).

To investigate if the “chaperone-assisted” delivery strategy with AP, an FDA approved food additive, has any cytotoxicity to the macrophages, we examined the viability of the infected macrophages after the treatment with AP-MSN and AP/CFZ-MSN for 4 days. No significant decrease in macrophage viability was detected (Figure 2.12c) at the concentrations studied. No adverse effect on the morphological appearance of the macrophages treated with AP-MSN or AP/CFZ-MSN was observed. Taken together, these results show that the “chaperone-assisted”

CFZ delivery strategy *via* MSNs has no evident toxicity to macrophages but can selectively and efficiently kill the bacteria residing inside them due to the significant release of CFZ from MSNs.

2.4. Conclusions

In this study, we have developed a novel “chaperone-assisted” strategy based on mesoporous silica nanoparticles (MSNs) to both load water-insoluble drugs into MSN carriers and release them into aqueous biological environment. First, we utilized the concept of “hydrotrophy” to explore the nine candidate small molecules for their utility to enhance the water solubility of a water-insoluble antibiotics — clofazimine (CFZ), who has good efficacy against multidrug-resistant Tuberculosis (TB). Acetophenone (AP) was selected as the most efficacious solvent to enhance 10.1-fold of the water solubility of CFZ. Acting as a chaperone, AP not only brought a great amount of CFZ cargos (26.8% loading capacity of CFZ) into the MSN nanocarriers, but carried a significant amount of CFZ cargos (47.2% release efficiency of CFZ) out from MSNs into the aqueous solution. This release efficiency of CFZ achieved is 2300 times higher than that by conventional method using DMSO (0.02%). This considerable increase in CFZ release is mainly driven by the release of AP chaperone from the chaperone-rich pores of MSNs, which allows CFZ cargo to be carried together into the aqueous solution, and can be supported by our three findings: (1) a lower loading concentration of CFZ (1 mM) gave a higher release efficiency of CFZ (47.2%) compared with a higher loading concentration of CFZ (0.1%); (2) AP in the solution outside of MSNs only minimally increased the release efficiency of CFZ (4.3%); (3) without AP, the release efficiency of CFZ was only 0.02%. We examined this delivery strategy in a macrophage model of *Mycobacterium tuberculosis* (*M. tuberculosis*) infection using MSNs loaded with the optimized

ratio of CFZ and AP (10 mM CFZ in AP). *M. tuberculosis* residing inside macrophages were efficiently killed (reduced by 1 log CFU) by the high amount of the released CFZ, which is comparable to that with the same amount of CFZ dissolved in a mixture of DMSO and culture medium. No adverse effect on the morphological appearance of the macrophages treated with either MSNs loaded with AP or MSNs loaded with CFZ and AP was observed. This novel “chaperone-assisted” delivery strategy for CFZ could also be applied to other hydrophobic drugs with their suitable loading solvents (chaperone), opening up opportunities to apply this drug delivery strategy for further use in medicine and biomedical research.

2.5 Acknowledgment

We gratefully acknowledge financial support by Defense Threat Reduction Agency Grant HDTRA1-13-1-0046.

2.6 References

- (1) Khadka, P.; Ro, J.; Kim, H.; Kim, I.; Kim, J. T.; Kim, H.; Cho, J. M.; Yun, G.; Lee, J. Pharmaceutical Particle Technologies: An Approach to Improve Drug Solubility, Dissolution and Bioavailability. *Asian J. Pharm. Sci.* **2014**, *9*, 304–316.
- (2) Ferris, D. P.; Lu, J.; Gothard, C.; Yanes, R.; Thomas, C. R.; Olsen, J. C.; Stoddart, J. F.; Tamanoi, F.; Zink, J. I. Synthesis of Biomolecule-Modified Mesoporous Silica Nanoparticles for Targeted Hydrophobic Drug Delivery to Cancer Cells. *Small* **2011**, *7*, 1816–1826.
- (3) Wu, S. H.; Mou, C. Y.; Lin, H. P. Synthesis of Mesoporous Silica Nanoparticles. *Chem. Soc. Rev.* **2013**, *42*, 3862–3875.
- (4) Tarn, D.; Ashley, C. E.; Xue, M.; Carnes, E. C.; Zink, J. I.; Brinker, C. J. Mesoporous Silica Nanoparticle Nanocarriers: Biofunctionality and Biocompatibility. *Acc. Chem. Res.* **2013**, *46*, 792–801.
- (5) Ruehle, B.; Saint-Cricq, P.; Zink, J. I. Externally Controlled Nanomachines on Mesoporous Silica Nanoparticles for Biomedical Applications. *Chemphyschem* **2016**, *17*, 1769–1779.
- (6) Tang, F.; Li, L.; Chen, D. Mesoporous Silica Nanoparticles: Synthesis, Biocompatibility and Drug Delivery. *Adv. Mater.* **2012**, *24*, 1504–1534.
- (7) Chou, C. C.; Chen, W.; Hung, Y.; Mou, C. Y. Molecular Elucidation of Biological Response to Mesoporous Silica Nanoparticles in Vitro and in Vivo. *ACS Appl. Mater. Interfaces* **2017**, *9*, 22235–22251.
- (8) Li, Z.; Barnes, J. C.; Bosoy, A.; Stoddart, J. F.; Zink, J. I. Mesoporous Silica Nanoparticles in Biomedical Applications. *Chem. Soc. Rev.* **2012**, *41*, 2590–2605.
- (9) Li, Y.; Shi, J. Hollow-Structured Mesoporous Materials: Chemical Synthesis, Functionalization and Applications. *Adv. Mater.* **2014**, *26*, 3176–3205.
- (10) Wei, J.; Sun, Z.; Luo, W.; Li, Y.; Elzatahry, A. A.; Al-Enizi, A. M.; Deng, Y.; Zhao, D. New Insight into the Synthesis of Large-Pore Ordered Mesoporous Materials. *J. Am. Chem. Soc.* **2017**, *139*, 1706–1713.
- (11) Suteewong, T.; Sai, H.; Hovden, R.; Muller, D.; Bradbury, M. S.; Gruner, S. M.; Wiesner, U. Multicompartment Mesoporous Silica Nanoparticles with Branched Shapes: An Epitaxial Growth Mechanism. *Science* **2013**, *340*, 337–341.
- (12) Zhang, Q.; Wang, X.; Li, P. Z.; Nguyen, K. T.; Wang, X. J.; Luo, Z.; Zhang, H.; Tan, N. S.; Zhao, Y. Biocompatible, Uniform, and Redispersible Mesoporous Silica Nanoparticles for Cancer-Targeted Drug Delivery in Vivo. *Adv. Funct. Mater.* **2014**, *24*, 2450–2461.

- (13) Argyo, C.; Weiss, V.; Bräuchle, C.; Bein, T. Multifunctional Mesoporous Silica Nanoparticles as a Universal Platform for Drug Delivery. *Chem. Mater.* **2014**, *26*, 435–451.
- (14) Lu, J.; Liong, M.; Zink, J. I.; Tamanoi, F. Mesoporous Silica Nanoparticles as a Delivery System for Hydrophobic Anticancer Drugs. *Small* **2007**, *3*, 1341–1346.
- (15) Ruehle, B.; Clemens, D. L.; Lee, B.-Y.; Horwitz, M. A.; Zink, J. I. A Pathogen-Specific Cargo Delivery Platform Based on Mesoporous Silica Nanoparticles. *J. Am. Chem. Soc.* **2017**, *139*, 6663–6668.
- (16) Li, Z.; Clemens, D. L.; Lee, B. Y.; Dillon, B. J.; Horwitz, M. A.; Zink, J. I. Mesoporous Silica Nanoparticles with pH-Sensitive Nanovalves for Delivery of Moxifloxacin Provide Improved Treatment of Lethal Pneumonic Tularemia. *ACS Nano* **2015**, *9*, 10778–10789.
- (17) Yan, H.; Teh, C.; Sreejith, S.; Zhu, L.; Kwok, A.; Fang, W.; Ma, X.; Nguyen, K. T.; Korzh, V.; Zhao, Y. Functional Mesoporous Silica Nanoparticles for Photothermal-Controlled Drug Delivery in Vivo. *Angew. Chem. Int. Ed.* **2012**, *51*, 8373–8377.
- (18) Chen, W.; Tsai, P. H.; Hung, Y.; Chiou, S. H.; Mou, C. Y. Nonviral Cell Labeling and Differentiation Agent for Induced Pluripotent Stem Cells Based on Mesoporous Silica Nanoparticles. *ACS Nano* **2013**, *7*, 8423–8440.
- (19) Chang, J. H.; Tsai, P. H.; Chen, W.; Chiou, S. H.; Mou, C. Y. Dual Delivery of siRNA and Plasmid DNA Using Mesoporous Silica Nanoparticles to Differentiate Induced Pluripotent Stem Cells into Dopaminergic Neurons. *J. Mater. Chem. B* **2017**, *5*, 3012–3023.
- (20) Xia, T.; Kovochich, M.; Liong, M.; Meng, H.; Kabehie, S.; George, S.; Zink, J. I.; Nel, A. E. Polyethyleneimine Coating Enhances the Cellular Uptake of Mesoporous Silica Nanoparticles and Allows Safe Delivery of siRNA and DNA Constructs. *ACS Nano* **2009**, *3*, 3273–3286.
- (21) Wu, M.; Meng, Q.; Chen, Y.; Du, Y.; Zhang, L.; Li, Y.; Zhang, L.; Shi, J. Large-Pore Ultrasmall Mesoporous Organosilica Nanoparticles: Micelle/precursor Co-Templating Assembly and Nuclear-Targeted Gene Delivery. *Adv. Mater.* **2015**, *27*, 215–222.
- (22) Chen, Y. P.; Chen, C. T.; Hung, Y.; Chou, C. M.; Liu, T. P.; Liang, M. R.; Chen, C. T.; Mou, C. Y. A New Strategy for Intracellular Delivery of Enzyme Using Mesoporous Silica Nanoparticles: Superoxide Dismutase. *J. Am. Chem. Soc.* **2013**, *135*, 1516–1523.
- (23) Tu, J.; Boyle, A. L.; Friedrich, H.; Bomans, P. H. H.; Busmann, J.; Sommerdijk, N. A. J. M.; Jiskoot, W.; Kros, A. Mesoporous Silica Nanoparticles with Large Pores for the Encapsulation and Release of Proteins. *ACS Appl. Mater. Interfaces* **2016**, *8*, 32211–32219.
- (24) Chen, F.; Hong, H.; Zhang, Y.; Valdovinos, H. F.; Shi, S.; Kwon, G. S.; Theuer, C. P.; Barnhart, T.

- E.; Cai, W. In Vivo Tumor Targeting and Image-Guided Drug Delivery with Antibody-Conjugated, Radiolabeled Mesoporous Silica Nanoparticles. *ACS Nano* **2013**, *7*, 9027–9039.
- (25) Qu, Q.; Ma, X.; Zhao, Y. Anticancer Effect of α -Tocopheryl Succinate Delivered by Mitochondria-Targeted Mesoporous Silica Nanoparticles. *ACS Appl. Mater. Interfaces* **2016**, *8*, 34261–34269.
- (26) Liong, M.; Lu, J.; Kovochich, M.; Xia, T.; Ruehm, S. G.; Nel, A. E.; Tamanoi, F.; Zink, J. I. Multifunctional Inorganic Nanoparticles for Imaging, Targeting, and Drug Delivery. *ACS Nano* **2008**, *2*, 889–896.
- (27) Guardado-Alvarez, T. M.; Chen, W.; Norton, A. E.; Russell, M. M.; Connick, W. B.; Zink, J. I. Analyte-Responsive Gated Hollow Mesoporous Silica Nanoparticles Exhibiting Inverse Functionality and an AND Logic Response. *Nanoscale* **2016**, *8*, 18296–18300.
- (28) Kwon, D.; Cha, B. G.; Cho, Y.; Min, J.; Park, E. B.; Kang, S. J.; Kim, J. Extra-Large Pore Mesoporous Silica Nanoparticles for Directing in Vivo M2 Macrophage Polarization by Delivering IL-4. *Nano Lett.* **2017**, *17*, 2747–2756.
- (29) Kamkaew, A.; Cheng, L.; Goel, S.; Valdovinos, H. F.; Barnhart, T. E.; Liu, Z.; Cai, W. Cerenkov Radiation Induced Photodynamic Therapy Using Chlorin e6-Loaded Hollow Mesoporous Silica Nanoparticles. *ACS Appl. Mater. Interfaces* **2016**, *8*, 26630–26637.
- (30) Kempen, P. J.; Greasley, S.; Parker, K. A.; Campbell, J. L.; Chang, H. Y.; Jones, J. R.; Sinclair, R.; Gambhir, S. S.; Jokerst, J. V. Theranostic Mesoporous Silica Nanoparticles Biodegrade after pro-Survival Drug Delivery and Ultrasound/magnetic Resonance Imaging of Stem Cells. *Theranostics* **2015**, *5*, 631–642.
- (31) Rühle, B.; Datz, S.; Argyo, C.; Bein, T.; Zink, J. I. A Molecular Nanocap Activated by Superparamagnetic Heating for Externally Stimulated Cargo Release. *Chem. Commun.* **2016**, *52*, 1843–1846.
- (32) Hwang, A. A.; Lee, B. Y.; Clemens, D. L.; Dillon, B. J.; Zink, J. I.; Horwitz, M. A. Tuberculosis: pH-Responsive Isoniazid-Loaded Nanoparticles Markedly Improve Tuberculosis Treatment in Mice. *Small* **2015**, *11*, 5066–5078.
- (33) Paris, J. L.; Cabanas, M. V.; Manzano, M.; Vallet-Regí, M. Polymer-Grafted Mesoporous Silica Nanoparticles as Ultrasound-Responsive Drug Carriers. *ACS Nano* **2015**, *9*, 11023–11033.
- (34) Li, H.; Tan, L. L.; Jia, P.; Li, Q. L.; Sun, Y. L.; Zhang, J.; Ning, Y. Q.; Yu, J.; Yang, Y. W. Near-Infrared Light-Responsive Supramolecular Nanovalve Based on Mesoporous Silica-Coated Gold Nanorods. *Chem. Sci.* **2014**, *5*, 2804–2808.
- (35) Thomas, C. R.; Ferris, D. P.; Lee, J. H.; Choi, E.; Cho, M. H.; Kim, E. S.; Stoddart, J. F.; Shin, J. S.;

- Cheon, J.; Zink, J. I. Noninvasive Remote-Controlled Release of Drug Molecules in Vitro Using Magnetic Actuation of Mechanized Nanoparticles. *J. Am. Chem. Soc.* **2010**, *132*, 10623–10625.
- (36) Wang, H.; Wang, K.; Tian, B.; Revia, R.; Mu, Q.; Jeon, M.; Chang, F. C.; Zhang, M. Preloading of Hydrophobic Anticancer Drug into Multifunctional Nanocarrier for Multimodal Imaging, NIR-Responsive Drug Release, and Synergistic Therapy. *Small* **2016**, *12*, 6388–6397.
- (37) Palanikumar, L.; Kim, H. Y.; Oh, J. Y.; Thomas, A. P.; Choi, E. S.; Jeena, M. T.; Joo, S. H.; Ryu, J. H. Noncovalent Surface Locking of Mesoporous Silica Nanoparticles for Exceptionally High Hydrophobic Drug Loading and Enhanced Colloidal Stability. *Biomacromolecules* **2015**, *16*, 2701–2714.
- (38) Jiao, Y.; Sun, Y.; Tang, X.; Ren, Q.; Yang, W. Tumor-Targeting Multifunctional Rattle-Type Theranostic Nanoparticles for MRI/NIRF Bimodal Imaging and Delivery of Hydrophobic Drugs. *Small* **2015**, *11*, 1962–1974.
- (39) Neuberg, C. Hydrotropic Phenomena. I. *Biochem. Z.* **1916**, *76*, 107–176.
- (40) Kim, J. Y.; Kim, S.; Papp, M.; Park, K.; Pinal, R. Hydrotropic Solubilization of Poorly Water-Soluble Drugs. *J. Pharm. Sci.* **2010**, *99*, 3953–3965.
- (41) Shimizu, S.; Matubayasi, N. The Origin of Cooperative Solubilisation by Hydrotropes. *Phys. Chem. Chem. Phys.* **2016**, *18*, 25621–25628.
- (42) Subbarao, C. V.; Chakravarthy, I. P. K.; Sai Bharadwaj, A. V. S. L.; Prasad, K. M. M. Functions of Hydrotropes in Solutions. *Chem. Eng. Technol.* **2012**, *35*, 225–237.
- (43) Das, S.; Paul, S. Mechanism of Hydrotropic Action of Hydrotrope Sodium Cumene Sulfonate on the Solubility of Di-t-Butyl-Methane: A Molecular Dynamics Simulation Study. *J. Phys. Chem. B* **2016**, *120*, 173–183.
- (44) Booth, J. J.; Omar, M.; Abbott, S.; Shimizu, S. Hydrotrope Accumulation around the Drug: the Driving Force for Solubilization and Minimum Hydrotrope Concentration for Nicotinamide and Urea. *Phys. Chem. Chem. Phys.* **2015**, *17*, 8028–8037.
- (45) Das, S.; Paul, S. Exploring Molecular Insights into Aggregation of Hydrotrope Sodium Cumene Sulfonate in Aqueous Solution: A Molecular Dynamics Simulation Study. *J. Phys. Chem. B* **2015**, *119*, 3142–3154.
- (46) Shimizu, S.; Booth, J. J.; Abbott, S. Hydrotrope: Binding Models vs. Statistical Thermodynamics. *Phys. Chem. Chem. Phys.* **2013**, *15*, 20625–20632.
- (47) Shimizu, S.; Matubayasi, N. Hydrotropy: Monomer-Micelle Equilibrium and Minimum Hydrotrope Concentration. *J. Phys. Chem. B* **2014**, *118*, 10515–10524

- (48) Patel, A.; Malinowska, L.; Saha, S.; Wang, J.; Alberti, S.; Krishnan, Y.; Hyman, A. A. Biochemistry: ATP as a Biological Hydrotrope. *Science* **2017**, *356*, 753–756.
- (49) Dalcolmo, M.; Gayoso, R.; Sotgiu, G.; D’Ambrosio, L.; Rocha, J. L.; Borga, L.; Fandinho, F.; Braga, J. U.; Galesi, V. M. N.; Barreira, D.; Sanchez, D. A.; Dockhorn, F.; Centis, R.; Caminero, J. A.; Migliori, G. B. Effectiveness and Safety of Clofazimine in Multidrug-Resistant Tuberculosis: A Nationwide Report from Brazil. *Eur. Respir. J.* **2017**, *49*, 1602445.
- (50) Lechartier, B.; Cole, S. T. Mode of Action of Clofazimine and Combination Therapy with Benzothiazinones against Mycobacterium Tuberculosis. *Antimicrob. Agents Chemother.* **2015**, *59*, 4457–4463.
- (51) Tyagi, S.; Ammerman, N. C.; Li, S.-Y.; Adamson, J.; Converse, P. J.; Swanson, R. V.; Almeida, D. V.; Grosset, J. H. Clofazimine Shortens the Duration of the First-Line Treatment Regimen for Experimental Chemotherapy of Tuberculosis. *Proc. Natl. Acad. Sci. USA* **2015**, *112*, 869–874.
- (52) Cholo, M. C.; Steel, H. C.; Fourie, P. B.; Germishuizen, W. A.; Anderson, R. Clofazimine: Current Status and Future Prospects. *J. Antimicrob. Chemother.* **2012**, *67*, 290–298.
- (53) WHO. *WHO Global Tuberculosis Report 2016*; **2016**.
- (54) Clemens, D. L.; Lee, B. Y.; Xue, M.; Thomas, C. R.; Meng, H.; Ferris, D.; Nel, A. E.; Zink, J. I.; Horwitz, M. A. Targeted Intracellular Delivery of Antituberculosis Drugs to Mycobacterium Tuberculosis-Infected Macrophages via Functionalized Mesoporous Silica Nanoparticles. *Antimicrob. Agents Chemother.* **2012**, *56*, 2535–2545.
- (55) Huang, W. Y.; Zink, J. I. Effect of Pore Wall Charge and Probe Molecule Size on Molecular Motion inside Mesoporous Silica Nanoparticles. *J. Phys. Chem. C* **2016**, *120*, 23780–23787.
- (56) Koo, H.; Min, K. H.; Lee, S. C.; Park, J. H.; Park, K.; Jeong, S. Y.; Choi, K.; Kwon, I. C.; Kim, K. Enhanced Drug-Loading and Therapeutic Efficacy of Hydrotropic Oligomer-Conjugated Glycol Chitosan Nanoparticles for Tumor-Targeted Paclitaxel Delivery. *J. Control. Release* **2013**, *172*, 823–831.
- (57) Gao, L.; Gao, L.; Fan, M.; Li, Q.; Jin, J.; Wang, J.; Lu, W.; Yu, L.; Yan, Z.; Wang, Y. Hydrotropic Polymer-Based Paclitaxel-Loaded Self-Assembled Nanoparticles: Preparation and Biological Evaluation. *RSC Adv.* **2017**, *7*, 33248–33256.
- (58) Lee, S. C.; Huh, K. M.; Lee, J.; Cho, Y. W.; Galinsky, R. E.; Park, K. Hydrotropic Polymeric Micelles for Enhanced Paclitaxel Solubility: In Vitro and in Vivo Characterization. *Biomacromolecules* **2007**, *8*, 202–208.
- (59) Huh, K. M.; Lee, S. C.; Cho, Y. W.; Lee, J.; Jeong, J. H.; Park, K. Hydrotropic Polymer Micelle

System for Delivery of Paclitaxel. *J. Control. Release* **2005**, *101*, 59–68.

- (60) Lee, J.; Lee, S. C.; Acharya, G.; Chang, C. J.; Park, K. Hydrotropic Solubilization of Paclitaxel: Analysis of Chemical Structures for Hydrotropic Property. *Pharm. Res.* **2003**, *20*, 1022–1030.

Chapter 3

Spatial, Temporal, and Dose Control of Drug Delivery using Noninvasive Magnetic Stimulation

This chapter of the dissertation was adapted and reprinted with permission from Wei Chen, Chi-An Cheng, Jeffrey I. Zink *ACS Nano* **2019**, *13*, 1292–1308. Copyright 2019 American Chemical Society. Co-author contributions: Chen W., and Cheng C. A. performed the experiments, Jeffrey I. Zink was the P.I.

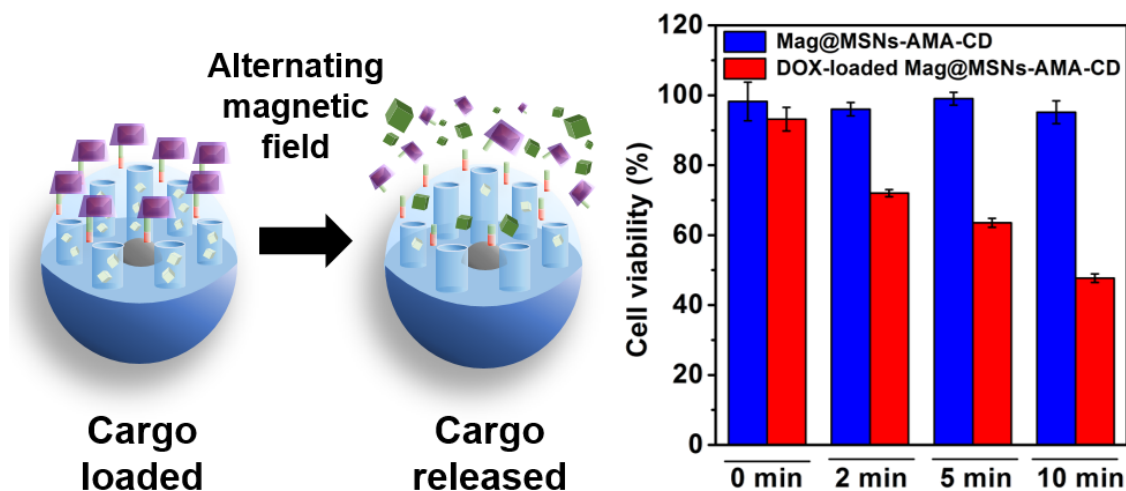
Keywords of this chapter: superparamagnetic nanoparticles, mesoporous silica nanoparticles, alternating magnetic field, magnetic heating, drug delivery, thermally sensitive gatekeeper, dosage-controlled release, chemotherapy

Abstract

Noninvasive stimuli-responsive drug delivery using magnetic fields in conjunction with superparamagnetic nanoparticles offers the potential for the spatial and temporal control of drug release. When hyperthermia is not desired and control of the dosage is required, it is necessary to design a platform in which local heating on the nanoscale releases the therapeutic cargo without the bulk heating of the surrounding medium. In this study, we report a design using a stimuli-responsive nanoparticle platform to control the dosage of the cargo released by an alternating magnetic field (AMF) actuation. A core@shell structure with a superparamagnetic doped iron oxide ($\text{MnFe}_2\text{O}_4@ \text{CoFe}_2\text{O}_4$) nanoparticle core in a mesoporous silica shell was synthesized. The core used here has a high saturation magnetization value and a high specific loss power for heat generation under an AMF. The mesoporous shell has a high cargo-carrying capacity. A

thermoresponsive molecular-based gatekeeper containing an aliphatic azo group was modified on the core@shell nanoparticles to regulate the cargo release. The mesoporous structure of the silica shell remained intact after exposure to an AMF, showing that the release of cargo is due to the removal of the gatekeepers instead of the destruction of the structure. Most importantly, we demonstrated that the amount of cargo released could be adjusted by the AMF exposure time. By applying multiple sequential exposures of AMF, we were able to release the cargo step-wise and increase the total amount of released cargo. *In vitro* studies showed that the death of pancreatic cancer cells treated by drug-loaded nanoparticles was controlled by different lengths of AMF exposure time due to different amount of drugs released from the carriers. The strategy developed here holds great promise for achieving the dosage, temporal, and spatial control of therapeutics delivery without the risk of overheating the particles' surroundings.

Table of Content Figure



3.1 Introduction

Precision medicine, defined as “right drug, right dosage at right timing to right patient”, is a rapidly developing and popular global trend for cancer treatment.¹ This emerging approach takes the individual variability into account for personalized disease treatment regimen design.¹ However, the necessity to deliver the desired therapeutic, at the desired time, to the specific site of the disease, and with accurate dosage of therapeutics remains a challenge.² Over the past decade, many examples of stimuli-responsive drug delivery platforms responsive to internal cellular stimuli (such as pH change,^{3–6} redox potential,^{7,8} enzymes⁹ or biomolecules^{10,11}) and external stimuli (such as light,^{12–15} heat,^{16–23} or ultrasound^{24,25}) have been developed for cancer treatment because they offer the ability to both enhance the therapeutic efficacy at the target sites and reduce the premature release of drug molecules thus reducing off-target side effects. Delivery of the accurate dosage is a key feature in chemotherapy.^{26–28} The dosage of the therapeutics should be in the optimal range called therapeutic window, where the dosages exceed the threshold concentration and can treat disease effectively, while below the concentration which is significantly toxic to normal cells.²⁹ In view of this, after getting information from genetic databases to find out the right drug to the right patients, the next challenge is to deliver the right dosage of therapeutics in a spatio-temporal controlled manner to the desired lesion location.^{2,30} However, important limitations of the above stimuli-responsive drug delivery exist: the platforms responsive to pH change, redox potential, and enzyme cannot precisely control the delivery time, the delivery location, and the delivery dosage; the light responsive platforms have the most focused spatial control (on the order of mm³) but suffer from the limited penetration depth in tissue; the heat

responsive platforms create a risk of inducing tumor metastasis when hyperthermia occurs;³¹⁻³⁵ and ultrasound suffers from blockage by bone and air even though under ideal condition can attain the spatial focus on the order of 10 mm³.³⁶

Non-invasive magnetic fields in conjunction with superparamagnetic nanoparticles offer a possible solution to overcome these limitations. Magnetic fields are harmless, are localized with dimensions governed by the size of the magnetic coil (on the order of cm³), and can be turned on and off under precise control. Superparamagnetic nanoparticles have been investigated extensively for a wide variety of biomedical applications including magnetic resonance imaging (MRI) contrast enhancement,^{37,38} hyperthermia therapy,³⁹ and drug delivery.^{22,40-42} Among them, drug delivery triggered by heat generated when magnetic nanoparticles are exposed to an alternating magnetic field (AMF) actuation is an emerging approach to externally and non-invasively triggered drug release.⁴³⁻⁴⁹ AMF actuation of drug delivery has the following benefits: (1) the release of drugs can be spatially and temporally controlled, offering the advantages for delivering a high local concentration of therapeutics to the lesion site and reducing off-site drug delivery from the carriers, (2) no penetration depth limitation of the magnetic field, enabling the actuation be initiated in the deep animal body without the concern of light scattering or absorption by tissues,^{22,50-52} and (3) less restriction on the type of tissues being treated compared with ultrasound stimulation that is strongly attenuated by air and bone structures.³⁶ In hyperthermia therapy, when the blood is congested locally during heating, more energy will be provided for the tumor growth.^{31-35,53} In this case, the original tumor cells suffering from necrosis, starvation or suffocation due to insufficient internal blood supply may be rescued, thus accelerating tumor cell

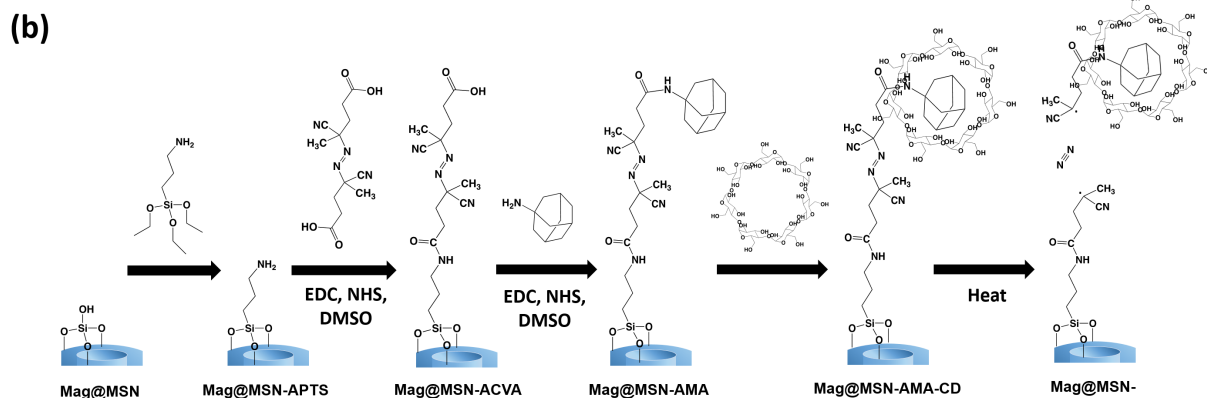
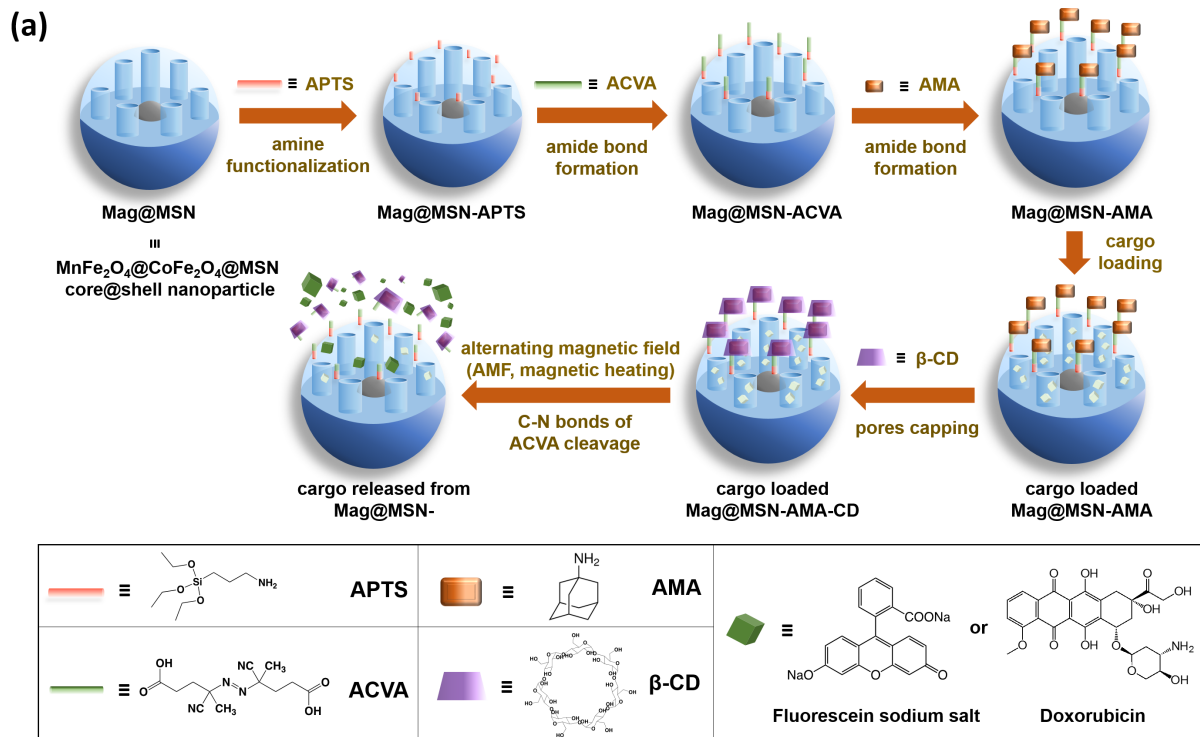
metastasis.³¹⁻³⁵ Therefore, it is critical to monitor the temperature while doing AMF actuation, in order to prevent the bulk solution from being overheated.

Only a limited amount of drugs can be carried on and released from the surface of a magnetic nanoparticle. To increase the amount of drugs that can be delivered, polymers,⁵⁴ dendrimers,^{55,56} and lipid bilayers,⁵⁷ have been attached to magnetic nanoparticles to enhance the payload of drugs. Mesoporous silica has aroused much attention during the past decade due to its high surface area and large pore volume for cargo loading and delivery.⁵⁸⁻⁶⁶ Additionally, the stability, high biocompatibility, high cellular internalization efficiency, and easy surface functionalization of mesoporous silica makes it a strong candidate for use as a coating of superparamagnetic nanoparticles in a drug delivery platform.^{17,18,67-70}

To achieve the controllable drug delivery under the magnetic field actuation, various thermal responsive gatekeepers have been developed during the past several years. Thomas *et al.* designed the first nanovalve for magnetic triggered release study based on MSNs, in which cucurbit[6]uril was used as a cap that released the cargo when the supramolecular interaction between the cap and the stalk on the surface of MSNs was decreased.⁴¹ Thermo-sensitive polymers such as azo-functionalized polyethylene glycol,¹⁷ poly(*N*-isopropylacrylamide),²¹ and poly[(ethylene glycol)-co-(L-lactide)]²³ polymer have also been used as the capping agents to prevent premature release. In this paper, we reported small molecular-based gatekeeper that is responsive to the heat generated by a superparamagnetic core in an AMF.

The nanoplatform consists of 4,4'-azobis(4-cyanovaleric acid) (ACVA), an aliphatic azo-containing compound which can be irreversibly cleaved by heat and ultrasound,^{43,71} that was

attached on the surface of core@shell nanoparticles consisting of a manganese and cobalt doped iron oxide magnetic nanoparticle cores and a mesoporous silica shell (Scheme 3.1). Adamantane molecules were conjugated to ACVA through an amide bond coupling reaction. After loading the cargo in the pores of core@shell nanoparticles, bulky β -cyclodextrin (β -CD) was used to bind with the adamantane forming a well-known supramolecular host-guest complex with a high association equilibrium constant ($5.2 \times 10^4 \text{ M}^{-1}$).^{7,14,72–79} The pores of core@shell nanoparticles were blocked by this bulky complex and the cargo inside was prevented from being released prematurely. We demonstrate that this small molecular-based gatekeeper can be triggered by magnetic heating with minimal bulk heating. In addition, we demonstrate that the exposure time to the AMF controlled the dosage of the released cargo. We quantify the cargo release efficiency while simultaneously monitoring the temperature of the bulk solution, and obtain both dosage and temporal controlled release with no dangerous bulk heating. This proof-of-concept of precision on command drug delivery establishes the opportunities to enhance the treatment efficacy, reduce the side effect of chemotherapy and at the same time avoid the risk of inducing tumor metastasis generated by hyperthermia.



Scheme 3.1. (a) Schematic illustration of the synthesis of azo snap-top core@shell mesoporous silica nanoparticles and triggered release under an alternating magnetic field. (b) Scheme of the conjugation and capping of APTS, ACVA, AMA, and β -CD on the surface of core@shell nanoparticles (EDC = 1-ethyl-3-(3-dimethylaminopropyl) carbodiimide; NHS = *N*-hydroxysuccinimide; DMSO = dimethyl sulfoxide). After the trigger with heat, the cleavage of C-N bonds of ACVA makes the bulky β -CD and AMA complexation leave from the surface, and the cargo could thus be released from Mag@MSN-.

3.2 Experimental Section

3.2.1 Materials

Iron(III) acetylacetonate ($\text{Fe}(\text{acac})_3$, 97%), Manganese(II) acetylacetonate ($\text{Mn}(\text{acac})_2$, 21%-23% Mn), cobalt(II) acetylacetonate ($\text{Co}(\text{acac})_2$, 97%), 1,2-dodecanediol (90%), oleic acid (90%), oleylamine (70%), benzyl ether (98%), hexane (98.5+%), chloroform (99.5+%), hexadecyltrimethylammonium bromide (CTAB, 99+%), tetraethyl orthosilicate (TEOS, 98%), (3-aminopropyl)triethoxysilane (APTS, 99%), 4,4'-azobis(4-cyanovaleric acid) (ACVA, 98+%) 1-adamantylamine (AMA, 97%), β -cyclodextrin (β -CD, 97+%), ammonium nitrate (NH_4NO_3 , 98+%), 1-Ethyl-3-(3-dimethylaminopropyl) carbodiimide (EDC, 98+%), *N*-hydroxysuccinimide (NHS, 98%), phosphate-buffered saline (PBS, 10X), bisBenzimide H 33342 trihydrochloride (Hoechst 33342, 98+%), and fluorescein sodium salt were purchased from Sigma-Aldrich. Doxorubicin hydrochloride (DOX-HCl) was purchased from Cayman Chemical. Dimethyl sulfoxide (DMSO, 99.9+%), sodium hydroxide (NaOH, 97+%), hydrochloric acid (HCl, 36.5%-38%, trace metal grade), and nitric acid (HNO_3 , 67%-70%, trace metal grade) were purchased from Fisher Scientific. Dulbecco's modified Eagle's medium (DMEM) with high glucose, fetal bovine serum (FBS), antibiotics (10,000 U/mL penicillin, 10,000 $\mu\text{g}/\text{mL}$ streptomycin, and 29.2 mg/mL L-glutamine), Dulbecco's phosphate-buffered saline (DPBS), and trypsin-ethylenediaminetetraacetic acid (trypsin-EDTA) (0.05 %) were purchased from Gibco. Cell counting kit-8 (CCK-8) was purchased from Dojindo Molecular Technologies, Inc. Paraformaldehyde solution (4 % in PBS) was purchased from USB Corporation. Ethanol (200

proof) was purchased from Decon Laboratories, Inc. All chemicals were used without further purification.

3.2.2 Characterization

The size and morphology of nanoparticles were investigated by transmission electron microscopy (TEM, Tecnai T12) with an operating voltage of 120 kV. $\text{MnFe}_2\text{O}_4@\text{CoFe}_2\text{O}_4$ or $\text{Mag}@MSN$ core@shell nanoparticles were dispersed in hexane or ethanol at a low concentration (0.2 mg/mL). The suspension (10 μL) of the nanoparticles was dropped onto the carbon-coated copper grid and dried at room temperature. The X-ray diffraction pattern of the powder was obtained by a PANalytical, X'Per PRO diffractometer with Cu K_α radiation ($\lambda = 1.5418 \text{ \AA}$); the operating voltage and current were 45 kV and 40 mA, respectively. The field-dependent magnetization of $\text{MnFe}_2\text{O}_4@\text{CoFe}_2\text{O}_4$ was measured using a superconducting quantum interference device (SQUID) Quantum Design MPMS7 magnetometer at 300 K. The iron/manganese/cobalt ratio of the $\text{MnFe}_2\text{O}_4@\text{CoFe}_2\text{O}_4$ nanoparticles was quantitatively determined by ICP-OES using a Shimadzu ICPE-9000 instrument. Typically, 2 mg of $\text{MnFe}_2\text{O}_4@\text{CoFe}_2\text{O}_4$ powder was dissolved in 0.5 mL of hydrochloric acid solution. The solution was diluted with 2 % HNO_3 for quantitative measurement. The calibration curves for iron, manganese, and cobalt were created from 0 ppm to 10 ppm. The surface area, pore volume, and pore size of $\text{Mag}@MSN$ core@shell nanoparticles were determined by N_2 adsorption-desorption isotherm measurements at 77 K (Autosorb-iQ, Quantachrome Instruments). $\text{Mag}@MSN$ core@shell was degassed at 110 $^\circ\text{C}$ for 12 h before the measurement. The surface area and pore size distribution of $\text{Mag}@MSN$ core@shell were determined by Brunauer-Emmett-Teller (BET)

and Barrett-Joyner-Halenda (BJH) methods. The dynamic light scattering (DLS) size and zeta potential values were determined by a laser particle analyzer LPA-3100 at room temperature. The functional groups on the surface of Mag@MSN core@shell were characterized by Fourier transform infrared spectroscopy (FTIR, JASCO FT/IR-420) spectrometer in the range of 4000–400 cm^{-1} . Thermogravimetric analysis (TGA) was performed on a Perkin-Elmer Pyris Diamond TG/DTA machine under air flow. About 10 mg of Mag@MSN core@shell were loaded in aluminum pans and the data were recorded from 50 °C to 550 °C at a scan rate of 10 °C/min. An empty aluminum pan was used as the reference. The loading capacities of fluorescein or DOX were determined by UV-Vis Spectroscopy (Cary 5000). The absorbance of the peaks at 477 nm (fluorescein) or 503 nm (DOX) was used for quantification, respectively. The release of fluorescein or DOX was measured by an Acton Spectra Pro 2300i CCD cooled with liquid nitrogen. Fluorescein or DOX were excited by a CUBE 445-40C laser (Coherent Inc.) at a wavelength of 448 nm and a power of 4 mW (fluorescein) or 2 mW (DOX).

3.2.3 Synthesis of magnetic $\text{MnFe}_2\text{O}_4@\text{CoFe}_2\text{O}_4$ nanoparticles

Synthesis of 6.3 nm MnFe_2O_4 nanoparticles: MnFe_2O_4 nanoparticles were synthesized following a previously reported method with a slight modification.^{37,38} Two mmol of $\text{Fe}(\text{acac})_3$, 1 mmol of $\text{Mn}(\text{acac})_2$, 10 mmol of 1,2-dodecanediol, 6 mmol of oleic acid, and 6 mmol of oleylamine were dissolved in 20 mL of benzyl ether in a three-neck flask. The reaction was heated to 200 °C under the flow of nitrogen with vigorously stirring and kept at that temperature for 1 h. The reaction mixture was then heated up and refluxed for 1 h (298 °C). Afterwards, the resulting solution containing MnFe_2O_4 nanoparticles was cooled to room temperature. The nanoparticles were

precipitated by adding 40 mL of ethanol and further separated by centrifugation (7830 rpm, 10 min). Finally, MnFe_2O_4 nanoparticles were dispersed in 10 mL of hexane with 50 μL of oleic acid and 50 μL of oleylamine.

Synthesis of 8.2 nm MnFe_2O_4 nanoparticles: The larger MnFe_2O_4 nanoparticles were synthesized by growing MnFe_2O_4 on the MnFe_2O_4 nanoparticles prepared previously. Generally, two mmol of $\text{Fe}(\text{acac})_3$, 1 mmol of $\text{Mn}(\text{acac})_2$, 10 mmol of 1,2-dodecanediol, 2 mmol of oleic acid, and 2 mmol of oleylamine were dissolved in 20 mL of benzyl ether in a 100 mL three-neck flask. The MnFe_2O_4 nanoparticles (90 mg) obtained previously in 10 mL of hexane were added to the reaction mixture. The reaction mixture was heated to 90 °C and kept at that temperature for 30 min to remove hexane. Then the reaction mixture was heated to 200 °C under the flow of nitrogen with vigorously stirring. After 1 h, the reaction mixture was heated to 298 °C and refluxed for 1 h. The nanoparticles were precipitated by adding 40 mL of ethanol and further separated by centrifugation. Finally, the MnFe_2O_4 nanoparticles were re-dispersed in 10 mL of hexane with 50 μL of oleic acid and 50 μL of oleylamine.

Synthesis of 10.1 nm $\text{MnFe}_2\text{O}_4@\text{CoFe}_2\text{O}_4$ nanoparticles: To coat CoFe_2O_4 on the surface of MnFe_2O_4 nanoparticles, two mmol of $\text{Fe}(\text{acac})_3$, 1 mmol of $\text{Co}(\text{acac})_2$, 10 mmol of 1,2-dodecanediol, 2 mmol of oleic acid, and 2 mmol of oleylamine were dissolved in 20 mL of benzyl ether in a 100 mL three-neck flask. MnFe_2O_4 (8.2 nm) nanoparticles (180 mg) obtained previously in 10 mL of hexane were added to the reaction mixture. The synthetic procedure and reaction temperature were the same as that of the 8.2 nm MnFe_2O_4 nanoparticles synthesis. Finally, $\text{MnFe}_2\text{O}_4@\text{CoFe}_2\text{O}_4$ nanoparticles (10.1 nm) were re-dispersed in 10 mL of hexane with 50 μL of

oleic acid and 50 μ L of oleylamine.

Synthesis of 11.4 nm MnFe₂O₄@CoFe₂O₄ nanoparticles: To coat CoFe₂O₄ on the surface of MnFe₂O₄@CoFe₂O₄ (10.1 nm) nanoparticles to obtain the larger nanoparticles, two mmol of Fe(acac)₃, 1 mmol of Co(acac)₂, 10 mmol of 1,2-dodecanediol, 2 mmol of oleic acid, and 2 mmol of oleylamine were dissolved in 20 mL of benzyl ether in a 100 mL three-neck flask. MnFe₂O₄@CoFe₂O₄ (10.1 nm) nanoparticles (270 mg) obtained previously in 10 mL of hexane were added to the reaction mixture. The synthetic procedure and reaction temperature were the same as that of 10.1 nm MnFe₂O₄@CoFe₂O₄ nanoparticle synthesis. Finally, MnFe₂O₄@CoFe₂O₄ nanoparticles (11.4 nm) were re-dispersed in 10 mL of hexane with 50 μ L of oleic acid and 50 μ L of oleylamine for further use.

3.2.4 Measurement of specific loss power

Measurement of the heat generation from 11.4 nm MnFe₂O₄@CoFe₂O₄ nanoparticles was performed using a magnetic hyperthermia system (MSI Automation, Inc.) The diameter of the five-turn copper coil was 50 mm. The alternating frequency, induction power, and magnetic field strength were 375 kHz, 5 kW, and 20 kAm⁻¹, respectively. The MnFe₂O₄@CoFe₂O₄ nanoparticles were dispersed in toluene in a 2 mL of glass sample vial and the concentrations were 2.5, 1, or 0.5 mg/mL. The temperature of the solution was recorded after the exposure to the AMF as a function of time. The specific loss power of MnFe₂O₄@CoFe₂O₄ was calculated using equation (1), where C is the volumetric heat capacity of solvent, V_s is the sample volume, m is the mass of MnFe₂O₄@CoFe₂O₄, and dT/dt is the initial slope of the time-dependent temperature increase curve.

$$\text{Specific loss power} = \frac{CV_s dT}{m dt} \quad (1)$$

3.2.5 Synthesis of APTS-functionalized MnFe₂O₄@CoFe₂O₄@mesoporous silica (Mag@MSNs-APTS) core@shell nanoparticles

MnFe₂O₄@CoFe₂O₄ nanoparticles (11.4 nm, 2.5 mg) were dispersed in 0.2 mL of chloroform. 2 mL of CTAB aqueous solution (40 mg of CTAB, 54 mM) was added to the MnFe₂O₄@CoFe₂O₄ colloidal solution, and the mixture was sonicated for 10 min with a fully sealed cover to generate oil-in-water emulsion. The emulsion was then sonicated for 1 h to evaporate chloroform. The clear well-dispersed MnFe₂O₄@CoFe₂O₄ colloidal aqueous solution (2 mL) was obtained and designated as MnFe₂O₄@CoFe₂O₄@CTAB. Meanwhile, 40 mg of CTAB was dissolved in 18 mL of water with 120 μL of NaOH solution (2 M) in a 100 mL flask. Then, the previous 2 mL of MnFe₂O₄@CoFe₂O₄@CTAB colloidal solution was added to the reaction solution with vigorously stirring, and the temperature of the solution was brought up to 70 °C. To coat mesoporous silica shell on the surface of MnFe₂O₄@CoFe₂O₄@CTAB, 200 μL of TEOS and 1.2 mL of ethyl acetate were added dropwise into the solution. After stirring for 2 h, 40 μL of APTS was added dropwise into the solution and stirred for another 2 h to generate amine functionalized MnFe₂O₄@CoFe₂O₄@MSNs (Mag@MSNs-APTS, Mag denotes magnetic). Afterwards, the solution was cooled to room temperature and Mag@MSNs-APTS was centrifuged and washed 3 times with ethanol. Subsequently, Mag@MSNs-APTS was dispersed in 20 mL of ethanol containing 120 mg of NH₄NO₃ and the reaction was stirred at 60 °C for 1 h to remove the surfactants. The surfactant removal procedures were repeated twice and Mag@MSNs-APTS was washed several times with D.I. water and ethanol to obtain the surfactant-free Mag@MSNs-APTS.

3.2.6 Synthesis of ACVA functionalized Mag@MSNs-APTS (Mag@MSNs-ACVA)

The conjugation of 4,4'-azobis(4-cyanovaleric acid) (ACVA) on the surface of Mag@MSNs-APTS was carried out by using an amide bond coupling reaction. At first, the carboxylic acid of ACVA (20 mg) was activated by 40 mg of EDC and 20 mg of NHS in 4 mL of DMSO. To crosslink the activated ACVA to the primary amine of APTS, after 30 min activation at room temperature, 20 mg of Mag@MSNs-APTS dispersed in 4 mL of DMSO were added dropwise to the activated ACVA in DMSO and stirred for 24 h. The ACVA functionalized Mag@MSNs-APTS (Mag@MSNs-ACVA) was washed, centrifuged, and re-suspended in DMSO 3 times to remove the excess ACVA, EDC, and NHS.

3.2.7 Synthesis of AMA functionalized Mag@MSNs-ACVA (Mag@MSNs-AMA)

The conjugation of 1-adamantylamine (AMA) on the surface of Mag@MSNs-ACVA was carried out through amide bond formation between the carboxylic acid group of ACVA and the primary amine of AMA. Typically, the carboxylic acid groups of Mag@MSNs-ACVA (20 mg) were activated by 40 mg of EDC and 20 mg of NHS in 4 mL of DMSO. To crosslink ACVA to AMA, after 30 min activation at room temperature, 20 mg of AMA dissolved in 4 mL of DMSO was added to the activated Mag@MSNs-ACVA in DMSO and stirred for 24 h. Finally, AMA functionalized Mag@MSNs-ACVA (Mag@MSNs-AMA) was washed, centrifuged, and re-suspended in DMSO 3 times to remove the excess AMA, EDC, and NHS.

3.2.8 Loading of fluorescein or DOX in Mag@MSNs-AMA and snap-top attachment (Mag@MSNs-AMA-CD)

The loading of fluorescein or DOX was carried out by using water as the solvent. In general, 1 mg of Mag@MSNs-AMA was dispersed in 1 mL of D.I. water with 3 mM fluorescein or 2.6

mM DOX. After stirring for 24 h, 16 mg of the β -CD capping agent was added to the solution to prevent fluorescein or DOX from being released. The sample was designated as Mag@MSNs-AMA-CD. After mixing for 48 h, the fluorescein or DOX-loaded Mag@MSNs-AMA-CD was centrifuged and washed with water 5 times (fluorescein) or with water 7 times followed by PBS 2 times (DOX) to remove the free fluorescein or DOX molecules. The final product was suspended in 2 mL of D.I. water for the water bath heating or magnetic heating triggered release experiments.

3.2.9 Triggered release of fluorescein from Mag@MSNs-AMA-CD by water bath heating

0.5 mg of fluorescein loaded Mag@MSNs-AMA-CD was dispersed in 1 mL of water in an Eppendorf tube. Water baths at 37, 60, or 80 °C were prepared. The samples were heated in the 37, 60, or 80 °C water baths for 10 min per heating cycle (heating on = 10 min). After each heating cycle, the solution was centrifuged and 20 μ L of supernatant was collected and diluted. The released fluorescein molecules were then monitored by fluorescence spectroscopy, followed by another heating cycle. The time period between each heating cycle was 10 min (heating off = 10 min). In total, 9 such heating/monitoring cycles were performed for the samples in both the 37 °C and the 60 °C water baths; 4 such heating/monitoring cycles were performed for the sample in the 80 °C water bath. For comparison, the supernatant of the sample in the air at room temperature (23 °C) was collected and the released fluorescein was monitored at the same time with the samples heated in water baths. The intensity of the fluorescein released from Mag@MSNs-AMA-CD was integrated from 510 nm to 520 nm.

3.2.10 Triggered release of fluorescein or DOX from Mag@MSNs-AMA-CD by single cycle of magnetic heating

0.5 mg of fluorescein or DOX-loaded Mag@MSNs-AMA-CD was dispersed in 1 mL of water in an Eppendorf tube. Before being triggered by magnetic heating, the fluorescein or DOX loaded nanoparticle solution at room temperature was centrifuged and 20 μ L of supernatant was collected every 20 min (fluorescein) or 30 min (DOX) and measured by fluorescence spectroscopy. After monitoring the release every 20 min over a period of 40 min (fluorescein) or every 30 min over a period of 60 min (DOX) at room temperature, the sample was exposed to an alternating magnetic field (AMF) in the center of a water-cooled five-turn copper coil (5 cm height and diameter) at a power of 5 kW and a frequency of 375 kHz for 1, 2, 3, 5, and 10 min, respectively, followed by monitoring the release of fluorescein or DOX. After that, several monitoring cycles were performed every 10 min (fluorescein), or every 30 min over a period of 180 min followed by every 2 h over a period of 6 h (DOX) until the release of fluorescein or DOX leveled off. The intensities of the fluorescein or DOX released from Mag@MSNs-AMA-CD was integrated from 510 nm to 520 nm or 580 nm to 605 nm, respectively.

3.2.11 Triggered release of fluorescein from Mag@MSNs-AMA-CD by sequential cycles of magnetic heating

0.5 mg of fluorescein loaded Mag@MSNs-AMA-CD was dispersed in 1 mL of water in an Eppendorf tube. Before being triggered by magnetic heating, the fluorescein loaded nanoparticle solution at room temperature was centrifuged and 20 μ L of supernatant was collected every 10 min and measured by fluorescence spectroscopy. After monitoring the release every 10 min over a period of 30 min at room temperature, the sample was exposed to an AMF in the center of a water-cooled five-turn copper coil (5 cm height and diameter) at a power of 5 kW and a frequency

of 375 kHz for 3 min, followed by monitoring the release of fluorescein. Several monitoring cycles were performed every 10 min until the release of fluorescein leveled off, followed by another AMF heating for 3 min. In total, 3 such heating/monitoring series were performed to achieve the maximum release of fluorescein. The intensity of the fluorescein released from Mag@MSNs-AMA-CD was integrated from 510 nm to 520 nm.

3.2.12 Zeta potential value measurement of Mag@MSNs-ACVA after bulk or magnetic heating

0.5 mg of Mag@MSNs-ACVA was dispersed in 1 mL of water in an Eppendorf tube. For bulk heating treatment, the Eppendorf tubes containing the samples were put in a hot water bath at 37, 60, or 80 °C for 10 min. Afterwards, the solution was centrifuged and the nanoparticles were washed and redispersed in D.I. water. For magnetic heating treatment, the Eppendorf tube containing the sample was exposed to an AMF at a power of 5 kW and a frequency of 375 kHz for 10 min. Similarly, after the treatment, the solution was centrifuged and the nanoparticles were washed and redispersed in D.I. water. The zeta potential values of the samples after bulk heating or magnetic heating treatment were measured.

3.2.13 Loading capacity analysis of fluorescein or DOX

After loaded with 3 mM fluorescein or 2.6 mM DOX and capped with β -CD, Mag@MSNs-AMA-CD were washed with water 5 times (fluorescein) or washed with water 7 times followed by PBS 2 times (DOX). The supernatants collected during each washing step were collected and their absorption spectra were measured by UV-Vis spectroscopy. To calculate the amount of fluorescein or DOX loaded in Mag@MSNs-AMA-CD, the amount of fluorescein or DOX removed during all the washing steps was subtracted from the total amount of fluorescein or DOX

in the initial loading solution. The loading capacities of fluorescein or DOX were calculated using the maximum absorbance at 491 nm (fluorescein) or 503 nm (DOX) and the following definition of loading capacity: (mass of loaded fluorescein or DOX / mass of particles) x 100%.

3.2.14 Release efficiency analysis of fluorescein or DOX

To determine the release efficiency of fluorescein, 0.5 mg of fluorescein or DOX-loaded Mag@MSNs-AMA-CD in 1 mL of water was put in a hot water bath at 90 °C. The fluorescein or DOX released from the nanoparticles was separated from the nanoparticles by centrifugation and recorded by spectrophotometry. The intensities of the fluorescein or DOX released from Mag@MSNs-AMA-CD were integrated from 510 nm to 520 nm or 580 nm to 605 nm, respectively. The fluorescence intensities corresponding to the fluorescein or DOX released after being heated at 90 °C for 50 min was set as the 100% release. The release efficiencies of fluorescein or DOX is defined as (mass of released cargo/mass of loaded cargo) x 100%.

3.2.15 Cell culture

Human pancreatic cancer cells (PANC-1) were cultured in T-75 flasks (Corning) with vented caps in a high glucose Dulbecco's modified Eagle's medium (DMEM) supplemented with 10 % fetal bovine serum (FBS), and 1 % antibiotics (100 U/mL penicillin and 100 µg/mL streptomycin) in a humidity-controlled incubator at 37 °C with 5 % CO₂. In all culture conditions, the PANC-1 culture media were daily changed and the cells were harvested by trypsinization with 0.05 % trypsin-ethylenediaminetetraacetic acid (EDTA) for passaging every 2-3 days.

3.2.16 *In vitro* cytotoxicity

The viabilities of PANC-1 after the treatment of Mag@MSNs-AMA-CD and DOX-loaded

Mag@MSNs-AMA-CD were examined by using a cell counting kit-8 (CCK-8) assay. The cells were seeded in 96-well plates at a density of 5×10^3 cells per well in 200 μL of Dulbecco's modified Eagle's medium (DMEM) supplemented with 10% FBS and 1% antibiotics in a humidity-controlled incubator at 37 °C for 24 h attachment. After the attachment, the medium was removed and the cells were incubated in 200 μL of fresh DMEM containing 0, 2, 5, 10, 15, 20, and 40 μg of Mag@MSNs-AMA-CD (*i.e.* 0, 10, 25, 50, 75, 100, and 200 $\mu\text{g}/\text{mL}$) for 20 or 70 h in an incubator at 37 °C. After incubation, the medium was removed and the treated cells were washed twice with DPBS. To measure the cell viability, 100 μL of DMEM and 10 μL of CCK-8 cellular cytotoxicity reagent were added to each well. Then, the plates were put in the incubator for 2 h at 37 °C. To measure the number of the viable cells in each condition, a plate reader (Tecan M1000) was used to measure the absorbance at 450 nm and 650 nm (as the reference). The DMEM medium (100 μL) mixed with CCK-8 reagent (10 μL) served as a background control.

3.2.17 *In vitro* drug delivery triggered by an AMF and cellular cytotoxicity

PANC-1 cells were seeded in 8-well chamber slides at a density of 2.5×10^4 cells per well in 500 μL of DMEM supplemented with 10% FBS and 1% antibiotics in a humidity-controlled incubator at 37 °C for 24 h attachment. After the attachment, the medium was removed and the cells were incubated in 300 μL of fresh DMEM containing 15 μg of DOX-loaded Mag@MSNs-AMA-CD (50 $\mu\text{g}/\text{mL}$) for 4 h in an incubator at 37 °C. The control groups including cells not treated by nanoparticles and those treated with Mag@MSNs-AMA-CD (50 $\mu\text{g}/\text{mL}$) without DOX were also investigated. After 4 h incubation, the medium was removed and the treated cells were washed twice with DPBS (500 $\mu\text{L} \times 2$).

The chamber slides containing the treated or untreated PANC-1 cells in 500 μL of medium were exposed to an AMF in the center of a water-cooled five-turn copper coil at a power of 5 kW and a frequency of 375 kHz for 2, 5, and 10 min, respectively. After the AMF treatment, the cells were further incubated in an incubator at 37 $^{\circ}\text{C}$ for 12 h. To measure the cell viability after the treatment, the medium was removed and 200 μL of DMEM and 20 μL of CCK-8 reagent were added to each well. Afterwards, the chamber slides were put in the incubator for 2 h at 37 $^{\circ}\text{C}$. Finally, 100 μL of the reaction solution was transferred to a 96-well plate and the viability was measured by a plate reader described above.

3.2.18 Fluorescence microscope images of PANC-1 cells after treatment

PANC-1 cells were seeded in 8-well chamber slides at a density of 2.5×10^4 cells per well in 500 μL of DMEM supplemented with 10% FBS and 1% antibiotics in a humidity-controlled incubator at 37 $^{\circ}\text{C}$ for 24 h attachment. After the attachment, the medium was removed and the cells were incubated in 300 μL of fresh DMEM containing 15 μg of DOX-loaded Mag@MSNs-AMA-CD (50 $\mu\text{g}/\text{mL}$) for 4 h in an incubator at 37 $^{\circ}\text{C}$ followed by washing with DPBS 2 times (500 $\mu\text{L} \times 2$). The control group including cells not treated by nanoparticles was also investigated. After the washing, the chamber slides containing the treated or untreated PANC-1 cells in 500 μL of medium were exposed to an AMF in the center of a water-cooled five-turn copper coil at a power of 5 kW and a frequency of 375 kHz for 10 min. After the AMF treatment, the cells were further incubated in an incubator at 37 $^{\circ}\text{C}$ for 12 h followed by washing with DPBS 3 times (500 $\mu\text{L} \times 3$) and fixed with 4 % paraformaldehyde in PBS for 20 min. Then, the fixed cells were washed with DPBS 3 times (500 $\mu\text{L} \times 3$) with slightly shake. Afterwards, the nuclei of the cells were

stained with Hoechst 33342 (500 μ L, 5 μ g/mL) for 20 min followed by washing with DPBS 5 times (500 μ L x 5). Finally, the stained cells covered by mounting medium cover glass before being visualized under a Zeiss fluorescence microscope.

3.3. Results and discussion

3.3.1 Synthesis and characterization of $\text{MnFe}_2\text{O}_4@\text{CoFe}_2\text{O}_4$ nanoparticles

To achieve superior magnetic heating efficacy, we synthesized $\text{MnFe}_2\text{O}_4@\text{CoFe}_2\text{O}_4$ nanoparticles with a magnetically soft MnFe_2O_4 core, and a magnetically hard CoFe_2O_4 shell using a seed-mediated method (Figure 3.1a).³⁹ First, 6.3 nm MnFe_2O_4 nanoparticles were synthesized by a thermal decomposition method.^{37,38,80} The larger MnFe_2O_4 nanoparticles (8.2 nm) were then obtained by using the synthesized 6.3 nm MnFe_2O_4 nanoparticles as the seeds. Next, the CoFe_2O_4 shell layer was grown on the surface of the synthesized 8.2 nm MnFe_2O_4 nanoparticles to form 10.1 or 11.4 nm $\text{MnFe}_2\text{O}_4@\text{CoFe}_2\text{O}_4$ nanoparticles (Figure 3.1bc). Both the MnFe_2O_4 (6.3 and 8.2 nm) and the $\text{MnFe}_2\text{O}_4@\text{CoFe}_2\text{O}_4$ (10.1 and 11.4 nm) nanoparticles have uniform size distributions as measured by transmission electron microscopy (TEM) (Figure 3.1bc and Figure 3.2ab). From the corresponding diffraction peaks in high angle X-ray diffraction patterns (Figure 3.3), the 11.4 nm core@shell $\text{MnFe}_2\text{O}_4@\text{CoFe}_2\text{O}_4$ nanoparticles possess the typical spinel structure.⁸¹

To quantify field dependent magnetization of $\text{MnFe}_2\text{O}_4@\text{CoFe}_2\text{O}_4$ at 300 K, a superconducting quantum interference device (SQUID) was used. The saturated magnetization of 11.4 nm $\text{MnFe}_2\text{O}_4@\text{CoFe}_2\text{O}_4$ is 105 emu/g (Figure 3.2c), higher than that of Fe_3O_4 nanoparticles (80 emu/g).⁸² The higher magnetization of the $\text{MnFe}_2\text{O}_4@\text{CoFe}_2\text{O}_4$ produces a greater magnetic heating efficiency compared with Fe_3O_4 under an AMF (vide infra). The tiny hysteresis loop (Figure 3.2c) shows almost no coercive force which validates the superparamagnetic property of $\text{MnFe}_2\text{O}_4@\text{CoFe}_2\text{O}_4$ nanoparticles.

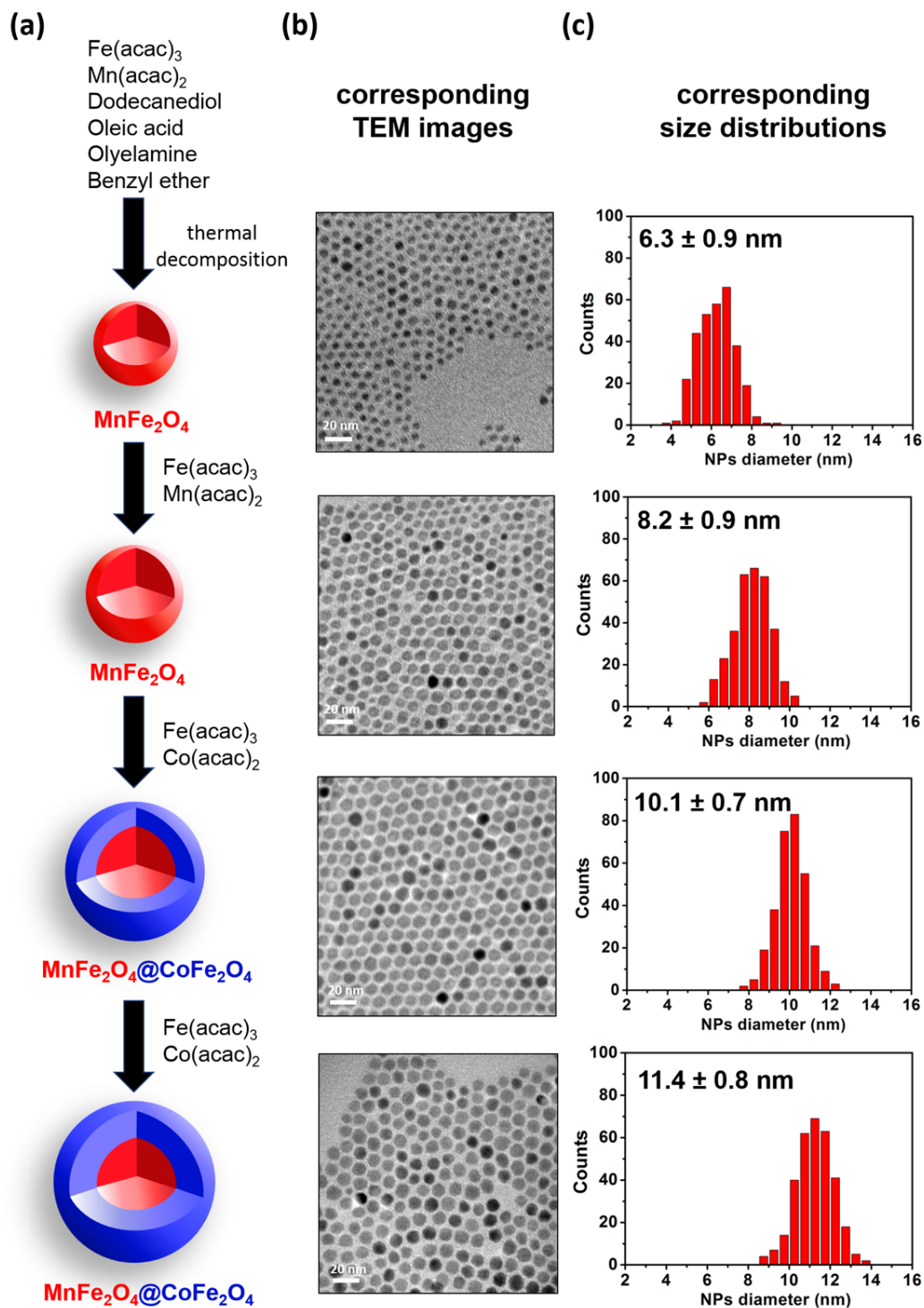


Figure 3.1. (a) Schematic illustration of the synthesis of MnFe₂O₄@CoFe₂O₄ nanoparticles by a seed-mediated thermal decomposition method. (b) Corresponding TEM images and (b) diameter distributions of MnFe₂O₄ and MnFe₂O₄@CoFe₂O₄ nanoparticles after each step.

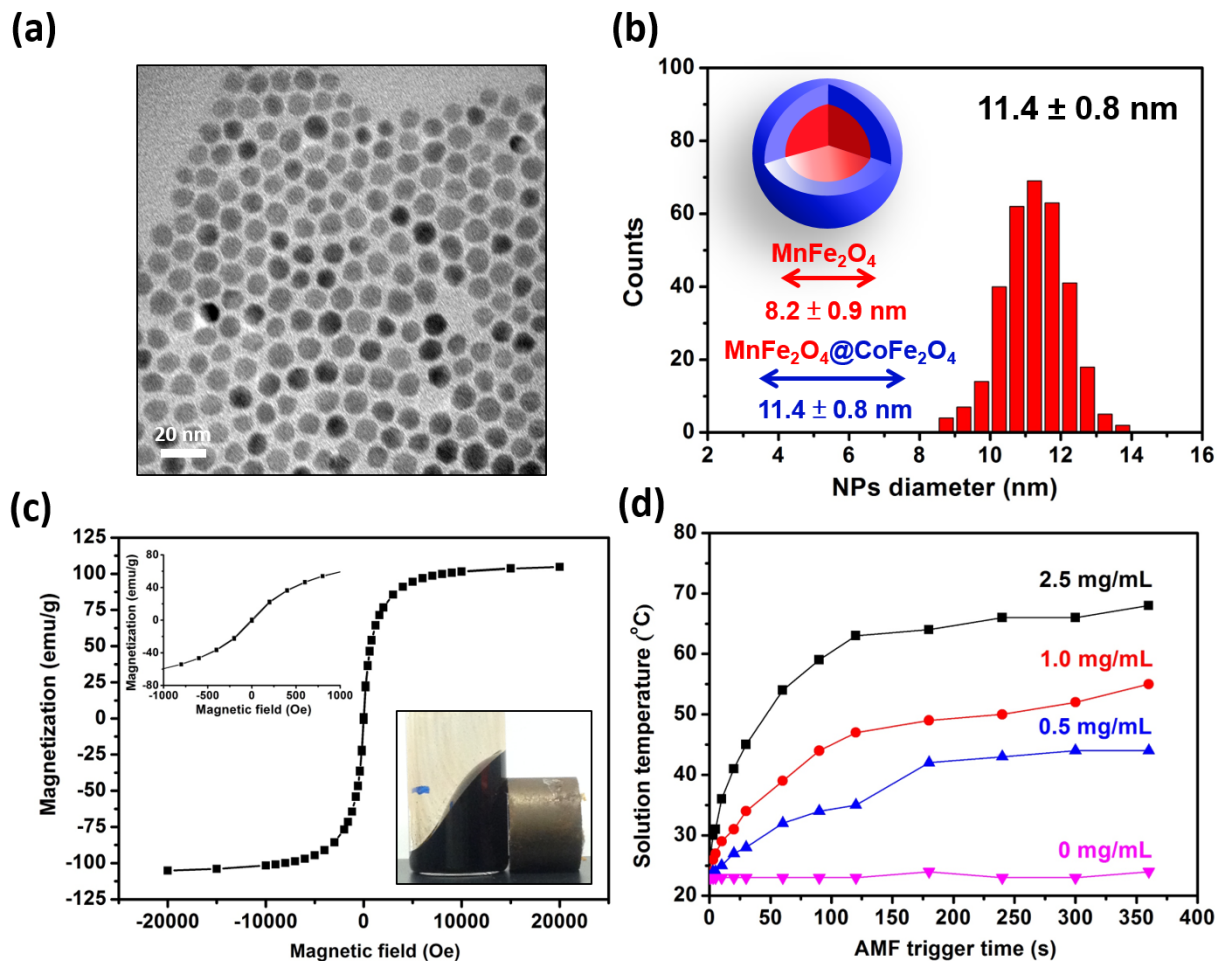


Figure 3.2. (a) TEM image and (b) size distribution of 11.4 nm $\text{MnFe}_2\text{O}_4@\text{CoFe}_2\text{O}_4$ nanoparticles. Inset shows the schematic illustration of magnetic core@shell $\text{MnFe}_2\text{O}_4@\text{CoFe}_2\text{O}_4$ structure. (c) Field dependent magnetization curve of $\text{MnFe}_2\text{O}_4@\text{CoFe}_2\text{O}_4$ nanoparticles at 300 K. Inset shows small scale of field dependent magnetization curves and $\text{MnFe}_2\text{O}_4@\text{CoFe}_2\text{O}_4$ nanoparticles in hexane were attracted by a magnet. (d) Time- and concentration-dependent temperature increase profiles of toluene solution containing $\text{MnFe}_2\text{O}_4@\text{CoFe}_2\text{O}_4$ nanoparticles triggered by an AMF.

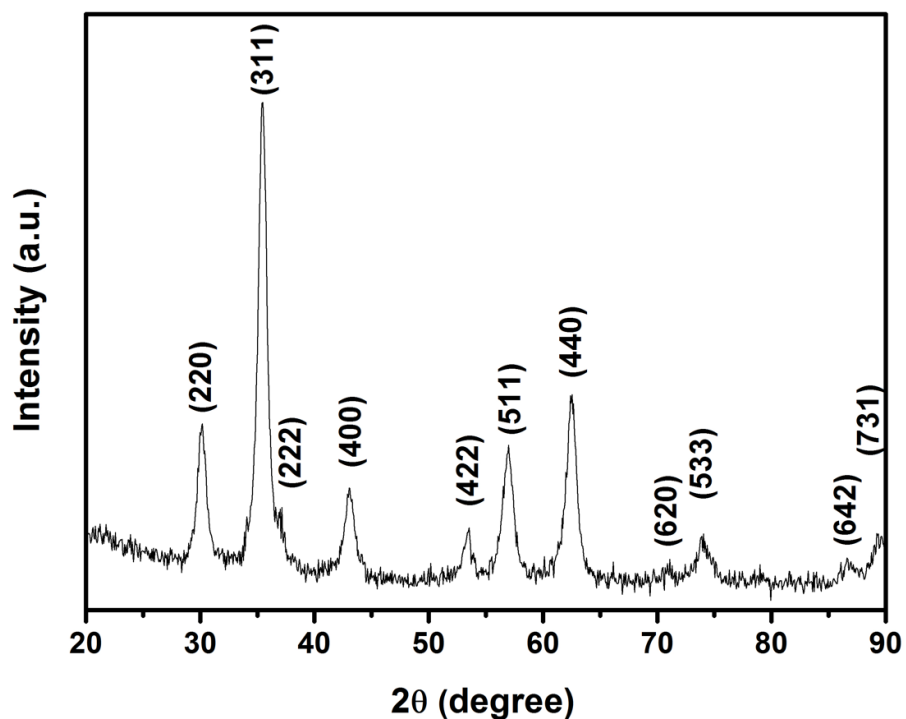


Figure 3.3. High angle X-ray diffraction pattern of $\text{MnFe}_2\text{O}_4@\text{CoFe}_2\text{O}_4$ nanoparticles.

To further confirm the nanoparticle identity, both Fourier transform-infrared (FT-IR) spectroscopy and thermogravimetric analysis (TGA) were conducted. In the FT-IR spectrum (Figure 3.4a), the three peaks at 2851, 2921, and 2955 cm^{-1} arise from the CH_2 symmetric and antisymmetric stretches in oleic acid and oleylamine and confirm that the surface of $\text{MnFe}_2\text{O}_4@\text{CoFe}_2\text{O}_4$ nanoparticles is covered with oleic acid and oleylamine. The TGA results show that the amount of oleic acid and oleylamine on the surface of $\text{MnFe}_2\text{O}_4@\text{CoFe}_2\text{O}_4$ nanoparticles is 13 wt% (Figure 3.4b). Due to the abundant capping agents with long hydrocarbon chains, the $\text{MnFe}_2\text{O}_4@\text{CoFe}_2\text{O}_4$ nanoparticles can be well suspended in hexane (Figure 3.2c).

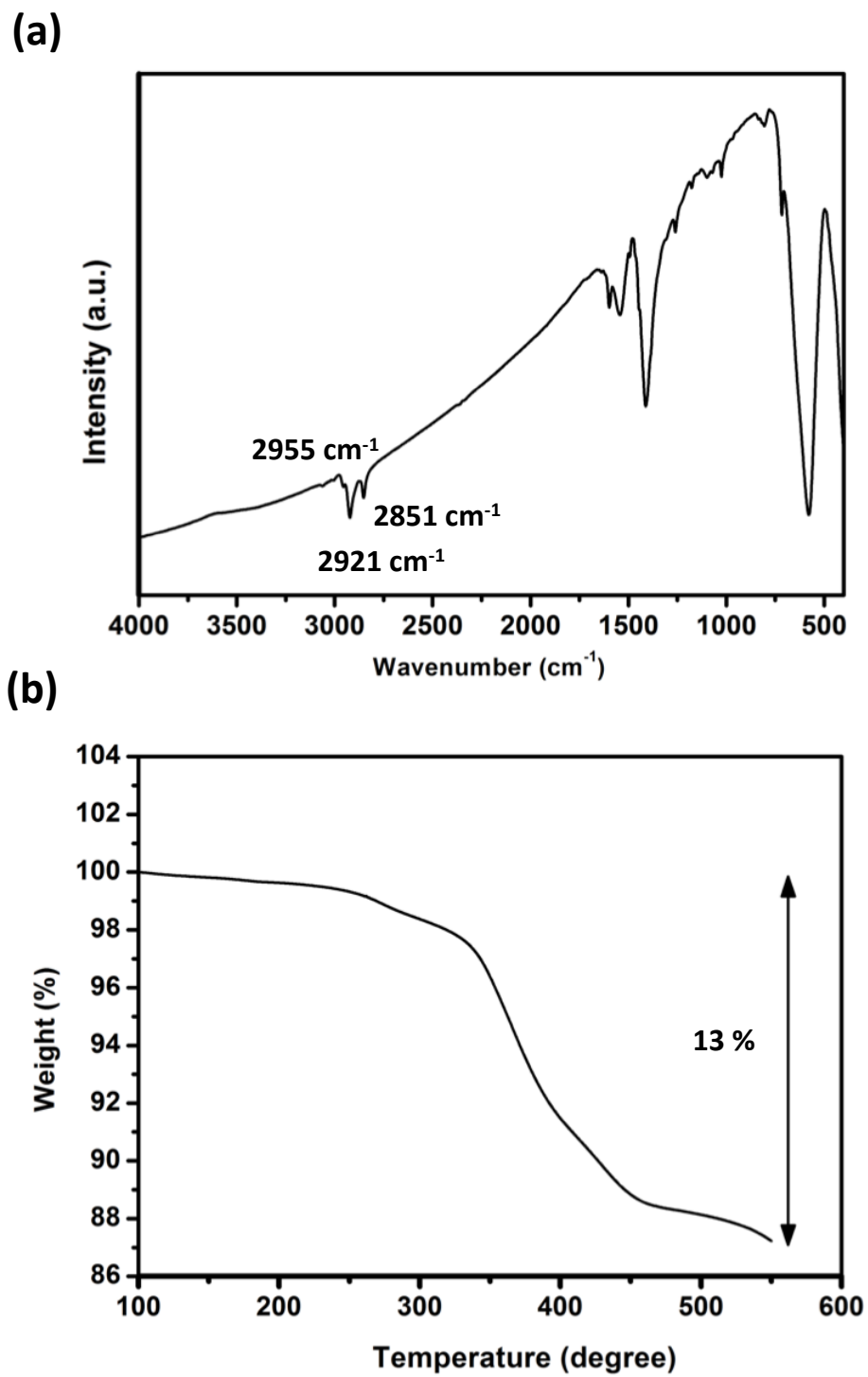


Figure 3.4. (a) Fourier-transform Infrared (FTIR) spectrum and (b) thermogravimetric analysis (TGA) of $\text{MnFe}_2\text{O}_4@\text{CoFe}_2\text{O}_4$ nanoparticles.

To investigate the heat generation efficiency of 11.4 nm MnFe₂O₄@CoFe₂O₄ nanoparticles, the specific loss power (SLP) was quantified. The SLP of MnFe₂O₄@CoFe₂O₄ was calculated using equation (1), where C is the volumetric heat capacity of solvent, V_s is the sample volume, m is the mass of MnFe₂O₄@CoFe₂O₄, and dT/dt is the initial slope of the time-dependent temperature increase curve.

$$\text{Specific loss power} = \frac{CV_s}{m} \frac{dT}{dt} \quad (1)$$

MnFe₂O₄@CoFe₂O₄ nanoparticles were dispersed in toluene and an AMF (375 kHz, 5kW) was applied for heat generation. Time- and concentration-dependent temperature increase profiles (Figure 3.2d) show that the solution temperature abruptly increased upon the application of AMF trigger. The temperature of the toluene solution containing nanoparticles finally achieved 44, 55, and 67 °C after 6 min magnetic actuation at the concentrations of MnFe₂O₄@CoFe₂O₄ are 0.5, 1, and 2.5 mg/mL, respectively. The SLP of the MnFe₂O₄@CoFe₂O₄ nanoparticles was calculated to be 1510.8 W/g (equation 2), 5 times higher than that of 20 nm Fe₃O₄ nanoparticles (302.2 W/g) (equation 3).⁸³ This superior heating performance of MnFe₂O₄@CoFe₂O₄ nanoparticles under the AMF shows its potential of serving as an efficacious heat source for thermal-triggered drug release.

For MnFe₂O₄@CoFe₂O₄:

$$\begin{aligned} \text{Specific loss power} &= \frac{CV_s}{m} \frac{dT}{dt} \quad (1) \\ &= \frac{1.5108 (J mL^{-1} K^{-1}) \times 1 (mL)}{1 \times 10^{-3} (g)} \times \frac{1 (K)}{1 (s)} \\ &= 1510.8 Wg^{-1}_{(Fe+Mn+Co)} \quad (2) \end{aligned}$$

For Fe₃O₄:

$$\begin{aligned} \text{Specific loss power} &= \frac{CV_s}{m} \frac{dT}{dt} \quad (1) \\ &= \frac{1.5108 (J mL^{-1} K^{-1}) \times 1 (mL)}{1 \times 10^{-3} (g)} \times \frac{1 (K)}{5 (s)} \\ &= 302.2 Wg^{-1}_{(Fe)} \quad (3) \end{aligned}$$

3.3.2 Synthesis and characterization of Mag@MSNs-APTS core@shell nanoparticles

To construct nanoparticles with cargo-carrying capability, we synthesized nanoparticles with a mesoporous silica shell around the superparamagnetic core. The coating was achieved by hydrolysis and condensation of tetraethyl orthosilicate (TEOS) in the presence of hexadecyltrimethylammonium bromide (CTAB) surfactant templates in basic solution.⁸⁴ The resulting nanoparticles are designated as Mag@MSNs (Mag denotes magnetic MnFe₂O₄@CoFe₂O₄ and MSNs denotes mesoporous silica nanoparticles).

In order to attach thermal sensitive caps, the surface of the mesoporous silica shell was functionalized with amine groups by hydrolysis and condensation reactions of 3-(aminopropyl)triethoxysilane (APTS). The modified nanoparticles are designated as

Mag@MSNs-APTS. By using TEM, the average diameter of Mag@MSNs-APTS core@shell nanoparticles is 55 nm and their shell thickness is 22 nm with obvious mesoporous structure (Figure 3.5a and Figure 3.6). From the dynamic light scattering (DLS) diameter distribution (Figure 3.7), the average diameter of Mag@MSNs-APTS is 105.6 nm at room temperature, showing that the nanoparticles are well dispersed in water.

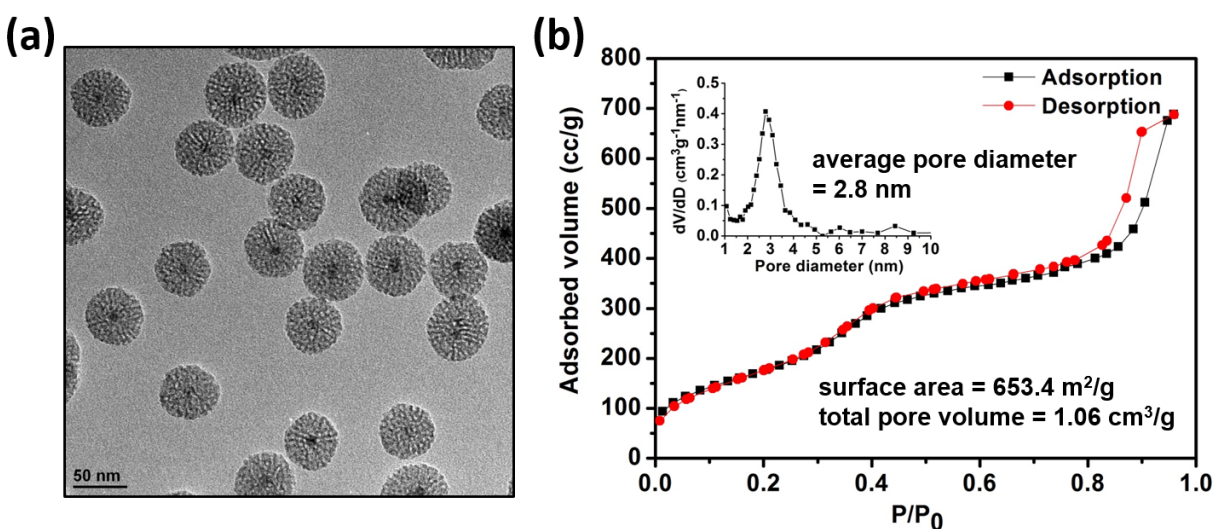


Figure 3.5. (a) TEM image of APTS functionalized core@shell nanoparticles (Mag@MSNs-APTS). (b) Nitrogen adsorption/desorption isotherms of Mag@MSNs-APTS at 77 K. The BET surface area and pore volume are 653.4 m²/g, and 1.06 cm³/g, respectively. Inset shows the pore diameter distribution of Mag@MSNs-APTS. The average pore diameter is 2.8 nm.

N₂ adsorption-desorption isotherms and pore diameter distribution were used to further characterize the pores of Mag@MSNs-APTS core@shell nanoparticles. The Brunauer-Emmett-Teller (BET) surface area, Barrett-Joyner-Halenda (BJH) average pore diameter, and total pore volume of Mag@MSNs-APTS are 653.4 m²/g, 2.8 nm, and 1.06 cm³/g, respectively (Figure 3.5b). In addition, the high surface area and pore volume of Mag@MSNs-APTS – the desired properties

of MSNs – suggest that cargos such as small molecules can be loaded inside the pores of Mag@MSNs-APTS (vide infra), allowing those cargos to be efficiently carried and delivered by the nanoparticles.

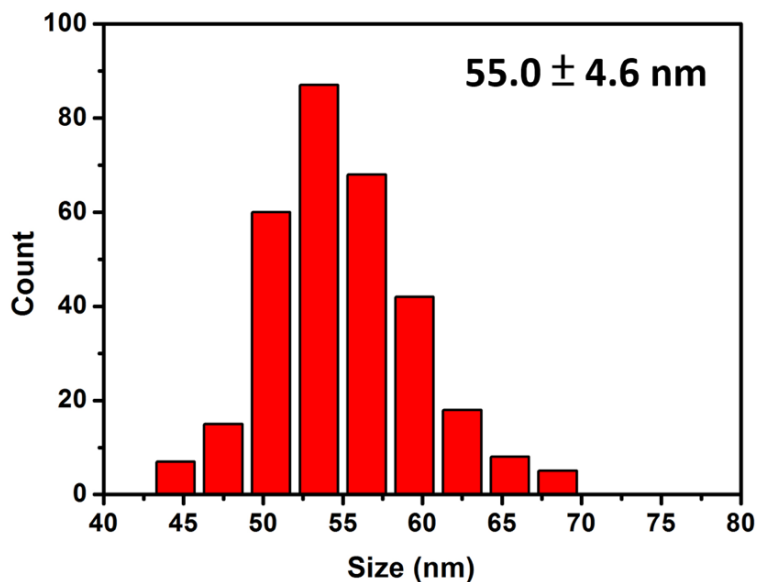


Figure 3.6. Size distribution of 55.0 nm Mag@MSNs-APTS core@shell nanoparticles.

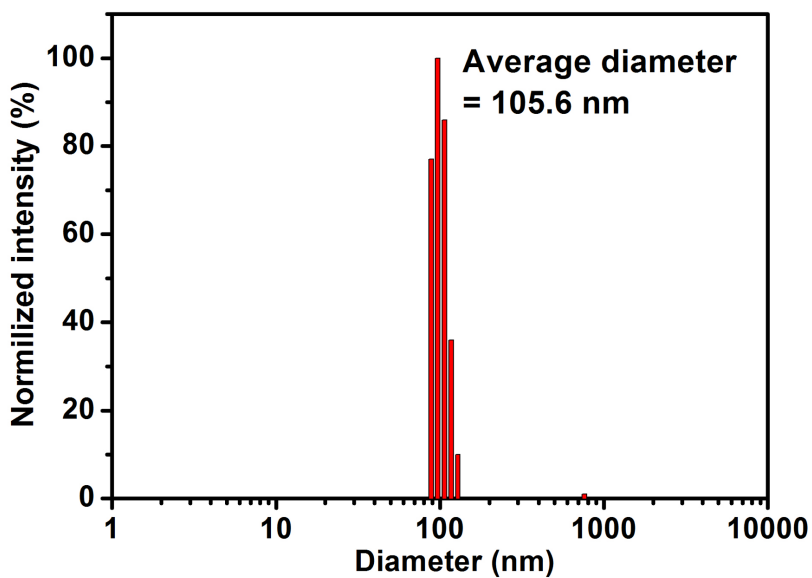


Figure 3.7. Dynamic light scattering diameter distribution of Mag@MSNs-APTS in deionized H₂O at room temperature.

3.3.3 Synthesis and characterization of Mag@MSNs-APTS, Mag@MSNs-ACVA and Mag@MSNs-AMA core@shell nanoparticles

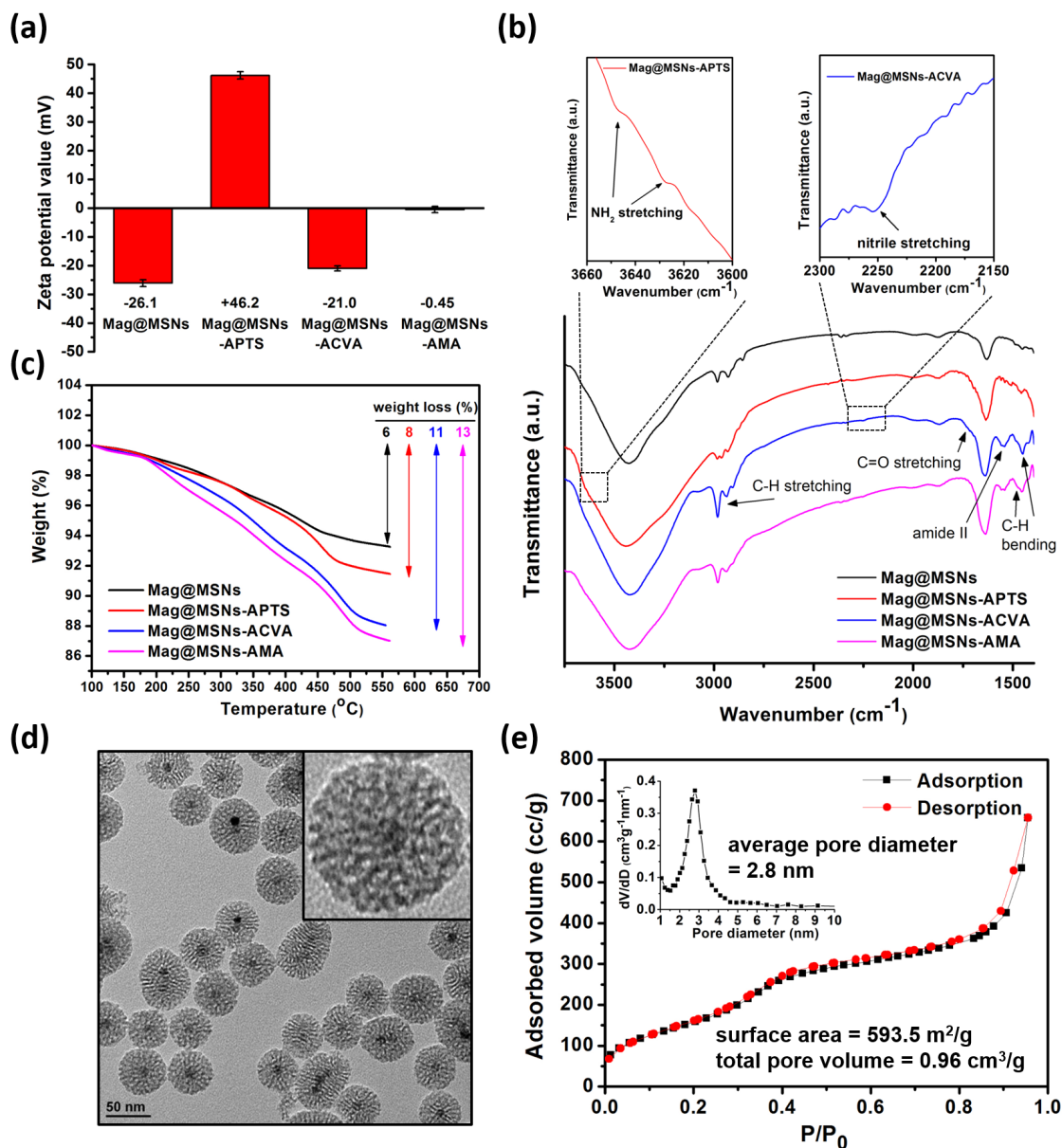


Figure 3.8. (a) Zeta potential values, (b) Fourier transform infrared spectroscopy (FT-IR), and (c) thermogravimetric analysis (TGA) of Mag@MSNs, Mag@MSNs-APTS, Mag@MSNs-ACVA, and Mag@MSNs-AMA, respectively. (d) TEM image of Mag@MSNs-AMA. Inset shows the enlarged Mag@MSNs-AMA. (e) N₂ adsorption/desorption isotherms of Mag@MSNs-AMA at 77 K. Inset shows the pore diameter distribution of Mag@MSNs-AMA. The BET surface area, pore volume, and average pore diameter are 593.5 m^2/g , 0.96 cm^3/g , and 2.8 nm, respectively.

Particles for magnetically stimulated release need not only cargo-carrying capability but also a stimulus-responsive capping mechanism. To introduce the latter functionality to the nanoparticles, the surface of the core@shell nanoparticles were conjugated with a thermolabile gatekeeper 4,4'-azobis(4-cyanovaleric acid) (ACVA).^{43,71} ACVA was chemically bonded to Mag@MSNs-APTS using 1-ethyl-3-(3-diethylaminopropyl) carbodiimide (EDC) and *N*-hydroxysuccinimide (NHS) coupling agents.⁸⁵ The carboxylic acid on ACVA formed an amide bond with the primary amine of APTS, and the resulting particles were designated as Mag@MSNs-ACVA (Scheme 3.1b). Subsequently, 1-adamantylamine (AMA) was conjugated on the surface of the nanoparticles through the same standard crosslinking method, with the terminal carboxylic acid of ACVA forming another amide bond with the primary amine of AMA. The nanoparticles modified with AMA were designated as Mag@MSNs-AMA (Scheme 3.1b).

The successful attachment of APTS, ACVA, and AMA on the surface of Mag@MSNs was confirmed by zeta potential measurements, FT-IR, and TGA after each step. The zeta potential of Mag@MSNs, Mag@MSNs-APTS, Mag@MSNs-ACVA, and Mag@MSNs-AMA were measured in deionized water at room temperature (Figure 3.8a). The zeta potential value of Mag@MSNs-APTS was +46.2 mV, much more positive than that of Mag@MSNs (-26.1 mV), showing abundant primary amines on the surface of Mag@MSNs-APTS. Mag@MSNs-ACVA has a negative zeta potential value of -21.0 mV. This significant decrease in the zeta potential value indicates that ACVA molecules with carboxylates on both ends were successfully attached to the surface of Mag@MSNs-APTS, with one end stretching out from the surface of Mag@MSNs-ACVA available for further AMA conjugation. Mag@MSNs-AMA with the nearly neutral zeta potential

value of -0.45 mV confirms the conjugation of the amine on AMA to the free carboxylate on the surface of Mag@MSNs-ACVA, leaving the uncharged functional group on AMA stretching out from the surface of the particles (Scheme 3.1b).

FT-IR spectroscopy was used to characterize surface functional groups after each conjugation step (Figure 3.8b). The appearance of two bands in the IR spectrum of Mag@MSNs-APTS due to N-H stretching vibrations at $\nu = 3628 \text{ cm}^{-1}$ and $\nu = 3648 \text{ cm}^{-1}$ shows the presence of primary amines attached to the surface of Mag@MSNs-APTS. The successful conjugation of ACVA to the surface of Mag@MSNs-APTS through secondary amide bond formation was confirmed by a new characteristic amide absorption (amide II) at $\nu = 1550 \text{ cm}^{-1}$. Additionally, a nitrile absorption appears at $\nu = 2253 \text{ cm}^{-1}$ (nitrile stretching) from ACVA also supports the successful conjugation of ACVA on the Mag@MSNs-APTS. This is also supported by newly emerging absorptions at $\nu = 1719 \text{ cm}^{-1}$ (C=O stretching), $\nu = 1451 \text{ cm}^{-1}$ (C-H bending), and three absorption peaks at $\nu = 2904 \text{ cm}^{-1}$, $\nu = 2934 \text{ cm}^{-1}$, and $\nu = 2981 \text{ cm}^{-1}$ (C-H stretching) from ACVA. Finally, the conjugation of AMA on the surface of Mag@MSNs-ACVA is confirmed by the appearance of the absorption at $\nu = 1474 \text{ cm}^{-1}$ (C-H bending) from AMA.

TGA was used to determine the weight of organic moieties on the particles (Figure 3.8c). The weight loss of Mag@MSNs, Mag@MSNs-APTS, Mag@MSNs-ACVA, and Mag@MSNs-AMA after heating to 550 °C in air were 6 %, 8 %, 11 %, and 13 %, respectively. The increase in weight loss after each conjugation indicates that the weight of APTS, ACVA, and AMA modified on the surface of core@shell nanoparticles were 2 %, 3 %, and 2 %, respectively. The results from zeta potential measurements, FT-IR, and TGA show that APTS, ACVA, and AMA were successfully

and sequentially attached on the surface of Mag@MSNs.

To confirm that the morphology and mesoporous structure of core@shell nanoparticles remains intact after surface modification, we conducted TEM and N₂ adsorption-desorption isotherms analysis of the core@shell nanoparticles after ACVA and AMA conjugation. By TEM, Mag@MSNs-AMA (Figure 3.8d) is 55 nm in size with obvious mesoporous structure, very similar to that of Mag@MSNs-APTS (Figure 3.5a), indicating that the particles were not damaged after the surface functionalization. The BET surface area, total pore volume, and BJH average pore diameter of Mag@MSNs-AMA are 593.5 m²/g, 0.96 cm³/g, and 2.8 nm, respectively (Figure 3.8e). Similar to Mag@MSNs-APTS (Figure 2b), Mag@MSNs-AMA preserves the characteristics of mesoporous structure – high surface area and large pore volume – enabling efficient loading and delivery of cargos. AMA and thermolabile ACVA are mainly attached to the outer surface rather than to the inner pore wall of the core@shell nanoparticles, as evidenced by the unchanged average pore diameter of Mag@MSNs-AMA and Mag@MSNs-APTS. Those thermal sensitive gatekeepers selectively bonded on the outer surface of the core@shell nanoparticles can effectively bind to β -cyclodextrin (β -CD) that blocks the pore openings to prevent cargos from leakage, and act as a thermal-sensitive switch to release the cargos on-demand.

3.3.4 Thermal responsiveness of the gatekeeper and bulk heating-triggered cargo release

To investigate the thermal responsiveness of the gatekeeper, we first demonstrated the cleavage of the gatekeeper triggered by increasing the temperature of the surrounding water. Sample tubes containing Mag@MSNs-ACVA dispersed in deionized water (0.5 mg/mL) were placed for 10 min in the hot water baths heated by a hot plate set at 37 °C, 60 °C, and 80 °C (called bulk heating)

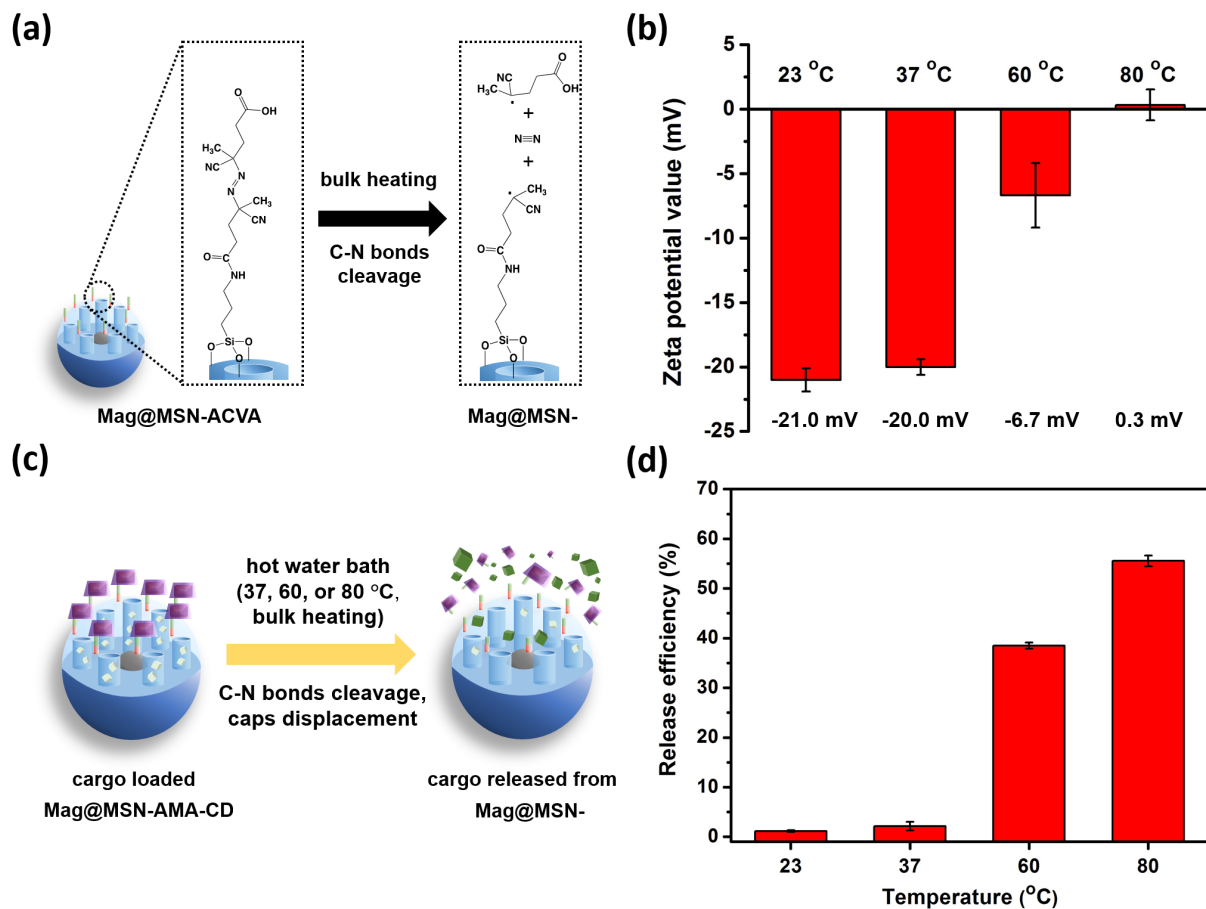


Figure 3.9. (a) The cleavage of C-N bonds caused by bulk heating for 10 min. (b) Zeta potential values of Mag@MSNs-ACVA after 10 min of bulk heating in D.I. water. The concentration of Mag@MSNs-ACVA in D.I. water is 0.5 mg/mL. (c) The release of fluorescein from Mag@MSN- caused by bulk heating trigger in water bath at 37 °C, 60 °C, or 80 °C. The sample stayed at room temperature (23 °C) was also recorded as a control. (d) Release efficiency of fluorescein from Mag@MSNs- after the bulk heating at 23 °C, 37 °C, 60 °C, or 80 °C trigger for 10 min (N = 3).

(Figure 3.9c). The cleavage of C-N bonds of ACVA was confirmed by the zeta potential measurement. After Mag@MSNs-ACVA was heated at 37 °C, 60 °C, and 80 °C for 10 min, the zeta potential values were -20.0 mV, -6.7 mV, and 0.3 mV, respectively (Figure 3.9ab). The sample heated at 37 °C shows very similar zeta potential value compared to that of the control without

heating (-21.0 mV), showing that the gatekeepers were stable at physiological temperature and the C-N bonds were intact. However, when the temperature increased, the C-N bonds were cleaved, producing fragments of 4-cyanopentanoic acid and nitrogen (Figure 3.9a). The removal of the carboxylate group after cleavage explains why the zeta potential becomes increasing after heating.

The bulk heating-triggered cargo release was studied using fluorescein as a model molecule due to its stability and size similar to that of many anticancer drugs (1.5 nm), *e.g.*, doxorubicin or paclitaxel. Fluorescein molecules were loaded in Mag@MSNs-AMA by soaking the particles in 3 mM of the fluorescein solution for 24 h. To trap fluorescein in the pores of core@shell nanoparticles, the pores were capped by bulky β -CD, which strongly binds to AMA on the surface of the nanoparticles and forms a non-covalent supramolecular bond with adamantane.^{72,73,86} The particles capped by β -CD were designated as Mag@MSNs-AMA-CD. Fluorescein loaded Mag@MSNs-AMA-CD were washed thoroughly with deionized water to remove the untrapped fluorescein molecules.

To trigger the release of fluorescein, the bulk heating was performed in hot water baths at various temperatures according to the following procedure (Figure 3.9c). Sample tubes containing fluorescein loaded Mag@MSNs-AMA-CD dispersed in deionized water (0.5 mg/mL) were placed in water baths set at 37 °C, 60 °C, and 80 °C for 10 min. To monitor the fluorescein released from Mag@MSNs-AMA-CD, the samples after heating were spun down and aliquots of the supernatants were collected for fluorescence measurements. An unheated sample at room temperature (23 °C) served as the control. The release efficiency is defined as (mass of released fluorescein/mass of loaded fluorescein) x 100 %. Only slight release (less than 3%) of fluorescein

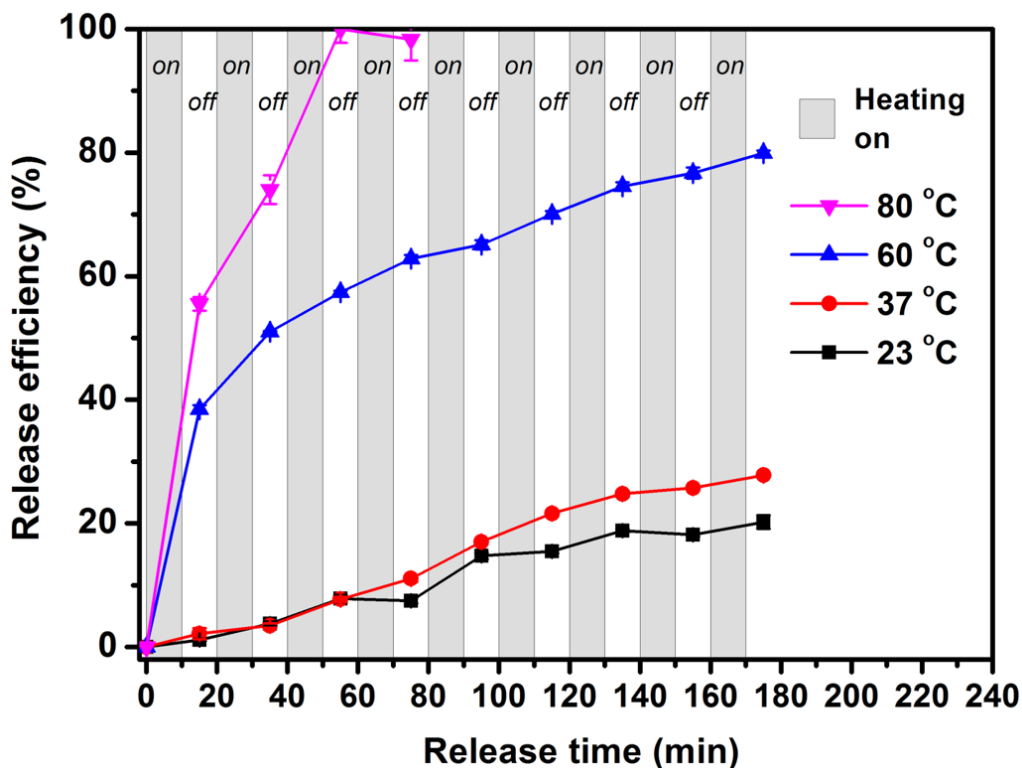


Figure 3.10. Time dependent release efficiency of fluorescein from Mag@MSN- caused by bulk heating trigger in water bath at 37 °C, 60 °C, and 80 °C. The sample stayed at room temperature (23 °C) was also recorded as a control.

from Mag@MSNs-AMA-CD at 23 °C and 37 °C after 10 min heating was observed (Figure 3.9d), indicating that the CD cap blocked the pore opening of the particles tightly and minimized premature leakage. The release efficiency of fluorescein strongly increased to 39 % upon heating at 60 °C for 10 min. When the samples were heated in a hot water bath at a higher temperature (80 °C), more than half (55 % release efficiency) of the fluorescein was released after 10 min heating. In addition, after 3 cycles of 10 min heating at 80 °C, almost all fluorescein (near 100 % release efficiency) was released after 3 cycles of 10 min heating (Figure 3.10). To determine the long-term release profile of fluorescein, the samples heated at 37 °C, 60 °C, and 80 °C were performed with

9, 9, and 4 such heating/monitoring cycles. The time period between each heating cycle is also 10 min. The cumulative release of fluorescein gradually increased with heating time and finally reached 78 % after 9 cycles of 10 min heating at 60 °C (Figure 3.10). On the contrary, the release efficiency of fluorescein after 9 cycles of 10 min heating at 37 °C is only 24 %, which is much lower than that from 60 °C heating, and is close to the control group at 23 °C (19 %). This implies that the CD cap was constructed successfully on the surface of the Mag@MSNs so that little premature leakage was observed either at room temperature or physiological temperature. Most importantly, the cargo release amount and cargo releasing rate can be controlled simply by tuning the temperature of the water bath.

3.3.5 Alternating magnetic field-triggered cargo release

Two types of release studies were conducted by using another heat source – an alternating magnetic field (AMF) – which can induce localized heating (here called magnetic heating): (a) a single exposure to AMF for different lengths of time, and (b) multiple sequential exposures each for the same length of time. Fluorescein loaded Mag@MSNs-AMA-CD particles were dispersed in deionized water (0.5 mg/mL) at room temperature. To confirm the tightness of the gatekeeper, release of fluorescein before triggering with magnetic heating was monitored by spinning down the nanoparticles and collecting aliquots of the supernatants for fluorescence measurements. After monitoring the release every 20 min over a period of 40 min at room temperature, the sample was placed in a water-cooled five-turn copper coil generating an AMF at a power of 5 kW and a frequency of 375 kHz (Figure 3.11a). Exposure times were 1, 2, 3, 5, or 10 min, followed again by monitoring the release. To have enough time for dye to diffuse out from the pores, monitoring

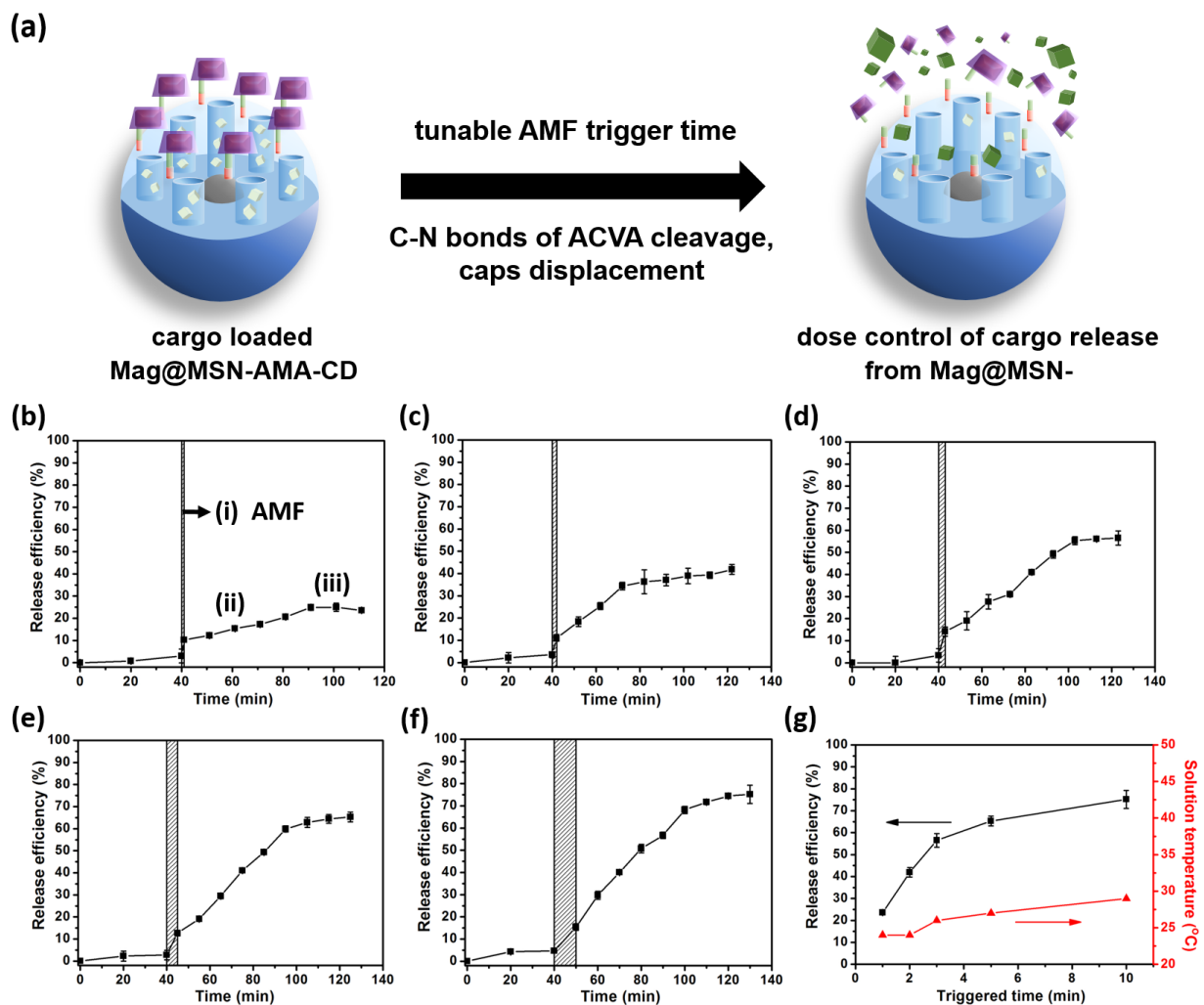


Figure 3.11. (a) Dose control of cargo release from Mag@MSNs- by adjusting the AMF “ON” time. Time-dependent release profile of fluorescein from Mag@MSNs- through magnetic actuation under AMF for (b) 1, (c) 2, (d) 3, (e) 5, and (f) 10 min, respectively. (g) The release efficiency of fluorescein at plateau and the solution temperature after the various time periods of trigger under AMF (N = 3).

cycles were performed every 10 min at room temperature until the maximum release of fluorescein was achieved. Only slight leakage (less than 5 %) of fluorescein was observed in the first 40 min at room temperature before exposure to an AMF, showing the effectiveness of the gatekeeper to prevent premature leakage of the dye (Figure 3.11b-f). The release efficiency of fluorescein was

10 % immediately after 1 min of the AMF trigger, showing that some caps were successfully removed by the magnetic heating. The amount of released fluorescein gradually increased over time at room temperature until it leveled off (total release efficiency of 23.6 %) at 70 min post-AMF trigger (Figure 3.11b). After the caps are removed, it takes time for fluorescein molecules to diffuse out from the pores of nanoparticles and reach equilibrium at the end. To correlate the release efficiency of fluorescein with the AMF trigger exposure time, the samples were exposed to the AMF for longer actuation times of 2, 3, 5, and 10 min. Similar time-dependent release profiles were observed in all cases: (i) the burst of release during magnetic heating, (ii) the gradual increase in the release at room temperature, and (iii) the plateau reached 80 min post-AMF trigger (Figure 3.11b-f). Even though the initial rise in release during the burst stage (i) was not obviously increased as a function of the longer magnetic heating time, the cumulative release efficiencies of fluorescein at plateau were significantly enhanced, reaching 41.9 %, 56.5 %, 65.3 %, and 75.9 % with 2, 3, 5, and 10 min of heating time, respectively. This suggested that the number of caps removed from the surface of nanoparticles is directly correlated with the AMF trigger time.

To know whether the removal of the cap is a result of localized internal heating from the magnetic core under the AMF or an increase in the ambient temperature, we simultaneously monitored the temperature of the solution containing Mag@MSNs-AMA-CD immediately after 1, 2, 3, 5, and 10 min of AMF actuation. Less than 6 degrees of temperature increase was observed, where the temperatures were found to be 24, 24, 26, 27, and 29 °C after 1, 2, 3, 5, and 10 min of AMF actuation (Figure 3.11g), respectively. Even the highest temperature of the solution after exposing to AMF was below 30 °C, indicating that the release of fluorescein was not triggered by

bulk heating from the surrounding solution. Instead, the fairly high local temperature (that can be above 65 °C)⁸³ achieved internally from the magnetic core was the main heat source to cleave the thermolabile ACVA, which will undergo thermolysis over 60 °C.^{17,71}

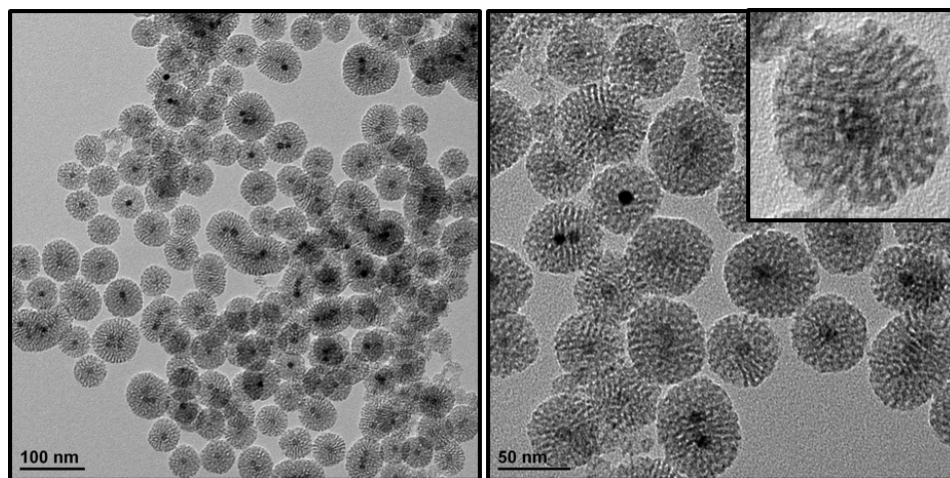


Figure 3.12. TEM images of fluorescein-loaded Mag@MSN-AMA-CD after 10 min exposure of the AMF trigger.

To confirm that the mesoporous structure of silica particles can withstand the temperature of localized magnetic heating, the structure of Mag@MSNs-AMA-CD after 10 min of the AMF actuation was analyzed by TEM. The TEM image (Figure 3.12) shows that the mesoporous silica structure was intact without any damage and the diameters of the particles didn't change after exposing to the internal heating from the inner magnetic core. The cleavage of the C-N bonds was supported by the change in the zeta potential of the Mag@MSN-ACVA particle from -21.0 mV before exposure to -1.8 mV after 10 min of exposure (Figure 3.13). The results confirm that the release of fluorescein molecules from Mag@MSNs-AMA-CD is through the removal of the

thermal-sensitive gatekeepers on the surface rather than the destruction of the mesoporous structure of silica particles.

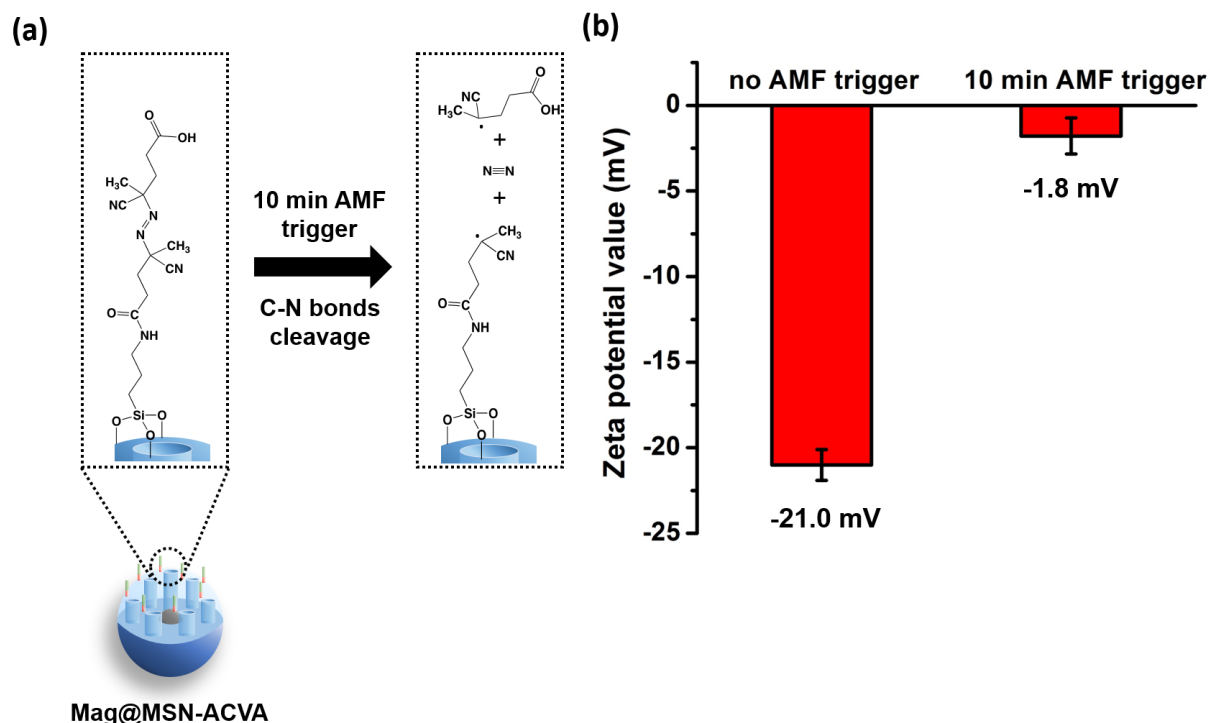


Figure 3.13. (a) The cleavage of C-N bonds caused by 10 min of AMF trigger. (b) Zeta potential values of Mag@MSNs-ACVA before and after 10 min of AMF trigger in D.I. water. The concentration of Mag@MSNs-ACVA in D.I. water is 0.5 mg/mL.

The second type of release study was performed with multiple sequential exposures of AMF to achieve the maximal release of fluorescein. To confirm the tightness of the gatekeeper, the release of fluorescein before each trigger was monitored by fluorescence spectroscopy every 10 min. Only slight leakage (less than 10 %) of fluorescein was observed in the first 30 min at room temperature before exposure to the first cycle of AMF actuation. Three cycles of AMF actuation for 3 min followed by 70 min of the monitoring at room temperature were carried out. The

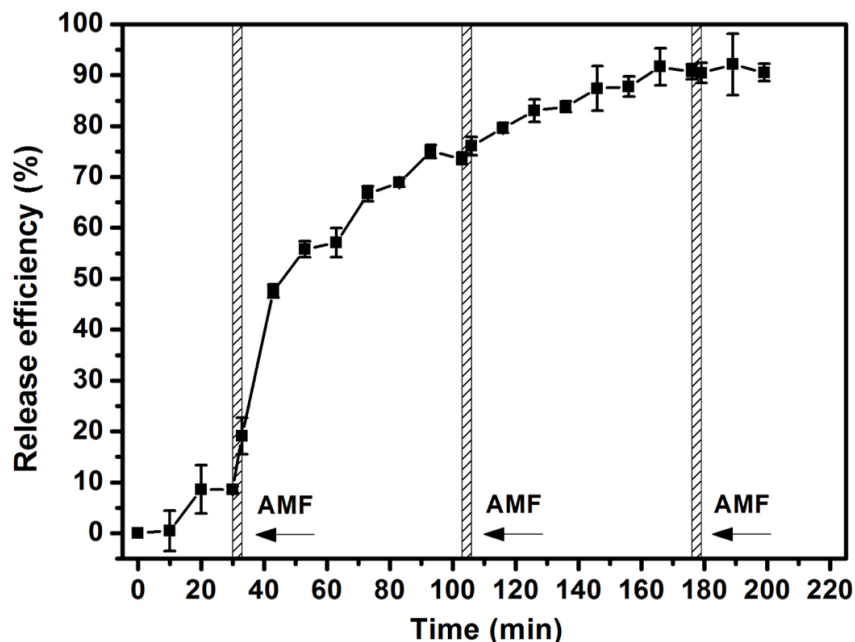


Figure 3.14. Time dependent release profile of fluorescein from Mag@MSNs- through magnetic actuation under AMF for 3 min for 3 cycles (N = 3). The temperature of the solution right after each exposure was measured to be 26 °C, 3 degrees higher than that before each AMF exposure.

temperature of the solution right after each AMF exposure was measured to be 26 °C, 26 °C, and 26 °C, respectively, only 3 degrees higher than that before each AMF exposure. The minimal temperature increase indicates that the observed release was not triggered by the bulk heating from the surrounding solution but by the higher local temperature achieved internally from the magnetic core. The release efficiency at plateau where fluorescein molecules achieved equilibrium after the first cycle was 60 % (Figure 3.14), which is similar to the release efficiency of fluorescein after 3 min of AMF actuation shown in Figure 3.11d (56.5 %). Subsequently, the second cycle of AMF actuation was applied and the release efficiency increased to approximate 80 % compared to the background. The second heating cycle caused an additional 20 % more fluorescein can be released. However, when the third cycle of AMF actuation was applied, no increase in the release of

fluorescein was observed. This implies two possibilities: (1) part of the caps still block the pore openings after the trigger, and/or (2) even after the caps are fully removed, some fluorescein molecules adhere to the pores of Mag@MSNs-AMA-CD. Stepwise time-dependent release profile triggered by multiple cycles of AMF actuation was observed in three stages which is similar to Figure 3.11b-f. Based on this stepwise release profile, we can control the release of desired amount of fluorescein in the specific time period.

3.3.6 Alternating magnetic field-triggered release of Doxorubicin

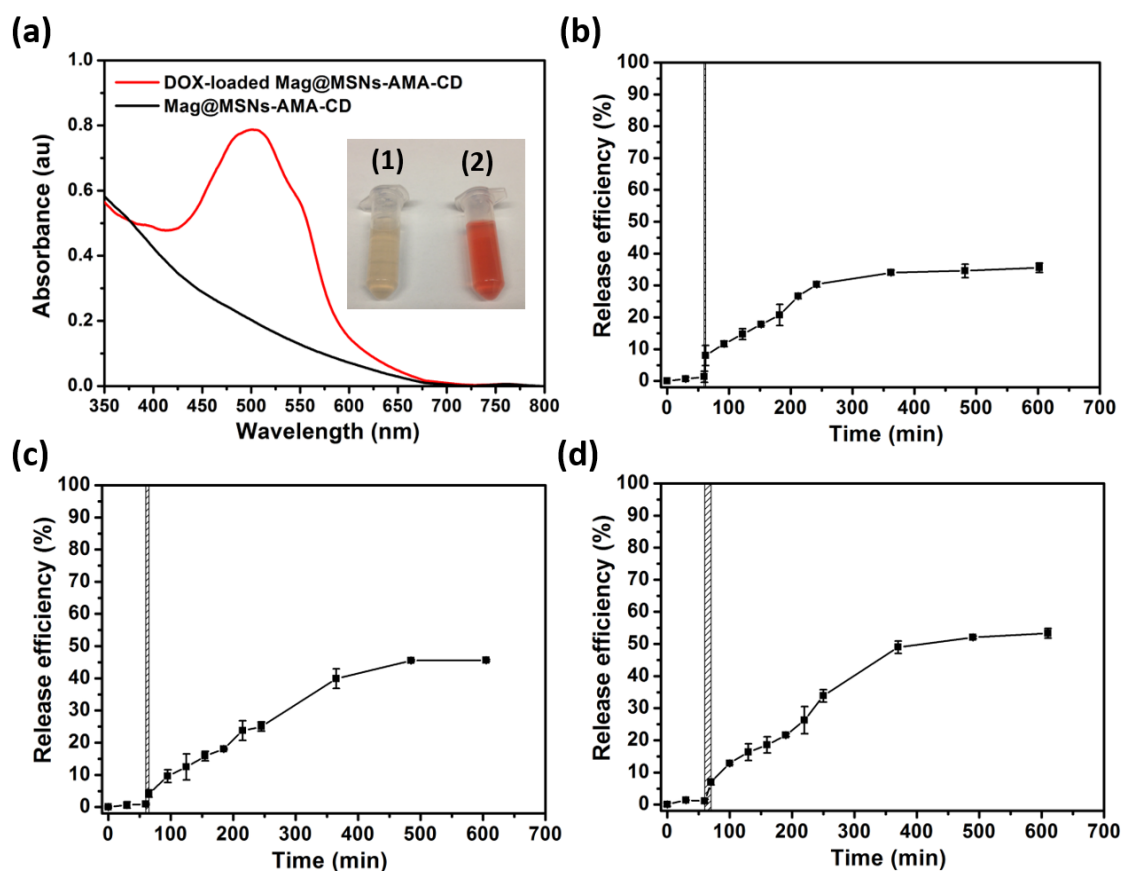


Figure 3.15. (a) UV-Vis spectra of Mag@MSNs-AMA-CD and DOX-loaded Mag@MSNs-AMA-CD in PBS. Inset shows the photograph of tubes containing (1) Mag@MSNs-AMA-CD and (2) DOX-loaded Mag@MSNs-AMA-CD in PBS. Time-dependent release profile of DOX from Mag@MSNs- in PBS through magnetic actuation under AMF for (b) 2, (c) 5, and (d) 10 min, respectively (N=3). The concentration of DOX-loaded Mag@MSNs-AMA-CD in PBS for each release study was 0.5 mg/mL.

In preparation for *in vitro* cancer cell studies, we investigated the loading and AMF release of doxorubicin (DOX), a widely used anticancer drug. DOX was loaded in Mag@MSNs-AMA by soaking the particles in a 2.6 mM DOX solution for 24 h followed by the capping by β -CD. The loading capacity of DOX in Mag@MSNs-AMA-CD was calculated to be 4 % after the DOX-loaded Mag@MSNs-AMA-CD was thoroughly washed with deionized water and PBS to remove the untrapped DOX molecules. The absorption peak at 503 nm of UV-vis spectrum (Figure 3.15a) provides spectroscopic evidence that DOX was loaded in Mag@MSNs-AMA-CD.

To prove that the dosage of released DOX from Mag@MSNs-AMA-CD could be controlled after being triggered by different durations of AMF exposure, sample tubes containing DOX-loaded Mag@MSNs-AMA-CD in PBS were placed in the center of the coil with 2, 5, or 10 min of exposure time. Before the AMF exposure, the release of DOX was monitored every 30 min over a period of 60 min at room temperature. Only slight leakage (less than 5 %) of DOX was observed in the first 60 min at room temperature before the AMF exposure. After the AMF exposure, the release of DOX was monitored every 30 min over a period of 3 h followed by every 2 h over a period of 6 h. The released DOX gradually increased over time at room temperature until it leveled off at 540 min post AMF exposure. The cumulative release efficiencies of DOX reach 35.6 %, 45.6 %, and 53.1 % with 2, 5, and 10 min of AMF exposure, respectively (Figure 3.15b-d). The temperature of the solution after the AMF exposure was measured to be 24, 26, and 28 °C, respectively. The minimal temperature increase shows that the release of DOX was not triggered by bulk heating from the surrounding solution but by the localized high temperature from the magnetic core. The results demonstrated that the release of DOX can be triggered by an AMF and

that the dosage of the DOX released from the nanocarriers can be controlled by different lengths of the AMF exposure.

3.3.7 *In vitro* studies of cytotoxicity and stability of drug delivery system

In vitro cytotoxicity studies were carried out to evaluate the potential biological applications of the drug delivery system. A pancreatic cancer cell line (PANC-1) was used to evaluate the cytotoxicity of Mag@MSNs-AMA-CD by a colorimetric cell counting kit-8 (CCK-8) assay. The cell viabilities of PANC-1 after 20 h and 70 h incubation at various nanoparticle concentrations are shown in Figure 3.16a. No significant decrease in cell viability was detected even at a very high particle concentration (200 $\mu\text{g/mL}$) at both 20 h and 70 h. The Mag@MSNs-AMA-CD particles we developed are not toxic and are suitable to be used as drug delivery carriers.

To test the stability of the gatekeepers of Mag@MSNs-AMA-CD *in vitro*, PANC-1 cells were treated with DOX-loaded Mag@MSNs-AMA-CD at various concentrations. The results show that no significant cell viability decrease was observed after 4 h incubation (Figure 3.16b). The minimal cytotoxicity proves the tightness of the gatekeepers which prevent the leakage of DOX from the nanocarriers in a biological environment at 37 °C. In addition, the proliferation of PANC-1 (Figure 3.16c) was not hindered in a 12 h growth in Dulbecco's modified Eagle's medium (DMEM) supplemented with 10 % fetal bovine serum (FBS) after 4 h treatment by DOX-loaded Mag@MSNs-AMA-CD. These results demonstrate that the drug delivery system prevents the leakage of DOX and thus minimizes the cytotoxicity before activation, and that the proliferation of the PANC-1 was not hindered.

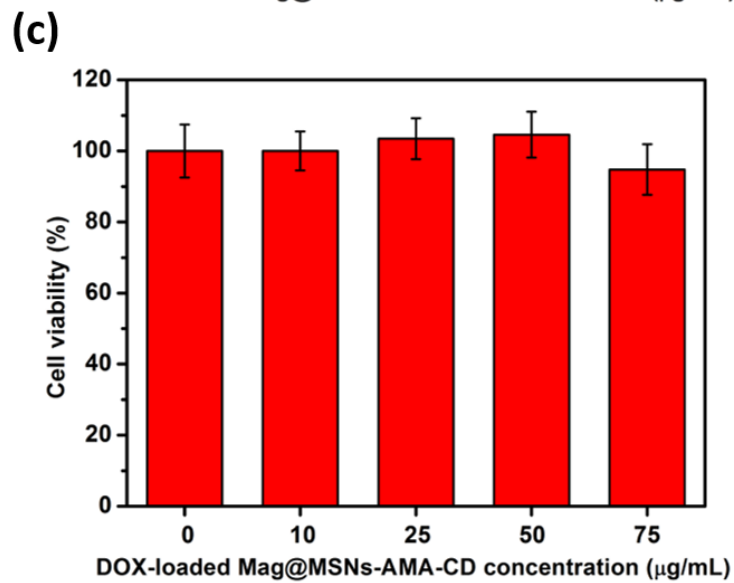
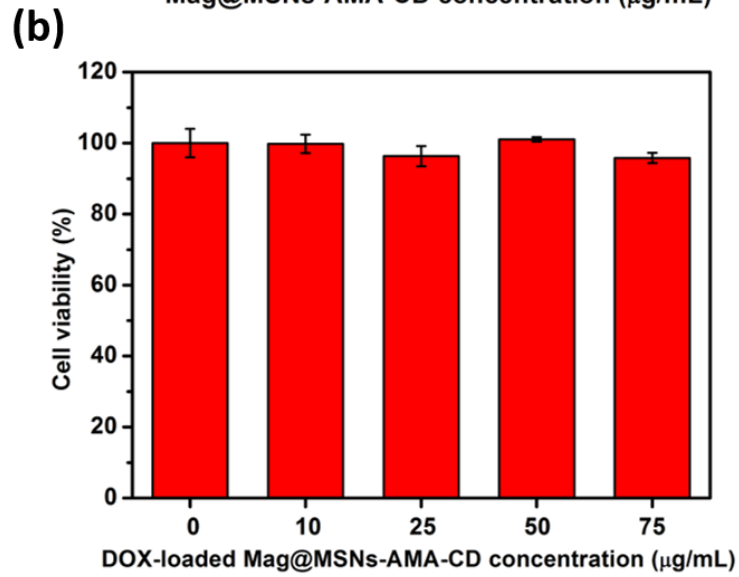
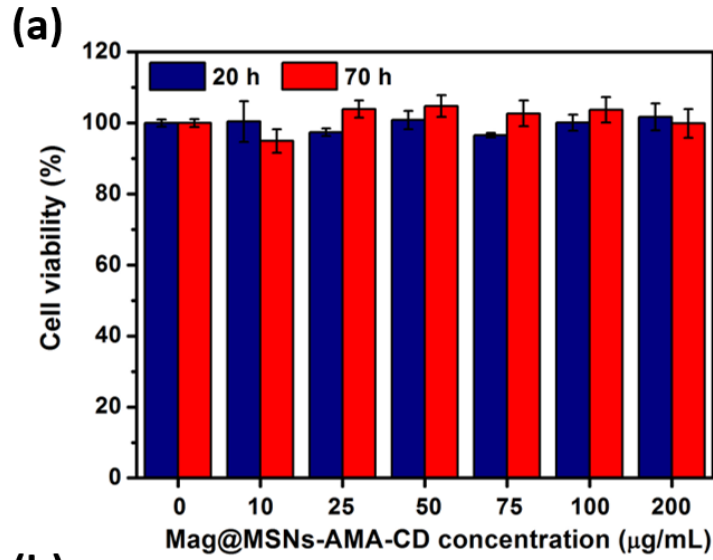


Figure 3.16. (a) Cytotoxicity of Mag@MSNs-AMA-CD. PANC-1 was incubated with Mag@MSNs-AMA-CD at various nanoparticle concentrations for 20 and 70 h, and the viability was determined by a CCK-8 assay and normalized to the control without Mag@MSNs-AMA-CD treatment. Data are means \pm SD of three independent experiments. (b) Cytotoxicity of DOX-loaded Mag@MSNs-AMA-CD. PANC-1 was incubated with DOX-loaded Mag@MSNs-AMA-CD at various concentrations for 4 h. The viability was determined by a CCK-8 assay and normalized to the control without DOX-loaded Mag@MSNs-AMA-CD nanoparticle treatment. Data are means \pm SD of three independent experiments. (c) After the 4 h treatment of DOX-loaded Mag@MSNs-AMA-CD, cells were allowed to grow in the regular culture medium for 12 h, and the viability was determined by a CCK-8 assay and normalized to the control without DOX-loaded Mag@MSNs-AMA-CD treatment. Data are means \pm SD of three independent experiments.

3.3.8 *In vitro* cellular killing studies

In vitro cellular killing by DOX-loaded Mag@MSNs-AMA-CD after AMF exposure was studied. PANC-1 cells were treated with DOX-loaded Mag@MSNs-AMA-CD for 4 h followed by the AMF exposure for 2, 5, and 10 min. (Figure 3.17a). The cell viabilities of the control groups including without the treatment by nanoparticles, and treatment by Mag@MSNs-AMA-CD without DOX were also investigated. Figure 3.17b shows that without the treatment by Mag@MSNs-AMA-CD, the exposure of the cells to AMF (2, 5, and 10 min) did not kill the PANC-1 cells. The results corroborated that the magnetic field was harmless to cells and is a safe stimulus for the drug delivery. No decrease of PANC-1 cell viability was observed after the 4 h incubation with 50 $\mu\text{g/mL}$ Mag@MSNs-AMA-CD followed by exposure to various lengths of AMF (2, 5, and 10 min). The results indicate that the localized heating generated from Mag@MSNs-AMA-CD during the AMF exposure was not harmful to the cells, and was desirable because killing by hyperthermia did not occur.

The effects of the release of DOX from Mag@MSNs-AMA-CD in PANC-1 cells triggered

by the AMF were studied. The PANC-1 cells were incubated with 50 $\mu\text{g/mL}$ DOX-loaded Mag@MSNs-AMA-CD followed by various lengths of exposure to AMF (2, 5, and 10 min). The results show that the viabilities of PANC-1 were 72 %, 63 %, and 47 % after 2, 5, and 10 min of AMF exposure, respectively (Figure 3.17b), which demonstrates that the loss of cell viabilities was correlated with the lengths of AMF exposure time. As AMF exposure time was increased, the dosage of released DOX from the nanocarriers increased and thus killed more PANC-1 cells. The results demonstrate that not only the release of DOX from Mag@MSNs-AMA-CD in cellular environment can be remotely triggered by an AMF, but also that the dosage of the released DOX is controlled by the lengths of AMF exposure and thus different levels of cell killing can be achieved.

Uptake of DOX-loaded Mag@MSNs-AMA-CD by PANC-1 cells and the release of DOX from the nanocarriers in PANC-1 cells after the exposure of the AMF were verified by fluorescence microscope images. PANC-1 cells were treated with 50 $\mu\text{g/mL}$ DOX-loaded Mag@MSNs-AMA-CD for 4 h. Before the AMF trigger, the red fluorescence derived from DOX was located around the nuclei but not overlapped with blue fluorescence derived from the nucleus stained by Hoechst 33342 dye ((ii) in Figure 3.17c), compared with that of control group (without the treatment of nanoparticles, (i) in Figure 3.17c). The results indicate that before the exposure to AMF, DOX was not released from the Mag@MSNs-AMA-CD nanoparticles taken up by the PANC-1 cells. However, after the AMF exposure, some of the red fluorescence derived from DOX overlapped with the blue fluorescence of the Hoechst-stained nuclei ((iii) in Figure 3.17c). This result demonstrates that DOX was released from Mag@MSNs-AMA-CD in PANC-1 cells after the

exposure of the AMF, and thus stained the nuclei and caused cell death.

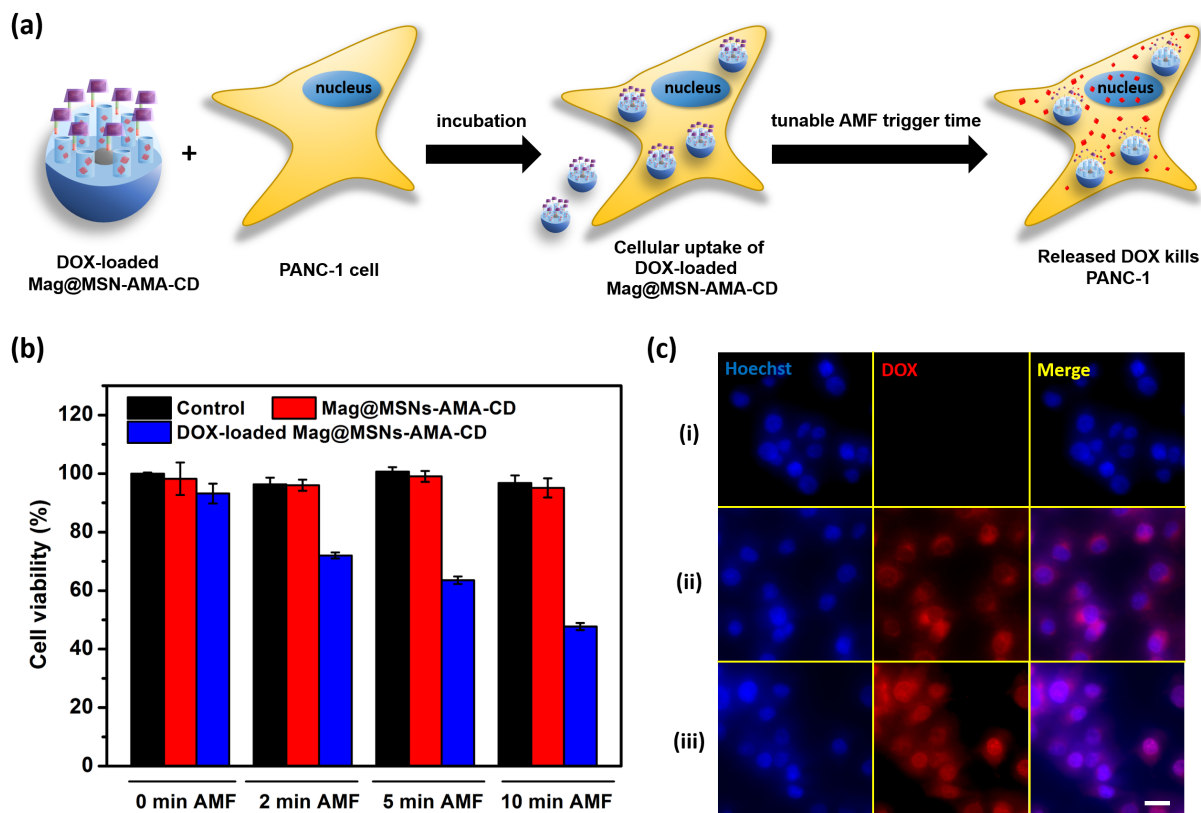


Figure 3.17. (a) *In vitro* cellular killing effect of DOX-loaded Mag@MSNs-AMA-CD after AMF exposure. PANC-1 cells were treated with DOX-loaded Mag@MSNs-AMA-CD followed by various lengths of AMF exposure. (b) The viability of PANC-1 after treatment by Mag@MSNs-AMA-CD, or DOX-loaded Mag@MSNs-AMA-CD. The control is cells without treatment by nanoparticles. The cells were treated for 4 h at a concentration of 50 $\mu\text{g}/\text{mL}$ followed by 2, 5, or 10 min of AMF exposure. The cells were allowed to grow in the regular culture medium for 12 h, and the viability was determined by a CCK-8 assay. Data are means \pm SD of four independent experiments. The viable cells in each sample were determined by the absorbance at 450 nm and 650 nm (as a reference). (c) Fluorescence microscope images of PANC-1 cells (ii) after 4 h treatment by DOX-loaded Mag@MSNs-AMA-CD, and (iii) after 4 h incubation with DOX-loaded Mag@MSNs-AMA-CD followed by 10 min of AMF exposure. The control group (i) is cells without the treatment by nanoparticles. Panels from left to right: cells of PANC-1 with the blue-emitting nucleus stained by Hoechst 33342; red emission from DOX; and the merged images. Scale bar is 20 μm .

3.3.9 Significance for potential biomedical applications

To reduce the side-effects of drugs, release of therapeutics within a specific time, to a targeted location, and with a controlled dosage has always been a goal for drug delivery applications. Although many proof-of-concept stimulated release of drugs have been studied, a majority of them are responsive to internal stimuli such as pH,^{3,87} redox,^{7,8} or enzymes,⁹ and it is almost impossible to precisely control the amount of therapeutics released from the carriers. Even though several studies have reported the externally triggered release of drugs *via* magnetic fields, none of them quantified the release efficiency of the cargos, making it hard to estimate the amount of cargo released upon trigger, nor did they test the tunable dosage released by changing the trigger duration under the magnetic field. In this work, we successfully demonstrated that the release efficiency (hence, the release amount) of fluorescein and DOX can be well controlled by manipulating the AMF trigger time (Figure 3.11g). Additionally, with the AMF as an external stimulus, the particles with therapeutics can be delivered and released to the target site on-demand. For those treatments to some disease requiring multiple dosing such as multiple dose insulin injection therapy, the common way is to inject therapeutics several times daily. With the drug delivery strategy developed in this study, by simply applying multiple sequential exposure of AMF, the therapeutics could be released stepwise *in situ* with the desired amount in the specific time period, and finally reach the required amount in its therapeutic window. The designed controllable drug delivery provides alternative method to those therapies required multiple injection, and at the same time reduces the off-target side effects in chemotherapy.

In addition to chemotherapy, high temperatures (hyperthermia) can also damage and kill cancer cells, usually with minimal injury to normal tissues. Although hyperthermia is a promising way to kill cancer cells, a number of challenges must be overcome including: (1) increasing probability of tumor metastasis,³¹⁻³⁵ (2) difficulty in accurate temperature measurement inside a tumor, (3) problems of keeping an area at a constant temperature without affecting nearby tissues, and (4) body tissue's heterogeneity in response to heat.³¹ Even using local hyperthermia for which energy (such as microwave, radiofrequency, or ultrasound) must be delivered to a small volume (*e.g.* a tumor) does not solve all the problems stated above. On the other hand, the internal heat source generated by applying AMF to magnetic cores only heats up a small local area (within a range of magnetic core) as compared to area affected by microwave, radiofrequency, and ultrasound. Thus, this magnetic heating method in combination with drug delivery provides an alternative approach of cancer treatment that has the potential to overcome the challenges faced with traditional chemotherapy and hyperthermia, and is especially beneficial to the case where thermal ablation or necrosis is undesired.

3.4 Conclusions

In summary, monodisperse manganese and cobalt doped iron oxide ($\text{MnFe}_2\text{O}_4@\text{CoFe}_2\text{O}_4$) nanoparticles with a high magnetization (105 emu/g) and high specific loss power (1510.8 W/g) were synthesized. The high magnetization of these superparamagnetic nanoparticles provides efficient magnetic heating under an alternating magnetic field (AMF), thus holding great promise for magnetic heating triggered drug delivery. To increase the amount of drug over that available using the nanoparticles themselves, mesoporous silica shell “containers” are synthesized around

the magnetic core, forming a core@shell structure with 55 nm in diameter. The spatial, temporal, and dose control of drug release was achieved using a thermal-responsive gatekeeper containing a thermal-labile molecule 4,4'-azobis(4-cyanovaleric acid), and a host guest complexation formed by adamantylamine and β -cyclodextrin. This gatekeeper was stable at physiological temperature, while at the higher temperature (60 or 80 °C) the gatekeeper was cleaved. When the fluorescein loaded gatekeeper modified nanoparticles were heated for 10 min in 60 or 80 °C water baths, 39 % or 55 % respectively of fluorescein was released. However, when the AMF was applied, the magnetic core served as a heat source, and the localized heating generated from the core led to more efficient fluorescein release (75.9 % of the highest) with the temperature rise of the bulk solution no more than 5 degrees. Most importantly, in this study we demonstrated externally-controlled dosage of fluorescein or doxorubicin (DOX) by controlling the AMF exposure time. Multiple sequential exposure of AMF allows cargo release in a stepwise manner. *In vitro* studies show that the drug delivery system is biocompatible. DOX-loaded nanoparticles did not cause a decrease in cell viability in the absence of AMF stimulation, but the viabilities of the pancreatic cancer cells decreased by 28 %, 37 %, and 53 % as the AMF exposure time increased from 2, 5 to 10 min. Taken together, the thermal-responsive drug delivery actuated by AMF offers the potential of becoming an emerging chemotherapy that non-invasively and precisely control the dosage of drugs, and avoiding the risk generated when overheating the bulk solution.

3.5 Acknowledgment

We gratefully acknowledge financial support by the Zink Student Research Support Fund. We thank Dr. Yao Cai for discussing the experimental procedures of cell studies.

3.6 References

- (1) Collins, F. S.; Varmus, H. A New Initiative on Precision Medicine. *N. Engl. J. Med.* **2015**, *372*, 793–795.
- (2) Peck, R. W. Precision Medicine Is Not Just Genomics: The Right Dose for Every Patient. *Annu. Rev. Pharmacol. Toxicol.* **2018**, *58*, 105–122.
- (3) Li, Z.; Clemens, D. L.; Lee, B. Y.; Dillon, B. J.; Horwitz, M. A.; Zink, J. I. Mesoporous Silica Nanoparticles with pH-Sensitive Nanovalves for Delivery of Moxifloxacin Provide Improved Treatment of Lethal Pneumonic Tularemia. *ACS Nano* **2015**, *9*, 10778–10789.
- (4) Felber, A. E.; Dufresne, M. H.; Leroux, J. C. pH-Sensitive Vesicles, Polymeric Micelles, and Nanospheres Prepared with Polycarboxylates. *Adv. Drug Deliv. Rev.* **2012**, *64*, 979–992.
- (5) Liu, J.; Huang, Y.; Kumar, A.; Tan, A.; Jin, S.; Mozhi, A.; Liang, X. J. pH-Sensitive Nano-Systems for Drug Delivery in Cancer Therapy. *Biotechnol. Adv.* **2014**, *32*, 693–710.
- (6) Gao, W.; Chan, J.; Farokhzad, O. C. pH-Responsive Nanoparticles for Drug Delivery. *Mol. Pharm.* **2010**, *7*, 1913–1920.
- (7) Lee, B. Y.; Li, Z.; Clemens, D. L.; Dillon, B. J.; Hwang, A. A.; Zink, J. I.; Horwitz, M. A. Redox-Triggered Release of Moxifloxacin from Mesoporous Silica Nanoparticles Functionalized with Disulfide Snap-Tops Enhances Efficacy Against Pneumonic Tularemia in Mice. *Small* **2016**, *12*, 3690–3702.
- (8) Remant, R. B.; Chandrashekar, V.; Cheng, B.; Chen, H.; Peña, M. M. O.; Zhang, J.; Montgomery, J.; Xu, P. Redox Potential Ultrasensitive Nanoparticle for the Targeted Delivery of Camptothecin to HER2-Positive Cancer Cells. *Mol. Pharm.* **2014**, *11*, 1897–1905.
- (9) Renoux, B.; Raes, F.; Legigan, T.; Péraudeau, E.; Eddhif, B.; Poinot, P.; Tranoy-Opalinski, I.; Alsarraf, J.; Koniev, O.; Kolodych, S.; Lerondel, S.; Le Pape, A.; Clarhaut, J.; Papot, S. Targeting the Tumour Microenvironment with an Enzyme-Responsive Drug Delivery System for the Efficient Therapy of Breast and Pancreatic Cancers. *Chem. Sci.* **2017**, *8*, 3427–3433.
- (10) Ruehle, B.; Clemens, D. L.; Lee, B.-Y.; Horwitz, M. A.; Zink, J. I. A Pathogen-Specific Cargo Delivery Platform Based on Mesoporous Silica Nanoparticles. *J. Am. Chem. Soc.* **2017**, *139*, 6663–6668.
- (11) Mo, R.; Jiang, T.; Disanto, R.; Tai, W.; Gu, Z. ATP-Triggered Anticancer Drug Delivery. *Nat. Commun.* **2014**, *5*, 3364.
- (12) Li, H.; Tan, L. L.; Jia, P.; Li, Q. L.; Sun, Y. L.; Zhang, J.; Ning, Y. Q.; Yu, J.; Yang, Y. W. Near-Infrared Light-Responsive Supramolecular Nanovalve Based on Mesoporous Silica-Coated Gold

- Nanorods. *Chem. Sci.* **2014**, *5*, 2804–2808.
- (13) Guardado-Alvarez, T. M.; Sudha Devi, L.; Russell, M. M.; Schwartz, B. J.; Zink, J. I. Activation of Snap-Top Capped Mesoporous Silica Nanocontainers Using Two Near-Infrared Photons. *J. Am. Chem. Soc.* **2013**, *135*, 14000–14003.
- (14) Tarn, D.; Ferris, D. P.; Barnes, J. C.; Ambrogio, M. W.; Stoddart, J. F.; Zink, J. I. A Reversible Light-Operated Nanovalve on Mesoporous Silica Nanoparticles. *Nanoscale* **2014**, *6*, 3335–3343.
- (15) Qiu, M.; Wang, D.; Liang, W.; Liu, L.; Zhang, Y.; Chen, X.; Sang, D. K.; Xing, C.; Li, Z.; Dong, B.; Xing, F.; Fan, D.; Bao, S.; Zhang, H.; Cao, Y. Novel Concept of the Smart NIR-Light-Controlled Drug Release of Black Phosphorus Nanostructure for Cancer Therapy. *Proc. Natl. Acad. Sci. USA* **2018**, *115*, 501–506.
- (16) Rühle, B.; Datz, S.; Argyo, C.; Bein, T.; Zink, J. I. A Molecular Nanocap Activated by Superparamagnetic Heating for Externally Stimulated Cargo Release. *Chem. Commun.* **2016**, *52*, 1843–1846.
- (17) Saint-Cricq, P.; Deshayes, S.; Zink, J. I.; Kasko, A. M. Magnetic Field Activated Drug Delivery Using Thermodegradable Azo-Functionalised PEG-Coated Core-Shell Mesoporous Silica Nanoparticles. *Nanoscale* **2015**, *7*, 13168–13172.
- (18) Thomas, C. R.; Ferris, D. P.; Lee, J.; Choi, E.; Cho, M. H.; Kim, E. S.; Stoddart, J. F.; Shin, J.; Cheon, J.; Zink, J. I. Noninvasive Remote Controlled Release of Drug Molecules *in Vitro* Using Magnetic Actuation of Mechanised Nanoparticles. *J. Am. Chem. Soc.* **2010**, *132*, 10623–10625.
- (19) Zhu, Y.; Tao, C. DNA-Capped Fe₃O₄/SiO₂ Magnetic Mesoporous Silica Nanoparticles for Potential Controlled Drug Release and Hyperthermia. *RSC Adv.* **2015**, *5*, 22365–22372.
- (20) Ruiz-Hernández, E.; Baeza, A.; Vallet-Regí, M. Smart Drug Delivery through DNA/Magnetic Nanoparticle Gates. *ACS Nano* **2011**, *5*, 1259–1266.
- (21) Baeza, A.; Guisasola, E.; Ruiz-Hernández, E.; Vallet-Regí, M. Magnetically Triggered Multidrug Release by Rybrid Mesoporous Silica Nanoparticles. *Chem. Mater.* **2012**, *24*, 517–524.
- (22) Guisasola, E.; Asín, L.; Beola, L.; De La Fuente, J. M.; Baeza, A.; Vallet Regí, M. Beyond Traditional Hyperthermia. *In Vivo* Cancer Treatment with Magnetic-Responsive Mesoporous Silica Nanocarriers. *ACS Appl. Mater. Interfaces* **2018**, *10*, 12518–12525.
- (23) Guo, W.; Yang, C.; Lin, H.; Qu, F. P(EO-Co-LLA) Functionalized Fe₃O₄@mSiO₂ Nanocomposites for Thermo/pH Responsive Drug Controlled Release and Hyperthermia. *Dalton Trans.* **2014**, *43*, 18056–18065.
- (24) Paris, J. L.; Cabanas, M. V.; Manzano, M.; Vallet-Regí, M. Polymer-Grafted Mesoporous Silica

- Nanoparticles as Ultrasound-Responsive Drug Carriers. *ACS Nano* **2015**, *9*, 11023–11033.
- (25) De Smet, M.; Heijman, E.; Langereis, S.; Hijnen, N. M.; Grüll, H. Magnetic Resonance Imaging of High Intensity Focused Ultrasound Mediated Drug Delivery from Temperature-Sensitive Liposomes: An *in Vivo* Proof-of-Concept Study. *J. Control. Release* **2011**, *150*, 102–110.
- (26) Peck, R. W. The Right Dose for Every Patient: A Key Step for Precision Medicine. *Nat. Rev. Drug Discov.* **2016**, *15*, 145–146.
- (27) Tucker, G. T. Personalized Drug Dosage – Closing the Loop. *Pharm. Res.* **2017**, *34*, 1539–1543.
- (28) Hawcutt, D. B.; Cooney, L.; Oni, L.; Pirmohamed, M. Precision Dosing in Children. *Expert Rev. Precis. Med. Drug Dev.* **2016**, *1*, 69–78.
- (29) Gonzalez, D.; Rao, G. G.; Bailey, S. C.; Brouwer, K. L. R.; Cao, Y.; Crona, D. J.; Kashuba, A. D. M.; Lee, C. R.; Morbitzer, K.; Patterson, J. H.; Wiltshire, T.; Easter, J.; Savage, S. W.; Powell, J. R. Precision Dosing: Public Health Need, Proposed Framework, and Anticipated Impact. *Clin. Transl. Sci.* **2017**, *10*, 443–454.
- (30) Wicki, A.; Witzigmann, D.; Balasubramanian, V.; Huwyler, J. Nanomedicine in Cancer Therapy: Challenges, Opportunities, and Clinical Applications. *J. Control. Release* **2015**, *200*, 138–157.
- (31) Hegyi, G.; Szigeti, G. P.; Szász, A. Hyperthermia *versus* Oncothermia: Cellular Effects in Complementary Cancer Therapy. *Evid. Based Complement. Alternat. Med.* **2013**, *2013*, 672873.
- (32) Hegewisch-Becker, S.; Braun, K.; Otte, M.; Corovic, A.; Atanackovic, D.; Nierhaus, A.; Hossfeld, D. K.; Pantel, K. Effects of Whole Body Hyperthermia (41.8 Degrees C) on the Frequency of Tumor Cells in the Peripheral Blood of Patients with Advanced Malignancies. *Clin. Cancer Res.* **2003**, *9*, 2079–2084.
- (33) Dickson, J. A.; Ellis, H. A. Stimulation of Tumour Cell Dissemination by Raised Temperature (42°C) in Rats with Transplanted Yoshida Tumours. *Nature* **1974**, *248*, 354–358.
- (34) Lord, P. F.; Kapp, D. S.; Morrow, D. Increased Skeletal Metastases of Spontaneous Canine Osteosarcoma after Fractionated Systemic Hyperthermia and Local X-Irradiation. *Cancer Res.* **1981**, *41*, 4331–4334.
- (35) Urano, M.; Epstein, R.; Rice, L.; Suit, H. D.; Chu, A. M. Effect of Whole-Body Hyperthermia on Cell Survival, Metastasis Frequency, and Host Immunity in Moderately and Weakly Immunogenic Murine Tumors. *Cancer Res.* **1983**, *43*, 1039–1043.
- (36) Klibanov, A. L.; Hossack, J. A. Ultrasound in Radiology: From Anatomic, Functional, Molecular Imaging to Drug Delivery and Image-Guided Therapy. *Invest. Radiol.* **2015**, *50*, 657–670.
- (37) Chen, W.; Lu, F.; Chen, C. C. V; Mo, K. C.; Hung, Y.; Guo, Z. X.; Lin, C. H.; Lin, M. H.; Lin, Y. H.;

- Chang, C.; Mou, C. Y. Manganese-Enhanced MRI of Rat Brain Based on Slow Cerebral Delivery of Manganese(II) with Silica-Encapsulated $Mn_xFe_{1-x}O$ Nanoparticles. *NMR Biomed.* **2013**, *26*, 1176–1185.
- (38) Wu, S. H.; Lin, C. Y.; Hung, Y.; Chen, W.; Chang, C.; Mou, C. Y. PEGylated Silica Nanoparticles Encapsulating Multiple Magnetite Nanocrystals for High-Performance Microscopic Magnetic Resonance Angiography. *J. Biomed. Mater. Res. B* **2011**, *99 B*, 81–88.
- (39) Lee, J. H.; Jang, J. T.; Choi, J. S.; Moon, S. H.; Noh, S. H.; Kim, J. W.; Kim, J. G.; Kim, I. S.; Park, K. I.; Cheon, J. Exchange-Coupled Magnetic Nanoparticles for Efficient Heat Induction. *Nat. Nanotechnol.* **2011**, *6*, 418–422.
- (40) Kumar, C. S. S. R.; Mohammad, F. Magnetic Nanomaterials for Hyperthermia-Based Therapy and Controlled Drug Delivery. *Adv. Drug Deliv. Rev.* **2011**, *63*, 789–808.
- (41) Thomas, C. R.; Ferris, D. P.; Lee, J. H.; Choi, E.; Cho, M. H.; Kim, E. S.; Stoddart, J. F.; Shin, J. S.; Cheon, J.; Zink, J. I. Noninvasive Remote-Controlled Release of Drug Molecules *in Vitro* Using Magnetic Actuation of Mechanized Nanoparticles. *J. Am. Chem. Soc.* **2010**, *132*, 10623–10625.
- (42) Guisasola, E.; Baeza, A.; Talelli, M.; Arcos, D. Magnetic-Responsive Release Controlled by Hot Spot Effect. *Langmuir* **2015**, *31*, 12777–12782.
- (43) Riedinger, A.; Guardia, P.; Curcio, A.; Garcia, M. A.; Cingolani, R.; Manna, L.; Pellegrino, T. Subnanometer Local Temperature Probing and Remotely Controlled Drug Release Based on Azo-Functionalized Iron Oxide Nanoparticles. *Nano Lett.* **2013**, *13*, 2399–2406.
- (44) Cazares-Cortes, E.; Espinosa, A.; Guigner, J. M.; Michel, A.; Griffete, N.; Wilhelm, C.; Ménager, C. Doxorubicin Intracellular Remote Release from Biocompatible Oligo(Ethylene Glycol) Methyl Ether Methacrylate-Based Magnetic Nanogels Triggered by Magnetic Hyperthermia. *ACS Appl. Mater. Interfaces* **2017**, *9*, 25775–25788.
- (45) Lee, J. H.; Chen, K. J.; Noh, S. H.; Garcia, M. A.; Wang, H.; Lin, W. Y.; Jeong, H.; Kong, B. J.; Stout, D. B.; Cheon, J.; Tseng, H. R. On-Demand Drug Release System for *in Vivo* Cancer Treatment through Self-Assembled Magnetic Nanoparticles. *Angew. Chem. Int. Ed.* **2013**, *52*, 4384–4388.
- (46) Noh, S. hyun; Moon, S. H.; Shin, T. H.; Lim, Y.; Cheon, J. Recent Advances of Magneto-Thermal Capabilities of Nanoparticles: From Design Principles to Biomedical Applications. *Nano Today* **2017**, *13*, 61–76.
- (47) Lee, N.; Yoo, D.; Ling, D.; Cho, M. H.; Hyeon, T.; Cheon, J. Iron Oxide Based Nanoparticles for Multimodal Imaging and Magneto-responsive Therapy. *Chem. Rev.* **2015**, *115*, 10637–10689.
- (48) Estelrich, J.; Escribano, E.; Queralto, J.; Busquets, M. A. Iron Oxide Nanoparticles for Magnetically-

- Guided and Magnetically-Responsive Drug Delivery. *Int. J. Mol. Sci.* **2015**, *16*, 8070–8101.
- (49) Mertz, D.; Sandre, O.; Bégin-Colin, S. Drug Releasing Nanoplatfoms Activated by Alternating Magnetic Fields. *Biochimica et Biophysica Acta* **2017**, *1861*, 1617–1641.
- (50) Gao, X.; Cui, Y.; Levenson, R. M.; Chung, L. W. K.; Nie, S. *In Vivo* Cancer Targeting and Imaging with Semiconductor Quantum Dots. *Nat. Biotechnol.* **2004**, *22*, 969–976.
- (51) Chopra, R.; Shaikh, S.; Chatzinoff, Y.; Munaweera, I.; Cheng, B.; Daly, S. M.; Xi, Y.; Bing, C.; Burns, D.; Greenberg, D. E. Employing High-Frequency Alternating Magnetic Fields for the Non-Invasive Treatment of Prosthetic Joint Infections. *Sci. Rep.* **2017**, *7*, 7520.
- (52) Schuerle, S.; Dudani, J. S.; Christiansen, M. G.; Anikeeva, P.; Bhatia, S. N. Magnetically Actuated Protease Sensors for *in Vivo* Tumor Profiling. *Nano Lett.* **2016**, *16*, 6303–6310.
- (53) Song, C. W. Effect of Local Hyperthermia on Blood Flow and Microenvironment: A Review. *Cancer Res.* **1984**, *44*, 4721–4730.
- (54) Ulbrich, K.; Holá, K.; Šubr, V.; Bakandritsos, A.; Tuček, J.; Zbořil, R. Targeted Drug Delivery with Polymers and Magnetic Nanoparticles: Covalent and Noncovalent Approaches, Release Control, and Clinical Studies. *Chem. Rev.* **2016**, *116*, 5338–5431.
- (55) Landarani-Isfahani, A.; Moghadam, M.; Mohammadi, S.; Royvaran, M.; Moshtael-Arani, N.; Rezaei, S.; Tangestaninejad, S.; Mirkhani, V.; Mohammadpoor-Baltork, I. Elegant pH-Responsive Nanovehicle for Drug Delivery Based on Triazine Dendrimer Modified Magnetic Nanoparticles. *Langmuir* **2017**, *33*, 8503–8515.
- (56) Chang, Y.; Liu, N.; Chen, L.; Meng, X.; Liu, Y.; Li, Y.; Wang, J. Synthesis and Characterization of DOX-Conjugated Dendrimer-Modified Magnetic Iron Oxide Conjugates for Magnetic Resonance Imaging, Targeting, and Drug Delivery. *J. Mater. Chem.* **2012**, *22*, 9594–9601.
- (57) Chen, Y.; Bose, A.; Bothun, G. D. Controlled Release from Bilayer-Decorated Magnetoliposomes *via* Electromagnetic Heating. *ACS Nano* **2010**, *4*, 3215–3221.
- (58) Tarn, D.; Ashley, C. E.; Xue, M.; Carnes, E. C.; Zink, J. I.; Brinker, C. J. Mesoporous Silica Nanoparticle Nanocarriers: Biofunctionality and Biocompatibility. *Acc. Chem. Res.* **2013**, *46*, 792–801.
- (59) Argyo, C.; Weiss, V.; Bräuchle, C.; Bein, T. Multifunctional Mesoporous Silica Nanoparticles as a Universal Platform for Drug Delivery. *Chem. Mater.* **2014**, *26*, 435–451.
- (60) Wu, S. H.; Mou, C. Y.; Lin, H. P. Synthesis of Mesoporous Silica Nanoparticles. *Chem. Soc. Rev.* **2013**, *42*, 3862–3875.
- (61) Guardado-Alvarez, T. M.; Chen, W.; Norton, A. E.; Russell, M. M.; Connick, W. B.; Zink, J. I.

- Analyte-Responsive Gated Hollow Mesoporous Silica Nanoparticles Exhibiting Inverse Functionality and an AND Logic Response. *Nanoscale* **2016**, *8*, 18296–18300.
- (62) Chen, W.; Tsai, P. H.; Hung, Y.; Chiou, S. H.; Mou, C. Y. Nonviral Cell Labeling and Differentiation Agent for Induced Pluripotent Stem Cells Based on Mesoporous Silica Nanoparticles. *ACS Nano* **2013**, *7*, 8423–8440.
- (63) Meng, H.; Wang, M.; Liu, H.; Liu, X.; Situ, A.; Wu, B.; Ji, Z.; Chang, C. H.; Nel, A. E. Use of a Lipid-Coated Mesoporous Silica Nanoparticle Platform for Synergistic Gemcitabine and Paclitaxel Delivery to Human Pancreatic Cancer in Mice. *ACS Nano* **2015**, *9*, 3540–3557.
- (64) Liu, X.; Situ, A.; Kang, Y.; Villabroza, K. R.; Liao, Y.; Chang, C. H.; Donahue, T.; Nel, A. E.; Meng, H. Irinotecan Delivery by Lipid-Coated Mesoporous Silica Nanoparticles Shows Improved Efficacy and Safety over Liposomes for Pancreatic Cancer. *ACS Nano* **2016**, *10*, 2702–2715.
- (65) Chen, W.; Cheng, C. A.; Lee, B. Y.; Clemens, D. L.; Huang, W. Y.; Horwitz, M. A.; Zink, J. I. Facile Strategy Enabling Both High Loading and High Release Amounts of the Water-Insoluble Drug Clofazimine Using Mesoporous Silica Nanoparticles. *ACS Appl. Mater. Interfaces* **2018**, *10*, 31870–31881.
- (66) Kumar, N.; Chen, W.; Cheng, C. A.; Deng, T.; Wang, R.; Zink, J. I. Stimuli-Responsive Nanomachines and Caps for Drug Delivery. *The Enzymes* **2018**, *43*, 31–65.
- (67) Chen, F.; Hong, H.; Zhang, Y.; Valdovinos, H. F.; Shi, S.; Kwon, G. S.; Theuer, C. P.; Barnhart, T. E.; Cai, W. *In Vivo* Tumor Targeting and Image-Guided Drug Delivery with Antibody-Conjugated, Radiolabeled Mesoporous Silica Nanoparticles. *ACS Nano* **2013**, *7*, 9027–9039.
- (68) Chou, C. C.; Chen, W.; Hung, Y.; Mou, C. Y. Molecular Elucidation of Biological Response to Mesoporous Silica Nanoparticles *in Vitro* and *in Vivo*. *ACS Appl. Mater. Interfaces* **2017**, *9*, 22235–22251.
- (69) Meng, H.; Xue, M.; Xia, T.; Ji, Z.; Tarn, D. Y.; Zink, J. I.; Nel, A. E. Use of Size and a Copolymer Design Feature to Improve the Biodistribution and the Enhanced Permeability and Retention Effect of Doxorubicin-Loaded Mesoporous Silica Nanoparticles in a Murine Xenograft Tumor Model. *ACS Nano* **2011**, *5*, 4131–4144.
- (70) Xia, T.; Kovoichich, M.; Liong, M.; Meng, H.; Kabehie, S.; George, S.; Zink, J. I.; Nel, A. E. Polyethyleneimine Coating Enhances the Cellular Uptake of Mesoporous Silica Nanoparticles and Allows Safe Delivery of siRNA and DNA Constructs. *ACS Nano* **2009**, *3*, 3273–3286.
- (71) Berkowski, K. L.; Potisek, S. L.; Hickenboth, C. R.; Moore, J. S. Ultrasound-Induced Site-Specific Cleavage of Azo-Functionalized Poly(Ethylene Glycol). *Macromolecules* **2005**, *38*, 8975–8978.

- (72) Zhang, Q.; Wang, X.; Li, P. Z.; Nguyen, K. T.; Wang, X. J.; Luo, Z.; Zhang, H.; Tan, N. S.; Zhao, Y. Biocompatible, Uniform, and Redispersible Mesoporous Silica Nanoparticles for Cancer-Targeted Drug Delivery *in Vivo*. *Adv. Funct. Mater.* **2014**, *24*, 2450–2461.
- (73) Guardado-Alvarez, T. M.; Devi, L. S.; Vabre, J.-M.; Pecorelli, T. A.; Schwartz, B. J.; Durand, J.-O.; Mongin, O.; Blanchard-Desce, M.; Zink, J. I. Photo-Redox Activated Drug Delivery Systems Operating under Two Photon Excitation in the Near-IR. *Nanoscale* **2014**, *6*, 4652–4658.
- (74) Granadero, D.; Bordello, J.; Pérez-Alvite, M. J.; Novo, M.; Al-Soufi, W. Host-Guest Complexation Studied by Fluorescence Correlation Spectroscopy: Adamantane-Cyclodextrin Inclusion. *Int. J. Mol. Sci.* **2010**, *11*, 173–188.
- (75) Xue, M.; Zink, J. I. An Enzymatic Chemical Amplifier Based on Mechanized Nanoparticles. *J. Am. Chem. Soc.* **2013**, *135*, 17659–17662.
- (76) Zhang, Z.; Wang, L.; Wang, J.; Jiang, X.; Li, X.; Hu, Z.; Ji, Y.; Wu, X.; Chen, C. Mesoporous Silica-Coated Gold Nanorods as a Light-Mediated Multifunctional Theranostic Platform for Cancer Treatment. *Adv. Mater.* **2012**, *24*, 1418–1423.
- (77) Ma, X.; Zhao, Y. Biomedical Applications of Supramolecular Systems Based on Host-Guest Interactions. *Chem. Rev.* **2015**, *115*, 7794–7839.
- (78) Villalonga, R.; Cao, R.; Frago, A. Supramolecular Chemistry of Cyclodextrins in Enzyme Technology. *Chem. Rev.* **2007**, *107*, 3088–3116.
- (79) Zhang, R.; Li, L.; Feng, J.; Tong, L.; Wang, Q.; Tang, B. Versatile Triggered Release of Multiple Molecules from Cyclodextrin-Modified Gold-Gated Mesoporous Silica Nanocontainers. *ACS Appl. Mater. Interfaces* **2014**, *6*, 9932–9936.
- (80) Sun, S.; Zeng, H.; Robinson, D. B.; Raoux, S.; Rice, P. M.; Wang, S. X.; Li, G. Monodisperse MFe_2O_4 ($M=Fe, Co, Mn$) Nanoparticles. *J. Am. Chem. Soc.* **2004**, *126*, 273–279.
- (81) Jang, J. T.; Nah, H.; Lee, J. H.; Moon, S. H.; Kim, M. G.; Cheon, J. Critical Enhancements of MRI Contrast and Hyperthermic Effects by Dopant-Controlled Magnetic Nanoparticles. *Angew. Chem. Int. Ed.* **2009**, *48*, 1234–1238.
- (82) Lee, N.; Hyeon, T. Designed Synthesis of Uniformly Sized Iron Oxide Nanoparticles for Efficient Magnetic Resonance Imaging Contrast Agents. *Chem. Soc. Rev.* **2012**, *41*, 2575–2589.
- (83) Dong, J.; Zink, J. I. Taking the Temperature of the Interiors of Magnetically Heated Nanoparticles. *ACS Nano* **2014**, *8*, 5199–5207.
- (84) Liong, M.; Lu, J.; Kovichich, M.; Xia, T.; Ruehm, S. G.; Nel, A. E.; Tamanoi, F.; Zink, J. I. Multifunctional Inorganic Nanoparticles for Imaging, Targeting, and Drug Delivery. *ACS Nano* **2008**,

- 2, 889–896.
- (85) Jiang, H.; Xu, F. J. Biomolecule-Functionalized Polymer Brushes. *Chem. Soc. Rev.* **2013**, *42*, 3394–3426.
- (86) Paolino, M.; Ennen, F.; Lamponi, S.; Cernescu, M.; Voit, B.; Cappelli, A.; Appelhans, D.; Komber, H. Cyclodextrin-Adamantane Host-Guest Interactions on the Surface of Biocompatible Adamantyl-Modified Glycodendrimers. *Macromolecules* **2013**, *46*, 3215–3227.
- (87) Hwang, A. A.; Lee, B. Y.; Clemens, D. L.; Dillon, B. J.; Zink, J. I.; Horwitz, M. A. Tuberculosis: pH-Responsive Isoniazid-Loaded Nanoparticles Markedly Improve Tuberculosis Treatment in Mice. *Small* **2015**, *11*, 5066–5078.

Chapter 4

Shortwave Infrared Imaging with J-aggregates Stabilized in Hollow Mesoporous Silica Nanoparticles

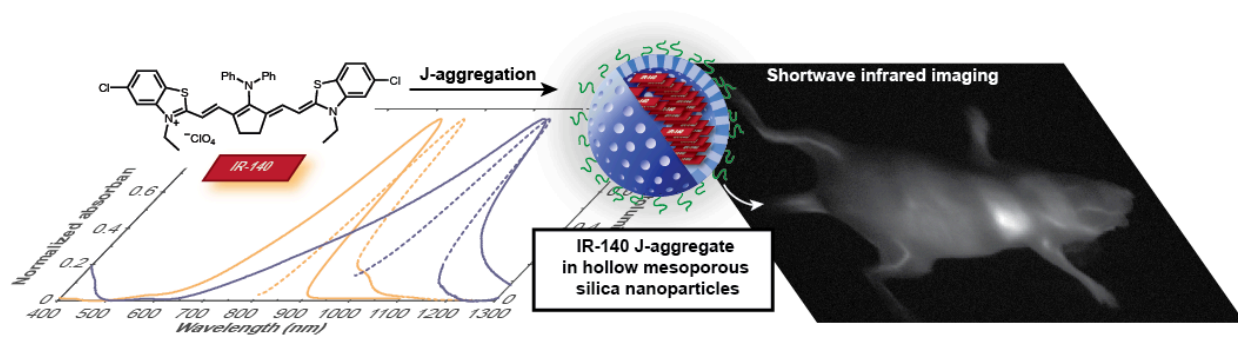
This chapter of the dissertation was adapted and reprinted with permission from Wei Chen, Chi-An Cheng, Emily D. Cosco, Shyam Ramakrishnan, Jakob G. P. Lingg, Oliver T. Bruns, Jeffrey I. Zink, Ellen M. Sletten *Journal of the American Chemical Society* **2019**, *141*, 12475–12480. Copyright 2019 American Chemical Society. Co-author contributions: Chen W., Cheng C. A., and Cosco E. D. performed the materials synthesis, characterization, photophysics, and cells studies. Cosco E. D., Ramakrishnan S., and Lingg J. G. P. performed the shortwave infrared imaging and animal studies. Oliver T. Bruns, Jeffrey I. Zink, and Ellen M. Sletten were the P.Is. The texts of introduction, result and discussion were mainly organized and written by Professor Ellen M. Sletten when preparing the manuscript for publication.

Keywords of this chapter: shortwave infrared, J-aggregates, hollow mesoporous silica nanoparticles, IR-140, near-infrared fluorophore, in vivo imaging

Abstract

Tissue is translucent to shortwave infrared (SWIR) light, rendering optical imaging superior in this region. However, the widespread use of optical SWIR imaging has been limited, in part, by the lack of bright, biocompatible contrast agents that absorb and emit light above 1000 nm. J-aggregation offers a means to transform stable, near-infrared (NIR) fluorophores into red-shifted SWIR contrast agents. Here we demonstrate that J-aggregates of NIR fluorophore IR-140 can be prepared inside hollow mesoporous silica nanoparticles (HMSNs) to result in nanomaterials that absorb and emit SWIR light. The J-aggregates inside PEGylated HMSNs are stable for multiple weeks in buffer and enable high resolution imaging *in vivo* with 980 nm excitation.

Table of Content Figure



4.1 Introduction

Optical imaging with shortwave infrared (SWIR, 1000–2000 nm) light has emerged as a powerful method of fluorescence imaging in animals due to the superior resolution and contrast one can achieve with low energy light (Figure 4.1A).¹ A primary challenge with SWIR imaging is the development of bright, biocompatible, SWIR contrast agents.² Originally, the advantageous qualities of imaging in the SWIR region were showcased with carbon nanotubes,³ quantum dots,⁴ and rare earth nanomaterials⁵. In efforts to set the stage for clinical translation, the past three years have seen a focus on the synthesis of non-toxic, SWIR-emissive organic fluorophores.⁶ This work has significantly expanded the suite of fluorophores that emit above 1000 nm; however, challenges remain in the stability, delivery, and brightness of SWIR dyes. Consequently, we looked to explore an alternative avenue to create SWIR organic materials: J-aggregation.

J-aggregation is the slip-stacked alignment of chromophores that leads to constructive coupling of the excited state transition dipoles (Figure 4.1B).⁷ The photophysical consequences of J-aggregation are bathochromically-shifted absorption and emission spectra, narrow absorption and emission bands with small Stokes shifts, enhanced absorbance coefficients (ϵ), and shortened fluorescence lifetimes which can result in enhanced quantum yields (Φ_F) and cycling rates. Many J-aggregate characteristics are beneficial qualities for *in vivo* imaging: red-shifted absorption and emission spectra will enable significant depth penetration during both the excitation and image acquisition,^{2,8} narrow bands can facilitate multiplexed imaging, and increased ϵ will result in bright materials. Despite the significant photophysical advantages J-aggregates typically have over the monomer, there are few reports of employing J-aggregates for *in vivo* imaging due to the difficulty

in obtaining and stabilizing the necessary chromophore alignment in complex settings.⁹

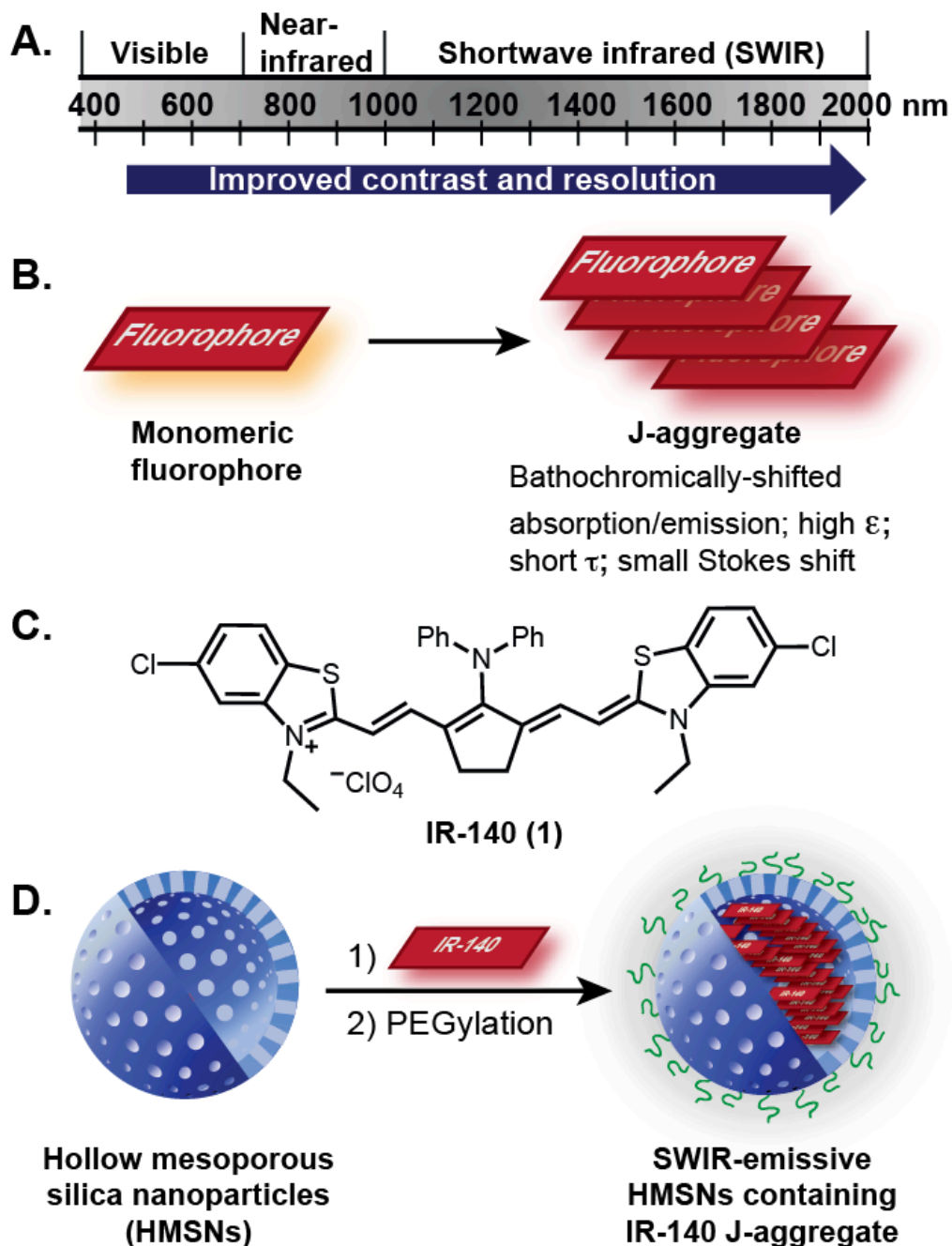


Figure 4.1. (A) Regions of the electromagnetic spectrum employed for optical imaging. For further details on contrast and resolution within regions of the SWIR see references 1bc; 8b-c. (B) J-aggregation and characteristic photophysical properties. (C) IR-140. (D) Work reported herein: the stabilization of IR-140 J aggregates in hollow mesoporous silica nanoparticles (HMSNs) to result in biocompatible SWIR-emissive contrast agents.

Nanostructures can sequester and protect payloads, rendering nanomaterials a promising approach toward stabilizing J-aggregates *in vivo*. In 2016, Zheng and coworkers performed image-guided surgery with porphyrin lipids that formed J-aggregates upon self-assembly into nanovesicles.¹⁰ The following year, Xu and coworkers prepared pyrrolopyrrole cyanine J-aggregate-containing polymer micelles, which could be visualized after subcutaneous injection.¹¹ In work recently published, Fan and coworkers reported a squaraine J-aggregate, stabilized in polymeric micelles, for SWIR image-guided photothermal therapy.¹² Each of these reports utilizes self-assembled organic nanomaterials,¹³ which are prone to disassembly when diluted in the presence of hydrophobic biomolecules, leading to destabilization of the J-aggregate.¹⁴ Here, we employ robust, biocompatible, hollow mesoporous silica nanoparticles to stabilize and protect SWIR-emissive J-aggregates of IR-140 for *in vivo* imaging (Figure 4.1C/D).

Hollow mesoporous silica nanoparticles (HMSNs) have 2–4 nm pores that open into a large, 10–200 nm cavity, allowing these nanostructures to carry significant cargo.¹⁵ The surfaces of the HMSNs can be modified to alter the biodistribution of the nanoparticles.¹⁶ Consequently, there are numerous reports of HMSNs as the core scaffold of multifunctional materials.^{15a,16b,17} Included in these studies are the loading or conjugation of visible¹⁸ and near-infrared^{15a,19} fluorophores and administering the resulting nanomaterials for imaging. However, the controlled assembly of J-aggregates in HMSNs has yet to be demonstrated.

To realize SWIR-emissive J-aggregates inside HMSNs, we utilized the heptamethine dye IR-140 (1). IR-140 is a commercially available NIR fluorophore ($\lambda_{\text{max,abs}}=826$ nm, $\lambda_{\text{max,em}}=875$ nm) that has been applied as a photopolymerization initiator,²⁰ fluorescent payload,²¹ component of

plasmonic arrays,²² as well as a Raman²³ and two-photon²⁴ imaging agent. In 2016, Wang and Weiss reported that introduction of IR-140 to glutathione coated quantum dots results in J-aggregate formation with two aggregates observed: J1 ($\lambda_{\text{max,abs}}=965$ nm, non-emissive), and J2 ($\lambda_{\text{max,abs}}=1040$ nm, $\lambda_{\text{max,em}}=1047$ nm).²⁵ We envisioned that similar IR-140 J-aggregates could be formed on the negatively charged pores and inner surface of HMSNs. Further, once the aggregates were assembled inside the particles, the hydrophobic nature of IR-140 would make them unlikely to disassemble in aqueous environments, rendering J-aggregates stable *in vivo*.

4.2 Experimental Section

4.2.1 Materials

IR-140 (95%), cetyltrimethylammonium chloride (CTAC, 25 wt% in water), cetyltrimethylammonium bromide (CTAB, 99+%), tetraethyl orthosilicate (TEOS, 98%), (3-aminopropyl)triethoxysilane (APTS, 99%), ammonium nitrate (NH₄NO₃, 98+%), triethanolamine (TEA, 99+%), 2-(*N*-morpholino)ethanesulfonic acid hydrate (MES hydrate, 99.5+%), and phosphate buffer saline (X10) were purchased from Sigma-Aldrich. Sodium carbonate anhydrous (99.5+%) was purchased from EMD Millipore. Alpha-methoxy-omega-carboxylic acid poly(ethylene glycol) (MeO-PEG-COOH, Mw = 23,000 Da) was purchased from Iris Biotech GmbH. Ethanol (200 proof) was purchased from Decon Laboratories, Inc. 1-Ethyl-3-(3-dimethylaminopropyl) carbodiimide hydrochloride (EDC-HCl, 99+%), and *N*-hydroxysulfosuccinimide sodium salt (sulfo-NHS, 99+%) were purchased from CovaChem. Dimethyl sulfoxide (DMSO, 99.9+%), sodium hydroxide (NaOH, 97+%), and ammonium hydroxide (NH₄OH) purchased from Fisher Scientific. Dulbecco's modified Eagle's medium

(DMEM) with high glucose, fetal bovine serum (FBS), antibiotics (10,000 U/mL penicillin, 10,000 µg/mL streptomycin, and 29.2 mg/mL L-glutamine), trypsin-ethylenediaminetetraacetic acid (trypsin-EDTA) (0.05 %), and Dulbecco's phosphate-buffered saline (DPBS) were purchased from Gibco. Cell counting kit-8 (CCK-8) was purchased from Dojindo Molecular Technologies, Inc. All chemicals were used without further purification.

4.2.2 Instrumentation

Bath sonication was performed using a Branson 3800 ultrasonic cleaner or an Elma S15 Elmasonic. Masses for analytical measurements were taken on a Sartorius MSE6.6S-000-DM or MSA6.6S-000-DM Cubis Micro Balance. Absorbance spectra were collected on a JASCO V-770 UV-Visible/NIR spectrophotometer with a 2000 nm/min scan rate after blanking with the appropriate solvent, on a Cary 5000 UV-Vis-NIR spectrophotometer or on a Shimadzu UV-1800 UV-Visible Scanning Spectrophotometer. Photoluminescence spectra were obtained on a Horiba Instruments PTI QuantaMaster Series fluorometer. Quartz cuvettes (10 mm, 3 mm and 2 mm) were used for absorbance and photoluminescence measurements. The dynamic light scattering (DLS) measurements were performed on a ZETAPALS instrument with a 660 nm red diode laser (Brookhaven Instruments Corporation). Zeta potential value was measured on a Malvern Zetasizer Nano at room temperature. Nitrogen adsorption/desorption isotherms were acquired at 77 K on a Autosorb-iQ, Quantachrome Instruments. Transmission electron microscopy was performed on a Tecnai T12 instrument with an operating voltage of 120 kV. Animal imaging was performed on custom instrumentation described below.

4.2.3 Synthesis of Stöber silica spheres

Stöber silica spheres were synthesized by a sol-gel reaction in basic solution as reported

previously. Briefly, NH_4OH (1.6 mL) was dissolved in a mixture of ethanol (71.4 mL) and D.I. water (10 mL) in a 250 mL flask with vigorous stirring. After stirring for 10 min at room temperature, TEOS (2 mL) was rapidly added to the solution which was further stirred for 1 h at room temperature for the formation of Stöber silica nanoparticles. Afterwards, the solution containing Stöber silica spheres was centrifuged (7830 rpm, 7197 g, 20 min) and washed with ethanol and D.I. water twice, respectively. The Stöber silica spheres were finally dispersed in 40 mL of D.I. water for further use.

4.2.4 Synthesis of hollow mesoporous silica nanoparticles (HMSNs)

The synthesis of hollow mesoporous silica nanoparticles (HMSNs) was carried out by using Stöber silica spheres as the hard templates which were later removed by selective etching in a basic solution. First, CTAC (2 g, 25 wt% in water solution) and TEA (20 mg) were dissolved in D.I. water (20 mL) in a 100 mL round-bottom flask with vigorous stirring at 80 °C. The reaction mixture was stirred for 5 min followed by the addition of 10 mL of Stöber silica sphere solution prepared as described above, and stirred for 20 min. To coat mesoporous silica on the surface of Stöber silica spheres, TEOS (150 μL) was added dropwise to the solution with vigorous stirring. The nanoparticles were designated as $\text{dSiO}_2@\text{MSNs}$ (Scheme 4.1). After 1 h, the solution was cooled to 50 °C and sodium carbonate (1.89 g) dissolved in D.I. water (3 mL) was added to selectively etch the Stöber silica sphere template in the mesoporous silica shell. The etching process was carried out at 50 °C for 2 h. Afterwards, the solution containing HMSNs were centrifuged (7830 rpm, 7197 g, 15 min) and washed with ethanol 3 times (3 x 50 mL) to remove the unreacted impurities. To remove the CTAC surfactant templates, HMSNs were dispersed in 50

mL of ethanol containing NH_4NO_3 (1 g). The solution was brought to 60 °C with vigorous stirring. After 1 h, the solution was cooled to room temperature, centrifuged (7830 rpm, 7197 g, 15 min), and washed once with ethanol (50 mL). The surfactant removal process was repeated two more times. Finally, surfactant free HMSNs were washed with D.I. water (2 x 50 mL) and ethanol (2 x 50 mL) twice, respectively and stored in 10 mL of absolute ethanol for further use.

4.2.5 Synthesis of APTS functionalized HMSNs (HMSNs-APTS)

APTS functionalized HMSNs (HMSNs-APTS) were synthesized by procedures similar to those of HMSNs. First, CTAC (2 g, 25 wt% in water solution) and TEA (20 mg) were dissolved in D.I. water (20 mL) in a 100 mL round-bottom flask with vigorous stirring at 80 °C. The reaction solution was stirred for 5 min followed by the addition of 10 mL of Stöber silica sphere solution prepared as described above. After stirring for 20 min, TEOS (150 μL) was added dropwise to the solution with vigorous stirring. After 1 h, a mixture of APTS (40 μL) and ethanol (120 μL) was added to the solution followed by stirring for another 1 h at 80 °C to conjugate APTS on the surface of HMSNs. The Stöber silica sphere etching and surfactant removal processes were the same as described in the synthesis of HMSNs section. The resulting nanoparticles were dispersed in ethanol and designated as HMSNs-APTS.

4.2.6 Synthesis of APTS functionalized Stöber silica Spheres

The Stöber silica spheres (80 mg) were dispersed in a mixture of ethanol (20 mL) and APTS (10 μL). The solution was stirred at room temperature for 5 min and was brought to 78 °C. Then, the solution was refluxed for 12 h with vigorous stirring. Subsequently, the solution was cooled to room temperature, and APTS functionalized Stöber silica spheres (Stöber silica spheres-APTS) were washed twice (2 x 20 mL) with ethanol and stored in 10 mL of absolute ethanol for further

use.

4.2.7 Loading of IR-140 in HMSNs, HMSNs-APTS, or dSiO₂@MSNs

HMSNs, HMSNs-APTS, or dSiO₂@MSNs (2 mg) dispersed in ethanol were centrifuged (14000 rpm, 16873 g, 15 min) and washed with DMSO (3 x 1 mL) before IR-140 loading. HMSNs or HMSNs-APTS were then dispersed in 200 µL of a DMSO solution containing 5, 10, or 20 mM IR-140 by sonication in a bath sonicator for 10 min. For dSiO₂@MSNs, the nanoparticles were dispersed in 200 µL of a DMSO solution containing 5, or 20 mM IR-140 by sonication in a bath sonicator for 10 min. After stirring the solution for 20 h to make IR-140 diffuse into the pores and cavity of HMSNs, HMSNs-APTS, or dSiO₂@MSNs, the solution containing the particles was centrifuged (14000 rpm, 16873 g, 15 min) and the supernatant was kept for loading capacity calculations. Then, IR-140 loaded HMSNs were washed with three different methods: (a) washed with PBS (1 mL) using a water bath sonication, (b) gently washed with PBS (1 mL) by using plastic transfer pipettes, and (c) washed with water (1 mL) by using plastic transfer pipettes, respectively, to remove free DMSO and DMSO loaded in the pores. IR-140 loaded HMSNs-APTS, or IR-140 loaded dSiO₂@MSNs were washed only by method (b). Afterwards, IR-140 loaded nanoparticles were centrifuged (8000 rpm, 5510 g, 3 min) to remove the supernatant. The washing steps were repeated 5 times. Finally, IR-140 loaded HMSNs, HMSNs-APTS, or dSiO₂@MSNs were re-dispersed in PBS (1 mL) solution by sonication.

4.2.8 PEG conjugation on the surface of IR-140 loaded HMSNs-APTS (HMSNs-PEG preparation)

To increase the colloidal stability, PEG was conjugated on the surface of IR-140 loaded

HMSNs-APTS via amide bond formation. After IR-140 was loaded in HMSNs-APTS, the nanoparticles were gently washed with PBS (5 x 1 mL), D.I. water (2 x 1 mL), and MES buffer solution (pH = 6.0, 10 mM) (1 x 1 mL), respectively. Finally, IR-140 loaded HMSNs-APTS (2 mg) were dispersed in MES buffer (1 mL) by sonication. Alpha-methoxy-omega-carboxylic acid poly(ethylene glycol) (MeO-PEG-COOH, CAS No. 92450-99-2) (10 mg) was dissolved in MES buffer (200 μ L) followed by the addition of EDC-HCl (5 mg) and sulfo-NHS (2.5 mg) pre-dissolved in MES buffer (300 μ L). The solution was stirred for 30 min. Then, the MES buffer solution containing the activated MeO-PEG-COOH (500 μ L) was added to 1 mL of 2 mg/mL IR-140 loaded HMSNs-APTS MES solution. The solution was further mixed and stirred for 20 h to conjugate PEG on the surface of IR-140 loaded HMSNs-APTS. Then, IR-140 loaded HMSNs-PEG were centrifuged (10000 rpm, 8609 g, 10 min) and washed with D.I. water (2 x 1 mL) and PBS (1 x 1 mL) to remove the excess MeO-PEG-COOH, EDC-HCl, sulfo-NHS, and MES buffer solution. Finally, IR-140 loaded HMSNs-PEG were dispersed in PBS buffer (1 mL) solution for UV-Vis-NIR or photoluminescence measurements.

4.2.9 Cell culture procedures

HeLa cells, a cervical cancer cells line, were cultured in T-75 flasks (Corning) with vented caps in a high glucose Dulbecco's modified Eagle's medium (DMEM) supplemented with 10 % fetal bovine serum (FBS), and 1 % antibiotics (100 U/mL penicillin and 100 μ g/mL streptomycin) in a humidity-controlled incubator at 37 °C with 5% CO₂. The HeLa culture media were daily changed and the cells were harvested by trypsinization with 0.05% trypsin-ethylenediaminetetraacetic acid (EDTA) for passaging every 2–3 days.

4.2.10 Animal procedures

Animal experiments were conducted in accordance with the approved institutional protocols of Helmholtz Zentrum München. Non-invasive whole mouse imaging was performed on two six-week old female CD-1 nude mice (22.4 g, 19.1 g), purchased from Charles River Laboratories. Mice were anesthetized with an i.p. injection of a ketamine/xylazine mixture. Tail vein injections were performed with a catheter assembled from a 30 ga needle connected through plastic tubing to a second 30 ga needle with syringe prefilled with isotonic saline solution. The bevel of the needle was then inserted into the tail vein and secured using tissue adhesive.

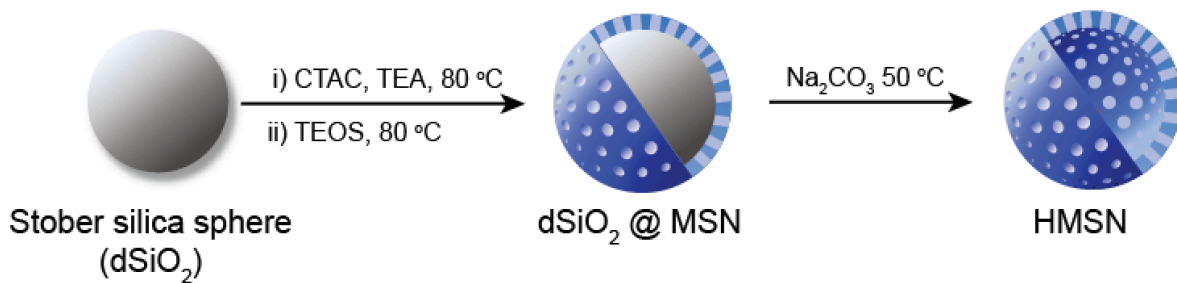
4.2.11 SWIR imaging apparatus

For whole mouse imaging, we used a custom-built setup. A 35 W 980 nm laser (Lumics LU0980D350-D30AN) was coupled in a fiber (600 μm core, Thorlabs BF46LS01) The output from the fiber was fixed in an excitation cube and reflected off of a mirror (Thorlabs BBE1-E03), and passed through a positive achromat (Thorlabs AC254-050-B), 1000 nm shortpass filter (Thorlabs FESH 1000), and an engineered diffuser (Thorlabs ED1-S20-MD) to provide uniform illumination over the working area. The excitation flux at the object was adjusted to be close to 100 mWcm^{-2} with an error of $\pm 3\%$ (power density used is defined separately in each experiment). The working area was covered by a heating mat coated with blackout fabric (Thorlabs BK5). A 4-inch square first-surface silver mirror (Edmund Optics, 84448) was used to direct the emitted light through a custom filter set (Thorlabs NF980-41, 3x FELH1000, 2x FGL1000) to an Allied Vision Goldeye G-032 Cool TEC2 camera at $-30 \text{ }^\circ\text{C}$, equipped with a C-mount camera lens (Navitar, SWIR-35). The assembly was partially enclosed to avoid excess light while enabling manipulation

of the field of view during operation. The image acquisition toolbox of MATLAB programming environment is used in combination with a custom MATLAB script to preview and collect the required image data. The prepared MATLAB script allows users to access basic functionalities of the image acquisition device by establishing a packet jitter free data streaming link between the desktop computer and the acquisition device.

4.3 Results and discussion

We prepared HMSNs by synthesizing a mesoporous silica coating on a Stöber sphere core that was subsequently removed via etching with sodium carbonate (Scheme 4.1, Figure 4.2). The HMSNs were treated with varying amounts of IR-140 in different solvents (Figure 4.3A). J-aggregate formation was assayed by UV/Vis/NIR spectroscopy evaluating loss of monomeric IR-140 at 826 nm and formation of the J-aggregates at 965 nm (J1) and 1040 nm (J2). Upon optimization, we found that SWIR J-aggregates could be obtained when IR-140 dissolved in dimethyl sulfoxide (DMSO) was combined with HMSNs and washed. The washing procedure proved essential for obtaining the desired J2 aggregate formation (Figure 4.3B, Figure 4.4), with gentle PBS washes yielding the largest amount of the desired J2 aggregate (dark blue, Figure 4.3B). When these optimized conditions were repeated on Stöber spheres that did not have pores or an inner surface for IR-140 to associate with, only a small J-band was observed (Figure 4.3B, gray line, Figure 4.5). Similar results were obtained when loading was performed on mesoporous silica coated Stöber spheres (Figure 4.4). These control experiment (Figure 4.6) suggests that the majority of IR-140 is protected inside the HMSN cavity. Through analysis of IR-140 collected after the washing procedures, we calculated the loading of IR-140 to be $\sim 10^3$ molecules/particle (Figure 4.7, Note S4.1)



Scheme 4.1. Synthesis of hollow mesoporous silica nanoparticles (HMSNs).

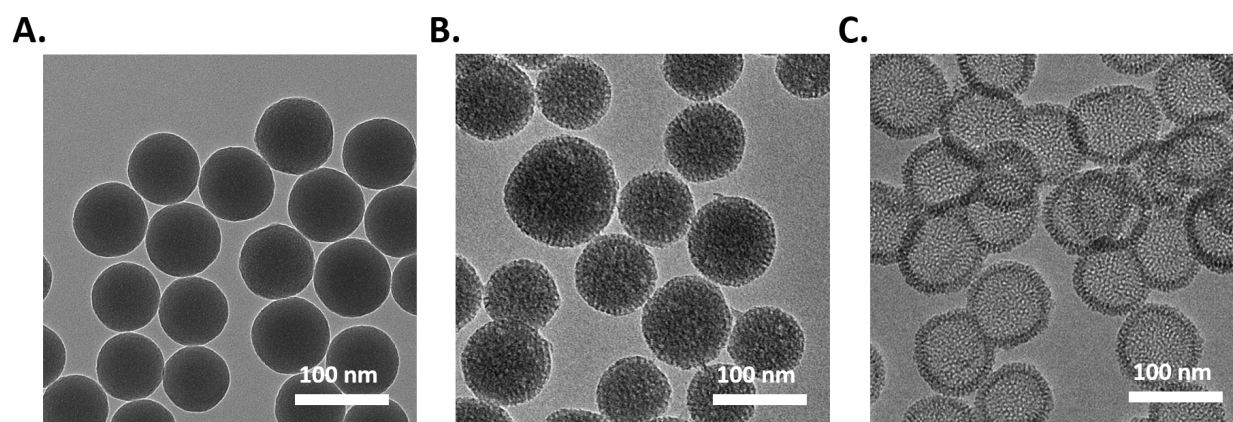


Figure 4.2. TEM images of (A) Stober silica spheres, (B) $d\text{SiO}_2 @ \text{MSNs}$, and (C) HMSNs. The nanoparticles were dispersed in ethanol at a concentration of 0.1 mg/mL. TEM images were measured on a Tecnai T12 instrument with an operating voltage of 120 kV.

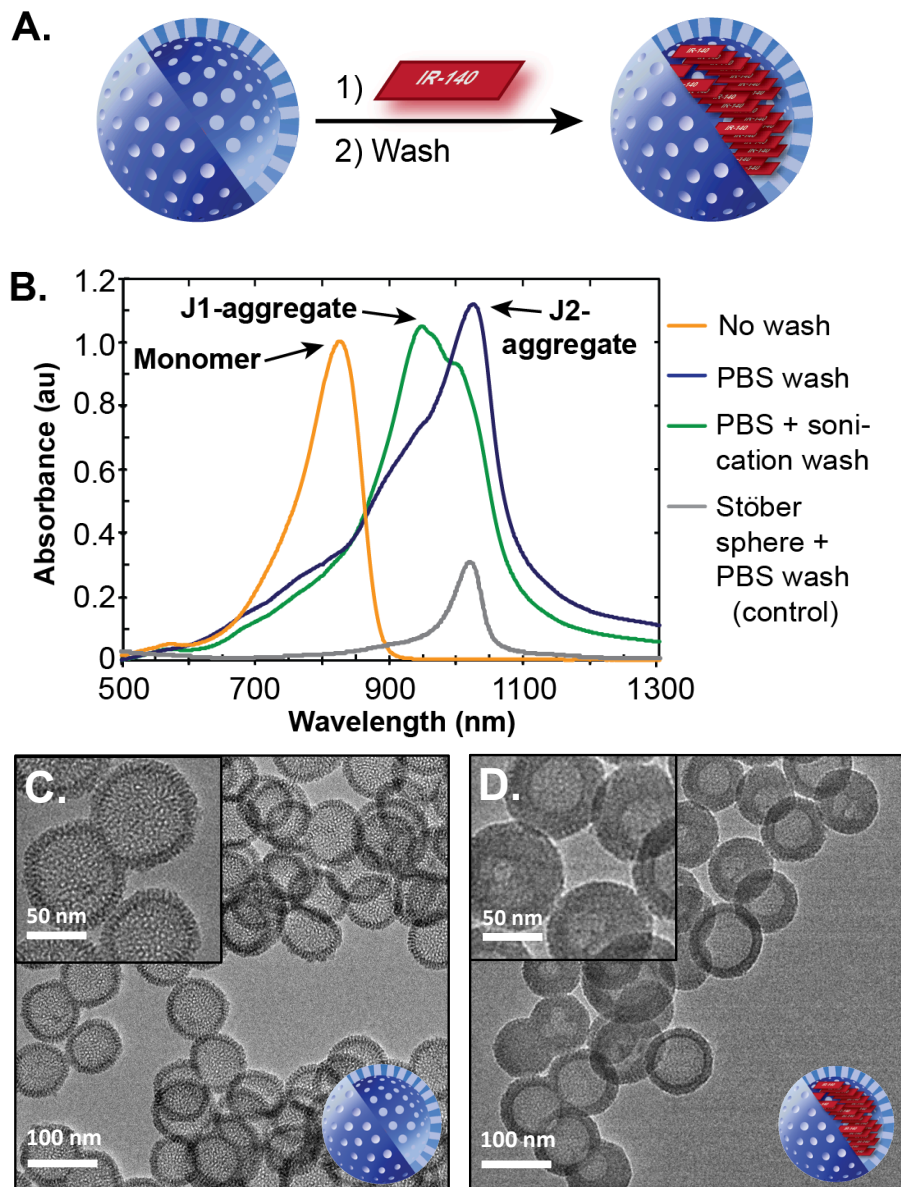


Figure 4.3. (A) Schematic of loading IR-140 into HMSNs. (B) Washing conditions facilitate J-aggregation. 10 mg/mL HMSNs were combined with 10 mM IR-140 in DMSO and washed with PBS with (green) and without (dark blue) sonication. Pre-wash spectrum, diluted 1:350 is shown in orange. Loading control for solid, non-porous Stöber spheres is shown in gray. (C/D) Transmission electron microscopy images of HMSNs with (D) and without (C) IR-140 treatment.

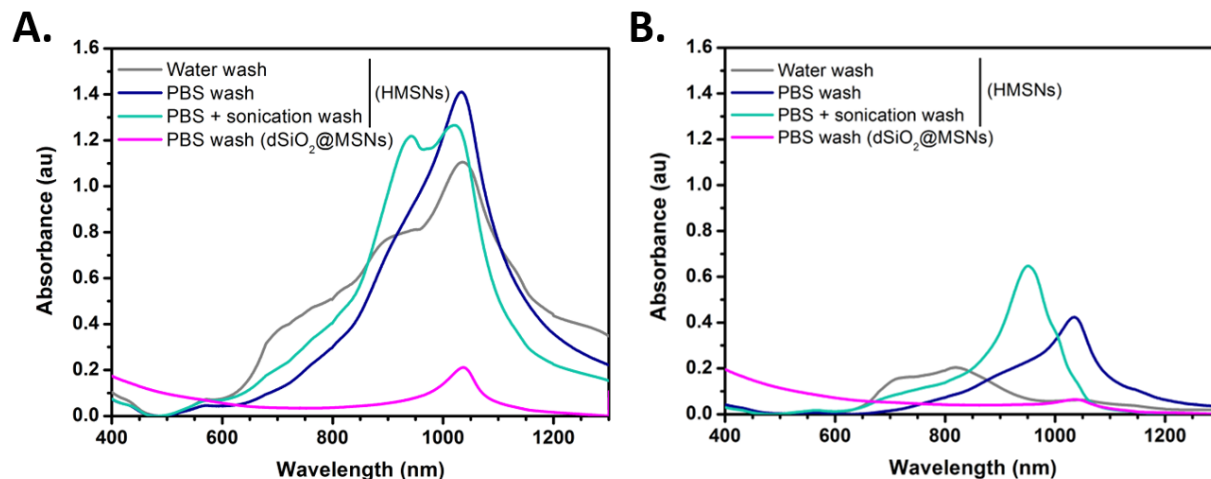


Figure 4.4. UV/Vis/NIR spectra of HMSNs or $\text{dSiO}_2\text{@MSNs}$ containing IR-140. The loading concentrations of IR-140 were (A) 20 mM and (B) 5 mM; HMSNs or $\text{dSiO}_2\text{@MSNs}$ were loaded at 10 mg/mL. The HMSNs particles were washed by methods (a, PBS with sonication, teal), (b, PBS, blue), or (c, water, gray) (5x, 1 mL), or the $\text{dSiO}_2\text{@MSNs}$ were washed by method (b, PBS, magenta) (see Section II, synthetic procedures). The absorbance spectra were measured with 10 mm quartz cuvettes at 0.25 mg nanoparticles/mL in PBS.

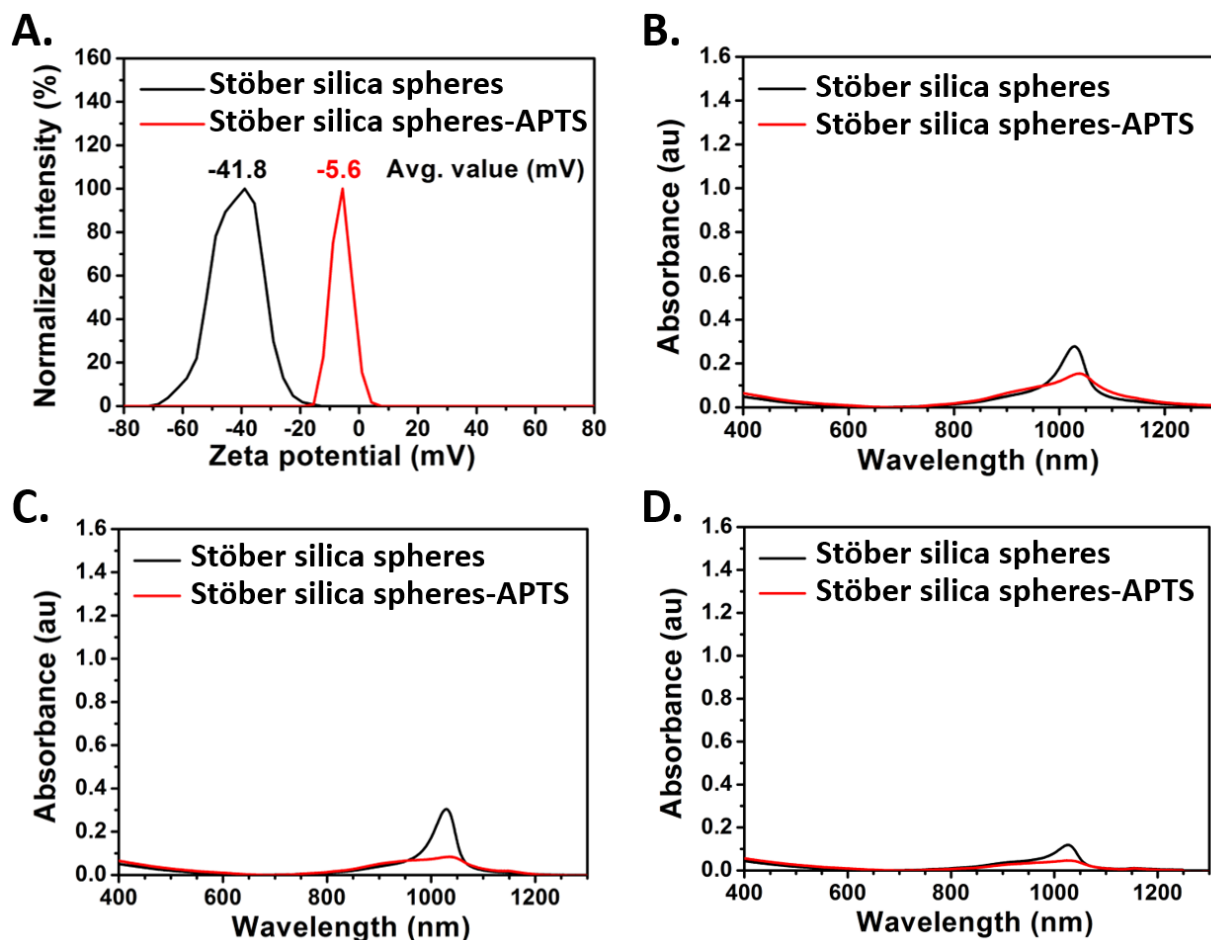


Figure 4.5. Control experiment with Stöber silica spheres. (A) The zeta potential of Stöber silica spheres (black), and Stöber silica spheres-APTS (red) in D.I. water at 0.05 mg/mL at room temperature. In the case of the APTS-modified Stöber spheres, we believe the surface is saturated with APTS as higher concentrations of APTS did not significantly change the zeta potential. (B/C/D) UV/Vis/NIR spectra of Stöber silica spheres (black) or Stöber silica spheres-APTS (red) containing IR-140. The loading concentrations of IR-140 were (B) 20 mM, (C) 10 mM, or (D) 5 mM; Stöber silica spheres or Stöber silica spheres-APTS were loaded at 10 mg/mL. After the loading, the particles were washed with PBS (5x, 1 mL). The absorbance spectra were measured with 10 mm quartz cuvettes at 0.25 mg nanoparticles/mL PBS.

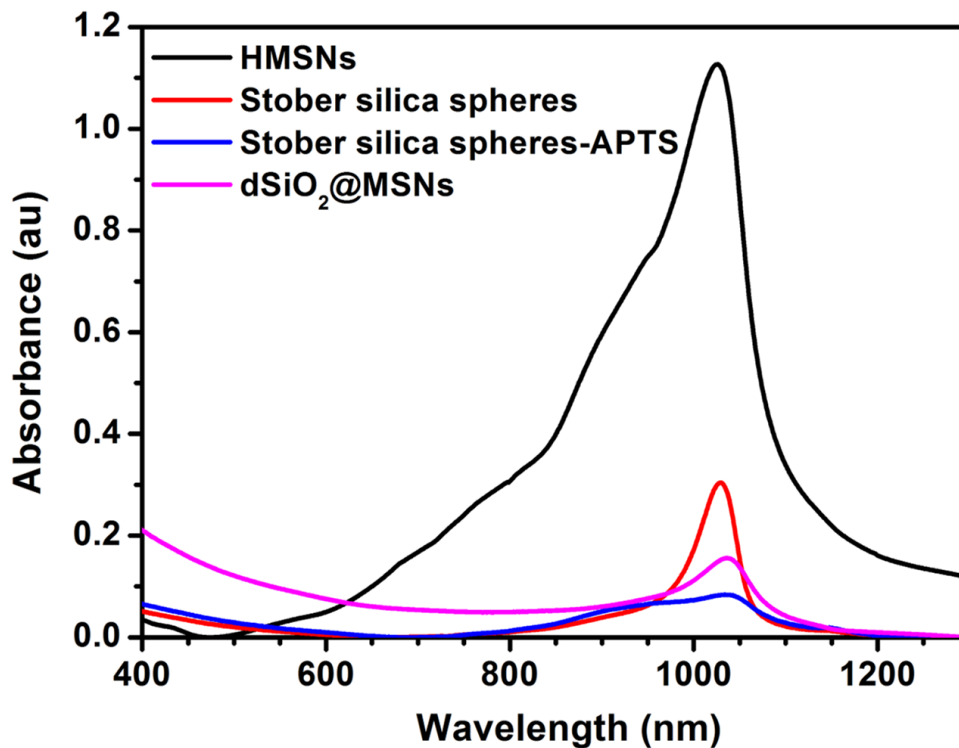


Figure 4.6. UV/Vis/NIR spectra of IR-140 loaded HMSNs, Stöber silica spheres, Stöber silica spheres-APTS, or dSiO₂@MSNs. The loading concentrations of IR-140 were 10 mM; HMSNs, Stöber silica spheres, Stöber silica spheres-APTS, or dSiO₂@MSNs were loaded at 10 mg/mL. After the loading, the particles were gently washed with PBS (5x, 1 mL). The absorbance spectra were measured with 10 mm quartz cuvettes at 0.25 mg nanoparticles/mL in PBS.

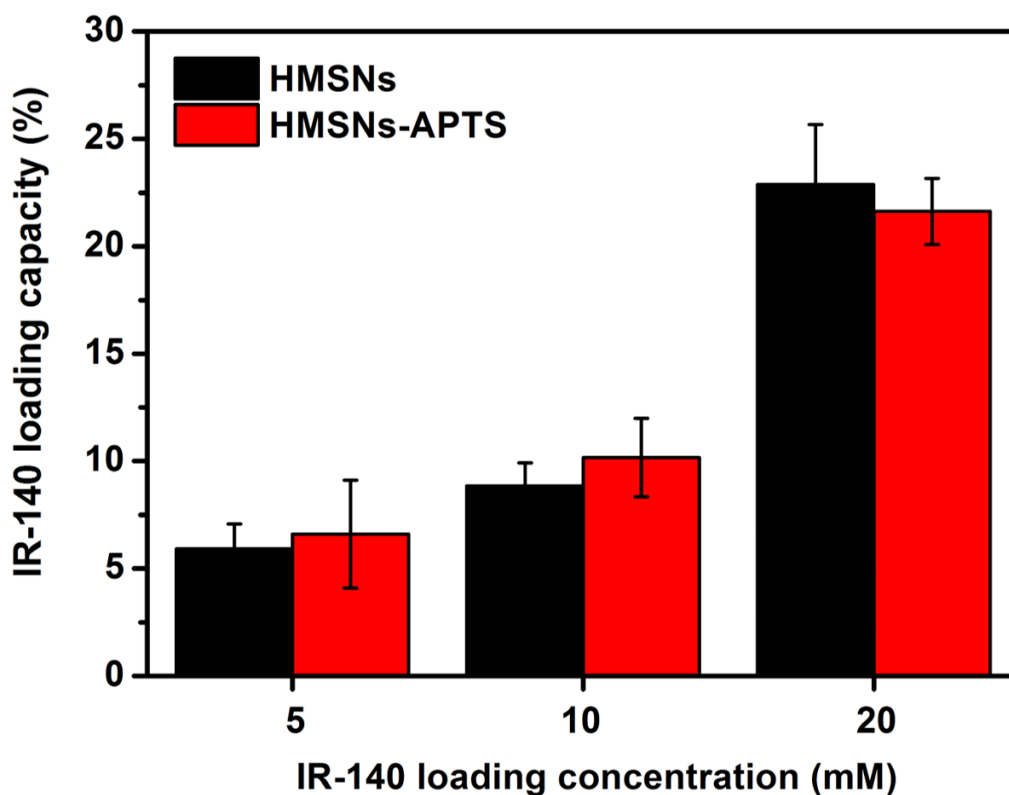


Figure 4.7. The loading capacity, defined as (grams IR-140/grams HMSNs or HMSNs-APTS) x 100%, of IR-140 in HMSNs (black) or HMSNs-APTS (red) at different IR-140 loading concentrations. The loading concentration of HMSNs or HMSNs-APTS was 10 mg/mL. Error represents the standard deviation of three replicates.

The HMSNs were further characterized through transmission electron microscopy (TEM), indicating ~85 nm particles with a distinct cavity and pores (Figure 4.3C). The pore size was quantified to be 3.2 nm through nitrogen adsorption experiments (Figure 4.8). While the pores are clearly visible in the TEM of the empty HMSNs, they are darkened after treatment with IR-140 (Figure 4.3D), suggesting the presence of IR-140. Control experiments in which HMSNs were subjected to PBS washing procedures but no IR-140 show no change in contrast of the pores upon TEM analysis (Figure 4.9).

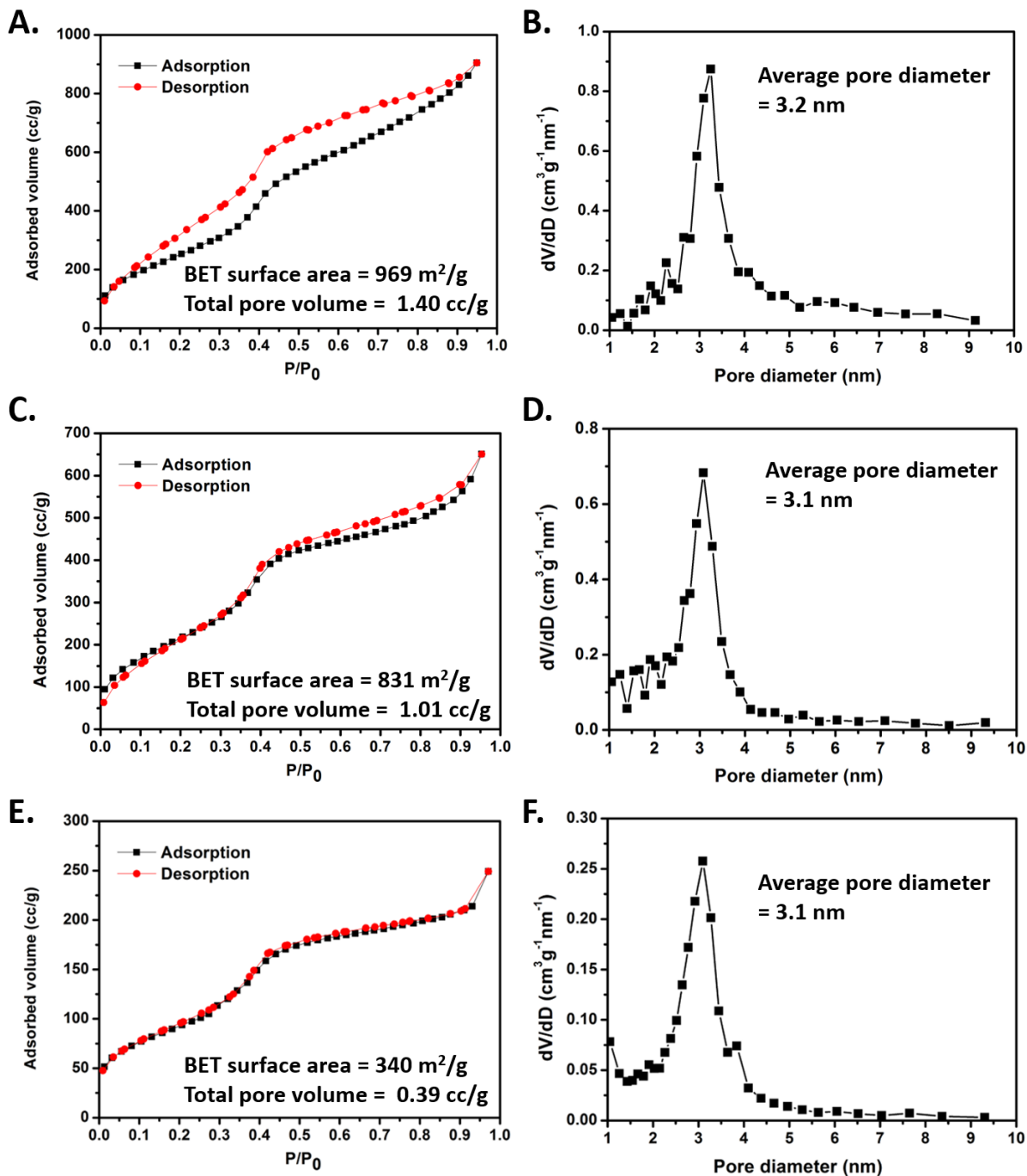


Figure 4.8. Nitrogen adsorption (black)/desorption (red) isotherms of (A) HMSNs, (C) HMSNs-APTS, and (E) dSiO₂@MSNs. The BET surface areas of HMSNs, HMSNs-APTS, and dSiO₂@MSNs are 969 m²/g, 831 m²/g, and 340 m²/g, respectively. The total pore volumes of HMSNs, HMSNs-APTS, and dSiO₂@MSNs are 1.40 cc/g, 1.01 cc/g, and 0.39 cc/g, respectively. Pore diameter distributions of (B) HMSNs, (D) HMSNs-APTS, and (F) dSiO₂@MSNs. The average pore diameters are 3.2 nm, 3.1 nm, and 3.1 nm, respectively.

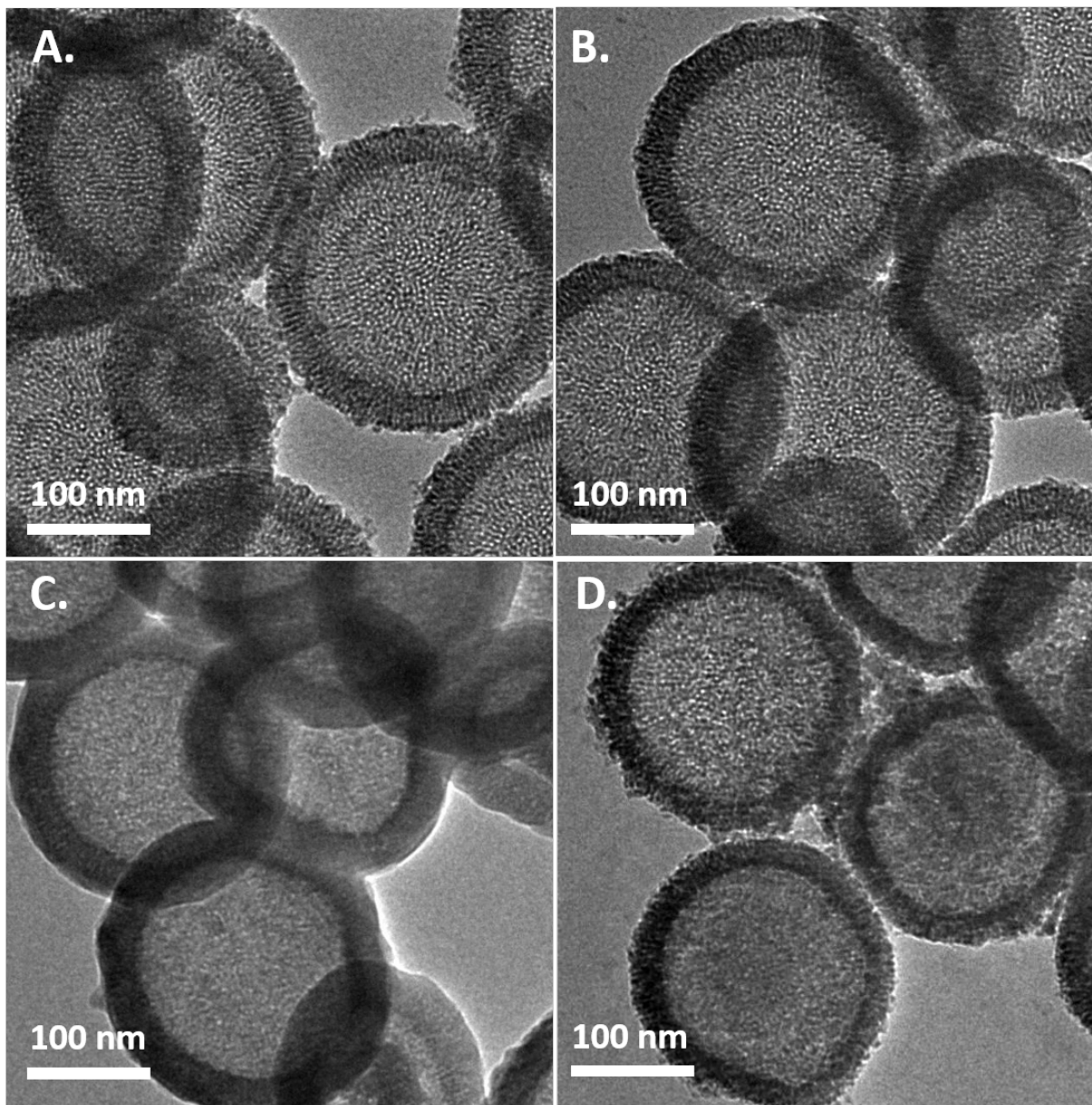
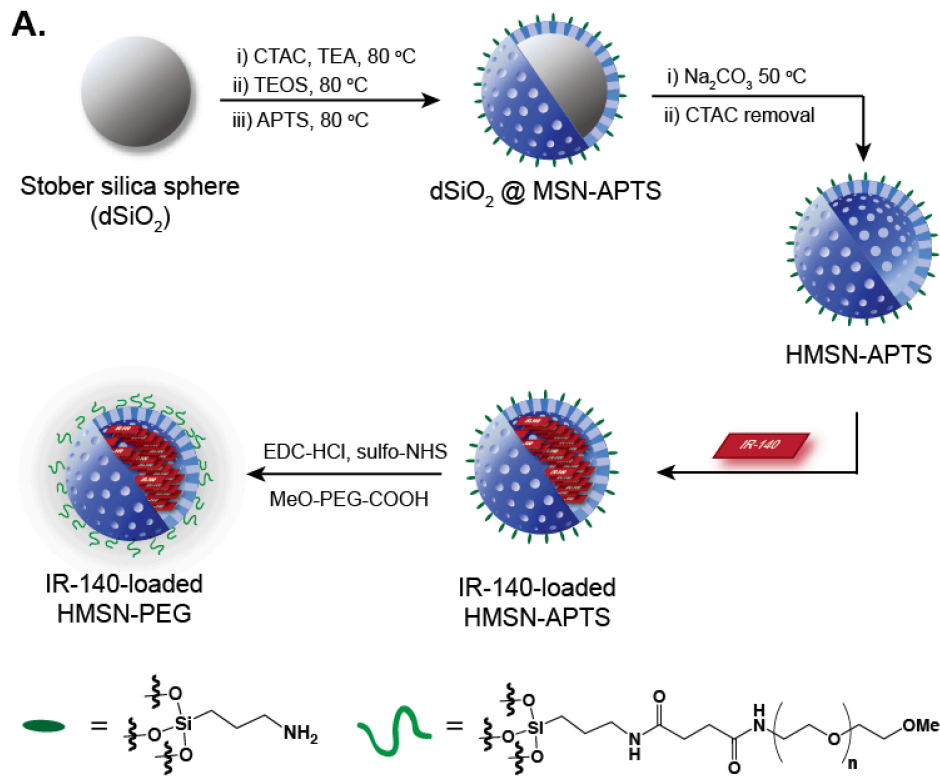
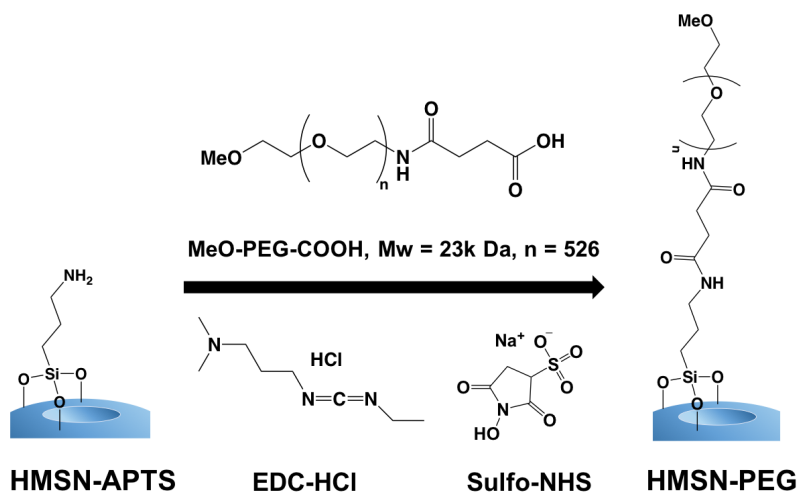


Figure 4.9. TEM images of HMSNs with (C) and without (A) IR-140 treatment. (A) HMSNs were dispersed in ethanol at a concentration of 0.1 mg/mL. (C) The loading concentration of IR-140 was 10 mM; HMSNs were loaded at 10 mg/mL. After loading, the particles were washed with PBS (5x, 1 mL) and dispersed in PBS at a concentration of 0.1 mg/mL. (B) As a control, HMSNs were washed with PBS (5x, 1 mL) but without the loading of IR-140. After washing, HMSNs were dispersed in PBS at a concentration of 0.1 mg/mL. (D) Mixture of HMSNs with and without IR-140 treatment. The mixed particles were prepared by mixing HMSNs in PBS solution (50 μ L, 0.2 mg/mL) with IR-140 loaded HMSNs in PBS solution (50 μ L, 0.2 mg/mL) at the mass ratio of 1:1. TEM images were measured on a Tecnai T12 instrument with an operating voltage of 120 kV.

After confirming that the HMSNs could facilitate J-aggregation of IR-140, we modified the surface with poly(ethylene glycol) (PEG) such that they could be suspended in aqueous media. This was accomplished by loading HMSNs that had undergone surface silanization with (3-aminopropyl)triethoxysilane (APTS) prior to Stöber sphere and surfactant removal (Scheme 4.2). This procedure resulted in HMSNs that were positively charged on the outside but still contained a negatively charged interior to associate with the cationic IR-140.²⁶ Nitrogen adsorption data (Figure 4.8) also suggests that the pores are not modified with APTS.²⁷ The introduction of IR-140 into the HMSNs-APTS proceeded similarly to the HMSNs, yielding analogous loading of IR-140 and a higher ratio of J2:J1 (Figure 4.10). Control experiments performed with Stöber spheres treated with APTS support that IR-140 is protected on the interior of the HMSNs (Figures 4.5 and 4.6). After loading, a 23kDa PEG-carboxylate was conjugated to the amines present on the outer surface of the HMSNs-APTS using carbodiimide chemistry (Scheme 4.2). Successful PEG conjugation was verified by changes in hydrodynamic diameter and zeta potential (Figures 4.11 and 4.12).



B.



Scheme 4.2. Synthesis of IR-140-loaded HMSN-PEG. (A) Overall synthesis starting from Stöber spheres. (B) Detailed schematic of conjugation of PEG to the surface of HMSN-APTS. Note that we believe the APTS modification is only on the outer surface due to the Stöber silica sphere blocking the inner surface and the CTAC surfactant blocking the pores.

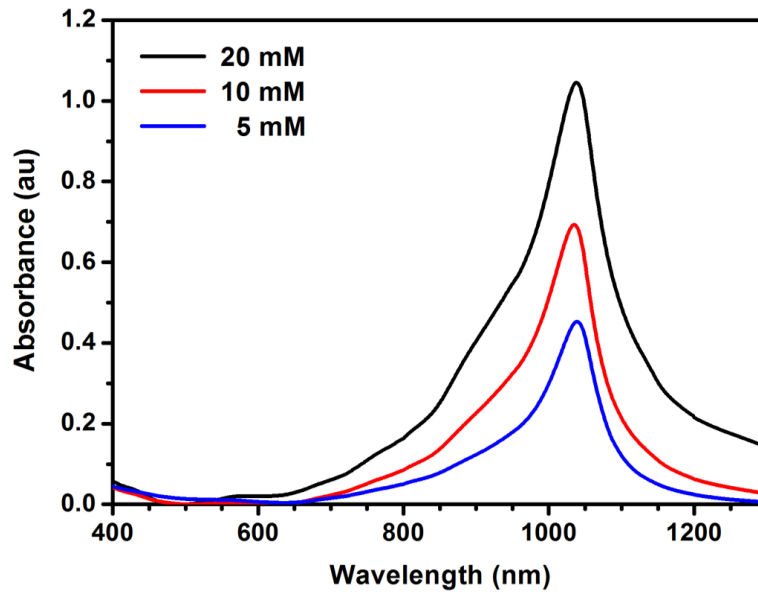


Figure 4.10. UV/Vis/NIR spectra of HMSNs-APTS containing IR-140 for dye loading concentrations of 20 mM (black), 10 mM (red), or 5 mM (blue) in PBS, after washing the particles with PBS (5 x 1 mL). The loading concentration of HMSNs-APTS was 10 mg/mL. The absorbance spectra were measured with 10 mm quartz cuvettes at 0.25 mg nanoparticles/mL.

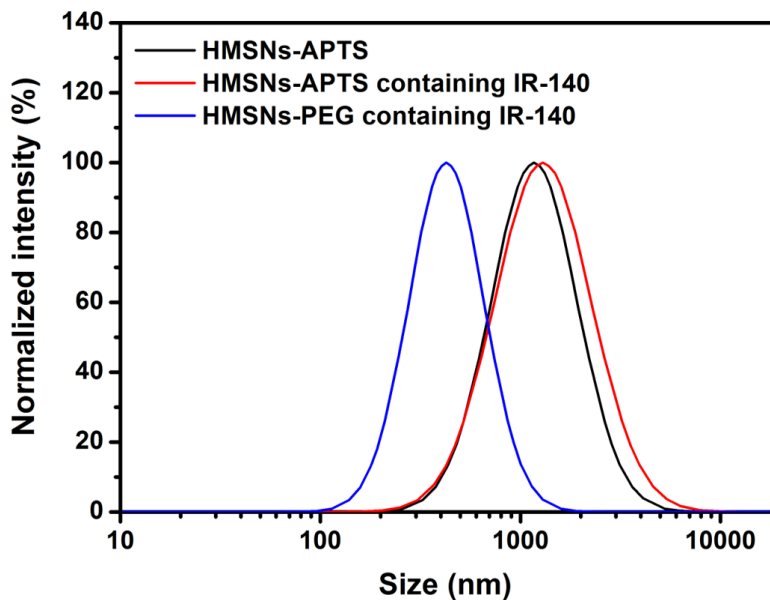


Figure 4.11. The dynamic light scattering size distribution of HMSNs-APTS (black), HMSNs-APTS containing IR-140 (red), and HMSNs-PEG containing IR-140 in PBS (blue) measured at 0.05 mg/mL at room temperature in PBS. Note that the HMSNs-APTS are not soluble in water and significant aggregation is observed in the DLS until after conjugation of PEG.

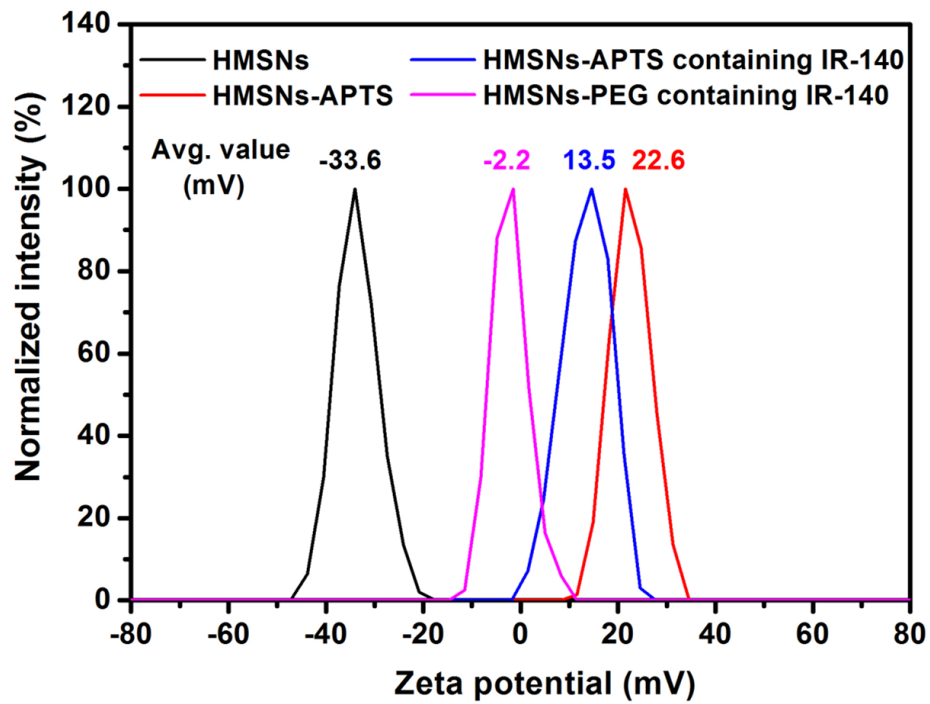


Figure 4.12. The zeta potential of HMSNs (black), HMSNs-APTS (red), HMSNs-APTS containing IR-140 (blue), and HMSNs-PEG containing IR-140 (pink) in D.I. water at 0.05 mg/mL at room temperature.

We evaluated the photophysical properties of the PEGylated HMSNs (HMSNs-PEG) containing IR-140 in comparison to IR-140 in solution as the monomer and J-aggregate (Figure 4.13A). Monomeric IR-140 has been well-characterized;²⁸ however, the solution J-aggregate of IR-140 had previously not been reported.²⁹ After screening numerous conditions (Figure 4.14), we found that 35% DMSO/0.9% NaCl in water afforded formation of the desired SWIR J-aggregate with a $\lambda_{\text{max,abs}}=1042$ nm, $\lambda_{\text{max,em}}=1043$ nm, $\epsilon=3.9 \times 10^5 \text{ M}^{-1}\text{cm}^{-1}$, and $\Phi_{\text{F}}=0.01\%$ (Table 4.1, Notes S4.2 and S4.3). The IR-140-containing HMSNs-PEG had similar spectral properties with a $\lambda_{\text{max,abs}}=1038$ nm, $\lambda_{\text{max,em}}=1047$ nm, although the absorbance was considerably broader, which we attribute to the presence of other non-emissive aggregate states. When solutions of IR-140 in DMSO, IR-140 in 35% DMSO/0.9% NaCl in water, and IR-140 loaded HMSNs-PEG in PBS were excited with a 980 nm laser, the wavelength to be used for *in vivo* imaging experiments, the IR-140 J-aggregate in solution and in the particles were similarly emissive, while the monomer was not excited by 980 nm light (Figures 4.13B and 4.15).³⁰ Thus, J-aggregation is essential for SWIR imaging with low energy excitation.

Table 4.1. Photophysical characterization of **1** (IR-140)

Species	$\lambda_{\text{max,abs}}$ (nm)	ϵ ($\text{M}^{-1}\text{cm}^{-1}$)	$\lambda_{\text{max,em}}$ (nm)	Φ (%)
1 monomer ^a	826	$1.7 \pm 0.1 \times 10^5$	875	20 ^[6]
1 J-aggregate ^b	1042	$3.9 \pm 0.4 \times 10^5$	1043	0.012 ± 0.007

^a in DMSO

^b in 35% DMSO/0.9% NaCl in water

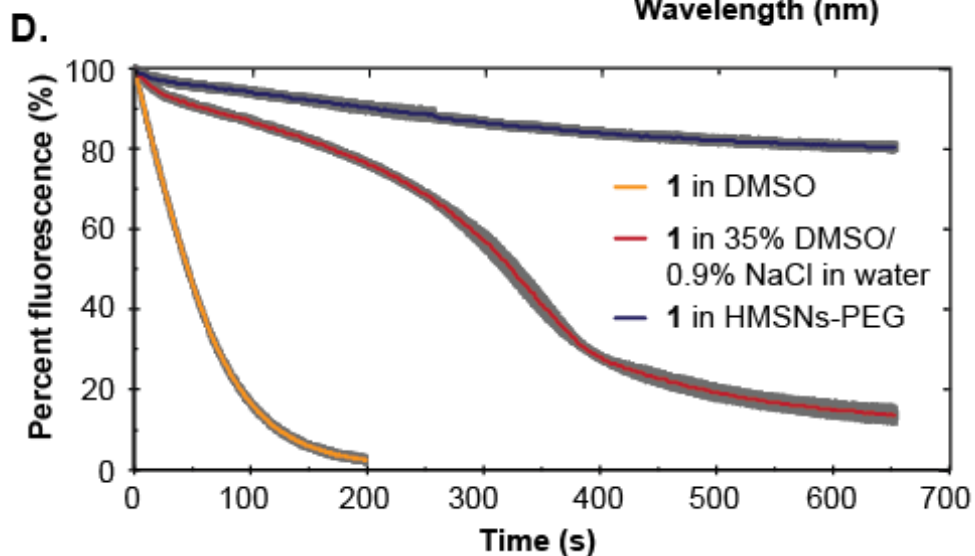
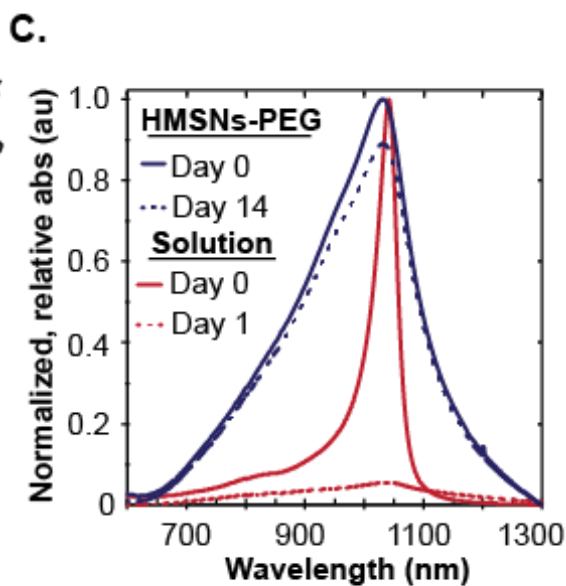
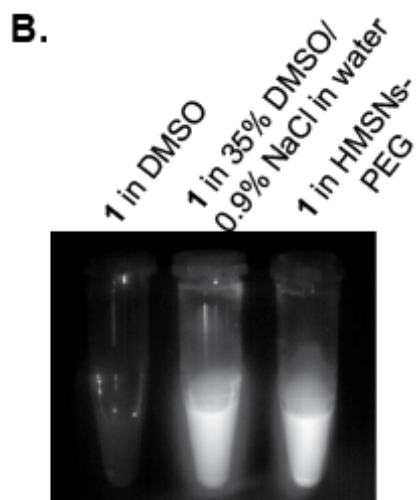
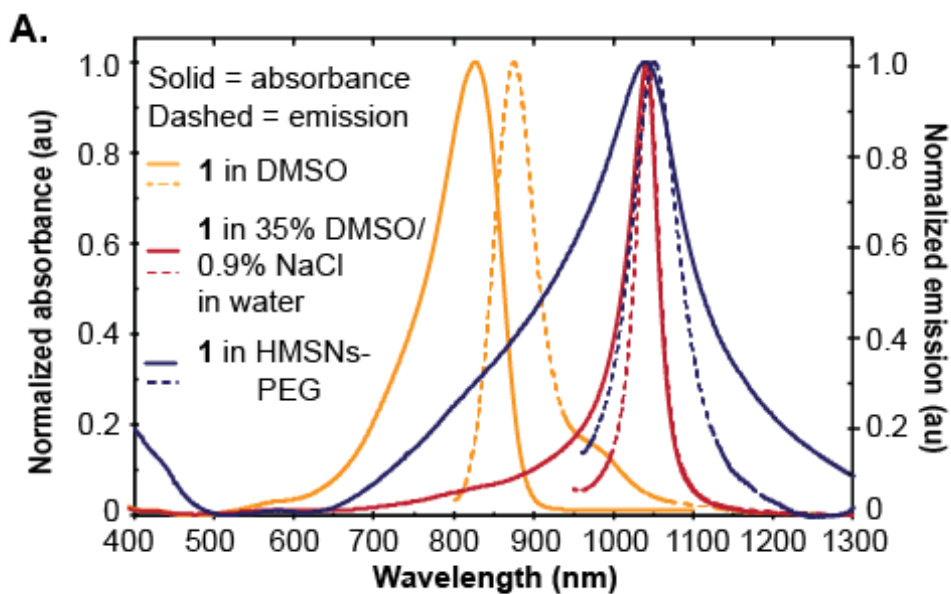


Figure 4.13. (A) Normalized absorption and emission of IR-140 J-aggregate in HMSNs-PEG (blue), J-aggregate in solution (red), and monomer (yellow). (B) Emission (1000–1700 nm) of IR-140 monomer (left), J-aggregate in solution (middle) and J-aggregate in HMSNs-PEG (right) upon 980 nm excitation. (C) Normalized relative absorption of IR-140 J-aggregate in 35% DMSO/0.9% NaCl in water (red) and in HMSNs-PEG in PBS (blue) on day zero (solid) and day 1 or 14 (dotted). (D) Photostability under laser irradiation (97 mW/cm^2) at 980 nm for IR-140 J-aggregate in HMSNs-PEG (blue) and IR-140 J-aggregate in 35% DMSO/0.9% NaCl in water (red), and at 785 nm for monomer in DMSO (yellow).

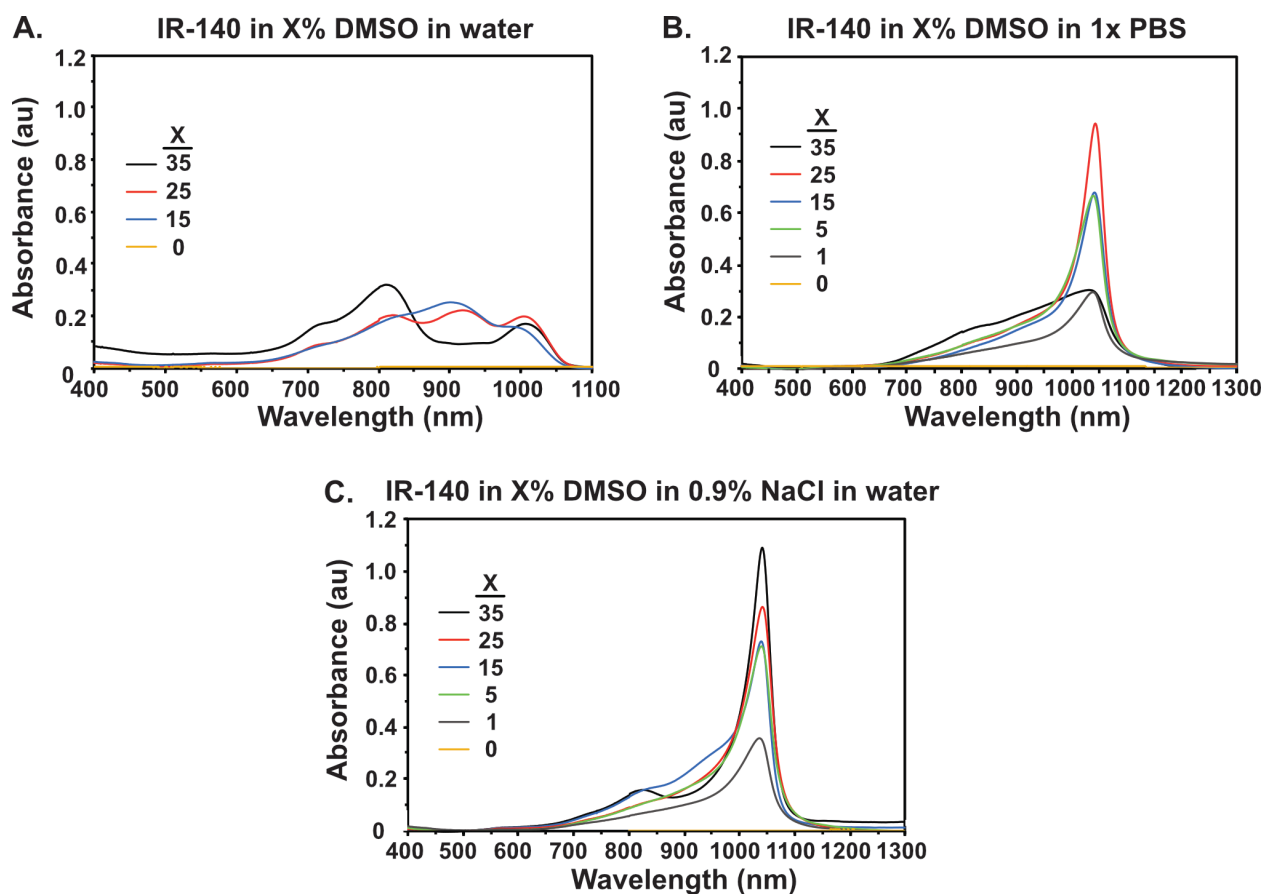


Figure 4.14. UV-Vis-NIR characterization of IR-140 J-aggregate formation in solution at 0.01 mg/mL in (A) DMSO/water, (B) DMSO/1xPBS, and (C) DMSO/0.9% NaCl in water.

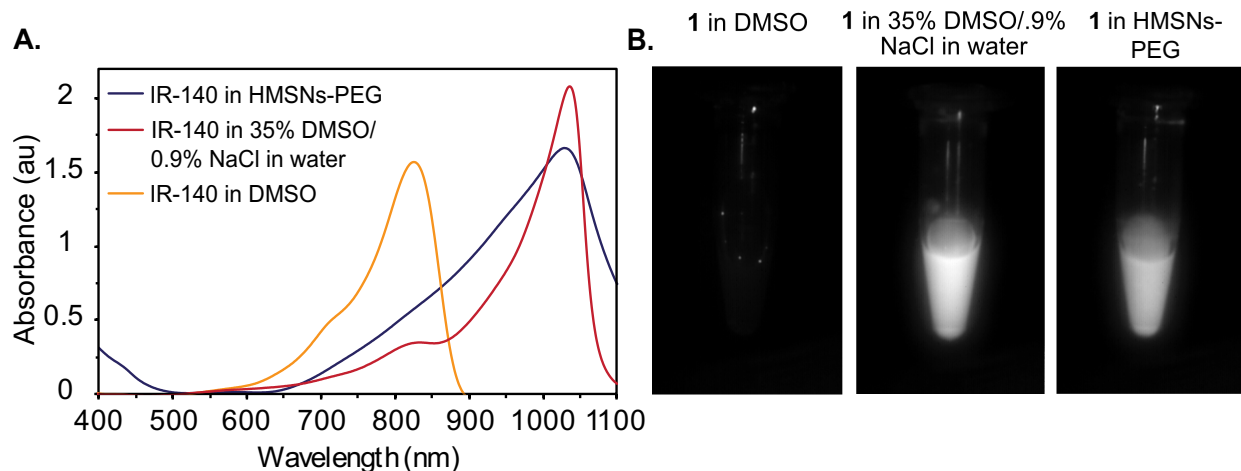


Figure 4.15. Emission of monomer and J-aggregate states of IR-140 under 980 nm excitation. (A) Absorbance traces of samples (10 mm path length) used in vial images in B and in Figure 4.13B, baseline corrected to 521 nm. (B) Images of IR-140 monomer in DMSO (left), IR-140 J-aggregate in solution (center) and J-aggregate in HMSNs-PEG (right) under 980 nm irradiation ($99 \pm 3 \text{ mWcm}^{-1}$). All Eppendorf tubes are placed in the same location, such that laser intensity across all samples is identical. See Figure 4.13B experimental procedure for sample preparation and acquisition settings. Displayed images were background subtracted, averaged over 10 frames and the contrast was set to identical values for comparison.

Next, we analyzed the role of the HMSNs in stabilizing IR-140 J-aggregates. Over two weeks in PBS at room temperature, we observed only a $\sim 10\%$ decrease in absorbance from the IR-140 loaded HMSNs-PEG and no evidence that the packing of the IR-140 within the nanoparticles was changing (Figures 4.13C, blue; Figure 4.16). Comparatively, only $\sim 8\%$ of the J-aggregate in solution remained after 1 day (Figure 4.13C, red; Figure 4.16). Not only do the HMSNs stabilize the assembly of the J-aggregate, but they also enhance the photostability. The fluorescence of solutions containing IR-140 J-aggregate in 35% DMSO/0.9% NaCl in water and HMSNs-PEG containing IR-140 J-aggregate in PBS were continually irradiated with a 980 nm laser (97 mW/cm^2) and the fluorescence intensity was measured with an InGaAs camera. The photostability of

monomeric IR-140 in DMSO was also evaluated via excitation at 785 nm (97 mW/cm²). As shown in Figure 4.13D, the J-aggregates within the HMSNs-PEG are 4-fold more stable than the J-aggregates in solution and ~60-fold more stable than the monomer (Table 4.2, Note S4.4). This result is consistent with the use of silica shells to overcome the poor photostability that is characteristic of J-aggregates by limiting the amount of reactive oxygen species that can access the aggregate.³¹ Photobleaching experiments in deoxygenated solvents support that the HMSNs protect the IR-140 J-aggregate from reactive oxygen species (Figure 4.17). Taken together, our data show that the HMSNs are critical for stabilizing J-aggregates to light and solution.

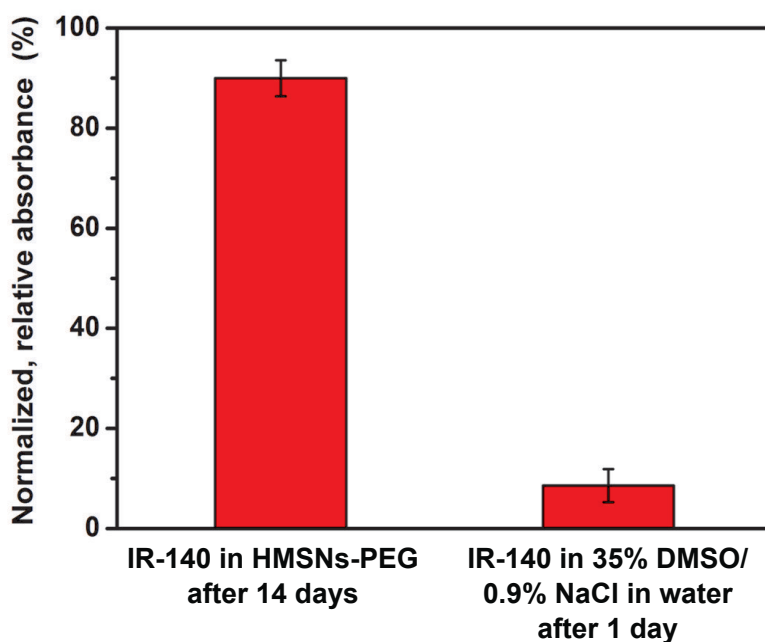


Figure 4.16. Stability of J-aggregates over time, displayed as the normalized, relative absorbance remaining for IR-140 in HMSNs-PEG after 14 days, and IR-140 in solution after 1 day. IR-140 loaded HMSNs-PEG were dispersed in PBS (0.25 mg/mL), and IR-140 J-aggregate was composed of 0.01 mg/mL IR-140 in 35% DMSO/0.9% NaCl in water. Error represents the standard deviation of three replicates.

Table 4.2. Photobleaching rates of IR-140 (1).

Species	λ_{ex} (nm)	$k_{\text{raw}} (\text{s}^{-1}) \times 10^3$	$k_{\text{rel}} (\text{s}^{-1}) \times 10^3$	Relative stability
1 monomer	785	19.54 ± 0.04	19 ± 1	1
1 J-aggregate	980	1.276 ± 0.008	1.28 ± 0.05	15 ± 1
1 in HMSNs-PEG	980	0.317 ± 0.002	0.32 ± 0.01	62 ± 5

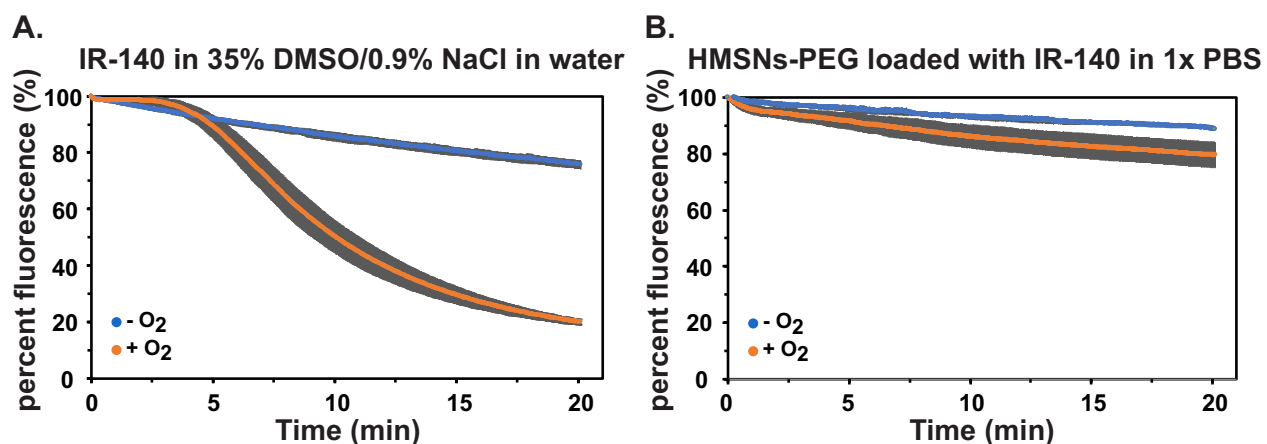


Figure 4.17. Photostability of J-aggregates in the presence and absence of oxygen. (A) Raw data of IR-140 J-aggregate in 35 % DMSO/0.9% NaCl at 0.01 mg/mL under 980 nm irradiation with 79 mWcm^{-2} power density. The relative rates of oxygenated to deoxygenated photobleaching is 7.1 to 1. (B) Raw data of HMSNs-PEG loaded with IR-140 at 1.0 mg/mL in 1x PBS under 980 nm irradiation with 101 mWcm^{-2} power density. The relative rates of oxygenated to deoxygenated photobleaching is 1.9 to 1. Error bars represent the standard deviation of three replicate experiments in (A) and (B) oxygenated and two replicate experiments in (B) deoxygenated. Deoxygenated samples were prepared by purging with N₂ for 30-60 min; oxygenated samples were not purged with N₂. **Note:** The photobleaching rate of the solution IR-140 aggregate is substantially attenuated by the removal of oxygen, ($\sim 7\times$) while the photobleaching of the HMSNs IR-140 is improved by only $\sim 2\times$. These data indicate that the IR-140 loaded inside the HMSNs are less affected by the presence of oxygen, which may be due to a shielding of reactive oxygen species by the dense silica shells.

Finally, with bright SWIR-emissive nanoparticles prepared and characterized, we evaluated their biocompatibility and *in vivo* imaging performance. *In vitro* studies showed no cytotoxicity of the IR-140 loaded HMSNs-PEG over 6 h at concentrations up to 200 $\mu\text{g/mL}$ (Figure 4.18). These data are consistent with other studies regarding mesoporous silica, which is generally considered non-toxic to animals.^{26,32} We performed *in vivo* imaging experiments using the IR-140 loaded HMSNs-PEG with excitation at 980 nm and collection from 1000–1700 nm. The SWIR-emissive HMSNs-PEG were intravenously injected into nude mice and the mice were immediately imaged (Figure 4.19). The HMSNs-PEG rapidly clear from the blood stream and intense signal can be seen in the lungs, liver, and spleen. Fifty minutes after injection, the signal intensity within these organs remained constant (Figure 4.20).

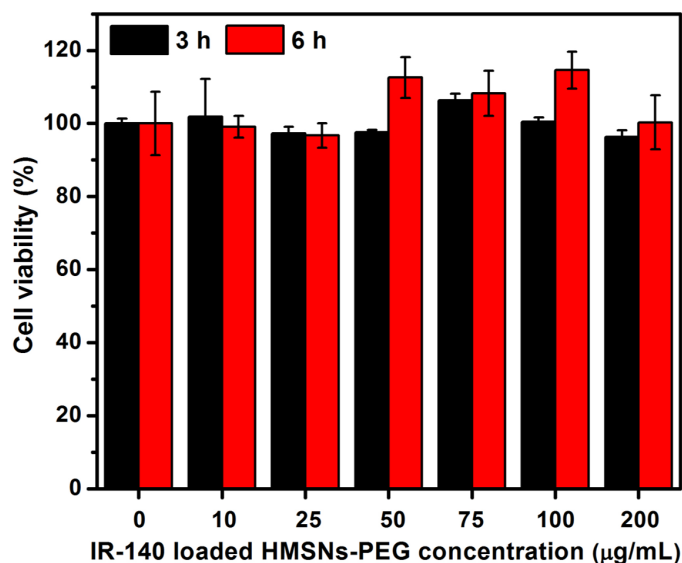


Figure 4.18. Cytotoxicity study of IR-140 loaded HMSNs-PEG examined by a CCK-8 assay. HeLa cells were incubated in 200 μL fresh DMEM containing 0, 2, 5, 10, 15, 20, and 40 μg of IR-140 loaded HMSNs-PEG (*i.e.* 0, 10, 25, 50, 75, 100, and 200 $\mu\text{g/mL}$) for 3 (black) or 6 (red) hours at 37 $^{\circ}\text{C}$. The viable cells in each condition was determined by the absorbance at 450 nm and 650 nm (as a reference). The DMEM (100 μL) mixed with CCK-8 reagent (10 μL) served as a background. Error bars represent the standard deviation of three replicate experiments.

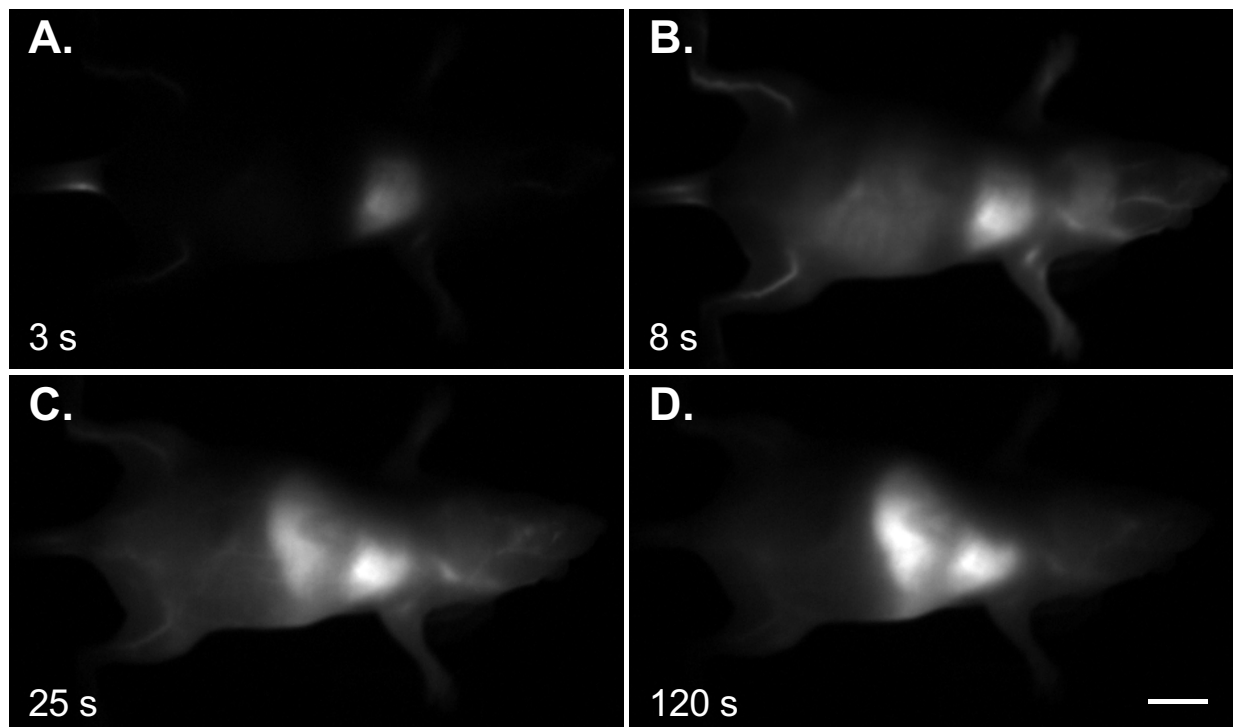


Figure 4.19. Whole-mouse imaging at 16 fps (980 nm, 91 mW/cm² excitation; 1000–1700 nm collection) upon i.v. delivery of IR-140 HMSNs-PEG. Background subtracted stills were averaged over 5 frames at 3 s (A), 8 s (B), 25 s (C), and 120 s (D) post injection. Scale bar represents 1 cm. Data are representative of two replicate experiments.

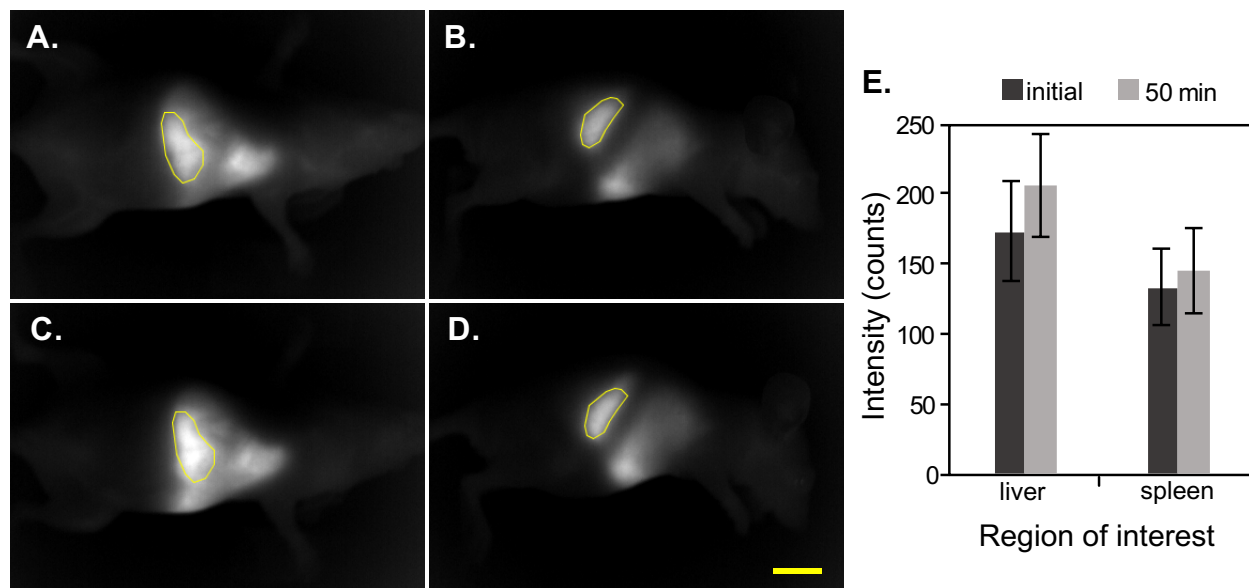


Figure 4.20. Images from the front (A/C) and left side (B/D) of a nude mouse directly after vascular clearance (>2 m post injection) (A/B), and after 50 minutes (C/D), showing uptake of IR-140 loaded HMSNs-PEG in the liver and spleen. Images were acquired with 60 ms exposure time at 16.65 fps with 980 nm ex. ($91 \pm 3 \text{ mW/cm}^2$) and 1000–1700 nm detection (see general experimental procedures, section I, for details of optical set up). Displayed images were background subtracted, averaged over 5 frames, outliers were removed, and the contrast was set to identical values for comparison. Regions of interest were defined and applied to quantify the intensity in the liver (A/C) and spleen (B/D) over time. Scale bar represents 1 cm. (E) Quantification of signal for liver and spleen showing no significant change in signal over 50 minutes. Error bars represent the standard deviation over the regions of interest. Data are representative of two replicate experiments.

4.4 Conclusions

In summary, we have presented J-aggregation as an approach to prepare biocompatible, SWIR contrast agents and demonstrated this concept by stabilizing J-aggregates of the NIR fluorophore IR-140 inside HMSNs. The bathochromically-shifted absorption and emission and small Stokes shifts of the IR-140 J-aggregate allow imaging with 980 nm excitation and 1000–1700 nm acquisition, providing high resolution *in vivo* images. The modularity of the HMSNs will enable facile exchange of the imaging agent as well as the addition of targeting agents and/or therapeutics, poising these materials to become SWIR theranostics.³³ While we did not observe an enhanced Φ_F with the IR-140 J-aggregate, likely due to disorder or intermolecular vibrations,³⁴ work is ongoing to access a SWIR J-aggregate that exhibits the superradiance phenomena predicted by Kasha.³⁵ Collectively, the use of J-aggregates stabilized in HMSNs as SWIR imaging agents has the potential to overcome the stability, toxicity, and brightness challenges of contrast agents for this compelling region of the electromagnetic spectrum.

4.5 Experimental procedures of the figures

Figure 4.2

Stöber silica spheres, dSiO₂@MSNs, or HMSNs were dispersed in ethanol at a concentration of 0.1 mg/mL. The suspension (5 μL) of the nanoparticles was dropped onto the carbon-coated copper grid and dried at room temperature. Transmission electron microscopy was measured on a Tecnai T12 instrument with an operating voltage of 120 kV.

Figure 4.3 B

Refer to Section II “Loading of IR-140 in HMSNs, HMSNs-APTS, or dSiO₂@MSNs”. 10 mM IR-140 was used as the loading solution. Then, IR-140 loaded HMSNs were washed by methods (a), (b), or (c) to compare the extent of IR-140 aggregate by using the above washing methods. The washing steps were repeated 5 times and finally IR-140 loaded HMSNs were re-dispersed in 1 mL of PBS solution by sonication.

Stöber silica spheres dispersed in ethanol were centrifuged (14000 rpm, 15 min) and washed with DMSO 3 times before IR-140 loading. Afterwards, Stöber silica spheres were dispersed in 200 μL of DMSO solution containing 10 mM IR-140 by sonication in a bath sonicator for 10 min. Then, the solution was stirred for 20 h. After the IR-140 loading, the solution containing the particles was centrifuged (14000 rpm, 15 min) to get IR-140 loaded Stöber silica spheres. Then, IR-140 loaded Stöber silica spheres were washed with 1 mL of PBS by gently washing with plastic transfer pipettes to remove free DMSO. After each washing step, IR-140-loaded Stöber silica spheres were centrifuged (8000 rpm, 3 min) to remove the supernatant. The washing steps were repeated for 5 times and finally IR-140-loaded Stöber silica spheres were re-dispersed in PBS.

solution (1 mL) by sonication. The absorbance spectra of IR-140 loaded HMSNs or IR-140 loaded Stöber silica spheres were measured with 10 mm quartz cuvettes at a concentration of 0.25 mg nanoparticles/mL PBS on a Cary 5000 UV-Vis-NIR spectrophotometer at room temperature. Absorbance traces were corrected for the non-linearity between gratings. Absorbance traces were corrected for the non-linearity between gratings.

For the prewash spectrum: after the IR-140 (10 mM) loading, the particles solution (10 mg/mL) was diluted 1:350 with DMSO for measurement. The absorbance spectrum of the prewash sample was measured with 3 mm quartz cuvettes on a JASCO V-770 UV-Vis-NIR spectrophotometer at room temperature.

Figure 4.3 C/D

HMSNs and IR-140 loaded HMSNs were dispersed in ethanol and D.I. water, respectively at a concentration of 0.1 mg/mL. The suspension (5 μ L) of the nanoparticles was dropped onto the carbon-coated copper grid and dried at room temperature. Transmission electron microscopy was measured on a Tecnai T12 instrument with an operating voltage of 120 kV.

Figure 4.4

Refer to Section II “Loading of IR-140 in HMSNs, HMSNs-APTS, or dSiO₂@MSNs”. 5 or 20 mM IR-140 was used as the loading solution. Then, IR-140 loaded HMSNs were washed by methods (a), (b), or (c). In addition, IR-140 loaded dSiO₂@MSNs were washed by method (b). The washing steps were repeated 5 times and finally IR-140 loaded HMSNs or IR-140 loaded dSiO₂@MSNs were re-dispersed in 1 mL of PBS solution by sonication. The absorbance spectra of IR-140 loaded HMSNs or IR-140 loaded dSiO₂@MSNs were measured with 10 mm quartz

cuvettes at a concentration of 0.25 mg nanoparticles/mL PBS on a Cary 5000 UV-Vis-NIR spectrophotometer at room temperature. Absorbance traces were corrected for the non-linearity between gratings.

Figure 4.5

Stöber silica spheres or Stöber silica spheres-APTS were prepared and described in synthetic procedures. Stöber silica spheres or Stöber silica spheres-APTS (2 mg for each) dispersed in ethanol were centrifuged (14000 rpm, 16873 g, 15 min) and washed with DMSO 3 times before IR-140 loading. Afterwards, Stöber silica spheres or Stöber silica spheres-APTS were dispersed in 200 μ L of DMSO solution containing 20, 10, or 5 mM IR-140 by sonication in a bath sonicator for 10 min. Then, the solution was stirred for 20 h. After the IR-140 loading, the solution containing the particles was centrifuged (14000 rpm, 16873 g, 15 min) to get IR-140 loaded Stöber silica spheres or Stöber silica spheres-APTS. Then, IR-140 loaded Stöber silica spheres or Stöber silica spheres-APTS were washed with 1 mL of PBS by gently washing with plastic transfer pipettes to remove free DMSO and DMSO loaded in the pores. After each washing step, IR-140 loaded Stöber silica spheres or Stöber silica spheres-APTS were centrifuged (8000 rpm, 5510 g, 3 min) to remove the supernatant. The washing steps were repeated for 5 times and finally IR-140 loaded Stöber silica spheres or Stöber silica spheres-APTS were re-dispersed in PBS solution (1 mL) by sonication. The absorbance spectra of Stöber silica spheres or Stöber silica spheres-APTS were measured with 10 mm quartz cuvettes at a concentration of 0.25 mg nanoparticles/mL PBS on a Cary 5000 UV/Vis/NIR Spectrophotometer at room temperature. Absorbance traces were corrected for the non-linearity between gratings.

For zeta potential measurement, Stöber silica spheres or Stöber silica spheres-APTS were dispersed in D.I. water (2 mL) at a concentration of 50 $\mu\text{g}/\text{mL}$. The measurement was performed on a Malvern Zetasizer Nano at room temperature.

Figure 4.6

HMSNs, Stöber silica spheres, Stöber silica spheres-APTS, or $\text{dSiO}_2@\text{MSNs}$ (2 mg for each) dispersed in ethanol were centrifuged (14000 rpm, 16873 g, 15 min) and washed with DMSO 3 times before IR-140 loading. Afterwards, HMSNs, Stöber silica spheres, Stöber silica spheres-APTS, or $\text{dSiO}_2@\text{MSNs}$ were dispersed in 200 μL of DMSO solution containing 10 mM IR-140 by sonication in a bath sonicator for 10 min. Then, the solution was stirred for 20 h. After the IR-140 loading, the solution containing the particles was centrifuged (14000 rpm, 16873 g, 15 min) to get IR-140 loaded nanoparticles. Then, IR-140 loaded nanoparticles were washed with 1 mL of PBS by gently washing with plastic transfer pipettes to remove free DMSO and DMSO loaded in the pores. After each washing step, IR-140 loaded nanoparticles were centrifuged (8000 rpm, 5510 g, 3 min) to remove the supernatant. The washing steps were repeated for 5 times and finally IR-140 loaded nanoparticles were re-dispersed in PBS solution (1 mL) by sonication. The absorbance spectra of IR-140 loaded HMSNs, Stöber silica spheres, Stöber silica spheres-APTS, or $\text{dSiO}_2@\text{MSNs}$ were measured with 10 mm quartz cuvettes at a concentration of 0.25 mg nanoparticles/mL PBS on a Cary 5000 UV/Vis/NIR Spectrophotometer at room temperature. Absorbance traces were corrected for the non-linearity between gratings.

Figure 4.7

The loading capacity of IR-140 in HMSNs or HMSNs-APTS was calculated based on the

absorbance difference between the IR-140 DMSO solution before and after loading. After loading with IR-140 for 20 h, HMSNs or HMSNs-APTS were centrifuged (14000 rpm, 16873 g, 15 min) and the supernatant was collected for absorbance measurements. The loading capacity of IR-140 was calculated using the difference of maximum absorbance at 831 nm and the following definition of loading capacity (%): (mass of loaded IR-140/mass of particles) x 100.

Figure 4.8

HMSNs (A/B) and HMSNs-APTS (C/D), and dSiO₂@MSNs (E/F) were prepared as described in the synthetic procedures and degassed at 120 °C under vacuum for 16 h before the measurement. The surface area and pore diameter distribution of HMSNs, HMSNs-APTS, and dSiO₂@MSNs were determined by Brunauer-Emmett-Teller (BET) and Barrett-Joyner-Halenda (BJH) methods, respectively.

Figure 4.9

(A) HMSNs were dispersed in ethanol at a concentration of 0.1 mg/mL. (B) The control HMSNs were subjected to washing by method (b) in the Section II “Loading of IR-140 in HMSNs, HMSNs-APTS, or dSiO₂@MSNs” but without the loading of IR-140. The particles were dispersed in PBS at a concentration of 0.1 mg/mL. (C) Refer to Section II “Loading of IR-140 in HMSNs, HMSNs-APTS, or dSiO₂@MSNs”. 10 mM IR-140 was used as the loading solution. IR-140 loaded HMSNs were dispersed in PBS at a concentration of 0.1 mg/mL. (D) The mixed samples were prepared by mixing 50 μL of HMSNs in PBS solution (0.2 mg/mL) and 50 μL of IR-140 loaded HMSNs in PBS solution (0.2 mg/mL) and were sonicated in a water bath sonicator for 20 s. The suspension (5 μL) of each of the nanoparticles was dropped onto the carbon-coated copper

grid and dried at room temperature. Transmission electron microscopy was measured on a Tecnai T12 instrument with an operating voltage of 120 kV.

Figure 4.10

HMSNs-APTS (2 mg) dispersed in ethanol were centrifuged (14000 rpm, 16873 g, 15 min) and washed with DMSO (3 x 1 mL) before IR-140 loading. Afterwards, HMSNs-APTS was dispersed in 200 μ L of DMSO solution containing 5, 10, or 20 mM IR-140 by sonication in a bath sonicator for 10 min. Then, the solution was stirred for 20 h to let IR-140 diffuse into the pores and cavity of HMSNs-APTS. After the IR-140 loading, the solution containing the particles was centrifuged (14000 rpm, 16873 g, 15 min) to get IR-140 loaded HMSNs-APTS. Then, IR-140 loaded HMSNs-APTS were washed with PBS (1 mL) by gently washing with plastic transfer pipettes to remove free DMSO and DMSO loaded in the pores. After each washing step, IR-140 loaded HMSNs-APTS were centrifuged (8000 rpm, 5510 g, 3 min) to remove the supernatant. The washing steps were repeated 5 times and finally IR-140 loaded HMSNs-APTS were re-dispersed PBS (1 mL) by sonication. The absorbance spectra of IR-140 loaded HMSNs-APTS were measured with 10 mm quartz cuvettes at a concentration of 0.25 mg nanoparticles/mL PBS on a Cary 5000 UV/Vis/NIR Spectrophotometer at room temperature. Absorbance traces were corrected for the non-linearity between gratings.

Figure 4.11

Refer to Section II “Loading of IR-140 in HMSNs, HMSNs-APTS, or $\text{dSiO}_2\text{@MSNs}$ ”. 20 mM IR-140 was used as the loading solution. The loading concentration of HMSNs-APTS was 10 mg/mL. Then, IR-140 loaded HMSNs-APTS were washed by method (b). The washing steps were

repeated 5 times and finally IR-140 loaded HMSNs-APTS were re-dispersed in PBS (1 mL) by sonication. The synthetic procedures of PEGylation of IR-140 loaded HMSNs-APTS can be referred to Section II “PEG conjugation on the surface of IR-140 loaded HMSNs-APTS”. For dynamic light scattering size measurement, HMSNs-APTS, HMSNs-APTS containing IR-140, and HMSNs-PEG containing IR-140 were dispersed in PBS (2 mL) at a concentration of 50 $\mu\text{g/mL}$. The measurement was performed on a ZETAPALS instrument with a 660 nm red diode laser at room temperature.

Figure 4.12

Refer to Section II “Loading of IR-140 in HMSNs, HMSNs-APTS, or $\text{dSiO}_2\text{@MSNs}$ ”. 20 mM IR-140 was used as the loading solution. The loading concentration of HMSNs-APTS was 10 mg/mL. Then, IR-140 loaded HMSNs-APTS were washed by method (b). The washing steps were repeated 5 times and finally IR-140 loaded HMSNs-APTS were re-dispersed in 1 mL of PBS solution by sonication. The synthetic procedures of PEGylation of IR-140 loaded HMSNs-APTS can be referred to Section II “PEG conjugation on the surface of IR-140 loaded HMSNs-APTS”. For zeta potential measurement, HMSNs, HMSNs-APTS, HMSNs-APTS containing IR-140, and HMSNs-PEG containing IR-140 were dispersed in D.I. water (2 mL) at a concentration of 50 $\mu\text{g/mL}$. The measurement was performed on a Malvern Zetasizer Nano at room temperature.

Figure 4.13A

All absorbance and emission traces were baseline corrected and normalized. Absorbance traces were acquired on a JASCO V-770 UV-Visible/NIR spectrophotometer. The slit widths used in fluorescence spectra were 5.76 mm for excitation and 11.52 mm for emission. The step size was

1.0 nm, integration time 0.1 s, and traces were acquired after an automatic detector background subtraction.

IR-140 monomer was dissolved in DMSO and diluted to an O.D. of ~ 0.7 for absorbance and less than 0.1 for fluorescence spectroscopy (ex. 785 nm) in a 1 cm path length cuvette. The monomer absorption trace was corrected for the non-linearity between gratings before baseline subtraction and normalization.

The IR-140 J-aggregate in 35% DMSO/0.9% NaCl was prepared by dissolving 0.02 mg of IR-140 in 350 μ L DMSO, vortexing briefly, adding 650 μ L 0.9% aqueous NaCl, and shaking briskly. The solution becomes warm and immediately loses the blue color. Absorbance and emission traces of the J-aggregate in solution were obtained with a 2 mm path length cuvette. For the fluorescence trace, a 10 mm path length was used on the excitation side and a 2 mm path length on the emission side. A reabsorption correction was performed on the emission trace analogous to that described in Note S4.2.

The IR-140 loaded HMSNs-PEG were prepared as described in the synthetic procedures, section VI. The absorbance was collected without dilution in a 10 mm cuvette. The fluorescence spectrum was obtained by diluting the sample to an O.D. of less than 0.1 in a 3 mm path length square quartz cuvette, and exciting at 885 nm with a shortpass filter (Thorlabs, FES0900).

Figure 4.13B

Samples consisted of IR-140 monomer: 0.01 mg/mL IR-140 in DMSO (left); IR-140 J-aggregate in solution: 0.01 mg/mL IR-140 in 35% DMSO/0.9% NaCl in water (center); IR-140 HSMNs-PEG: 1 mg/mL in PBS (right). Vials were excited with 980 nm light (with Thorlabs

FESH1000) with an average power density of $99 \pm 3 \text{ mWcm}^{-2}$. Power densities over the three samples were not identical due to varying distance from the excitation cube. See Figure 4.15 for images with consistent distances from the excitation cube. Collection was from 1000–1700 nm (1000 nm LP, Edmund Optics 84-776). The custom lens system consists of a 4f configuration with a $f=750.0\text{mm}$ lens (Thorlabs LB1247-C) and two $f=200.0\text{mm}$ lenses (Thorlabs LB1199-C). For ergonomic reasons a 2” protected silver-coated elliptical mirror (PFE20-P01) mounted to a kinematic mount (Thorlabs KCB2EC/M) was used. Images were acquired at 35 ms exposure time, 16.65 fps. Displayed image was background subtracted and averaged over 6 frames.

Figure 4.13C

Stability of IR-140 in HMSNs-PEG over time. IR-140 loaded HMSNs-PEG were dispersed in PBS at 0.25 mg/mL. The absorbance spectra were taken in a 3 mm path length cuvette immediately (day 0) and after 14 days (day 14) on a JASCO V-770 UV-Visible/NIR spectrophotometer. The absorbance was normalized, relative to spectrum (1). Results of the triplicate experiment are presented in Figure 4.16.

Stability of IR-140 in solution over time. IR-140 J-aggregate was prepared in DMSO as described in Figure 4.11A. The aggregate absorbance in a 2 mm path length cuvette was obtained immediately (day 0) and after 17 h storage in the dark (day 1) on a JASCO V-770 UV-Visible/NIR spectrophotometer. The absorbance was normalized, relative to spectrum at day 0. Results are reproduced in triplicate in Figure 4.16.

Figure 4.13D

Three solutions were prepared: (a) 1 mg/mL solution of HMSNs-PEG containing IR-140 (b)

0.01 mg/mL IR-140 in 35% DMSO/0.9% NaCl solution, and (c) 0.01 mg/mL IR-140 in DMSO. Each solution (400 μ L) was irradiated with 97 ± 3 mWcm⁻² of 980 nm (a and b) and 785 nm (c) light and their emission was monitored by a SWIR camera. Acquisition settings were 2 fps and (a) 25 ms, (b) 15 ms, and (c) 0.3 ms. Excitation and emission settings were identical to Figure 4.13B. Error represents the standard deviation of three measurements.

Figure 4.14

Samples were prepared as by dissolving 0.02 mg IR-140 in DMSO, and then adding to the appropriate aqueous phase (either MilliQ water, 1x PBS, or 0.9% NaCl in water) and shaking vigorously. The appropriate volumes of DMSO and aqueous phase were used to sum to 2.0 mL for each listed percentage. For the 0% DMSO traces, IR-140 is at its solubility limit, after sonicating 0.02 mg IR-140 in 1.0 mL of the appropriate solvent for 4 hours. Absorbance traces were measured in a 3.0 mm cuvette with blanking to the appropriate solvent mixture on a JASCO V-770 UV-Visible/NIR spectrophotometer.

Figure 4.15

Samples were prepared and excitation and acquisition was performed as described in Figure 4.13B. Absorbance traces were acquired on a Shimadzu UV-1800 UV-Visible Scanning Spectrophotometer.

Figure 4.16

IR-140 loaded HMSNs-PEG, obtained as described in the experimental procedures II “PEG conjugation on the surface of IR-140 loaded HMSNs-APTS,” were dispersed in PBS (0.25 mg/mL). The absorbance spectra were taken in a 3 mm path length cuvette immediately (day 0) and after

14 days storage in the dark. IR-140 J-aggregate in solution was prepared by dissolving 0.02 mg IR-140 in 700 μ L DMSO, and subsequently adding 1.3 mL 0.9% NaCl and briskly shaking. The aggregate absorbance in a 2 mm path length cuvette was obtained immediately and after 24 h storage in the dark.

Figure 4.17A

Deoxygenated IR-140 solution J-aggregates were prepared by adding 1.4 mL DMSO to 0.04 mg IR-140 in a purged dram vial, followed by 2.6 mL 0.9% NaCl solution in water and shaking. Solvents were deoxygenated by purging with N_2 for at least one hour. Oxygenated IR-140 solution J-aggregates were prepared analogously, but with solvents which had been exposed to air. Solutions (4 mL), sealed with septa, were irradiated for 20 min. The optical parameters for experiment in (A) consisted of the following: a 4-inch square first-surface silver mirror (Edmund Optics, 84448) was used to direct the emitted light through a custom filter set (Edmund optics #84-776, TL) to an Allied Vision Goldeye G-032 Cool TEC2 camera at -20 $^{\circ}C$, equipped with a C-mount camera lens (Navitar, SWIR-35). Excitation light was passed through a positive achromat (Thorlabs AC254-050-B), 1000 nm shortpass filter (Thorlabs FESH 1100), and an engineered diffuser (Thorlabs ED1-S20-MD) to provide uniform illumination over the working area. Exposure time used was 100 ms, with 2 fps.

Figure 4.17B

IR-140 containing HMSNs-PEG were prepared according to experimental procedures II, sections “Loading of IR-140 in HMSNs, HMSNs-APTS, or $dSiO_2@MSNs$ ” and “PEG conjugation on the surface of IR-140 loaded HMSNs-APTS”. Deoxygenated solutions were

purged with N₂ for at least 30 min, while oxygenated were left open to air. Both sample types (1 mg/L, 0.40 mL), sealed with septa, were irradiated for 20 minutes. The optical parameters for experiment in (B) consisted of the following: a 4-inch square first-surface silver mirror (Edmund Optics, 84448) was used to direct the emitted light through a custom filter set (Edmund optics #84-776, 3x FELH1000,) to an Allied Vision Goldeye G-032 Cool TEC2 camera at -20 °C, equipped with a C-mount camera lens (Navitar, SWIR-35). Excitation light was passed through a positive achromat (Thorlabs AC254-050-B), 1000 nm shortpass filter (Thorlabs FESH 1000), and an engineered diffuser (Thorlabs ED1-S20-MD) to provide uniform illumination over the working area. Exposure time used was 200 ms, with 2 fps.

Data were analyzed analogous to that discussed in Note S4.4, however only the relative rates between oxygenated and deoxygenated experiments were calculated and evaluated.

Figure 4.18

The viabilities of HeLa cells after the treatment of IR-140 loaded HMSNs-PEG were examined by using a cell counting kit-8 (CCK-8) assay. The cells were seeded in 96-well plates at a density of 5×10^3 cells per well in 200 μ L DMEM supplemented with 10% FBS and 1% antibiotics in a humidity-controlled incubator at 37 °C for 24 h attachment. After the attachment, the medium was removed and the cells were incubated in 200 μ L fresh DMEM containing 0, 2, 5, 10, 15, 20, and 40 μ g of IR-140 loaded HMSNs-PEG (*i.e.* 0, 10, 25, 50, 75, 100, and 200 μ g/mL) for 3 or 6 h in an incubator at 37 °C. After incubation, the medium was removed and the treated cells were washed with DPBS 1 time (200 μ L). To measure the cell viability, 100 μ L of DMEM and 10 μ L of CCK-8 cellular cytotoxicity reagent were added to each well. Then, the plates were

put in the incubator for 2 h at 37 °C. To measure the number of the viable cells in each condition, a plate reader (Tecan M1000) was used to measure the absorbance at 450 nm and 650 nm (as a reference). The DMEM (100 μ L) mixed with CCK-8 reagent (10 μ L) served as a background control.

Figure 4.19

The IR-140 HMSNs-PEG in PBS were sonicated (Elma S15 Elmasonic) for 30 mins prior to injection and filtered through a 40 μ m nylon filter. 200 μ L of the IR-140 HMSNs-PEG in PBS were injected via the tail vein and immediately imaged. The excitation flux (980 nm) had an average power density of 91 ± 3 mWcm⁻² over the field of view. Images were acquired at 60 ms exposure time and 16.65 fps, in 8-bit format. Displayed images were background subtracted with an average of 10-frames from the pre-injection time points, outliers were removed, and the stills were averaged over 5 frames.

Figure 4.20

Refer to Figure 4.17 experimental procedures.

4.6 Supplementary notes

Note S4.1: Estimation of the amount of dye molecules in a single HMSN and HMSN-PEG

In order to calculate how many IR-140 molecules loaded in a single HMSN or HMSN-APTS, we need to estimate the mass of a single HMSN or HMSN-APTS using the equation:

$$m_{amorphous\ silica} = V_{amorphous\ silica} \times \rho_{amorphous\ silica} \quad (1)$$

Amorphous silica is defined as the silica in HMSNs shell excluding mesopores. The density (ρ) of amorphous silica is known to be 2.5 (g/cm³ amorphous silica). There are several ways to estimate the volume of a single MSNs, as we have published previously.^[7] Here, we started to determine the shell volume of a single HMSN (V_{shell}) from the equation below:

$$V_{shell} = \frac{4\pi}{3} \times (R_1^3 - R_2^3) = V_{mesopore} + V_{amorphous\ silica} \quad (2)$$

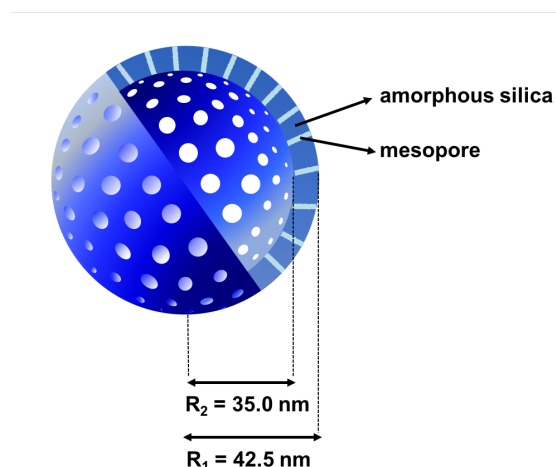


Figure S4.1. HMSN or HMSN-APTS used in this work. R_1 and R_2 are the outer radius and inner radius of HMSN or HMSN-APTS, respectively. V_{shell} is the shell volume of a single HMSN. $V_{mesopore}$ is the volume of the mesopores in the shell. $V_{amorphous\ silica}$ is the volume of silica in the shell excluding mesopores.

V_{shell} of the HMSNs used here (Figure S4.1) was calculated to be 141961 nm³ based on equation

(2). $V_{mesopore}$ was determined to be 0.94 (cm³/g amorphous silica) from N₂ adsorption-desorption isotherm analysis.

Although we cannot directly calculate $V_{amorphous\ silica}$ from the equation (2) at this point because $V_{mesopore}$ is a function of the mass of amorphous silica, we can first determine the ratio (a) between $V_{mesopore}$ and $V_{amorphous\ silica}$ which would facilitate determination of $V_{amorphous\ silica}$.

$$V_{mesopore} \div V_{amorphous\ silica} = a \quad (3)$$

From the density of amorphous silica, 1 g of amorphous silica has a volume of 0.4 cm³, and thus $a = 2.35$, which is derived from $V_{mesopore}/V_{amorphous\ silica} = 0.94\text{ cm}^3/0.4\text{ cm}^3$. Now, plug the ratio in equation (2):

$$\begin{aligned} V_{shell} &= V_{mesopore} + V_{amorphous\ silica} = 2.35 V_{amorphous\ silica} + V_{amorphous\ silica} \\ &= 3.35 V_{amorphous\ silica} \end{aligned} \quad (4)$$

From above, we determine that the percentage (b) of $V_{amorphous\ silica}$ occupying V_{shell} is:

$$(V_{amorphous\ silica} \div V_{shell}) \times 100\% = b \quad (5)$$

b was calculated to be 30%. Since we already calculated V_{shell} to be 141961 nm³, $V_{amorphous\ silica}$ was then determined to be 42446 nm³ from (5). The mass of a single HMSN ($m_{amorphous\ silica}$) was then calculated by plugging in $V_{amorphous\ silica}$ in the equation (1), which was determined to be 1.06×10^{-16} (g).

To estimate the amount of dye molecules in a single HMSN, the average loading capacities of IR-140 in HMSNs ($5.9 \pm 1.2\%$, $8.9 \pm 1.1\%$, and $22.9 \pm 2.8\%$ with 5 mM, 10 mM, and 20

mM IR-140 as the loading solution, respectively) were used to determine the mass of IR-140 loaded in a single HMSN. Then, the number of IR-140 molecules loaded in a single HMSN could be calculated as:

$$\text{number of IR-140 molecules loaded in a single HMSN} = [(\text{the loading capacity of IR-140 in HMSNs}) \times m_{\text{amorphous silica}} \div \text{molecular weight of IR-140}] \times N_A \quad (6)$$

where N_A is the Avogadro's constant. For example, using equation (6), with 5 mM IR-140, the number of IR-140 molecules loaded in a single HMSN was then determined to be $4.87 \times 10^3 \pm 0.99 \times 10^3$ molecules. The number of IR-140 molecules loaded in a single HMSN with 10 and 20 mM IR-140 were $7.35 \times 10^3 \pm 0.91 \times 10^3$ and $1.89 \times 10^4 \pm 0.23 \times 10^4$, respectively.

By applying the above calculation to HMSNs-APTS, we can also estimate how many IR-140 molecules were loaded in a single HMSN-APTS. Given that V_{mesopore} of HMSNs-APTS is $0.73 \text{ cm}^3/\text{g}$, the mass of a single HMSN-APTS is calculated to be $1.26 \times 10^{-16} \text{ g}$.

Given that the loading capacity of IR-140 in HMSN-APTS is $6.6 \pm 2.5 \%$, $10.2 \pm 1.8 \%$, and $21.6 \pm 1.5 \%$ with 5, 10, and 20 mM IR-140, respectively, the number of IR-140 molecules loaded in a single HMSN-APTS were estimated to be $6.43 \times 10^3 \pm 2.44 \times 10^3$, $9.94 \times 10^3 \pm 1.76 \times 10^3$, and $2.10 \times 10^4 \pm 0.15 \times 10^4$, respectively.

Note S4.2: absorption coefficients

Absorption coefficients were calculated according to the Lambert - Beer-Lambert law,

$$A = \epsilon lc \quad (7)$$

where A represents absorbance (unitless), ϵ the absorption coefficient ($\text{M}^{-1}\text{cm}^{-1}$), l the path length (cm), and c the concentration (M). Masses were determined on a microbalance and diluted using Hamilton microsyringes to concentrations within the linear range of the UV-Vis-NIR spectrophotometer. Four concentrations were obtained for each experiment and the reported error represents the standard deviation of three measurements.

The monomer absorption coefficient was straightforward as only one species is present in solution. These data were collected using a 10 mm quartz cuvette in DMSO. The raw data was corrected for non-linearity between gratings, and baseline corrected to 478 nm. The absorption coefficient at all relevant wavelengths is displayed below in Figure S4.2. The absorption coefficient at $\lambda_{\text{max,abs}} = 826 \text{ nm}$ was $1.7 \pm 0.1 \times 10^5 \text{ M}^{-1}\text{cm}^{-1}$.

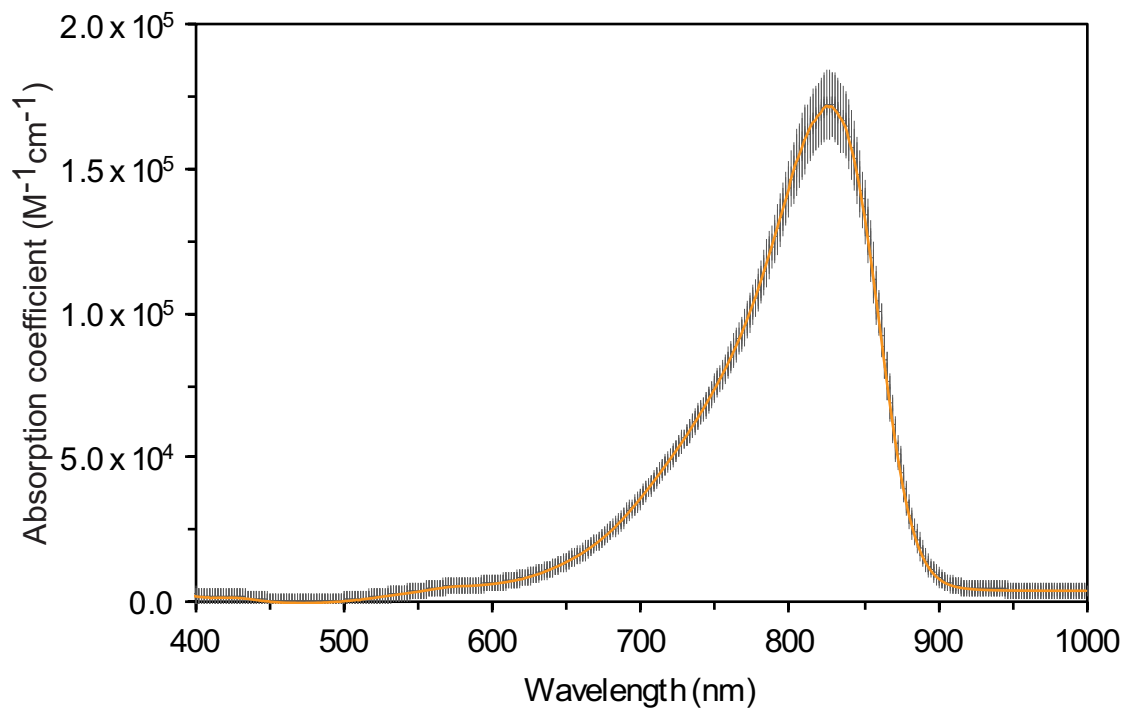


Figure S4.2. Absorption coefficient of IR-140 monomer in DMSO.

The J-aggregate absorption coefficient is more complex due to the requirement of high concentrations for selective formation of the J-aggregate over the monomer. As a result, to use higher concentrations, yet stay in the linear range of the spectrometer, these data were collected using a 3 mm cuvette. The raw data were baseline corrected to 449 nm and are included below in Figure S4.3. The uncorrected absorption coefficient (ϵ_{raw}) at $\lambda_{\text{max,abs}} = 1043 \text{ nm}$ was $3.3 \pm 0.3 \times 10^5 \text{ M}^{-1}\text{cm}^{-1}$.

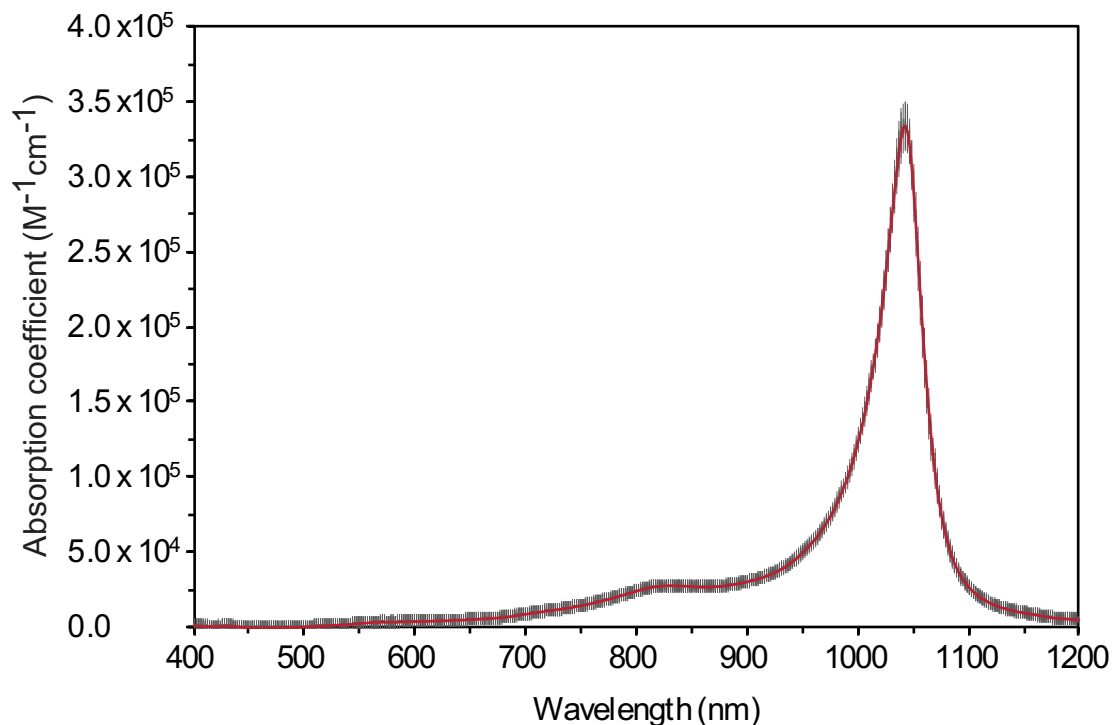


Figure S4.3. Uncorrected absorption coefficient of IR-140 J-aggregate in 35% DMSO/0.9% NaCl in water.

Despite the higher concentrations, some monomer remained in solution. The uncorrected data can be corrected for the remaining monomer in solution using the absorption coefficient of the monomer at its $\lambda_{\text{max,abs}}$ and making the assumption that the absorption coefficient of the monomer does not change significantly between 100% DMSO and 35% DMSO/0.9% NaCl in water. We used the equation:

$$\alpha_m + a_j = 1 \quad (8)$$

where α_m represents the mole fraction of monomer and α_j the mole fraction of J-aggregate. The value α_m for each absorbance trace was obtained using the Beer-Lambert law from the absorption coefficient of the monomer and the known concentration of total dye. The value a_j was then used as a multiplicative factor to correct the concentration of J-aggregate in solution. The absorption

coefficient was then recalculated with the corrected concentration values. The corrected absorption coefficient at $\lambda_{\text{max,abs}} = 1043 \text{ nm}$ was $3.9 \pm 0.4 \times 10^5 \text{ M}^{-1}\text{cm}^{-1}$. Error was taken as the standard deviation of the three replicates. The corrected absorption coefficient is displayed below in Figure S4.4.

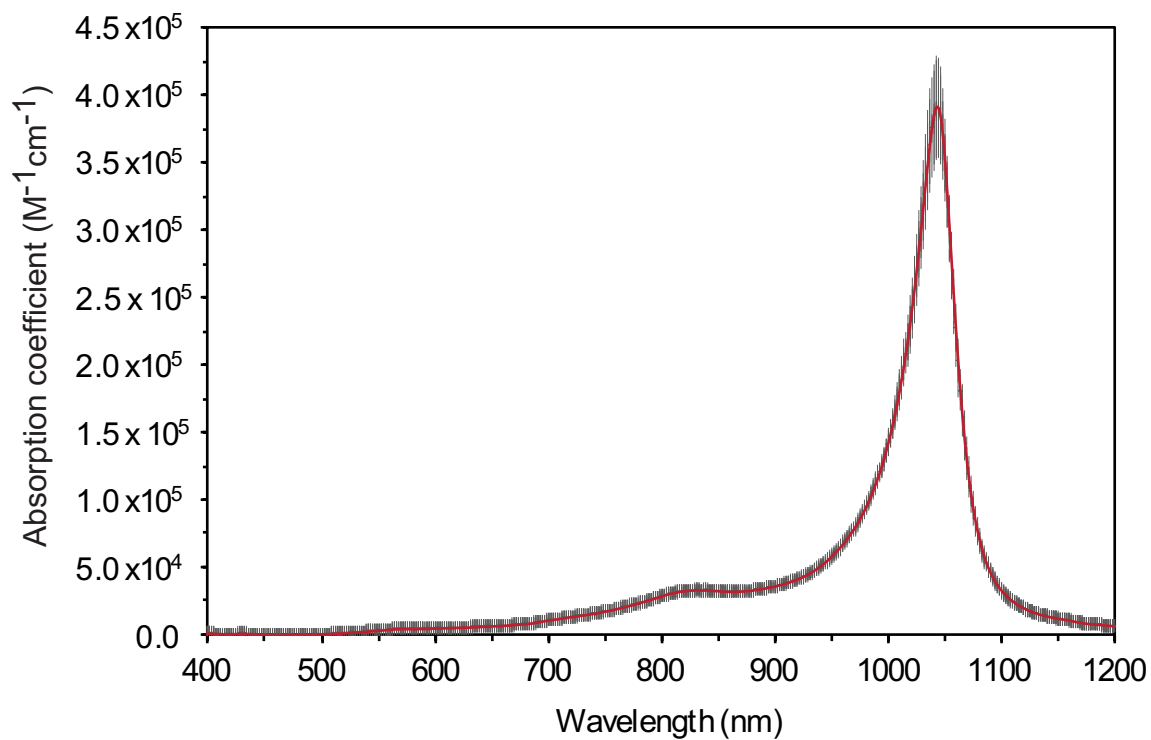


Figure S4.4. Corrected absorption coefficient of IR-140 J-aggregate in 35% DMSO/0.9% NaCl in water.

Note S4.3: Quantum yield

The photoluminescence quantum yield (Φ_F) of a molecule or material is defined as follows,

$$\Phi_F = \frac{P_E}{P_A} \quad (9)$$

where P_E and P_A are the number of photons absorbed and emitted, respectively. To determine the quantum yield, we either use a relative method with a known standard in the same region of the electromagnetic spectrum, or an absolute method, in which the number of photons absorbed and emitted are measured independently. Here, due to the limits of our petite integrating sphere (Horiba KSPHERE-Petite with InGaAs detector Horiba Edison DSS IGA 020L), we use a relative method, with IR-26 as the known standard.

The quantum yield was measured at three different excitation wavelengths, 885 nm, 900 nm, and 915 nm and the results were averaged to obtain the value reported.

To compare an unknown to a reference with a known quantum yield, the following relationship was used:

$$\Phi_{F,x} = \Phi_{F,r} (m_x/m_r) (\eta_x^2/\eta_r^2) \quad (10)$$

Where m represents the slope of the line ($y = mx + b$) obtained from graphing integrated fluorescence intensity versus optical density across a series of samples, η is the refractive index of the solvent, and the subscripts x and r represent values of the unknown and reference, respectively.

The ($\Phi_{F,r}$) of IR-26 was taken to be $0.05 \pm 0.03\%$, as we have previously measured^[8], and which agrees with several recent measurements.^[6,9]

To obtain a plot of integrated fluorescence intensity versus absorbance for the reference and unknown, five solutions and a solvent blank were prepared and their absorbance and emission spectra were acquired. IR-26 was diluted in dichloroethane to concentrations with optical densities less than 0.1 to minimize effects of reabsorption. The baseline corrected (to 1500 nm) fluorescence traces were integrated from 950 – 1500 nm, and the raw integrals were corrected by subtracting the integral over an identical range from fluorescence traces of the blank solvent (Figure S4.5A). The methods employed here were validated with comparison of IR-26 to IR-1061, giving a Φ_F value of $0.3 \pm 0.2 \%$, which is in agreement with our prior absolute quantum yield measurement,^[8] but with lower precision due to the uncertainty in IR-26 absolute Φ_F .

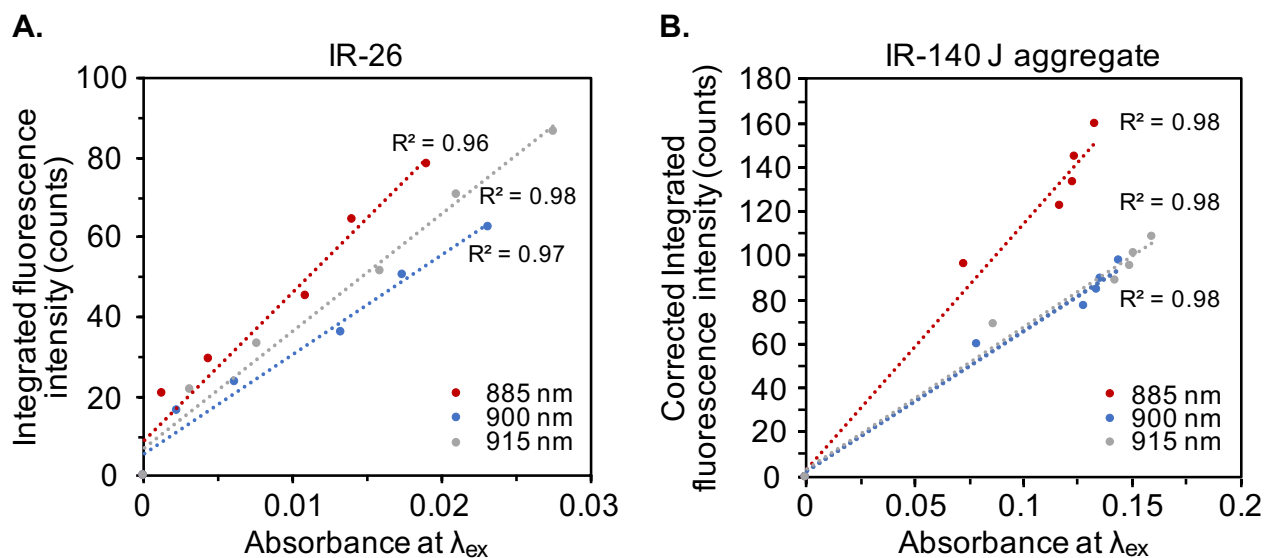


Figure S4.5. Solvent corrected integrated fluorescence intensity versus absorbance plots for (A) IR-26 and (B) IR-140 J-aggregate, also corrected for reabsorption.

The IR-140 J-aggregate was prepared as described in Figure 4.11A, in 35% DMSO/0.9% NaCl in water. Due to the necessity of using concentrated samples for IR-140 to remain in the J2

aggregate state, high concentrations of IR-140 J-aggregate were used for quantum yield measurements (the OD with a 2 mm path length at the relevant excitation wavelengths ranged from 0.07 – 0.16). The baseline corrected (to 1400 nm) fluorescence traces of the optically dense IR-140 J-aggregate samples were corrected for reabsorption by the relationship,

$$I(\lambda) = I_o(\lambda)[- \ln (10^{-OD(\lambda)}) / (1 - 10^{-OD(\lambda)})] \quad (11)$$

where $I(\lambda)$ and $I_o(\lambda)$ are the corrected and experimental fluorescence intensities at each wavelength, and $OD(\lambda)$ is the optical density of the sample at the corresponding wavelength. The corrected fluorescence traces were then integrated from 965 nm – 1400 nm, and the raw integrals were corrected by subtracting the integral over an identical range from fluorescence traces of the blank solvent.

The integrated fluorescence intensities were then plotted against the baseline corrected absorbance values at the relevant wavelength, and the slope and error in slope were obtained ($R^2 > 0.95$ for all traces) (Figure S4.5B)

The refractive index for DCE was taken as 1.440^[10], while that of the 35% DMSO/0.9% NaCl solution in water was approximated as a binary mixture of 35% DMSO in water and taken to be 1.383.^[11] Both values were designated to have a precision to ± 0.001 .

The average quantum yield value (over 885 nm, 900 nm, and 915 nm excitations) was calculated to be 0.012 ± 0.007 . Errors were propagated from the error in IR-26 Φ_F (± 0.03)^[8], slope of the integrated fluorescence intensity versus optical density plot (unique for each trace, but ranged from 7-10% of the slope value), and refractive indices (± 0.001).

For quantum yield measurements, fluorescence traces were acquired with ex. 885 nm, 900

nm, and 915 nm with a 950 nm shortpass filter (Thorlabs FESH0950) and collection from 950–1400 nm for IR-140 J-aggregate and 950–1500 for IR-26. The slits were 5.76 mm for excitation and 11.52 mm for emission. The step size used was 1.0 nm, integration time 0.1 s, and traces were acquired after an automatic detector background subtraction, and with the default excitation correction. All absorbance and fluorescence traces were taken in a 10 mm x 2 mm path length cuvette. For absorbance traces, the 2 mm path length was used, while emission traces were acquired with 10 mm at the excitation side and 2 mm on the emission side, with emission detection occurring at 90° from excitation.

Note S4.4: Photobleaching rates

All photobleaching data were fit to a mono-exponential decay and the rate constants were obtained from the first order reaction equation:

$$\ln[A] = -kt + \ln [A]_o \quad (12)$$

where A and A_o represent the emission collected at time t and the initial emission collected, respectively. All R^2 values were > 0.96 . Error bars represent the standard deviation of three measurements. If a change in slope occurred in the $\ln[A]$ values (*i.e.* in the IR-140 J-aggregate bleaching in 35% DMSO/0.9% NaCl in water solution), the rate was taken as the initial rate and the lines were fit only to the linear region (Figure S4.6). This analysis conservatively estimates the photobleaching rate of the solution phase aggregate as slower than it appeared in subsequent time points (see Figure 4.11D).

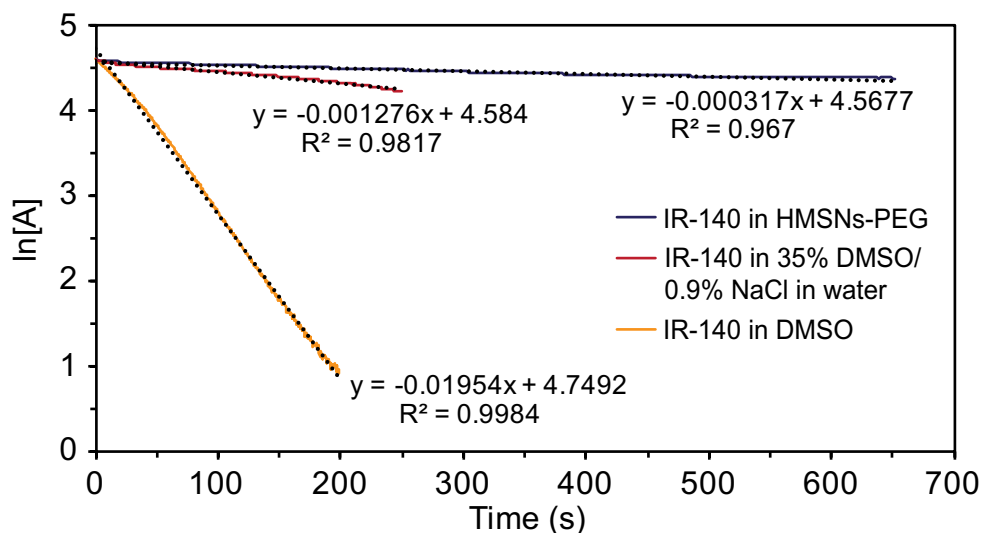


Figure S4.6. Photobleaching data plotted as the $\ln[A]$ vs time and the corresponding linear fits.

To compare photobleaching rates between samples irradiated at distinct wavelengths, it is necessary to consider the relative number of photons absorbed by each species. This requires

corrections for (1) the difference in photon energy between the two wavelengths, and (2) the difference in photons absorbed by the two samples.

To account for photons of different energy, we go back to the common unit of number of photons per second per surface unit N_p , ($\text{cm}^{-2}\text{s}^{-1}$). This value can be obtained by first calculating energy of a photon E_p , (J) at the wavelength of irradiation:

$$E_p = \frac{hc}{\lambda} \quad (13)$$

where h is Planck's constant, and c the speed of light. The N_p can then be found from the irradiance I (Wcm^{-2}) and E_p by the following equation:

$$N_p = \frac{I}{E_p} \quad (14)$$

The N_p for 980 nm and 785 nm light is 4.8×10^{17} and $3.8 \times 10^{17} \text{ cm}^{-2}\text{s}^{-1}$, respectively.

To account for the difference in photons absorbed, we use the absorption coefficients at the wavelength of irradiation, λ_{ex} . For the IR-140 J-aggregate, the corrected absorption value was used. The absorption coefficient of IR-140 in HMSNs-PEG was taken to be that of the J-aggregate in solution. The relative values of $N_p \times \epsilon$ can then be compared to obtain a ratio, X for each wavelength,

$$X_{785} = (N_{p,785} \times \epsilon_m) / (N_{p,980} \times \epsilon_j) \quad (15)$$

$$X_{980} = (N_{p,980} \times \epsilon_j) / (N_{p,980} \times \epsilon_j) \quad (16)$$

where ϵ_m and ϵ_j represent the absorbance coefficient of the monomer and J-aggregate, respectively, at their appropriate excitation wavelength, λ_{ex} . The ratio X_{785} was calculated to be

0.998, providing a correction factor for the relative number of photons absorbed per second in the 785 nm experiment compared to the 980 nm experiments, while the ratio X_{980} is 1.000. These values can be related to the relative rate, k_{rel} by the equation:

$$k_{rel} = \frac{k_{raw}}{X} \quad (17)$$

The relative rates with intermediate values used in the calculations are listed below in Table S4.1.

Table S4.1. Photobleaching rates and values used in calculations and corrections.

Sample	λ_{ex} (nm)	Fluence (mWcm ⁻²)	k_{raw} (s ⁻¹) x 10 ³	ϵ at λ_i (M ⁻¹ cm ⁻¹) x 10 ⁻⁵	N_p	k_{rel} (s ⁻¹) x 10 ³	Relative stability
1 monomer	785	97 ± 3	19.54 ± .04	1.18 ± 0.07	3.83 x10 ¹⁷	19 ± 1	1
1 J-aggregate	980	97 ± 3	1.276 ± 0.008	0.95 ± 0.04	4.79 x 10 ¹⁷	1.28 ± 0.05	15 ± 1
1 in HMSNs- PEG	980	97 ± 3	0.317 ± 0.002	0.95 ± 0.04	4.79 x 10 ¹⁷	0.32 ± 0.01	62 ± 5

4.6 Acknowledgment

We thank Prof. Matthias Tschöp, Prof. Vasilis Ntziachristos, Dr. Thomas Schwarz-Romond, Uwe Klemm and all members of the Helmholtz Pioneer Campus and Institute for Biological and Medical Imaging for their support. No competing financial interests have been declared. This work was supported by grants to E.D.C (NSF GRFP DGE-1144087, Christopher S. Foote Fellowship), O.T.B. (Emmy-Noether-Programm of DFG BR 5355/2-1, Helmholtz Pioneer Campus Institute for Biomedical Engineering), J.I.Z. (Zink student research fund), and E.M.S. (UCLA, Sloan Research Award FG-2018-10855, NIH 1R01EB027172-01).

4.7 References

1. (a) Hong, G.; Antaris, A.L.; Dai, H. "Near-infrared fluorophores for biomedical imaging." *Nat. Biomed. Eng.* **2017**, *1*, 0010. (b) Carr, J.A.; Aellen, M.; Franke, D.; So, P.T.C.; Bruns, O.T.; Bawendi, M.G. "Absorption by water increases fluorescence image contrast of biological tissue in the shortwave infrared." *Proc. Natl. Acad. Sci. U.S.A.* **2018**, *37*, 9080–9085. (c) Smith, A.M.; Mancini, M.C.; Nie, S.M. "Second window for in vivo imaging." *Nat. Nanotechnol.* **2009**, *4*, 710–711.
2. Thimsen, E.; Sadtler, B.; Berezin, M.Y. "Shortwave-infrared (SWIR) emitters for biological imaging: a review of challenges and opportunities" *Nanophotonics* **2017**, *6*, 1043–1054.
3. Welsher, K.; Liu, Z.; Sherlock, S.P.; Robinson, J.T.; Chen, Z.; Daranciang, D.; Dai, H. "A route to brightly fluorescent carbon nanotubes for near-infrared imaging in mice." *Nat. Nanotechnol.* **2009**, *4*, 773–780.
4. (a) Hong, G.; Tobinson, J.T.; Zhang, Y.J.; Diao, S.; Antaris, A.L.; Wang, Q.B.; Dai, H. "In vivo fluorescence imaging with Ag₂S quantum dots in the second near-infrared window." *Angew. Chem. Int. Ed.* **2012**, *24*, 9818–9821. (b) Bruns, O.T.; Bischof, T.S.; Harris, D.K.; Franke, D.; Shi, Y.; Riedemann, L.; Bartelt, A.; Jaworski, F.B.; Carr, J.A.; Rowlands, C.J.; Wilson, M.W.B.; Chen, O.; Wei, H.; Hwang, G.W.; Montana, D.M.; Coropceanu, I.; Achorn, O.B.; Kloepper, J.; Heeren, J.; So, P.T.C.; Fukumura, D.; Jensen, K.F.; Jain, R.K.; Bawendi, M.G. "Next-generation in vivo optical imaging with short-wave infrared quantum dots." *Nat. Biomed. Eng.* **2017**, *1*, 0056.
5. (a) Chen, G.; Ohulchanskyy, T.Y.; Liu, S.; Law, W.-C.; Wu, F.; Swihart, M.T.; Agren, H.; Prasad, P.N. "Core/shell NaGdF₄:Nd³⁺/NaGdF₄ nanocrystals with efficient near-infrared to near-infrared downconversion photoluminescence for bioimaging applications." *ACS Nano* **2012**, *6*, 2969–2977. (b) Naczynski, D.J.; Tan, M.C.; Zevon, M.; Wall, B.; Kohl, J.; Kulesa, A.; Chen, S.; Roth, C.M.; Riman, R.E.; Moghe, P.V. "Rare-earth doped biological composites as in vivo shortwave infrared reporters." *Nat. Commun.* **2013**, *4*, 2199.
6. (a) Yang, Q.; Ma, Z.; Wang, H.; Zhou, B.; Zhu, S.; Zhong, Y.; Wang, J.; Wan, H.; Antaris, A.; Ma, R.; Zhang, X.; Yang, J.; Zhang, X.; Sun, H.; Liu, W.; Liang, Y.; Dai, H. "Rational design of molecular fluorophores for biological imaging in the NIR-II window." *Adv. Mater.* **2017**, *29*, 1605497. (b) Cosco, E.D.; Caram, J.R.; Bruns, O.T.; Franke, D.; Day, R.A.; Farr, E.P.; Bawendi, M.G.; Sletten, E.M. "Flavylium polymethine fluorophores for near- and shortwave infrared imaging." *Angew. Chem. Int. Ed.* **2017**, *56*, 13126–13129. (c) Xu, G.; Yan, Q.; Lv, X.; Zhu, Y.; Xin, K.; Shi, B.; Wang, R.; Chen, J.; Gao, W.; Shi, P.; Fan, C.; Zhao, C.; Tian, H. "Imaging of colorectal cancers using activatable nanoprobe with second near-infrared window emission." *Angew. Chem. Int. Ed.* **2018**, *57*, 3626–3630. (d) Li, B.;

- Lu, L.; Zhao, M.; Lei, Z.; Zhang, F. “An efficient 1064 nm NIR-II excitation fluorescent molecular dye for deep-tissue high-resolution dynamic bioimaging.” *Angew. Chem. Int. Ed.* **2018**, *57*, 7483–7487. (e) Yang, Q.; Hu, Z.; Zhu, S.; Ma, R.; Ma, H.; Ma, Z.; Wan, H.; Zhu, T.; Jiang, Z.; Liu, W.; Jiao, L.; Sun, H.; Liang, Y.; Dai, H. “Donor engineering for NIR-II molecular fluorophores with enhanced fluorescent performance.” *J. Am. Chem. Soc.* **2018**, *140*, 1715–1724. (f) Sheng, Z.H.; Guo, B.; Hu, D.H.; Xu, S.D.; Wu, W.B.; Liew, W.H.; Yao, K.; Jiang, J.Y.; Liu, C.B.; Zheng, H.R.; Liu, B. “Bright aggregation-induced emission dots for targeted synergetic NIR-II fluorescence and NIR-I photoacoustic imaging of orthotopic brain tumors.” *Adv. Mater.* **2018**, *30*, 1800766.
7. (a) Wuerthner, F.; Kaiser, T.E.; Saha-Moeller, C.R. “J-aggregates: From serendipitous discovery to supramolecular engineering of functional dye materials.” *Angew. Chem. Int. Ed.* **2011**, *50*, 3376–3410. (b) Kobayashi, T. *J-aggregates*; World Scientific: Singapore, **1996**. (c) Jelley, E.E. “Spectral absorption and fluorescence of dyes in the molecular state.” *Nature* **1936**, *138*, 1009–1010. (d) Scheibe, G. “Über die veränderlichkeit der absorptionsspektren in lösungen und die nebenvalezenzen als ihre ursache.” *Angew. Chem.* **1937**, *50*, 51. (e) Hestand, N.J.; Spano, F.C. “Molecular aggregate photophysics beyond the Kasah Model: Novel design principles for organic materials.” *Acc. Chem. Res.* **2017**, *50*, 341–350.
8. (a) Bashkatov, A. N.; Genina, E. A.; Kochubey, V. I.; Tuchin, V. V. “Optical properties of human skin, subcutaneous and mucous tissues in the wavelength range from 400 to 2000 nm.” *J. Phys. D Appl. Phys.* **2005**, *38*, 2543–2555. (b) Lim, Y.T.; Kim, S.; Nakayama, A.; Stott, N.E.; Bawendi, M.G.; Frangioni, J.V. “Selection of quantum dot wavelengths for biomedical assays and imaging.” *Mol. Imaging* **2003**, *2*, 50–64. (c) Won, N.; Jeon, S.; Kim, K.; Kwag, J.; Park, J.; Kim, S.G.; Kim, S. “Imaging depths of near-infrared quantum dots in first and second optical windows.” *Mol. Imaging* **2012**, *11*, 338–352.
9. Bricks, J.L.; Slominskii, Y.L.; Panas, I.D.; Demchenko, A.P. “Fluorescent J-aggregates of cyanine dyes: basic research and applications review.” *Methods Appl. Fluoresc.* **2018**, *6*, 012001.
10. Shakiba, M.; Ng, K.K.; Huynh, E.; Chan, H.; Charron, D.M.; Chen, J.; Muhanna, N.; Foster, F.S.; Wilson, B.C.; Zheng, G. “Stable J-aggregation enabled dual photoacoustic and fluorescence nanoparticles for intraoperative cancer imaging.” *Nanoscale* **2016**, *8*, 12618–12625.
11. Yang, C.; Wang, X.; Wang, M.; Xu, K.; Xu, C. “Robust colloidal nanoparticles of pyrrolopyrrole cyanine J-aggregates with bright near-infrared fluorescence in aqueous media: From spectral tailoring to bioimaging applications.” *Chem. Eur. J.* **2017**, *23*, 4310–4319.
12. Sun, P.; Wu, Q.; Sun, X.; Miao, H.; Deng, W.; Zhang, W.; Fan, Q.; Huang, W. “J-aggregate squaraine nanoparticles with bright NIR-II fluorescence for imaging guided photothermal therapy.” *Chem. Commun.* **2018**, *54*, 13395–13398.

13. Two other J-aggregates have been employed *in vivo* for photothermal therapy and photoacoustic imaging. (a) Song, X.; Gong, H.; Liu, T.; Cheng, L.; Wang, C.; Sun, X.; Liang, C.; Liu, Z. “J-aggregates of organic dye molecules complexed with iron oxide nanoparticles for imaging-guided photothermal therapy under 915 nm light.” *Small* **2014**, *10*, 4362–4370. (b) Dumani, D.S.; Brecht, H.-P.; Ivanov, V.; Deschner, R.; Harris, J.T.; Homan, K.A.; Cook, J.R.; Emelianov, S.Y.; Ermilov, S.A. “Co-registered photoacoustic and fluorescent imaging of a switchable nanoprobe based on J-aggregates of indocyanine green.” *Proc. SPIE 10494, Photons Plus Ultrasound: Imaging and Sensing* **2018**, 104942W.
14. Kim, S.; Shi, Y.; Kim, J.Y.; Park, K.; Cheng, J.X. “Overcoming the barriers in micellar drug delivery: Loading efficiency, *in vivo* stability, and micelle-cell interaction.” *Expert Opin. Drug. Deliv.* **2010**, *7*, 49–62.
15. (a) Chen, F.; Hong, H.; Shi, S.; Goel, S.; Valdovinos, H.F.; Hernandez, R.; Theuer, C.P.; Barnhart, T.E.; Cai, W. “Engineering of hollow mesoporous silica nanoparticles for remarkably enhanced tumor active targeting efficacy.” *Sci. Rep.* **2014**, *4*, 5080. (b) Guardado-Alvarez, T.M.; Chen, W.; Norton A.E.; Russell M.M.; Connick, W.B.; Zink, J.I. “Analyte-responsive gated hollow mesoporous silica nanoparticles exhibiting inverse functionality and an AND logic response.” *Nanoscale* **2016**, *8*, 18296–18300.
16. (a) He, Q.; Zhang, Z.; Gao, F.; Li, Y.; Shi, J. “*In vivo* biodistribution and urinary excretion of mesoporous silica nanoparticles: Effects of particle size and PEGylation.” *Small* **2011**, *7*, 271–280. (b) Liu, J.; Luo, Z.; Zhang, J.; Luo, T.; Zhou, J.; Zhao, X.; Cai, K. “Hollow mesoporous silica nanoparticles facilitated drug delivery via cascade pH stimuli in tumor microenvironment for tumor therapy.” *Biomaterials* **2016**, *83*, 51–65.
17. (a) Li, Y.; Li, N.; Pan, W.; Yu, Z.; Yang, L.; Tang, B. “Hollow mesoporous silica nanoparticles with tunable structures for controlled drug delivery.” *ACS Appl. Mater. Interfaces* **2017**, *9*, 2123–2129. (b) Chakravarty, R.; Goel, S.; Hong, H.; Chen, F.; Valdovinos, H. F.; Hernandez, R.; Barnhart, T. E.; Cai, W. “Functionalized hollow mesoporous silica nanoparticles for tumor vasculature targeting and PET image-guided drug delivery.” *Nanomedicine (Lond)* **2015**, *10*, 1233–1246. (c) Luo, Z.; Hu, Y.; Cai, K.; Ding, X.; Zhang, Q.; Li, M.; Ma, X.; Zhang, B.; Zeng, Y.; Li, P.; Li, J.; Liu, J.; Zhao, Y. “Intracellular redox-activated anticancer drug delivery by functionalized hollow mesoporous silica nanoreservoirs with tumor specificity.” *Biomaterials* **2014**, *35*, 7951–7962. (d) Du, L.; Liao, S.; Khatib, H.A.; Stoddart, J.F.; Zink, J.I. “Controlled-access hollow mechanized silica nanocontainers.” *J. Am. Chem. Soc.* **2009**, *131*, 15136–15142.

18. (a) Singh, R.K.; Kim, T.H.; Mahapatra, C.; Patel, K.D.; Kim, H.W. "Preparation of self-activated fluorescence mesoporous silica hollow nanoellipsoids for theranostics." *Langmuir* **2015**, *31*, 11344–11352. (b) Yang, S.; Chen, D.; Li, N.; Xu, Q.; Li, H.; Gu, F.; Xie, J.; Lu, J. "Hollow mesoporous silica nanocarriers with multifunctional capping agents for in vivo cancer imaging and therapy." *Small* **2016**, *12*, 360–370. (c) Huang, C.C.; Huang, W.; Yeh, C.S. "Shell-by-shell synthesis of multi-shelled mesoporous silica nanospheres for optical imaging and drug delivery." *Biomaterials* **2011**, *32*, 556–564. (d) Fan, Z.; Li, D.; Yu, X.; Zhang, Y.; Cai, Y.; Jin, J.; Yu, J. "AIE luminogen-functionalized hollow mesoporous silica nanospheres for drug delivery and cell imaging." *Chem. Eur. J.* **2016**, *22*, 3681–3685.
19. Hong, S.; Kim, H.; Choi, Y. "Indocyanine green-loaded hollow mesoporous silica nanoparticles as an activatable theranostic agent." *Nanotechnology* **2017**, *28*, 185102.
20. (a) Soppera, O.; Turck, C.; Lougnot, D.J. "Fabrication of micro-optical devices by self-guiding photopolymerization in the near IR." *Opt. Lett.* **2009**, *34*, 461–463. (b) Bonardi, A.H.; Dumar, F.; Grant, T.M.; Noirbent, G.; Gigmes, D.; Lessard, B.H.; Fouassier, J.-P.; Lalevee, J. "Higher performance near-infrared (NIR) photoinitiating systems operating under low light intensity and in the presence of oxygen." *Macromolecules* **2018**, *51*, 1314–1324.
21. Leung, K.C.F.; Nguyen, T.D.; Stoddart, J.F.; Zink, J.I. "Supramolecular nanovalves controlled by proton abstraction and competitive binding." *Chem. Mater.* **2006**, *18*, 5919–5928.
22. (a) Zhou, W.; Dridi, M.; Suh, J.Y.; Kim, C.H.; Co, D.T.; Wasielewski, M.R.; Schatz, G.C.; Odom, T.W. "Lasing action in strongly coupled plasmonic nanocavity arrays." *Nat. Nanotechnol.* **2013**, *8*, 506–511. (b) Yang, A.; Hoang, T.B.; Dridi, M.; Deeb, C.; Mikkelsen, M.H.; Schatz, G.C.; Odom, T.W. "Real-time tunable lasing from plasmonic nanocavity arrays." *Nat. Commun.* **2015**, *6*, 6939.
23. Oseledchyk, A.; Andreou, C.; Wall, M.A.; Kircher, M.F. "Folate-targeted surface-enhanced resonance Raman scattering nanoprobe ratiometry for detection of microscopic ovarian cancer." *ACS Nano* **2017**, *11*, 1488–1497.
24. Berezin, M.Y.; Zhan, C.; Lee, H.; Joo, C.; Akers, W.J.; Yazdanfar, S.; Achilefu, S. "Two-photon optical properties of near-infrared dyes at 1.55 μm excitation." *J. Phys. Chem. B.* **2011**, *115*, 11530–11535.
25. Wang, C.; Weiss, E.A. "Sub-nanosecond resonance energy transfer in the near-infrared within self-assembled conjugates of PbS quantum dots and cyanine dye J-aggregates." *J. Am. Chem. Soc.* **2016**, *138*, 9557–9564.
26. Modification of pores with APTS is predicted to have a size change of 0.5 nm, whereas we didn't observe pore size change. See: (a) Chen, W.; Tsai, P.H.; Hung, Y.; Chiou, S.H.; Mou, C.Y. "Nonviral cell labeling and differentiation agent for induced pluripotent stem cells based on mesoporous silica

- nanoparticles.” *ACS Nano* **2013**, *7*, 8423–8440. (b) Chou, C.C.; Chen, W.; Hung, Y.; Mou, C.Y. “Molecular elucidation of biological response to mesoporous silica nanoparticles in vitro and in vivo.” *ACS Appl. Mater. Interfaces* **2017**, *9*, 22235–22251. (c) Chen, W.; Cheng, C.A.; Zink, J.I. “Spatial, temporal, and dose control of drug delivery using noninvasive magnetic stimulation.” *ACS Nano* **2019**, *13*, 1292–1308. (d) Zhang, Y.; Ang, C.Y.; Li, M.; Tan, S.Y.; Qu, Q.; Luo, Z.; Zhao, Y. “Polymer-coated hollow mesoporous silica nanoparticles for triple-responsive drug delivery.” *ACS Appl. Mater. Interfaces* **2015**, *7*, 18179–18187.
- 27.** Modification of pores with APTS is predicted to have a size change of 0.5 nm, whereas we didn’t observe pore size change. See ref 26.
- 28.** (a) Rurack, K.; Spieles, M. “Fluorescence quantum yields of a series of red and near-infrared dyes emitting at 600–1000 nm.” *Anal. Chem.* **2011**, *83*, 1232–1242. (b) Hatami, S.; Würth, C.; Kaiser, M.; Leubner, S.; Gabriel, S.; Bahrig, L.; Lesnyak, V.; Pauli, J.; Gaponik, N.; Eychmüller, A.; Resch-Genger, U. “Absolute photoluminescence quantum yields of IR-26 and IR-emissive Cd_{1-x}Hg_xTe and PbS quantum dots- method and material-inherent challenges.” *Nanoscale* **2015**, *7*, 133–143.
- 29.** A sulfonated variant of the IR-140 chromophore has been characterized to J-aggregate in solution. See ref 27b.
- 30.** NIR fluorophores have emission that extends into the SWIR. (a) Carr, J.A.; Franke, D.; Caram, J.R.; Perkinson, C.F.; Askoxylakis, V.; Datta, M.; Rukumura, D.; Jain, R.K.; Bawendi, M.G.; Bruns, O.T. “Shortwave infrared fluorescence imaging with the clinically-approved near-infrared dye indocyanine green.” *Proc. Natl. Acad. Sci. U.S.A.* **2018**, *115*, 4465–4470. (b) Starosolski, Z.; Bhavane, R.; Ghaghada, K.B.; Vasudevan, S.A.; Kaay, A.; Annapragada, A. “Indocyanine green fluorescence in second near-infrared (NIR-II) window.” *PLoS ONE* **2017**, *12*, e0187563. (c) Zhu, S.; Hu, Z.; Tian, R.; Yung, B.C.; Yang, Q.; Zhao, S.; Kiesewetter, D.O.; Niu, G.; Sun, H.; Antaris, A.L.; Chen, X. “Repurposing cyanine NIR-I dyes accelerates clinical translation of near-infrared-II (NIR-II) bioimaging.” *Adv. Mater.* **2018**, *30*, 1802546.
- 31.** Qiao, Y.; Polzer, F.; Kirmse, H.; Kirstein, S.; Rabe, J.P. “Nanohybrids from nanotubular J-aggregates and transparent silica nanoshells.” *Chem. Commun.* **2015**, *51*, 11980–11982.
- 32.** (a) Ruhle, B.; Saint-Cricq, P.; Zink, J.I. “Externally controlled nanomachines on mesoporous silica nanoparticles for biomedical applications.” *Chemphyschem* **2016**, *17*, 1769–1779. (b) Chen, W.; Cheng, C.A.; Lee, B.Y.; Clemens, D.L.; Huang, W.Y.; Horwitz M.A.; Zink, J.I. “Facile strategy enabling both high loading and high release amounts of the water-insoluble drug Clofazimine using mesoporous silica nanoparticles.” *ACS Appl. Mater. Interfaces* **2018**, *10*, 31870–31881. (c) Chen, W.; Glackin, C.A.;

- Horwitz, M.A.; Zink, J.I. “Nanomachines and other caps on mesoporous silica nanoparticles for drug delivery.” *Acc. Chem. Res.* **2019**, *52*, 1531–1542. (d) Cheng, C.A.; Deng, T.; Lin, F.C.; Cai, Y.; Zink, J.I. “Supramolecular nanomachines as stimuli-responsive gatekeepers on mesoporous silica nanoparticles for antibiotic and cancer drug delivery.” *Theranostics* **2019**, *9*, 3341–3364.
- 33.** (a) Sumer, B.; Gao, J. “Theranostic nanomedicine for cancer.” *Nanomedicine* **2008**, *3*, 137–140. (b) Chakravarty, R.; Goel, S.; Hong, H.; Chen, F.; Valdovinos, H.F.; Hernandez, R.; Barnhart, T.E.; Cai, W. “Functionalized hollow mesoporous silica nanoparticles for tumor vasculature targeting and PET image-guided drug delivery.” *Nanomedicine* **2015**, *10*, 1233–1246. (c) Ni, D.; Jiang, D.; Ehlerding, E.B.; Huang, P.; Cai, W. “Radiolabeling silica-based nanoparticles via coordination chemistry: basic principles, strategies, and applications.” *Acc. Chem. Res.* **2018**, *51*, 778–788. (d) Zhao, N.; Yan, L.; Zhao, X.; Chen, X.; Li, A.; Zheng, D.; Zhou, X.; Dai, X.; Xu, F.J. “Versatile types of organic/inorganic nanohybrids: From strategic design to biomedical applications.” *Chem. Rev.* **2019**, *119*, 1666–1762.
- 34.** (a) Brixner, T.; Hildner, R.; Kohler, J.; Lambert, C.; Wurthner, F. “Exciton transport in molecular aggregates– from natural antennas to synthetic chromophore systems.” *Adv. Energy Mater.* **2017**, *7*, 1700236. (b) Doria, S.; Sinclair, T.S.; Klein, N.F.; Bennett, D.I.G.; Chuang, C.; Freyria, F.S.; Steiner, C.P.; Foggi, P.; Nelson, K.A.; Cao, J.; Aspuru-Guzik, A.; Llyod, S.; Caram, J.R.; Bawendi, M.G. “Photochemical control of exciton superradiance in light-harvesting nanotubes.” *ACS Nano* **2018**, *12*, 4556–4564.
- 35.** Kasha, M.; Rawls, H. R.; El-Bayoumi, M. A. “The exciton model in molecular spectroscopy.” *Pure Appl. Chem.* **1965**, *11*, 371–392.

Chapter 5

Analyte-Responsive Gated Hollow Mesoporous Silica Nanoparticles Exhibiting Inverse Functionality and an AND Logic Response

This chapter of the dissertation was adapted and reprinted with permission from Tania M. Guardado-Alvarez, Wei Chen, Amie E. Norton, Melissa M. Russell, William B. Connick, Jeffrey I. Zink *Nanoscale* **2016**, 8, 18296–18300. Copyright 2016 The Royal Society of Chemistry. Co-author contributions: Guardado-Alvarez T. M., Chen W., Norton A. E., and Russell, M. M. performed the experiments. William B. Connick, and Jeffrey I. Zink were the P.Is.



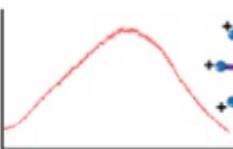
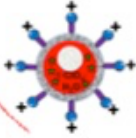
Keywords of this chapter: hollow mesoporous silica nanoparticles, perchlorate ion sensor, crystalline platinum complex, core@shell structure, acid-responsive gate, Boolean AND logic

Abstract

A multifunctional nanoparticle with designed selectivity was made using hollow mesoporous silica, ship-in-a-bottle synthesis of a crystalline solid-state detector, and protection of the crystal by acid-responsive nanogates. The system demonstrates the inverse application of the usual trapping of contents by the gate followed by their release. Instead, the gate protects the contents followed by selective exposure. Crystallization of [Pt(tpy)Cl](PF₆) (tpy = 2,2':6',2''-terpyridine) inside the cavity of hollow mesoporous silica created the unique core/shell nanoparticle. The crystalline core becomes fluorescent in the presence of perchlorate. By condensing an acid-sensitive gate onto the particle, access to the pores is blocked and the crystal protected. The new nanomaterial obeys Boolean AND logic; only the presence of both the analyte (ClO₄⁻) and acid

results in the optical response.

Table of Content Figure

Input 1 (Acid)	Input 2 (Perchlorate)	Output (Luminescence)
1  + 	1 ClO_4^-	1  

5.1 Introduction

Core/shell nanoparticles have attracted much attention in recent years¹⁻¹⁴ due to their adaptability to many different fields and applications such as electronics,^{5,15,16} biomedical,^{11,17-19} pharmaceutical,²⁰ optics,²¹⁻²³ and catalysis.^{24,25} Hollow mesoporous silica nanoparticles (MSNs) are of particular interest because the presence of the hollow cavity can act as a reservoir which can be controllably filled with another material yielding a core/shell nanoparticle.^{8,26,27} Chemical modification of pore entrances at the surface produces gated MSNs that are gaining wide acceptance as useful drug delivery vehicles by carrying cargo molecules such as therapeutic drugs to a desired target and releasing them in response to a specific predetermined stimulus. Many imaginative methods of trapping cargo in pores and releasing it in response to external signals or intracellular biological molecules have been developed, including nanogates such as those used in this work.

The inverse function, namely protecting an entity inside the particle until it is desirable and useful to expose it to an outside influence, has not been widely utilized. Many possible scenarios can be imagined where it would be desirable to carry a cargo unexposed and unharmed through an intermediary environment to a site and then expose it at a location where its output can be used. For example, this capability is attractive for maintaining cargo functionality and performance over multiple cycles, preventing contamination of the environment due to cargo leaching, and realizing high levels of cargo recovery. A recent example from our laboratories is a nanovalve-based chemical amplifier involving an enzyme sequestered in a pore. Opening the pore allows substrate molecules to enter resulting in a catalytic production of fluorescent molecules.²⁸ In the example in

this work, nanocrystals sensitive to an aqueous analyte are grown in the interior of a hollow MSN where they are subsequently protected by closed gates. When the gates are opened the crystals are exposed and give an optical response.

Even more selectivity can be introduced if the nanocarrier possesses a second function made possible by the nanogate: Boolean AND logic. In Boolean logic, which is fundamental to modern computing, values are either True or False. For a so-called AND gate, an event is only triggered if two specific values are True. MSNs have been designed to have pore valves that respond to dual stimuli and release trapped molecules in response;²⁹⁻³⁵ two examples have been reported to release molecules with true AND logic.^{29,36} In this work, we selected an ionic molecular crystal as representative of a solid state optical indicator that is responsive to dissolved molecules or ions that enter the porous particle. The resulting porous nanoparticle with accessibility controlled by gates was designed to have a selective response following AND logic.

5.2 Experimental Section

5.2.1 Materials and characterizations

All reagents including tetraethyl orthosilicate, dodecyltrimethylammonium bromide (DTAB), sodium hydroxide, hydrogen chloride, sodium bicarbonate, *N*-phenylaminomethyltriethoxysilane (PhAMTES), sodium 1-allyloxy-2-hydroxypropane sulfonate, aerosol MA-80-1, α -cyclodextrin, triethylamine, ammonium persulfate, divinyl benzene, styrene, are commercially available and were used without further purification. The structure of hollow mesoporous silica nanoparticles was confirmed by powder X-ray diffraction (XRD) experiments in Bragg-Brentano geometry (θ - 2θ) on a Philips X'Pert Powder Diffractometer operated at 40 kV, 40 mA using CuK α radiation

($\lambda=1.54 \text{ \AA}$). To confirm the presence of the hollow core, shell thickness, and confirmation that 1-PF_6 crystalized inside the hollow core, transmission electron microscopy (TEM) was done. The particles were dispersed in ethanol and then deposited and dried on a carbon film-coated Cu grid. Images were taken on a JEM1200-EX (JEOL) electron microscope operating at 50 kV. Fourier transform infrared (FT-IR) spectroscopy measurements were acquired on a Jasco Model 420 spectrometer to confirm the attachment of PhAMTES. For monitoring the emission of 1-PF_6 , the samples were illuminated using the 514 nm line of a Coherent I306C argon ion laser (40 mW). The photoluminescence spectra of the samples were collected using an Acton 2300i monochromator and a Princeton Instruments CCD. A 550 nm cut-off filter was placed in front of the CCD to block stray laser light.

5.2.2 Synthesis of polystyrene beads

Polystyrene beads were made using a previously published procedure. In a reaction vessel, 0.171 g of sodium bicarbonate was added to 138 mL of water under nitrogen. The water solution was then deoxygenated by bubbling nitrogen through the solution for 40 minutes. Afterwards, 2.5 g of Aerosol MA-80-1 was dissolved in 10 mL of water and then added to the solution. The solution was brought to 50 °C and 2.33 g of divinyl benzene and 60 mL of styrene was slowly added. Sodium 1-allyloxy-2-hydroxypropane sulfonate was dissolved in 10 mL of water and was immediately injected into the solution 5 minutes after the addition of divinyl benzene and styrene. The temperature was then brought to 70 °C at which point a solution of 0.75 g of ammonium persulfate in 5 mL of water was injected. The reaction continued for 4 hours. The particles were washed through dialysis for 3 days changing the water twice a day. They were then centrifuged

with water twice and then with methanol two more times. They were then left to dry under vacuum. The size of the particles was confirmed by taking a TEM image of the particles.

5.2.3 Synthesis of Hollow Mesoporous Silica Nanoparticles

Hollow mesoporous silica nanoparticles were synthesized by adding 0.5 g of DTAB and 0.25 g of the polystyrene beads into 20 mL of water. The solution was sonicated for 20 minutes and then allowed to rest for 30 minutes to allow any large aggregates of the polystyrene beads to settle. The solution was then carefully poured into 100 mL of water and 450 μ L of 2 M NaOH was added. After 30 minutes, 500 μ L of TEOS was added and the reaction was left at room temperature for 24 hours. The particles were washed thoroughly with water and methanol and then calcined at 500 $^{\circ}$ C to remove the surfactant and the polystyrene beads. N₂ adsorption-desorption isotherms and XRD were used to measure the pore size of hollow mesoporous silica nanoparticles and TEM images were taken to confirm the presence of the hollow cavity.

5.2.4 Surface modification of the hollow mesoporous silica nanoparticles

50 mg of the hollow mesoporous silica nanoparticles and 50 μ L of PhAMTES were placed in 3 mL of toluene and the reaction was left overnight stirring at room temperature. The particles were then washed with methanol and then with water and then dried in a vacuum. An FT-IR spectrum of the particles was taken to confirm the presence of PhAMTES on the hollow mesoporous silica nanoparticles.

5.2.5 Crystalizing 1•PF₆ inside the hollow core

A highly concentrated solution of 1•PF₆ was made by taking 10 mg of the crystal and dissolving it in 300 μ L of dimethyl sulfoxide. 20 mg of the particles were added to the solution

and it was left stirring for 24 hours. The solution was then allowed to slowly evaporate until the particles were dry.

5.2.6 Blocking the pore openings with α -cyclodextrin

The particles were washed twice with dimethyl sulfoxide and then twice with water to remove any $\mathbf{1}\cdot\text{PF}_6$ from the surface of the hollow particles. The particles were then left in 1.5 mL of water and 50 mg of α -cyclodextrin was added. The particles were then left stirring overnight.

5.2.7 Controlled Activation of the System

The operation of the system was monitored using fluorescence spectroscopy. 10 mg of the particles were placed in an NMR tube. Enough water was added to just wet the particles and the NMR tube was placed in front of a CCD. The emission of $\mathbf{1}\cdot\text{PF}_6$ was measured as a function of time at 1-second intervals by using a 514 nm excitation beam (40 mW). The activation profile of the system was obtained by plotting luminescence intensities of $\mathbf{1}\cdot\text{PF}_6$ at the emission maximum (670 nm) as a function of time. 40 μL of a 30 mM solution of NaClO_4 was added to the sample followed by addition of 40 μL of an acid solution to bring the pH to 3 in order to activate the system.

5.3 Results and discussion

A schematic diagram of the system is shown in Figure 5.1. The nanogate initially selected for this study is composed of a *N*-phenylaminomethyltriethoxysilane (PhAMTES) stalk and a α -cyclodextrin cap (α CD).²⁶ The α CD has a pH dependent supramolecular interaction with the aniline-based stalk that blocks the pore openings at neutral pH. Protonation of the stalk under acidic conditions reduces the binding constant and α CD dissociates. In prior applications of this system, physical blockage of the pore opening by α CD caused the gating. Surprisingly in the case of perchlorate anion, the stalk itself provided the gating as described below. The ionic crystal is the perchlorate ion-responsive [Pt(tpy)Cl](PF₆) (tpy = 2,2':6',2''-terpyridine) (1•PF₆), which is a yellow solid that is practically insoluble in water.³⁷ Solid platinum(II) terpyridyl salts of this type have attracted considerable attention because of their promising vapor³⁸⁻⁴⁶ and ion sensing properties.³⁷ Specifically, 1•PF₆ which rapidly changes from yellow to red and becomes intensely luminescent upon exposure to aqueous ClO₄⁻,³⁷ an important groundwater contaminant.^{47,48} The response is extraordinarily selective, and it is a consequence of anion exchange at the surface of solid [Pt(tpy)Cl](PF₆). The resulting 1•ClO₄•H₂O is deep red and intensely luminescent. Strong intermolecular metal–metal interactions (Pt...Pt: 3.3031(5), 3.3692(5) Å) (Figure 5.2) account for the low-lying metal-metal-to-ligand charge-transfer MMLCT[d σ^* (Pt)- π^* (tpy))] band near 525 nm, where the d σ^* arises from the interaction of the d_{z²}(Pt) orbitals of adjacent complexes. Green light selectively excites this material resulting in intense MMLCT emission near 690 nm.³⁷

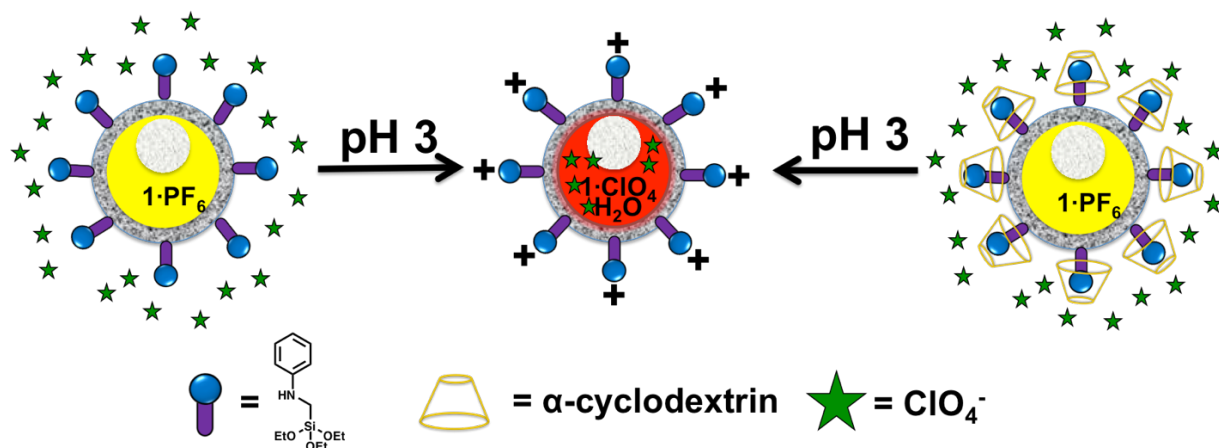


Figure 5.1. The stalks on the nanoparticles (left) protect the $1\cdot\text{PF}_6$ crystal in the hollow interior from perchlorate until pH 3 is reached. After acidification, perchlorate is able to access the nanoparticle, reach the crystal and produce brightly luminescent $1\cdot\text{ClO}_4\cdot\text{H}_2\text{O}$ (middle). Particles capped with αCD (right) function similarly.

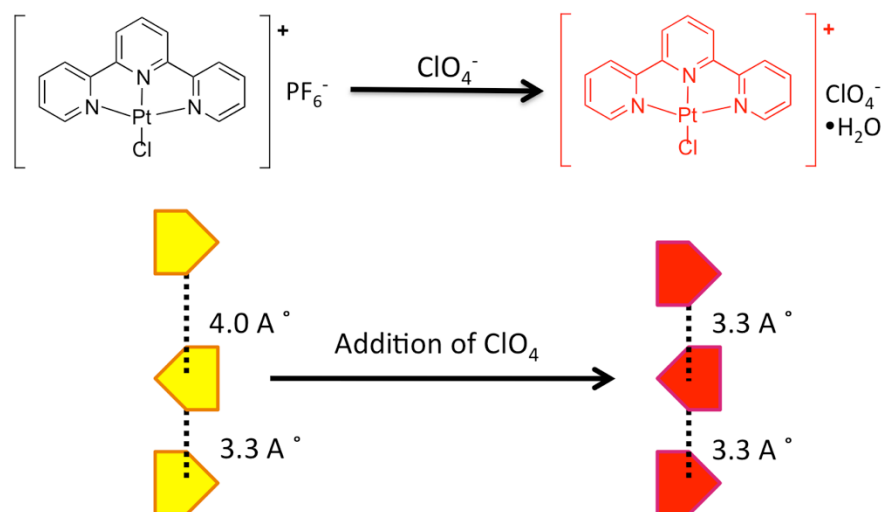


Figure 5.2. $1\cdot\text{PF}_6$ converting to $1\cdot\text{ClO}_4\cdot\text{H}_2\text{O}$ after the addition of ClO_4^- anion.

The core-shell MSNs used in this work consist of spherical particles about 130 nm in diameter with a hollow core and a ~35 nm thick shell. These were synthesized using the sol-gel method, where polystyrene spheres and dodecyltrimethylammonium bromide (DTAB) were used as the templates for the hollow core and the mesopores, respectively. First, highly charged monodispersed polystyrene beads were made by emulsion polymerization.^{49,50} The polystyrene beads (~90 nm in diameter Figure 5.3) were then placed in an aqueous solution of DTAB and NaOH. TEOS was then added to the solution and the reaction was allowed to continue for 24 hours. The resulting white particles were washed and calcined at 500 °C to remove surfactant and polystyrene. A TEM image of the resulting particles (Figure 5.4) show that the shell thickness was about 35 nm. N₂ adsorption-desorption isotherms show that the Brunauer-Emmett-Teller (BET) surface area, total pore volume, and average pore diameter are 1143 m²/g, 0.75 cm³/g, and 2.5 nm respectively (Figure 5.5). In addition, the high surface area and pore volume of hollow MSNs – the desired properties of MSNs – suggest that cargos such as [Pt(tpy)Cl](PF₆) can be loaded inside the pores and cavity of hollow MSNs, allowing those loaded cargos to be efficient sensor to detect the presence of ClO₄⁻ in the water solution.

The stalk was attached to the particles' surfaces by stirring PhAMTES and the particles in toluene at room temperature overnight. The particles were washed several times in ethanol followed by water, using centrifugation. After the final washing, the particles were dried at room temperature under vacuum. Successful attachment of the stalk was confirmed by Fourier transform infrared (FT-IR) spectroscopy (Figure 5.6).

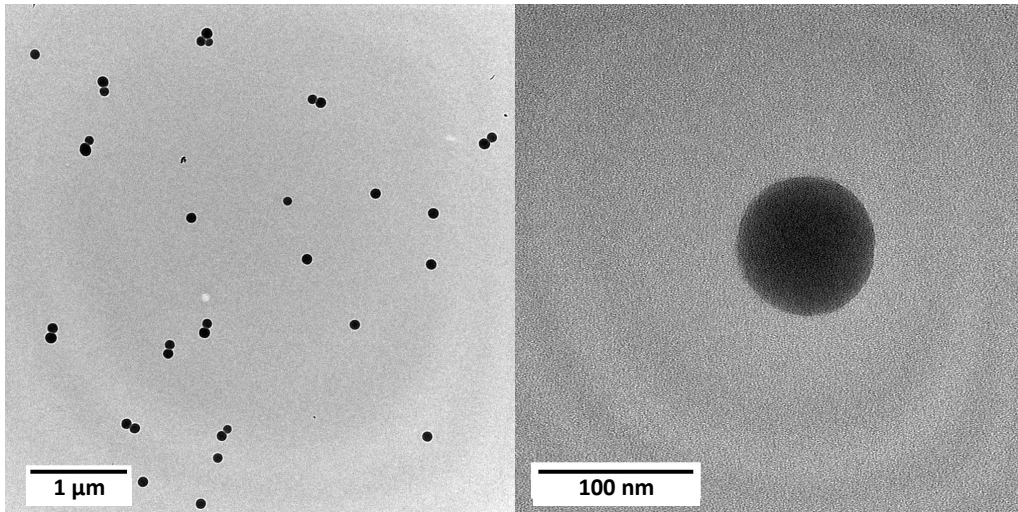


Figure 5.3. TEM images of the polystyrene beads.

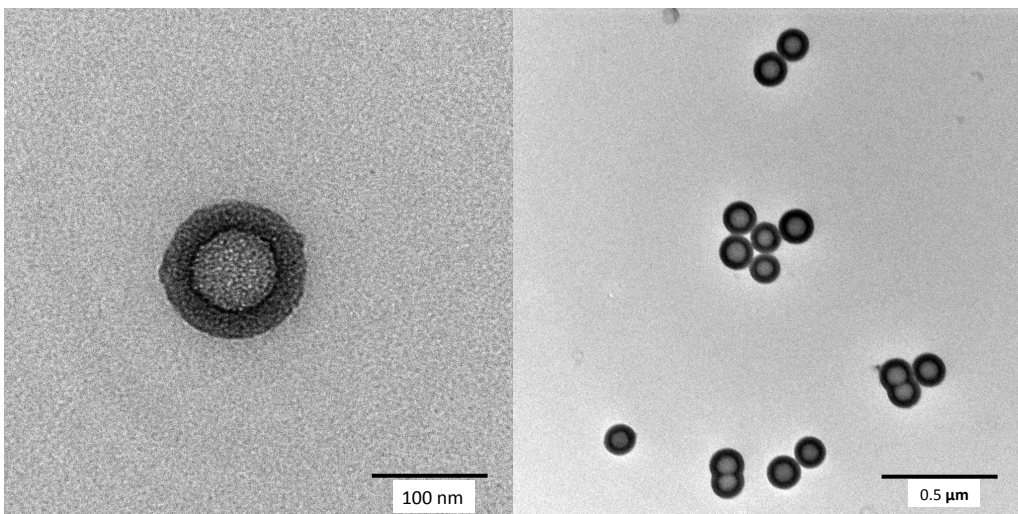


Figure 5.4. TEM images of template free hollow mesoporous silica nanoparticles.

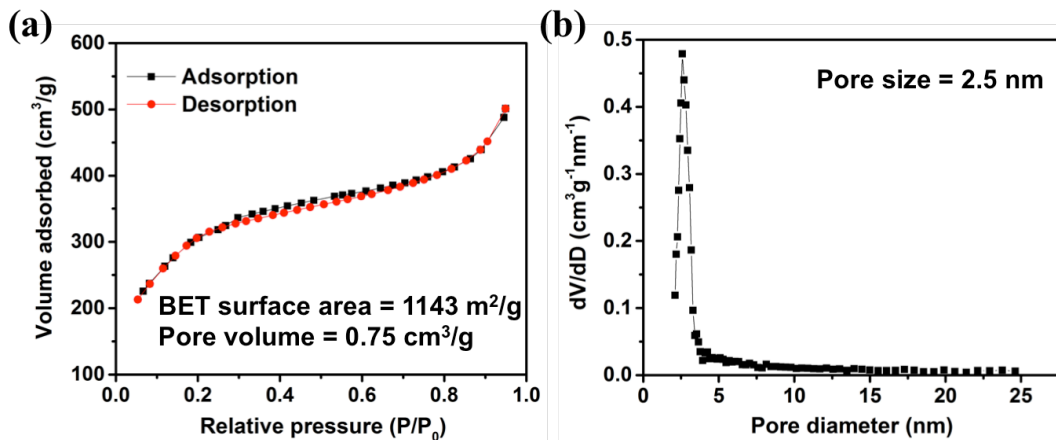


Figure 5.5. (a) N_2 adsorption/desorption isotherms of hollow mesoporous silica nanoparticles. The BET surface area and pore volume are $1143 \text{ m}^2/\text{g}$, and $0.75 \text{ cm}^3/\text{g}$, respectively. (b) Pore size distribution of hollow mesoporous silica nanoparticles. The pore size is 2.5 nm .

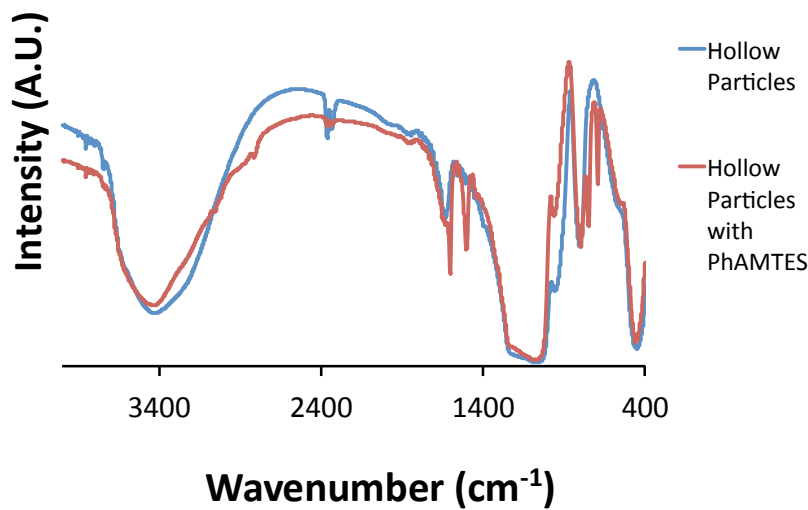


Figure 5.6. FT-IR spectra of hollow particles and hollow particles after PhAMTES modification. The band at 2900 cm^{-1} is assigned to C-H stretches and that at 1475 cm^{-1} is from aromatic C=C stretches.

In order to crystallize the metal salt inside the hollow cavity, the particles were added to a saturated solution of $1\cdot\text{PF}_6$ in DMSO/ H_2O followed by slow evaporation of the solvent at room temperature. The resulting material was washed twice with DMSO to remove residual $1\cdot\text{PF}_6$ from the surface and ensure that the surface phenyl groups on the silanes were accessible to αCD . Treatment with αCD in water completed the assembly of the $1\cdot\text{PF}_6$ -loaded mechanized core shell particles.

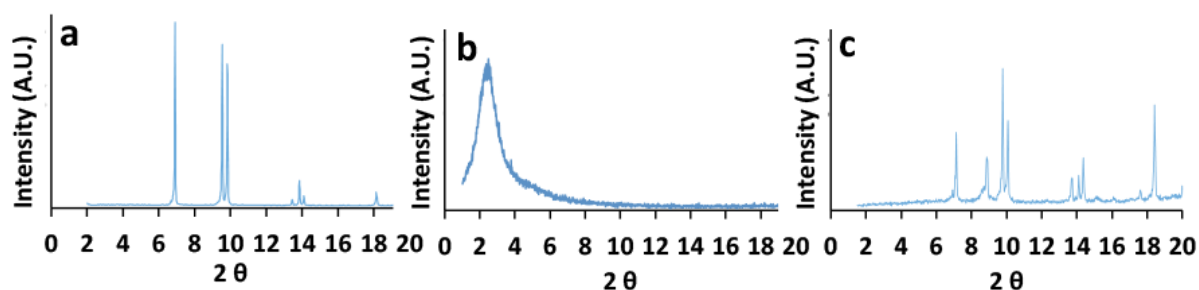


Figure 5.7. Powder XRD of (a) crystalline $1\cdot\text{PF}_6$, (b) bare hollow MSNs showing a peak around 2.3° from the ordered mesopores, and (c) hollow MSNs containing the crystallized $1\cdot\text{PF}_6$.

To establish that the hollow MSNs contained the crystalline form of the $1\cdot\text{PF}_6$, powder X-ray diffraction (pXRD) data were collected. Figure 5.7a shows a pXRD of the $1\cdot\text{PF}_6$ crystal displaying the expected diffraction peaks.³⁷ A pXRD of the bare hollow MSNs showed a very broad 2θ peak near 2.3° (Figure 5.7b), which gives a d spacing of 37 \AA , consistent with a pore diameter around 1.7 nm . The pXRD of the hollow MSNs with $1\cdot\text{PF}_6$ crystallized inside (Figure 5.7c) showed the peaks corresponding to the diffraction pattern of $1\cdot\text{PF}_6$ crystal. Slight peak shifting in the pXRD is attributed to the use of a different pXRD sample holder for the hollow MSNs containing $1\cdot\text{PF}_6$. These pXRD patterns provide evidence of the presence of crystalline $1\cdot\text{PF}_6$ inside the hollow cavity of the MSNs.

The response of the particles to perchlorate ions and changes in the pH in the aqueous environment was monitored by emission spectroscopy. 10 mg of the particles were placed in an NMR tube and a sufficient amount of water was added to just wet the particles (Figure 5.8). The emission spectra were excited at 448 nm and 514 nm. The wet sample of particles showed very weak emission as expected for crystals of the $\mathbf{1}\cdot\text{PF}_6$ salt. As shown in Figure 5.9ab, the emission signal at 690 nm remained essentially unchanged. After the addition of 40 μL of 0.03 M NaClO_4 , no change in intensity was observed. The absence of luminescence confirms that $\mathbf{1}\cdot\text{PF}_6$ inside the hollow particles is not accessible to perchlorate ion in the surrounding medium. It also proves that $\mathbf{1}\cdot\text{PF}_6$ is not on the surface of the particles. Then the pH was lowered to 3 by addition of 40 μL of an HCl solution to protonate the stalk. The emission intensity began to increase immediately and then began to level off to constant intensity after about 3 hours (Figure 5.10). This indicates that protonation of the anilinoalkane group allowed the ClO_4^- to enter inside the particles, converting $\mathbf{1}\cdot\text{PF}_6$ to $\mathbf{1}\cdot\text{ClO}_4\cdot\text{H}_2\text{O}$. Since $\mathbf{1}\cdot\text{PF}_6$ is practically insoluble in water, the luminescence also indicates that the reaction happens inside the particle where the crystal is located and does not arise from $\mathbf{1}\cdot\text{PF}_6$ being released from the particles. In order to ensure that the increase in intensity was caused by the perchlorate and not just the pH change, the same experiment was conducted without perchlorate (Figure 5.9c), and no change in the intensity was observed. This indicates that the acid alone has no effect on the emission intensity. Perchlorate was not blocked at all pH from particles without stalks (Figure 5.11).

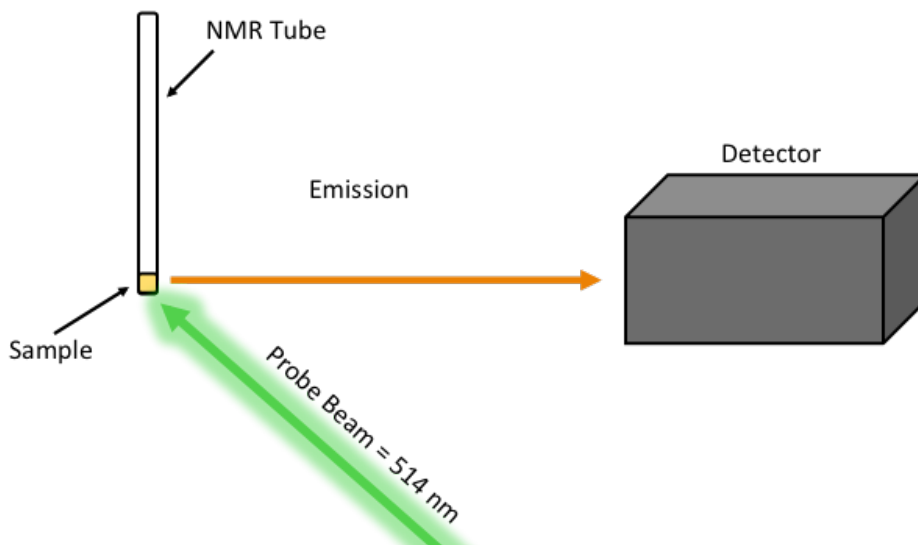


Figure 5.8. Experimental set up for sequential fluorescence spectra measurements.

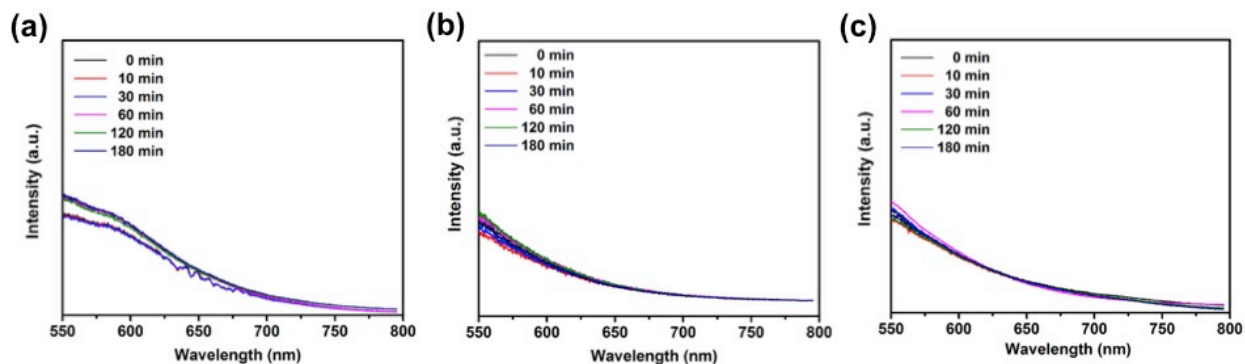


Figure 5.9. Luminescence spectra of the $1\cdot\text{PF}_6$ crystal-loaded hollow mesoporous nanoparticles with aniline stalks as a function of time (a) without the addition, (b) after the addition of ClO_4^- , and (c) after the addition of HCl when αCD is not used as a cap.

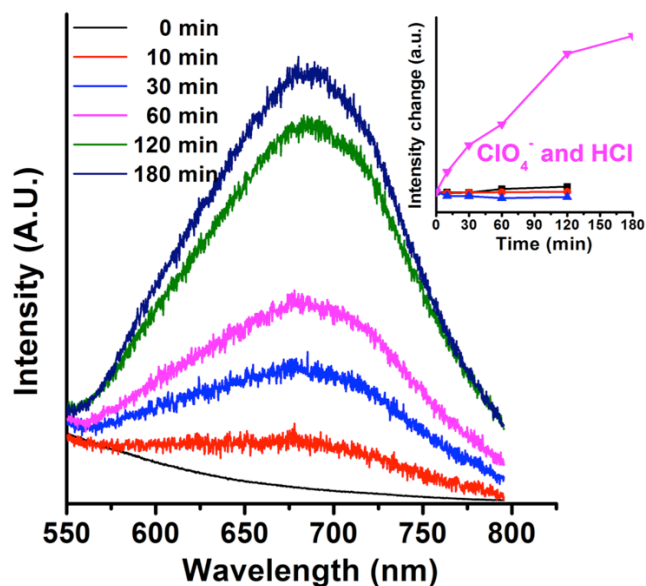


Figure 5.10. Luminescence spectra of nanoparticles gated by the PhAMTES stalk as a function of time after the addition of acid and perchlorate. A similar response occurs with particles capped with α CD.

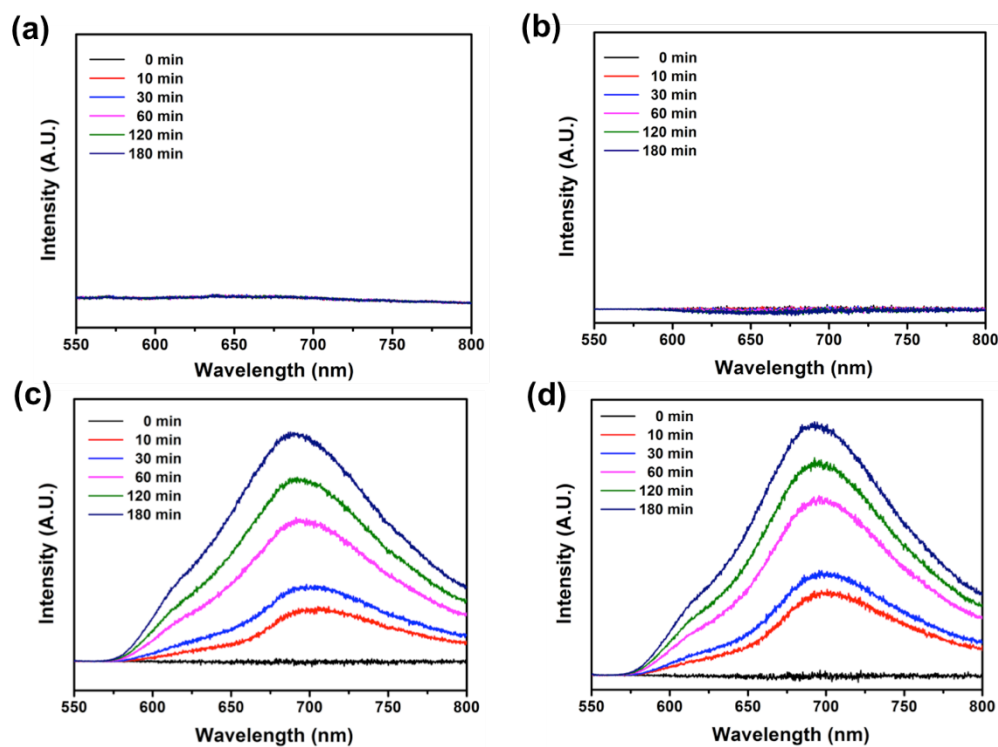


Figure 5.11. Luminescence spectra of the $1 \cdot \text{PF}_6$ crystal-loaded hollow mesoporous nanoparticles without aniline stalks as a function of time (a) without the addition, (b) after the addition of the HCl, (c) after the addition of ClO_4^- , and (d) after the addition of HCl and ClO_4^- .

The same series of experiments discussed above was repeated with particles capped by the bulky α CD, and the same results were obtained (Figure 5.12 and Figure 5.13). Thus, although the bulky neutral α CD may play a role, it is not necessary for gating the perchlorate anion. The combination of electrostatic repulsion of perchlorate from the negatively charged silanol groups on the particles and the presence of the hydrophobic anilinoalkane stalks prevents entrance of perchlorate. Upon protonation, the cationic stalk attracts perchlorate to the pores. However, in applications where the analytes are neutral or cationic molecules, the physical pore-blocking capability of α CD may be required.

Selectivity based on “AND” logic requires two inputs. In this case, the inputs are chemical stimuli that both must be present in order to trigger a response. A handful of nanoparticles responsive to dual stimuli have been reported, all involving cargo release. The stimuli include pH and light, pH and redox, pH and temperature, pH and ATP. But in each of these cases, the responses involve “OR” logic because either one or the other of the inputs opens the valve and releases the cargo. The system described here exhibits true “AND” logic where both chemical stimuli, namely pH and perchlorate analyte, are required to form the luminescent crystal inside the particle. The Boolean ‘truth table’ is shown in Figure 5.14. This additional level of control is proof of concept of a nanomaterial designed to operate only under specific, predefined conditions (in this case an aquatic location containing acidic perchlorate). The active element is protected and can travel to the target site before it is activated by the specific condition.

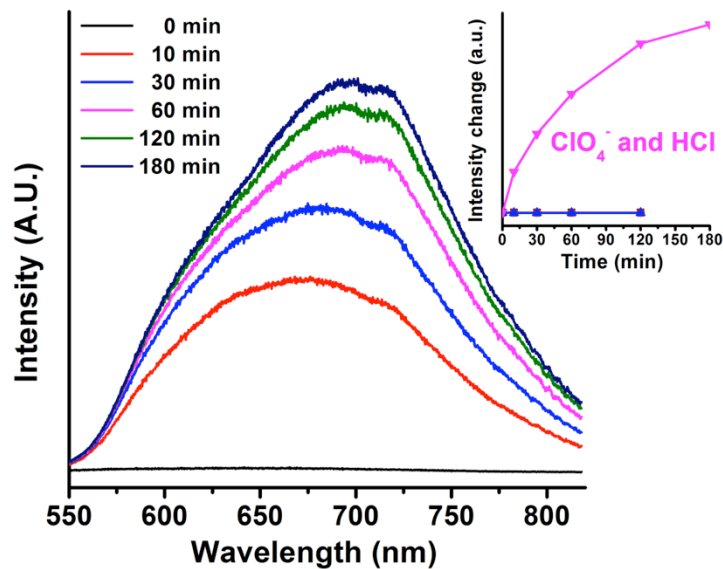


Figure 5.12. Luminescence spectra of nanoparticles gated by the PhAMTES stalk and α CD as a function of time after the addition of acid and perchlorate.

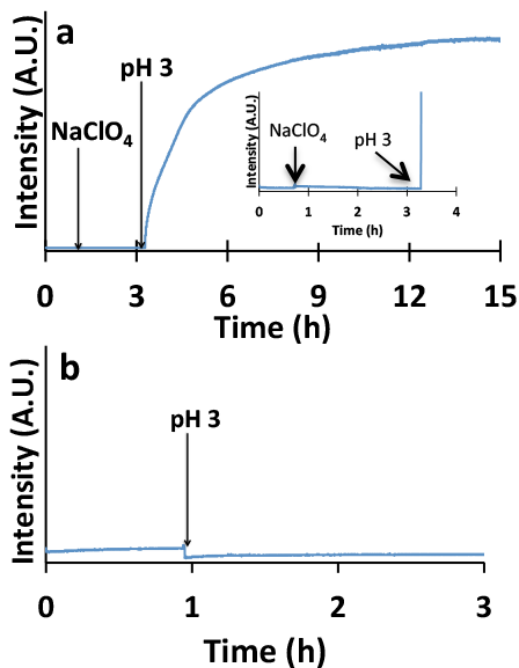


Figure 5.13. (a) Emission intensity at 690 nm as a function of time. At ~ 45 minutes NaClO_4^- was added and after 2.5 hours the system was brought to a pH of 3. Inset shows close up of NaClO_4^- addition and pH lowering. (b) Emission intensity at 690 nm as a function of time. At ~ 55 minutes the system was brought to a pH of 3 and no change in the intensity was observed.

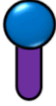


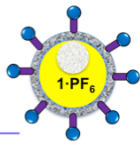



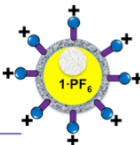
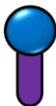


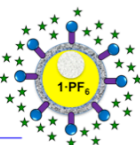


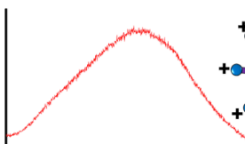
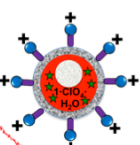
Input 1 (Acid)	Input 2 (Perchlorate)	Output (Luminescence)
0 	0 NONE 	0  
1 + 	0 + 	0  
0 	1 	0  
1 + 	1 + 	1  

Figure 5.14. Truth table of the AND gate. Input 1 is acidification to pH 3, and input 2 is the perchlorate ion. The numbers 1 and 0 in the figure represent “True” and “False”, respectively. The output is the luminescence of $1 \cdot \text{ClO}_4 \cdot \text{H}_2\text{O}$ inside the hollow nanoparticles. Nanoparticles with only the stalk (left of dashed line) and those capped by αCD (right) function similarly.

5.4 Conclusions

In summary, a gated nanoparticle with designed selectivity was synthesized using hollow mesoporous silica, ship-in-a-bottle synthesis of the molecular crystalline solid state detector, and protection of the crystal by the pores' gates. In contrast to the usual nanovalves where gating is caused by steric blockage by a cyclodextrin (CD) cap, gating of perchlorate is governed by the stalk. The system demonstrates the inverse application of the gate – protection of the contents followed by selective exposure rather than trapping of contents followed by their release. This concept may find future applications in environmental sensing and in biomedical diagnostics.

5.5 Acknowledgment

This work was funded by NIH RO1 CA133697, the NSF (CHE-1152853, CHE-1566438), and the STAR fellowship Assistance Agreement no. FP-917659 awarded by EPA.

5.6 References

1. S. Alayoglu, A. U. Nilekar, M. Mavrikakis and B. Eichhorn, *Nat. Mater.* **2008**, *7*, 333-338.
2. A. Z. M. Badruddoza, M. T. Rahman, S. Ghosh, M. Z. Hossain, J. Shi, K. Hidajat and M. S. Uddin, *Carbohydr. Polym.* **2013**, *95*, 449-457.
3. Y. T. Chang, P. Y. Liao, H. S. Sheu, Y. J. Tseng, F. Y. Cheng and C. S. Yeh, *Adv. Mater.* **2012**, *24*, 3309-3314.
4. R. G. Chaudhuri and S. Paria, *Chem. Rev.* **2012**, *112*, 2373-2433.
5. C. F. Hoener, K. A. Allan, A. J. Bard, A. Campion, M. A. Fox, T. E. Mallouk, S. E. Webber and J. M. White, *J. Mater. Chem.* **1992**, *96*, 3812-3817.
6. Y. Jiao, J. Guo, S. Shen, B. Chang, Y. Zhang, X. Jiang and W. Yang, *J. Mater. Chem.* **2012**, *22*, 17636-17643.
7. J. Joo, J. F. Cruz, S. Vijayakumar, J. Grondek and M. J. Sailor, *Adv. Funct. Mater.* **2014**, *24*, 5687-5687.
8. A. Khanal, Y. Inoue, M. Yada and K. Nakashima, *J. Am. Chem. Soc.* **2007**, *129*, 1534-1535.
9. N. Ž. Knežević, E. Ruiz-Hernández, W. E. Hennink and M. Vallet-Regí, *RSC Adv.* **2013**, *3*, 9584-9593.
10. I. S. Lee, N. Lee, J. Park, B. H. Kim, Y.-W. Yi, T. Kim, T. K. Kim, I. H. Lee, S. R. Paik and T. Hyeon, *J. Am. Chem. Soc.* **2006**, *128*, 10658-10659.
11. V. Salgueiriño-Maceira and M. A. Correa-Duarte, *Adv. Mater.* **2007**, *19*, 4131-4144.
12. A. K. Samal, L. Polavarapu, S. Rodal-Cedeira, L. M. Liz-Marzán, J. Pérez-Juste and I. Pastoriza-Santos, *Langmuir* **2013**, *29*, 15076-15082.
13. A. Schloßbauer, A. M. Sauer, V. Cauda, A. Schmidt, H. Engelke, U. Rothbauer, K. Zolghadr, H. Leonhardt, C. Bräuchle and T. Bein, *Adv. Healthcare Mater.* **2012**, *1*, 316-320.
14. J. Zhang and R. D. K. Misra, *Acta Biomater.* **2007**, *3*, 838-850.
15. A. Kortan, R. Hull, R. Opila, M. Bawendi, M. Steigerwald, P. Carroll and L. E. Brus, *J. Am. Chem. Soc.* **1990**, *112*, 1327-1332.
16. L. Qi, J. Ma, H. Cheng and Z. Zhao, *Colloids Surf. A* **1996**, *111*, 195-202.
17. S. Balakrishnan, M. J. Bonder and G. C. Hadjipanayis, *J. Magn. Magn. Mater.* **2009**, *321*, 117-122.
18. M.-J. Kim, Y.-H. Choa, D. H. Kim and K. H. Kim, *Magnetics, IEEE Transactions on* **2009**, *45*, 2446-2449.
19. S. Laurent, D. Forge, M. Port, A. Roch, C. Robic, L. Vander Elst and R. N. Muller, *Chem. Rev.* **2008**, *108*, 2064-2110.
20. F. Caruso, *Adv. Mater.* **2001**, *13*, 11-22.
21. J. Amalvy, M. Percy, S. Armes and H. Wiese, *Langmuir* **2001**, *17*, 4770-4778.

22. M. Lal, L. Levy, K. Kim, G. He, X. Wang, Y. Min, S. Pakatchi and P. Prasad, *Chem. Mater.* **2000**, *12*, 2632-2639.
23. X. Xu, G. Friedman, K. D. Humfeld, S. A. Majetich and S. A. Asher, *Chem. Mater.* **2002**, *14*, 1249-1256.
24. M.-C. Daniel and D. Astruc, *Chem. Rev.* **2004**, *104*, 293-346.
25. S. Phadtare, A. Kumar, V. Vinod, C. Dash, D. V. Palaskar, M. Rao, P. G. Shukla, S. Sivaram and M. Sastry, *Chem. Mater.* **2003**, *15*, 1944-1949.
26. L. Du, S. Liao, H. A. Khatib, J. F. Stoddart and J. I. Zink, *J. Am. Chem. Soc.* **2009**, *131*, 15136-15142.
27. P. Yang, H. Gai, J. Lin, *Chem. Soc. Rev.* **2012**, *41*, 3679-3698.
28. M. Xue and J. I. Zink, *J. Am. Chem. Soc.* **2013**, *135*, 17659-17662.
29. X. Chen, A. H. Soeriyadi, X. Lu, S. M. Sagnella, M. Kavallaris and J. J. Gooding, *Adv. Funct. Mater.* **2014**, *24*, 6999-7006.
30. D. Xiao, H. Z. Jia, J. Zhang, C. W. Liu, R. X. Zhuo and X. Z. Zhang, *Small* **2014**, *10*, 591-598.
31. H. Yan, C. Teh, S. Sreejith, L. Zhu, A. Kwok, W. Fang, X. Ma, K. T. Nguyen, V. Korzh and Y. Zhao, *Angew. Chem. Int. Ed.* **2012**, *51*, 8373-8377.
32. X. Ma, O. S. Ong and Y. Zhao, *Biomater. Sci.* **2013**, *1*, 912-917.
33. E. Aznar, R. Casasús, B. García-Acosta, M. D. Marcos, R. Martínez-Máñez, F. Sancenón, J. Soto and P. Amorós, *Adv. Mater.* **2007**, *19*, 2228-2231.
34. B. Chang, D. Chen, Y. Wang, Y. Chen, Y. Jiao, X. Sha and W. Yang, *Chem. Mater.* **2013**, *25*, 574-585.
35. A. Agostini, L. Mondragón, L. Pascual, E. Aznar, C. Coll, R. n. Martínez-Máñez, F. I. Sancenón, J. Soto, M. D. Marcos and P. Amorós, *Langmuir* **2012**, *28*, 14766-14776.
36. S. Angelos, Y.-W. Yang, N. M. Khashab, J. F. Stoddart and J. I. Zink, *J. Am. Chem. Soc.* **2009**, *131*, 11344-11346.
37. S. D. Taylor, W. Howard, N. Kaval, R. Hart, J. A. Krause and W. B. Connick, *Chem. Commun.* **2010**, *46*, 1070-1072.
38. T. J. Wadas, Q.-M. Wang, Y.-j. Kim, C. Flaschenreim, T. N. Blanton and R. Eisenberg, *J. Am. Chem. Soc.* **2004**, *126*, 16841-16849.
39. M. L. Muro, C. A. Daws and F. N. Castellano, *Chem. Commun.* **2008**, *46*, 6134-6136.
40. P. Du, J. Schneider, W. W. Brennessel and R. Eisenberg, *Inorg. Chem.* **2008**, *47*, 69-77.
41. A. Kobayashi, Y. Fukuzawa, S.-i. Noro, T. Nakamura and M. Kato, *Chem. Lett.* **2009**, *38*, 998-999.
42. P. Du, *Inorg. Chim. Acta* **2010**, *363*, 1355-1358.

43. J. S. Field, C. D. Grimmer, O. Q. Munro and B. P. Waldron, *Dalton Trans.* **2010**, *39*, 1558-1567.
44. E. J. Rivera, C. Barbosa, R. Torres, L. Grove, S. Taylor, W. B. Connick, A. Clearfield and J. L. Colón, *J. Mater. Chem.* **2011**, *21*, 15899-15902.
45. R. Zhang, Z. Liang, A. Han, H. Wu, P. Du, W. Lai and R. Cao, *CrystEngComm* **2014**, *16*, 5531-5542.
46. S. D. Taylor, A. E. Norton, R. T. Hart, M. K. Abdolmaleki, J. A. Krause and W. B. Connick, *Chem. Commun.* **2013**, *49*, 9161-9163.
47. E. T. Urbansky, *Biorem. J.* **1998**, *2*, 81-95.
48. B. Gu and J. D. Coates, *Perchlorate: environmental occurrence, interactions and treatment*, Springer Science & Business Media, **2006**.
49. S.-C. Shen, W. K. Ng, Z. Shi, L. Chia, K. G. Neoh and R. B. H. Tan, *J. Mater. Sci. - Mater. Med.* **2011**, *22*, 2283-2292.
50. C. E. Reese, C. D. Guerrero, J. M. Weissman, K. Lee and S. A. Asher, *J. Colloid Interface Sci.* **2000**, *232*, 76-80.